Engineered silk-based biomimetic hydrogels for cell growth

By

Jasmin Whittaker

(B. Eng. Hons)

A thesis submitted for the degree of

Doctor of Philosophy

Engineering: Minerals and Materials

Ian Wark Research Institute

Division of Information Technology, Engineering and the Environment



October 2015

Dedication

This thesis is dedicated to the memory of my Nanna,

for her endless love and support throughout my life

Table of contents

Abstract x

List of Abbreviations and Symbols xv

Declaration xviii

Acknowledgements xix

List of publications xxi

Chapter 1: Introduction and Literature Review 1

1.1 Introduction 1

1.1.1 Tissue engineering 1

1.2 Fundamentals of hydrogels 3

1.3 Physical hydrogels 7

1.3.1 Physical hydrogels from stimuli-responsive polymers 8

1.3.1.1 Physical hydrogels from thermo-responsive biopolymers 9

1.3.1.2 Physical hydrogels from thermo-responsive synthetic polymers 10

1.3.2 Self-assembling peptide and protein hydrogels 11

1.3.3 Coassembled hydrogels with tuneable responsiveness 14

1.3.3.1 Structural investigation of self- and coassembling protein-based systems 15

1.3.4 Natural and synthetic physically crosslinked hydrogels used for cartilage tissue engineering 17

1.4 Chemical hydrogels 18

1.4.1 Chemically crosslinked hydrogels from naturally occurring polymers 19

1.4.2 Chemically crosslinked hydrogels based on synthetic polymers 22

1.4.3 Natural and synthetic chemically crosslinked hydrogels used for cartilage tissue engineering 24

1.5 Hybrid hydrogels 26

1.5.1 Hybrid material synthesis 26

1.5.2 Methods of fabricating hybrid hydrogels with enhanced properties 27

1.5.3 Fabrication and mechanical properties of DN hydrogels 28

1.6 Understanding the microstructure of hydrogels using small angle neutron scattering techniques 31

1.7 Evaluation of hybrid hydrogels for tissue engineering applications 32

1.8 Biomimetic fabrication of nanofibrous materials by electrospinning 36

1.8.1 Electrospinning to form nanofibrous mats for tissue engineering 36

1.8.2 Co-axial electrospinning to form core/shell nanofibrous mats 37

1.8.3 Core/shell electrospun fibres/mats for tissue engineering 38
1.9 Effect of elasticity, stiffness and swelling capacity on cellular interaction and differentiation 40
1.10 Aims and Scope of the Project 42
1.11 References 44
Chapter 2: Experimental methodology 56
2.1 Chemicals, solvents and materials 56
2.2 Synthesis and fabrication methods 58
2.2.1 Preparation of regenerated silk fibroin solution 58
2.2.2 Synthesis and purification of Rec1-resilin 59
2.2.3 Synthesis of Poly(N-vinylcaprolactam) by free radical polymerisation 61
2.2.4 Hydrogel formation by photo-chemical crosslinking 61
2.2.5 Electrospinning of RSF and PVCL (conventional and co-axial) 62
2.3 Characterisation techniques 64
2.3.1 Spectroscopic techniques 64
2.3.1.1 Circular dichroism (CD) spectroscopy 64
2.3.1.2 Photo-acoustic Fourier transform infrared (PA-FTIR) spectroscopy 65
2.3.1.3 Nuclear magnetic resonance (NMR) spectroscopy 66
2.3.2 Scattering techniques 66
2.3.2.1 Dynamic light scattering (DLS) 66
2.3.2.2 Small angle scattering – background 67
2.3.2.3 Small angle X-ray scattering (SAXS) 69
2.3.2.4 Small angle neutron scattering (SANS) 69
2.3.2.5 Ultra small angle neutron scattering (USANS) 70
2.3.3 Microscopic techniques 70
2.3.3.1 Scanning electron microscopy (SEM) 70
2.3.3.2 Transmission electron microscopy (TEM) 71
2.3.3.3 Atomic force microscopy (AFM) 72
2.3.4 Thermal analysis techniques 73
2.3.4.1 Differential scanning calorimetry (DSC) 73
2.3.4.2 Thermogravimetric analysis (TGA) 74
2.3.5 Mechanical testing 75
2.3.5.1 Dynamic mechanical analysis (DMA) 75
2.3.5.2 Tensile testing 75
2.3.6 Contact angle measurement – sessile drop technique 76
2.3.7 X-ray diffraction (XRD) 76

2.3.8 Photophysical characterisation 77
2.3.8.1 UV-vis absorption spectroscopy 77
2.3.8.2 Fluorescence spectroscopy 78
2.4 Cell culture study 78
2.4.1 ATDC5 pre-chondrocyte cell line 78
2.4.2 Assessment of ATDC5 cell adhesion on BMWS-based hydrogels 78
2.4.3 Culture of ATDC5 cells on RSF-based hydrogels 79
2.4.4 Cell fixation and SEM analysis to assess cell adhesion and proliferation 79
2.4.5 Assessment of cell proliferation and viability 80
2.4.6 Evaluation of the chondrogenic differentiation of ATDC5 cells cultured on RSF-based hydrogels 80
2.5 References 83
Chapter 3: Tunable thermo-responsiveness of Resilin via coassembly with rigid biopolymers 85
3.1 Research article 86
3.2 Supplementary information 96
Chapter 4: Facile and rapid ruthenium mediated photo-crosslinking of *Bombyx mori* silk fibroin 103
4.1 Research article 104
4.2 Supplementary information 116
Chapter 5: Engineering silk-based hybrid hydrogels 120
5.1 Fabrication of highly elastic resilin/silk fibroin based hydrogel by rapid photo-crosslinking reaction 121
5.1.1 Research article 121
5.1.2 Supplementary information 125
5.2 Engineered DN hydrogels from regenerated silk fibroin and poly(N-vinylcaprolactam) 134
5.2.1 Abstract 134
5.2.2 Introduction 134
5.2.3 Experimental 136
5.2.3.1 Materials 136
5.2.3.2 Dynamic light scattering (DLS) 137
5.2.3.3 Hydrogel preparation 137
5.2.3.4 Thermogravimetric analysis (TGA) 137
5.2.3.5 Water uptake studies 138
5.2.3.6 Differential scanning calorimetry (DSC) 138

5.2.3.7 Dynamic mechanical analysis (DMA) 138
5.2.3.8 Tensile testing 138
5.2.3.9 Photo-acoustic Fourier transform infrared spectroscopy (PA-FTIR) 139
5.2.3.10 Hydrogel degradation in Phosphate buffered saline 139
5.2.4 Results and Discussion 139
5.2.4.1 Effect of RSF on the phase transition behaviour of PVCL 139
5.2.4.2 Compositional analysis of the RSF/PVCL DN hydrogels from TGA 141
5.2.4.3 Effect of RSF/PVCL hydrogel composition on swelling capacity 144
5.2.4.4 Phase behaviour of dehydrated and swollen RSF/PVCL hydrogels 145
5.2.4.5 Viscoelastic properties of the RSF/PVCL DN hydrogels by DMA 146
5.2.4.6 Toughness of the RSF and $S_{70}P_{30}$ hydrogels 149
5.2.4.7 RSF/PVCL hydrogel secondary structure by FTIR 150
5.2.4.8 Degradation in PBS 152
5.2.5 Conclusions 152
5.2.6 References 153
5.2.7 Supplementary information 157
Chapter 6: Electrospinning to form biomimetic nanofibrous mats 160
6.1 Induced insolubility of electrospun Poly(N-vinylcaprolactam) fibres through hydrogen bonding with Tannic acid 161
6.1.1 Abstract 161
6.1.2 Introduction 161
6.1.3 Materials and methods 163
6.1.3.1 Materials 163
6.1.3.2 Solution preparation 164
6.1.3.3 Measurement of solution viscosity 164
6.1.3.4 Electrospinning 164
6.1.3.5 Electrospun fibre characterisation by scanning electron microscopy 164
6.1.3.6 Porosity measurement 165
6.1.3.7 Interactions of water with the electrospun fibres 165
6.1.3.8 Contact angle measurements 165
6.1.3.9 Fourier transform infrared spectroscopy of TA/PVCL electrospun fibres 165
6.1.3.10 Thermogravimetric analysis of TA/PVCL electrospun fibres 166
6.1.4 Results and Discussion 166
6.1.4.1 Interaction of TA and PVCL in solution using rheology 166
6.1.4.2 Characterisation of TA/PVCL electrospun fibre diameter and morphology 169

6.1.4.3 Effect of water on the morphology of electrospun TA/PVCL fibres 171
6.1.4.4 Wettability of TA/PVCL electrospun mats 173
6.1.4.5 Structural analysis of TA/PVCL electrospun mats 175
6.1.4.6 Thermogravimetric analysis of TA/PVCL electrospun mats 176
6.1.5 Conclusions 177
6.1.6 References 178
6.1.7 Supplementary information 180
6.2 Facile fabrication of shell crosslinked core/shell Poly(N-vinylcaprolactam)/ Silk fibroin fibres by co-axial electrospinning 183
6.2.1 Abstract 183
6.2.2 Introduction
6.2.3 Materials and methods 185
6.2.3.1 Materials 185
6.2.3.2 RSF and PVCL solution preparation 185
6.2.3.3 Measurement of solution viscosity 186
6.2.3.4 Conventional electrospinning of RSF and PVCL 186
6.2.3.5 Co-axial electrospinning of PVCL/RSF to form core/shell fibres 186
6.2.3.6 SEM analysis of electrospun fibres 187
6.2.3.7 Thermogravimetric analysis (TGA) 187
6.2.3.8 Transmission electron microscopy (TEM) 187
6.2.4 Results and Discussion 187
6.2.4.1 Electrospinning of RSF from HFIP 191
6.2.4.2 Electrospinning of PVCL from HFIP 193
6.2.4.3 Optimisation of co-axial electrospinning of PVCL and RSF for the production of core/shell fibres 195
6.2.4.4 Composition of PVCL/RSF fibres from co-axial electrospinning 198
6.2.4.5 TEM analysis of PVCL/RSF core/shell fibres 201
6.2.5 Conclusions 203
6.2.6 References 203
Chapter 7: Investigation into the microstructure of silk-based hydrogels using small and ultra small angle neutron scattering 205
7.1 Abstract 206
7.2 Introduction 206
7.3 Experimental 208
7.3.1 Materials 208
7.3.2 Solution preparation 208

7.3.3 Hydrogel preparation and properties 209
7.3.4 Small angle X-ray scattering 209
7.3.5 Small angle neutron scattering 210
7.3.6 Ultra small angle neutron scattering 210
7.3.7 Background to hydrogel structure and data analysis 210
7.4 Results 214
7.4.1 Physical properties of RSF-based hydrogels 214
7.4.2 Structure, conformational ensemble and morphology of RSF, Rec1-resilin And PVCL in dilute solution by SANS 214
7.4.3 Effect of concentration on the size and morphology of RSF in solution by SAXS and SANS 216
7.4.4 USANS/SANS data for RSF-based hydrogels 220
7.4.4.1 SANS analysis of RSF-based hydrogels 221
7.4.4.2 USANS analysis of RSF-based hydrogels 228
7.5 Discussion 231
7.5.1 Solution study by SANS, USANS and SAXS 231
7.5.2 USANS/SANS study of RSF-based hydrogels 232
7.5.3 *GuinierPorod* fitting of SANS data of RSF-based hydrogels 233
7.5.4 *GuinierPorod* fitting of USANS data of RSF-based hydrogels 234
7.6 Conclusions 235
7.7 References 235
Chapter 8: Chondrocyte response to regenerated silk fibroin-based hybrid hydrogels 239
8.1 Abstract 240
8.2 Introduction 240
8.3 Experimental 242
8.3.1 Assessment of ATDC5 cell adhesion and proliferation 242
8.3.2 Total RNA extraction, cDNA synthesis, and real-time PCR (RT-PCR) analysis 243
8.3.3 Statistical analysis 245
8.4 Results and Discussion 246
8.4.1 Physical properties of RSF-based hydrogels 246
8.4.2 Comparison of growth of ATDC5 cells on RSF hydrogels and TCP 246
8.4.3 Gene analysis for chondrogenic and osteogenic markers on RSF hydrogels and TCP 249
8.4.4 ATDC5 cell growth on Rec1-resilin/RSF hybrid hydrogels 252
8.4.5 ATDC5 cell growth on RSF/PVCL DN hydrogels 254

8.4.6 Analysis of chondrogenic markers on RSF-based hybrid hydrogels 256
8.5 Conclusions 259
8.6 References 260
Chapter 9: Summary and Recommendations 262
9.1 Summary 262
9.2 Recommendations 264

Abstract

Hydrogels are an important class of material that are suitable for a wide range of applications because of their high water content and tuneable elasticity. They have demonstrated great potential to stimulate the regeneration of soft and hard tissues in the body. The structure of hydrogels, which are made up of physically or chemically crosslinked polymers of natural or synthetic origin, mimics the structure of the native extracellular matrix (ECM); which makes them ideal candidates for tissue engineering applications. The required characteristics of a hydrogel for tissue engineering are diverse and include suitable elastic modulus, mechanical strength, toughness, water retention and swelling capacity, biocompatibility and biodegradability. However, the specific mechanical requirements differ depending on the location and function of the tissues in the body and thus tuneability of the hydrogel properties is important for versatility of use. Currently, significant work has been carried out in the area of hydrogels for tissue engineering applications, and these include hydrogels prepared from natural and synthetic origin. Synthetic hydrogels provide the opportunity to precisely control their properties; however, a key shortcoming of many synthetic gels is their bioinertness. On the contrary, protein and peptide based materials, due to their inherent structure and composition, create bioactive materials that elicit controlled cellular adhesion and maintain expression of the differentiated phenotype. Also, hydrogels are typically soft and fragile materials, which limit their use for tissue engineering where mechanical integrity is required, in particular for load-bearing tissues such as cartilage that possess modulus values on the mega Pascal (MPa) scale. In order to address the deficiencies of hydrogels composed of single network polymers, a range of hybrid hydrogels have been developed in recent years. Current hybrid hydrogel materials generally possess time consuming preparation methods, do not provide a conducive biomimetic environment, or have insufficient mechanical properties. Thus, the significant challenge exists to develop new rapid methods of preparing hybrid hydrogels that can be applied as injectable systems, whilst also retaining the required elasticity, toughness, swelling and biomimetic properties. The *in vitro* facile fabrication of such hydrogels represents a significant step towards the advancement of tissue engineering. Therefore, one of the key questions is how to create a three-dimensional gel platform equipped with relevant cues to achieve specific biological response. The present research

focuses on a pivotal study primarily on engineering silk-based hydrogels as a platform for *in vitro* cell growth.

Regenerated silk fibroin (RSF) prepared from the raw silk extracted from the *Bombyx mori* silkworm is a unique natural material, which possesses excellent properties for biomaterials development, including mechanical strength, biocompatibility, ability to support cell adhesion and proliferation and controlled biodegradability. Extensive work has been carried out on the formation of physically crosslinked RSF hydrogels; however, the formation of chemically crosslinked RSF hydrogels with tuneable elasticity and stiffness remains an area to be studied. Also, one drawback of RSF is its rigidity, which is limiting for applications that require elasticity. Cellular growth and differentiation in two-dimensional as well as three-dimensional space requires the presence of a structured environment with which the cell can interact. Understanding the role of matrix modulus/elasticity in cell signalling processes, and using this knowledge to develop unique strategies for tissue regeneration is highly challenging and requires significant research.

In light of the above challenges and need, it is hypothesised that RSF-based hybrid biomaterials will provide an ideal biomimetic environment for cell growth. Thus, three types of RSF-based hydrogels were investigated in this study that employ physical interactions, chemical crosslinking, and chemical crosslinking in the presence of non-covalent interactions. The RSF-based hybrid hydrogels were formed with a highly elastic and resilient biomimetic protein, Rec1-resilin, and a synthetic thermo-responsive polymer, poly(N-vinylcaprolactam). In addition, the formation of electrospun mats that harness physical interactions and thermo-responsiveness were prepared. A range of experimental methods were employed to understand the fundamental structure-property relationship of the hydrogels and evaluate their capacity to support the growth and differentiation of chondrocytes (cartilage cells). The RSF-based hydrogels exhibited tuneable swelling and elasticity properties that provide potential for their use in a range of tissue engineering applications and serve as a platform for further development of RSF-based biomaterials.

The thesis is presented in 9 chapters. Chapter 1 gives an introduction to the fundamentals of hydrogels and the different types of physical and chemical hydrogels that have been studied for tissue engineering applications. Also, the different types of hybrid hydrogels and their associated properties and deficiencies are presented. A discussion of electrospinning to form alternate biomimetic materials to hydrogels is presented, with a focus on the use of co-axial

electrospinning to form hybrid core/shell fibres. In addition, a detailed discussion on the microstructure analysis of hydrogels using neutron scattering is presented. Finally, a summary of the current knowledge of the effect of biomaterial properties on cellular interactions and differentiation is detailed. Based on the reported literature, the hypothesis, aim and scope of this research are discussed.

Chapter 2 is related to the materials, synthesis and fabrication methods used in this research. Also, the working principles of different instruments, including spectroscopic, scattering, microscopic and thermal analysis techniques are discussed. Furthermore, the details of the cell culture methods used to assess the biocompatibility of the materials and evaluate their potential for cartilage tissue engineering are presented.

In Chapter 3 the formation of a physical hydrogel by coassembly of Rec1-resilin with a rigid model polypeptide (poly-L-proline) and a hydrophobic rigid protein (RSF) is presented for the first time. The change in conformation and morphology of the coassemblies were studied with time using a range of techniques including spectroscopic, scattering, thermal analysis and microscopic techniques. The present work confirms that the lower critical solution temperature (LCST) of the hybrid hydrogels can be tuned to lower values by inducing more ordered conformations and increasing the hydrophobicity. Also, this process allows for the formation of a Rec1-resilin/RSF hydrogel with irreversible physical interactions. This work provides new insight into the ability to employ facile coassembly to tune thermo-responsiveness, which are useful for a wide range of application, including drug delivery and soft tissue engineering applications.

Chapter 4 demonstrates the facile and rapid fabrication of ruthenium catalysed photo-crosslinked RSF hydrogels for the first time. A detailed study into the effect of reactant concentrations is presented. Also, the RSF hydrogels have been characterised using a range of techniques, including water uptake, differential scanning calorimetry (DSC), dynamic mechanical analysis (DMA), photo-acoustic Fourier transform infrared spectroscopy (PA-FTIR), and X-ray diffraction (XRD). The ability to tune the physical properties of the RSF hydrogels through the change in the level of hydration is presented. Furthermore, the structural analysis demonstrated that the chemically crosslinked hydrogels contained predominantly the amorphous RSF. The cell culture studies demonstrated the potential for these hydrogels in tissue engineering applications. This work provides a new and rapid way of chemically crosslinking RSF, which has not been demonstrated before.

Chapter 5 is presented in two parts. Part 5.1 reports the fabrication of a new type of hybrid hydrogel combining the highly elastic soft phase of a biomimetic elastic protein, Rec1-reslin, and the mechanically strong hard phase of RSF through a rapid ruthenium-mediated photo-crosslinking method. The Rec1-resilin/RSF hybrid hydrogels were shown to exhibit tuneable swelling and modulus values suggesting their suitability for cartilage tissue engineering. A detailed characterisation of the hydrogels using water uptake, DSC, DMA and PA-FTIR is presented. In Part 5.2, a series of double network (DN) hydrogels fabricated using a one-pot method is presented. The DN hydrogels combine the photo-crosslinked rigid phase of RSF with the softer synthetic polymer (PVCL) through strong physical interactions; and are shown to exhibit tuneable water uptake capacity, elasticity and toughness. The enhanced DN hydrogel properties studied through water uptake, DSC, DMA, tensile testing and PA-FTIR make them promising materials for cartilage regeneration applications. This chapter provides insight in the formation of hybrid materials by forming interactions with rigid and hard phases and how this results in biomaterials with enhanced properties.

Chapter 6 is presented in two parts. In Part 6.1, the excellent electrospinnability and thermo-responsiveness of PVCL were harnessed and a facile one-step procedure was employed to prepare PVCL/tannic acid (TA) fibres that are insoluble in water. This process has the potential to widen the application fields of PVCL, which dissolves rapidly when electrospun on its own. The hydrogen bonding interactions between TA and PVCL were confirmed through rheological and PA-FTIR measurements. This method requires no chemical modification or complex post-synthesis steps and facilitates the use of the biocompatible PVCL polymer as scaffolds, which mimic the structure of the ECM. Part 6.2 demonstrates the fabrication of shell crosslinked PVCL/RSF core/shell nanofibres by co-axial electrospinning. The optimum solution concentrations and processing conditions for making core/shell fibres were identified and confirmed through scanning electron microscopy (SEM), thermogravimetric analysis (TGA) and transmission electron microscopy (TEM) analysis. This chapter provides insight into novel ways of fabricating hybrid electrospun materials that improves their properties and use for tissue engineering applications.

Chapter 7 is concerned with the microstructure analysis of the RSF-based hydrogels using small angle neutron scattering (SANS) and ultra-small angle neutron scattering (USANS). In this chapter an understanding of the network structure of the hybrid hydrogels is presented and correlates to the observed bulk properties. This is the first work, to our knowledge, that delves into the structure of chemically crosslinked RSF hydrogels using neutron scattering

techniques, and the use of a wide Q range allows for the analysis of the hydrogels over an extremely wide size range (~10 Å to 10 μm). The scattering of the RSF-based gels exhibited features that indicated a gel-like structure; however it was not possible to fit the experimental data using the classical gel models. Insight into the frozen-in structures and evidence of porosity were demonstrated with the use of the *PowerLaw* and *GuinierPorod* models. This chapter presents a unique analysis of the structure of RSF hydrogels in the swollen state using the powerful neutron scattering techniques.

In Chapter 8 the potential of the engineered RSF-based hydrogels to provide a biomimetic environment for cell growth is presented. The adhesion, proliferation and differentiation of a mouse pre-chondrocyte cell line (ATDC5) were studied *in vitro* using microscopic analysis, a cell proliferation assay and real-time polymerase chain reaction (RT-PCR). This study demonstrates that the RSF-based hybrid hydrogels have the potential to be used for cartilage tissue regeneration. This chapter provides new insight into the effect of stiffness and water uptake capacity on the hydrogels capacity to support cellular proliferation and differentiation.

Chapter 9 concludes the study with future recommendations. The work presented in this thesis demonstrates that chemical and physical interactions can be employed to tune the properties and responsiveness of the RSF-based hydrogels that can provide a biomimetic environment conducive to cell growth. The current work has established a platform for the formation of RSF-based hybrid hydrogels and there is significant scope to develop these biomaterials further and study their behaviour *in vivo*.

List of Abbreviations and Symbols

ABS	Australian Bureau of Statistics
AC	Articular cartilage
AFM	Atomic force microscopy
AIBN	2,2'-azoisobutyronitrile
Alpl	Alkaline phosphatise
APS	Ammonium peroxodisulfate
ATDC5	Mouse pre-chondrocyte cell line
BC	Bacterial cellulose
Bglap	Osteocalcin
BMSC	Bovine mesenchymal stem cell
BMWS	Water-soluble freeze dried regenerated silk fibroin powder
BSA	Bovine serum albumin
CD	Circular dichroism
$CDCl_3$	Deuterated chloroform
cDNA	Complementary DNA
CG	Cationized gelatin
Col I	Collagen type I
Col II	Collagen type II
CS	Chitosan
D_2O	Deuterated water
DIT	Digital integration time
DLS	Dynamic light scattering
DMA	Dynamic mechanical analysis
DMF	N,N'-dimethylformamide
DN	Double network
DPB	Dual-phase transition behaviour
DSC	Differential scanning calorimetry
DW	Distilled water
E'	Storage modulus
E"	Loss modulus
ECM	Extracellular matrix
ELP	Elastin-like polypeptide
FCS	Fetal calf serum
FTIR	Fourier transform infrared spectroscopy

GA	Glutaraldehyde
GAG	Glycosaminoglycan
GGMA	Gellan gum methacrylates
GP	Glycerophosphate
h	Water uptake capacity
HA	Hyaluronic acid
HFIP	Hexafluoroisopropanol
HMZ	Hexamethyldisilazane
Ibsp	Integrin-binding saloprotein
IDP	Intrinsically disordered protein
IVD	Intervertebral disc
LCST	Lower critical solution temperature
MBAm	N,N'-methylenebisacrylamide
M_c	Molecular weight between crosslinks
MP	Microparticles
MSC	Mesenchymal stem cell
n	Crosslink density
NMR	Nuclear magnetic resonance
OA	Osteoarthritis
OPF	Oligo(poly(ethylene glycol) fumarate)
PAA	Poly(acrylic acid)
PAAm	Poly(acrylamide)
PA-FTIR	Photo-acoustic Fourier transform infrared
PAMPS	Poly(2-acrylamido-2-methylpropanesulfonic acid)
PBS	Phosphate buffered saline
PCL	Polycaprolactone
PDMAAm	Poly(N,N'-dimethylacrylamide)
PEG	Poly(ethylene glycol)
PG	Proteoglycan
PGA	Poly(glycolic acid)
PHEMA	Poly(hydroxyethyl methacrylates)
PLA	Poly(lactic acid)
PLG	Poly(D,L-lactide-co-glycolide)
PNIPAM	Poly(N-isopropylacrylamide)
PP	Polyproline
PPII	Polyproline II helical structure

PVA	Poly(vinyl alcohol)
PVCL	Poly(N-vinylcaprolactam)
PVP	Poly(vinylpyrrolidone)
R	Universal gas constant
R_g	Radius of gyration
RLP	Resilin-like polypeptide
RSF	Regenerated silk fibroin
RT-PCR	Real-time polymerase chain reaction
SANS	Small angle neutron scattering
SAS	Small angle scattering
SAXS	Small angle X-ray scattering
SELP	Silk-elastin-like protein polymer
SEM	Scanning electron microscopy
SLD	Scattering length density
SN	Single network
Sp7	Osterix
Sparc	Osteonectin
SPCL	Starch-compounded polycaprolactone
Spp1	Osteopontinc
T	Absolute temperature
TA	Tannic acid
TCP	Tissue culture polystyrene
TEM	Transmission electron microscopy
T_g	Glass transition temperature
TGA	Thermogravimetric analysis
TGF-β1	Transforming growth factor-β1
THPP	B-[tris(hydroxymethyl)-phosphino]propionic acid
UCST	Upper critical solution temperature
USANS	Ultra-small angle neutron scattering
VCL	N-vinylcaprolactam
XRD	X-ray diffraction
α-MEM	Alpha modified minimum medium
ξ	Mesh size

Declaration

I declare that this thesis does not incorporate without acknowledgement any material previously submitted for a degree or diploma in any university. To the best of my knowledge it does not contain any materials previously published or written by another person except where due reference is made in the text; and all contributions by others to the work presented, including jointly authored publications, are clearly acknowledged.



Jasmin Whittaker

Acknowledgements

First and foremost, I would like to acknowledge my supervisor, Professor Namita Roy Choudhury and my co-supervisor, Professor Naba Dutta for their guidance, support and patience during my PhD. I appreciate the tremendous amount of work and effort that both of you have put in to make this research possible. Your constructive feedback, guidance and honesty have helped me grow significantly in terms of my scientific achievements and personal qualities. This has been a very rewarding and challenging journey for me and it would not have been possible without both of your support, and I thank you sincerely for that.

I would also like to especially thank Professor Andrew Zannettino for giving me the opportunity to collaborate and perform my biological studies in your group. It was a wonderful experience for me and I got to learn so many new things that I am sure will be helpful for my future career. I really appreciate your patience and humour, especially when things were initially quite challenging!

Also, I would like to acknowledge the instrument scientists at the Australian Nuclear Science and Technology Organisation (ANSTO), Dr. Robert Knott, Dr. Liliana de Campo, Dr. Jitendra Mata and Dr. Christine Rehm, for their help in performing the neutron and X-ray scattering studies and data analysis. I would especially like to thank Robert for your assistance in analysing the hydrogel neutron scattering data; I learnt a lot from you and I appreciate your efforts very much.

In addition, I would like to thank all of the administration and technical support staff at the Wark, including Louise Jennings, Scott Abbott and Andrew Robinson, for their assistance for instrument training and administration matters. I am also grateful to The Wark, UniSA and the Australian Research Council (ARC) for financial support during my PhD through scholarship and project funding. Thank you to Sharon Paton for teaching me how to perform my cell culture experiments and aseptic technique.

I would like to especially thank my group members and friends, Mona Taghavikish, Xuan Wu, Rajkamal Balu and Surya Subianto. It has been a pleasure to see and work with you every day and has made my PhD time so much more fun and memorable. Thank you very much to Raj for always being willing to help out and give advice on my experiments. Also, a big thank you to Surya for giving me guidance for the electrospinning systems and reviewing my manuscripts. Also, thank you so much to my best friends Mona and Xuan for your

support, encouragement, patience and advice over the past few years. I cherish your friendship and all of the fun memories we have shared. Mona, thank you especially for always being willing to help me with anything and everything at uni, for always celebrating in my achievements and supporting me when things have been difficult. I know we will be lifelong friends.

Also, I would like to express my heartfelt thanks to my parents for your never-ending love, support, guidance and patience throughout my entire education and particularly during the years of my PhD. Since I was young you have both instilled in me the knowledge that I can achieve anything I set my mind to and this has helped me so much, especially when things have been difficult. I love you more than I can say and want thank you for providing me with my education and everything else I have ever needed. I would also like to express my thanks and love to my siblings, Kai and Georgie, for putting up with me, supporting me, and celebrating my achievements with me during my PhD. In addition, thank you to my Papa, Nanny and Grandpa for your love and always being happy to hear about my achievements and progress during my PhD.

Last but not least, thank you so very much to my partner Matt for being my rock throughout my PhD journey. You have celebrated my achievements with me and patiently and lovingly supported me through the difficult times when I doubted myself. Your faith in me has given me that confidence that I can achieve anything and I feel so lucky to have you to share this journey with. I love you more than anything and couldn't have done it without you.

List of publications

Journal articles

1. **Whittaker, J. L.**; Dutta, N. K.; Knott, R.; McPhee, G.; Voelcker, N.; Elvin, C.; Hill, A.; Choudhury, N. R., Tuneable Thermo-responsiveness of Resilin via Co-assembly with Rigid Biopolymers. *Langmuir* **2015**, *31*, 8882-8891.
2. **Whittaker, J. L.**; Choudhury, N. R.; Dutta, N. K.; Zannettino, A., Facile and rapid ruthenium mediated photo-crosslinking of Bombyx mori silk fibroin. *Journal of Materials Chemistry B* **2014**, *2* (37), 6259-6270.
3. **Whittaker, J. L.**; Dutta, N. K.; Elvin, C. M.; Choudhury, N. R., Fabrication of highly elastic Resilin/Silk fibroin based hydrogel by rapid photo-crosslinking reaction. *Journal of Materials Chemistry B* **2015**, *3*, 6576-6579.
4. **Whittaker, J. L.**; Dutta, N. K.; Choudhury, N. R., Engineering DN hydrogels from regenerated silk fibroin and poly(N-vinylcaprolactam). *Macromolecules* **2015** (Submitted).
5. **Whittaker, J. L.**; Subianto, S.; Dutta, N. K.; Choudhury, N. R., Induced insolubility of electrospun Poly(N-vinylcaprolactam) fibres through hydrogen bonding with Tannic acid. *Polymer* **2015** (Submitted).
6. **Whittaker, J. L.**; Subianto, S.; Dutta, N. K.; Choudhury, N. R., Facile fabrication of shell crosslinked core/shell Poly(N-vinylcaprolactam)/Silk fibroin fibres by co-axial electrospinning. To be submitted for peer review publication.
7. **Whittaker, J. L.**; Knott, R.; Mata, J.; de Campo, L.; Rehm, C.; Dutta, N. K.; Choudhury, N. R., Investigation into the microstructure of silk-based hydrogels using small and ultra small angle neutron scattering" to be submitted for peer review publication.
8. **Whittaker, J. L.**; Zannettino, A.; Dutta, N. K.; Choudhury, N. R., Chondrocyte response to regenerated silk fibroin-based hybrid hydrogels. To be submitted for peer review publication.
9. **Whittaker, J.**; Balu, R.; Choudhury, N. R.; Dutta, N. K., Biomimetic protein-based elastomeric hydrogels for biomedical applications. *Polymer International* **2014**, *63* (9), 1545-1557.

10. Balu, R.; **Whittaker, J.**; Dutta, N. K.; Elvin, C. M.; Choudhury, N. R., Multi-responsive biomaterials and nanobioconjugates from resilin-like protein polymers. *Journal of Materials Chemistry B* **2014**, *2* (36), 5936-5947.

Conference publications

11. **Whittaker, J.**; Choudhury, N.; Dutta, N., Role of environment on the secondary structure of a biomimetic protein-based elastomer. 34th Australian Polymer Symposium, 7-10 July 2013. Published in conference proceedings.
12. **Whittaker, J.**; Choudhury, N.; Dutta, N.; Zannettino, A., Hybrid hydrogel biomaterials containing silk fibroin. RACI National Congress, 7-12 December 2014. Published in conference proceedings.
13. Choudhury, N. R.; **Whittaker, J.**; Dutta, N., Electrospinning of silk fibroin/poly(N-vinylcaprolactam) to form hybrid nanofibres. 3rd International Conference on Electrospinning, 4-7 August 2014, San Fransisco, CA, USA. Published in conference proceedings.

Chapter 1: Introduction and Literature Review

1.1 Introduction

Hydrogels currently represent a powerful platform to promote regeneration of soft and hard tissues in the body or cell carriers for tissue engineering. Elastomeric hydrogels are critical constituents of dynamic biological structures that functionally require elasticity, swelling capacity and biocompatibility. Thus, hydrogels have been identified as ideal materials for tissue engineering applications due to their high water absorption capacity and resemblance to the extracellular matrix (ECM).[1-3] Crucial requirements to the biomedical application of hydrogels and injectable hydrogels are facile and mild fabrication approach, modular modification and finely tuneable control over mechanical properties, as well as rapid gelation following injection. Moreover, to replace natural tissue with hydrogels, a number of significant engineering requirements need to be addressed, such as suitable elastic modulus, mechanical strength, toughness, water retention and swelling capacity of the gel, biocompatibility and biodegradability. Most hydrogels are brittle with very low fracture energies of ~10 J/m^2.[4] By comparison, the fracture energy of cartilage is 1,000 J/m^2 and that of natural rubber is 10,000 J/m^2.[4] Thus, facile fabrication of hydrogels with novel microstructure and excellent mechanical properties that provides a biomimetic environment for cell growth and tissue engineering is a highly challenging task.

1.1.1 Tissue engineering

Tissue engineering is a promising method for the regeneration of human tissues and employs the interdisciplinary fields of engineering, materials science, chemistry and biology to fabricate biomaterials that restore, maintain, or improve the functionality of damaged tissues.[5] Three important characteristics of tissue engineering are i) cells, ii) cell signalling molecules and iii) scaffolds. Cellular growth and differentiation requires the presence of a structured scaffold environment, such as a hydrogel, with which cells can interact and that mimics the ECM and promotes synthesis of the natural ECM ideally at the same rate as the degradation of the scaffold. Consequently, material choices for tissue engineering scaffolds are guided by the need to restore cell signalling and to match the tissue being engineered, so the scaffolds can serve as an informational template to the cells. Hydrogels formed from natural materials are inherently bioactive, but often weak and require crosslinking; however, synthetic

hydrogels are biologically inert and require the addition of bioactive molecules to regulate cell function. Therefore, in order to investigate cellular growth *in vitro*, it is important to design three-dimensional microenvironments that mimic the microenvironments of these cells *in vivo* or create a tissue mimetic environment. The requirements for tissue engineering scaffolds thus include:

1. Interconnected network allowing for diffusion of nutrients and waste.
2. Biocompatible and/or biodegradable.
3. Allows for cell attachment, proliferation and differentiation.
4. Mechanical properties that match that of the loading environment.

Hydrogels of natural and synthetic origin have been widely studied for a range of tissue engineering applications, including bone, cartilage, intervertebral disc (IVD), smooth muscle, skin, and nerves.[6] Notably, the stiffness of these tissues is different and plays a central role in adhesion and cytoskeletal organisation. Table 1.1 summarises the mechanical properties of a number of human tissues and highlights their vast differences in the Young's modulus and tensile strength depending on the location and function in the body. In particular, avascular load-bearing soft tissues including cartilage possess particularly stringent mechanical requirements due to their nature of function in the body. In particular, cartilage has compressive moduli of ~180 to 2500 kPa and it was reported that cartilage present in human knee joints has a tensile modulus of ~10 MPa.[5, 7-9]

Table 1.1 Summary of mechanical properties of different human tissues

Tissue	**Young's modulus (MPa)**	**Tensile strength (MPa)**	**Ref.**
Cartilage	0.7-15.3	3.7-10.5	[10]
Cancellous bone	20-500	7.4	[10]
Cortical bone	3000-30,000	7.4	[10]
Ligament	65-541	24-112	[10]
Human bladder	0.25	0.27	[11]
Skin	~0.025-0.100	~27	[12, 13]

Injuries to articular cartilage (AC) and growth plate are a major health care problem worldwide. As many as 80% of people, over the age of 65, suffer from some form of cartilage damage and osteoarthritis. Osteoarthritis (OA) is a common type of arthritis and is caused by

loss of or damage to the articular cartilage tissue present in the joints of the hips, knees, hands and spine.[14] Thus, loss of cartilage due to age or trauma results in a number of symptoms, including pain, stiffness and limitation of movement. Estimates from the Australian Bureau of Statistics (ABS) from the 2011-12 National Health Survey found that OA affects ~8 million Australians and was estimated to cost the Australian economy ~$2.03 billion in 2007.[15] OA is rarely a life-threatening health problem; however significant costs are associated with it, including medical expenses, workers' compensation benefits, and lost productivity.[16] In addition, OA causes significant pain, which affects the quality of life of patients with these conditions. Cartilage damage can also result from sports injury. Therefore, it is a great challenge to repair damaged cartilage as it is avascular, aneural and alymphatic, and has limited intrinsic capacity for self repair. A distinct need remains to develop functional biomaterials for cartilage tissue engineering as current treatments, such as surgery, autologous grafting, and synthetic replacement do not provide adequate repair and function.[17-19] Moreover, to design hydrogels with tuneable properties that meet the mechanical and biomimetic requirements to successfully regenerate tissues, a fundamental understanding of the molecular interactions and microstructure of hydrogels and how this dictates the observed cellular response is necessary. In this chapter an in-depth discussion of the structure, characterisation and biomimetic properties of different types of hydrogels is presented with a particular focus on the ability of various hydrogels to direct cell attachment, growth, proliferation, differentiation including gene expression and preservation of the phenotype in vitro.

1.2 Fundamentals of hydrogels

Hydrogels are a class of three-dimensional chemically or physically crosslinked synthetic or biopolymer networks that are insoluble and able to capture large amounts of water.[20-22] The type of crosslinking can significantly modify the properties of the hydrogel. Hydrogels are generally prepared from monomers, oligomers, natural or synthetic polymers or from recombinant protein polymers or biomimetic polymers. Physically crosslinked hydrogels are formed due to strong secondary interactions, including hydrogen bonding, hydrophobic interactions and ionic interactions, which can be reversible. Self-assembly or co-assembly via non-covalent crosslinking or intermolecular interaction also provides a route to fabricate either dynamic reversible or irreversible physical hydrogels. Chemically crosslinked hydrogels are formed by employing covalent linkages between polymer chains, which

undergo irreversible gelation and are characterised by irreversibility of their crosslinks. The high swelling capacity and hydrophilicity of hydrogels is attributed to the presence of hydrophilic functional groups, including hydroxyl, carboxyl, amide, and amino that are present in the backbone of natural and synthetic polymers.[23] However, the gels are unable to dissolve due to the presence of the crosslinked network, but can swell extensively depending on the network density. The balance between the osmotic driving forces that encourage the penetration of water inside the hydrogel matrix on immersion and the cohesive forces exerted by the crosslinked polymer chains result in an equilibrium swelling capacity. As a result, the equilibrium swelling capacity of a hydrogel is dependent on the crosslink density and the hydrophilicity of the polymer material. When swollen, hydrogels are soft and rubbery materials, which mimic the structure of natural tissue.[23] Also, depending on the precursor materials used, hydrogels can be biocompatible and provide a biomimetic environment suitable for cell growth.

The performance of hydrogels is largely dependent on their overall structure.[24] The important parameters employed to characterise the network structure of hydrogels are: the molecular weight of the polymer chain between crosslinks (M_c), the corresponding mesh size (ξ) and the polymer volume fraction in the swollen state.[24] The M_c between crosslinks indicates the degree of crosslinking of the polymer and can be calculated using a number of techniques, including equilibrium swelling theory and rubber elasticity theory.[24] Notably, the M_c value calculated from either technique is an average value due to the random nature of the crosslinking process. The mesh size (ξ) is defined as the distance between two adjacent crosslinks and indicates the space available between the chains in the hydrogel.[24]

The structure of a hydrogel can be analysed using Flory-Rehner theory, which is widely used to determine the M_c of hydrogels, which states that the swelling of a crosslinked polymer hydrogel is dictated by a combination of thermodynamic and elastic forces.[24] This can be described by the Gibbs free energy of the system:

$$\Delta G_{total} = \Delta G_{elastic} + \Delta G_{mixing} \quad (1)$$

where $\Delta G_{elastic}$ is the contribution due to the elastic retractive forces due to the gel structure, and ΔG_{mixing} is the result of the spontaneous mixing of fluid molecules with the polymer chains in the gel.[24] In particular, on immersion in a fluid the crosslinked hydrogel reaches equilibrium swelling due to the balance of the thermodynamic force of mixing and the retractive force of the polymer chains.[24] As a result, the modified Flory-Rehner equation can

thus be employed to calculate the M_c and crosslink density for a neutral hydrogel in water and is defined as:[24, 25]

$$\frac{1}{M_c} = \frac{2}{M_{n,p}} - \frac{\frac{1}{\rho_p V_2}[\ln(1-v_{1,s}) + v_{1,s} + \chi v_{1,s}}{v_{1,r}\left[\left(\frac{v_{1,s}}{v_{1,r}}\right)^{\frac{1}{3}} + \frac{1}{2}\left(\frac{v_{1,s}}{v_{1,r}}\right)\right]} \quad (2)$$

where, $\upsilon_{1,r}$ is the polymer volume fraction in the relaxed state and is set to 1.[25] Also, generally $M_{n,p}$ is large and thus $2/M_{n,p}$ is neglected in equation 2.[25] The crosslink density, υ_e, is defined as the number of network junctions per unit volume (mol/cm^3) and is calculated using equation 3:

$$v_e = \frac{\rho_p}{M_c} \quad (3)$$

Thus, by combining equations 2 and 3, assuming $\upsilon_{1,r}$ is equal to 1, the crosslink density can be calculated using equation 4:

$$v_e = \frac{\rho_p}{M_c} = \frac{-\ln(1-v_{1,s}) + v_{1,s} + \chi v_{1,s}}{V_2(v_{1,s} - \frac{1}{2}v_{1,s})} \quad (4)$$

where χ is the Flory-Huggins interaction parameter between the polymer and water, V_2 is the molar volume of water.[25]

The $\upsilon_{1,s}$ is the polymer volume fraction in the swollen state and can be calculated using equation 5:

$$v_{1,s} = \frac{\frac{w_p}{\rho_p}}{\frac{w_{T,s} - w_p}{\rho_2} + \frac{w_p}{\rho_p}} \quad (5)$$

where ρ_p is the density of the dry gel, ρ_2 is the density of water at room temperature, w_p is the weight of the dry gel, and $w_{T,s}$ is the weight of the equilibrium swollen gel.[25]

Crosslinked hydrogels behave in a similar way to natural rubbers in that they have the ability to respond elastically to an applied stress.[24] Thus, rubber elasticity theory can be used to determine the crosslink density, n (mol/m^3), and M_c (g/mol) of physically and chemically crosslinked hydrogels using equation 6:

$$n = \frac{E'}{3RT} = \frac{\rho}{M_c} \quad (6)$$

where E' is the tensile storage modulus, R is the universal gas constant (8.341 J/mol.K), T is the absolute temperature and ρ is the density of the dry gel.[26-28]

A number of general relationships have been drawn between the structure and crosslink density and the observed bulk properties of the hydrogel. In particular, an increase in the crosslink density results in a decrease in the swelling capacity and an increase in the hydrophilicity leads to an increased extent of swelling. Thus, when designing hydrogels, the material choice and extent of crosslinking will dictate the resultant hydrogel swelling properties. In addition, the crosslinks that occur between the polymer chains in the hydrogel results in viscoelastic behaviour and this can be tuned by modifying the crosslink density, crosslinking method, and forming hybrid hydrogels with other materials. Thus, hydrogels may be designed to possess a desired selection of morphological, biocompatible, mechanical, and biodegradable properties by careful choice of the polymer building blocks, which dictates their interactions, structure and bulk properties.

Depending on the type of crosslinking, the hydrogels can be classified as physical, chemical and hybrid hydrogels. Figure 1.1 summarises an overview of various types of hydrogels that can be made using covalent or dynamic intermolecular interactions. An insight into different types of hydrogels and their characteristic features is presented in the following sections.

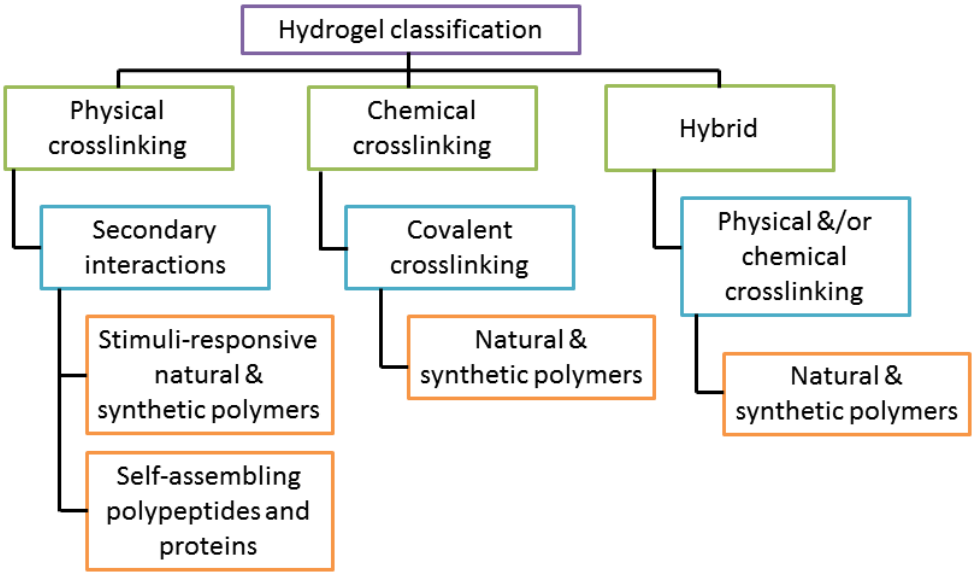


Figure 1.1 Overview of types of hydrogels and the interactions and materials that can be used to prepare hydrogels with tuneable properties.

1.3 Physical hydrogels

Physical hydrogels are classified as polymer networks that are held together by molecular entanglement and/or non-covalent secondary molecular interactions.[29] Physical hydrogels are formed by polymer self-assembly that results in crosslinks due to non-covalent interactions, including hydrogen bonding, hydrophobic interactions, electrostatic interactions, π-π stacking and weak van der Waals interactions.[23, 30] The strength of interactions between the polymer components dictate the nature and density of the crosslinks, which impacts the overall swelling capacity and mechanical properties of the hydrogels.[29, 30] A general schematic of the structure of self-assembled hydrogels that form due a range of non-covalent interactions is shown in Figure 1.2. Physical hydrogels can be prepared from a range of natural and synthetic polymers. In particular, stimuli-responsive natural and synthetic polymers and self-assembling proteins and polypeptides have been of significant interest in recent years and a more detailed description of these is given in the following sections.

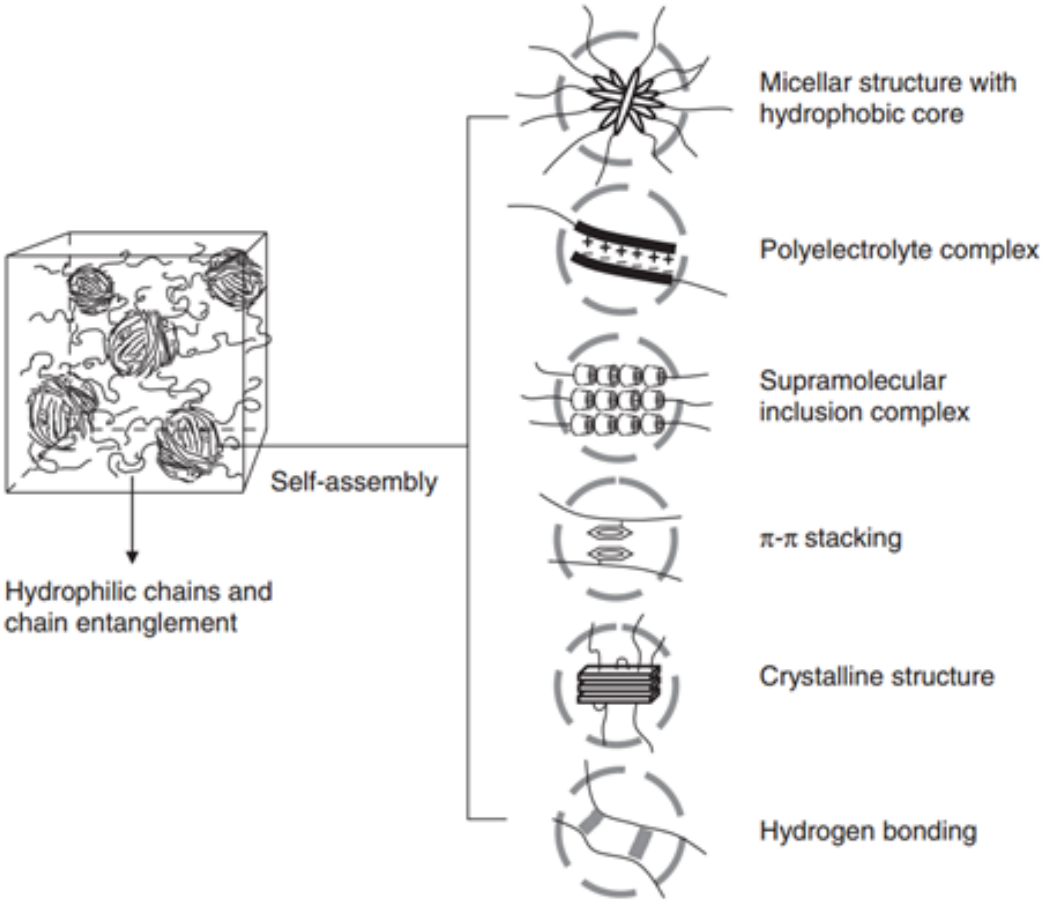


Figure 1.2 Summary of different types of physical interactions and how they result in self-assembled hydrogels.[30]

1.3.1 Physical hydrogels from stimuli-responsive polymers

Stimuli-responsive natural and synthetic polymers represent a particularly unique class of materials that self-assemble to form physical hydrogels in response to external stimuli, such as temperature, pH, ionic strength and light.[31] Temperature or thermo-responsive polymers are particularly useful for biomedical engineering applications due to their ability to self-assemble in response to temperature and thus can be employed for *in situ* gelation at body temperature. Thermo-responsive polymers may possess an upper critical solution temperature (UCST), a lower critical solution temperature (LCST), or both in some cases. The polymer system will separate into two phases below the UCST, become soluble when the temperature is between the UCST and LCST, and will phase separate above the LCST (Figure 1.3). This is due to the switching of the thermo-sensitive polymer components from hydrophilic to hydrophobic due to the weakening and disruption of hydrogen bonding with water molecules at particular temperatures and leads to phase separation and gelation of the polymer.[30] Temperature-responsive polymers are particularly useful for biomedical applications as it may be possible to induce *in situ* gelation by raising the temperature to the physiological range, which allows for injectable implantation.[32] Thus, for these types of applications it is essential that the phase transition behaviour occurs in the physiological temperature range. There are numerous natural and synthetic thermo-responsive polymers that have been studied for biomedical applications and a description of these is given below.

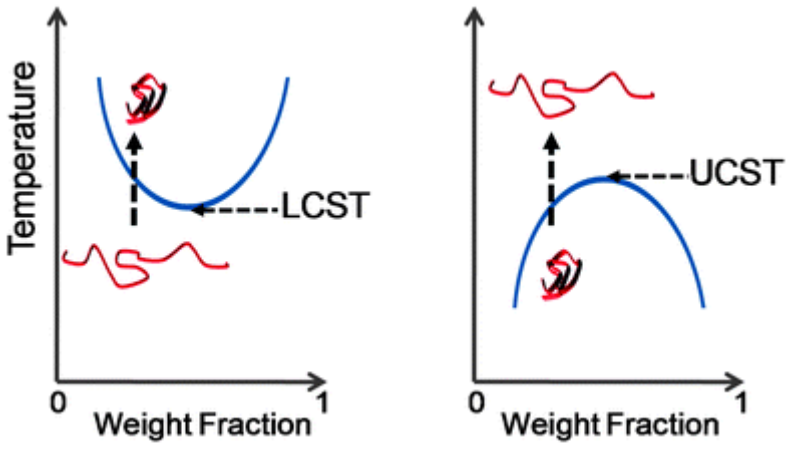


Figure 1.3 Schematic showing the coil-to-globule phase transition occurring above the LCST and below the UCST. The blue line represents the boundary of the phase separation.[33]

1.3.1.1 Physical hydrogels from thermo-responsive biopolymers

A number of naturally occurring stimuli-responsive proteins may be appropriate for the development of novel materials. In particular, the temperature-responsive behaviour of elastin is of high interest for biomedical applications. Elastin is present in tissues in the human body, such as cartilage, muscle, ligaments and skin and is responsible for their elasticity.[34, 35] Elastin demonstrates a LCST at 37˚C and below this temperature the protein is soluble in aqueous solutions with a disordered chain structure.[36] However, above 37˚C elastin undergoes self-assembly to form a coacervate with inter-chain hydrophobic interactions dominating.[36-38] In addition, the elastin structure becomes more ordered as the temperature increases above the LCST, which results in a loss of entropy and the subsequent release of water.[36, 37] Furthermore, the stimuli-responsive behaviour of elastin is reversible upon cooling of the protein.[36, 37] Identification of the gene sequence of human elastin allowed for the development of artificial elastin-like polypeptides (ELPs) that consist of the pentapeptide repeat sequence Val-Pro-Gly-Xaa-Gly, where Xaa is any amino acid except proline.[34] This sequence was found to be responsible for the thermo-responsive behaviour of elastin and ELPs, which coacervate to form a hydrogel above a specific phase transition temperature.[34] Physical hydrogels based on thermo-responsive ELPs have been synthesised and studied for a range of biomedical applications and will be discussed in more details later on.

Another elastomeric, structural protein that demonstrated stimuli-responsiveness is resilin that is found in the cuticle region of many arthropods.[39, 40] The advantage of resilin when compared to elastin is that it demonstrates multi stimuli-responsive behaviour as a result of a number of different stimuli, which allows for more versatile control over the properties.[41] Resilin is temperature-, pH-, and photo-responsive, and thus there is enormous potential for its use in a range of applications. Elvin et al. produced one type of resilin-like polypeptide (RLP) using recombinant technology from *Drosophila melanogaster*, which they named Rec1-reslin, and was based on the first exon of the *Drosophila melanogaster* CG15920 gene.[39] The gene encodes for the first exon of native resilin, which contains 17 repeats of the elastic motif, GGRPSDSYGAPGGGN.[39] Rec1-resilin has been shown to exhibit dual phase transition behaviour, a very rare occurrence, which means that it possesses both an LCST (70˚C) and a UCST (6˚C) (Figure 1.4).[42] However, the fact that the thermo-responsiveness occurs outside the physiological temperature range has limited the utilisation of the unique thermo-responsiveness of Rec1-resilin for biomedical applications to date. Also, the reversibility of the sol-gel transition for thermo-responsive polymers limits their use for

applications such as tissue engineering where integrity of the network structure is required. Thus, there is a distinct need to fine tune the LCST close to room temperature and identify a facile method to form an irreversible self-assembled responsive natural hydrogel that provides a biomimetic environment for cell growth.

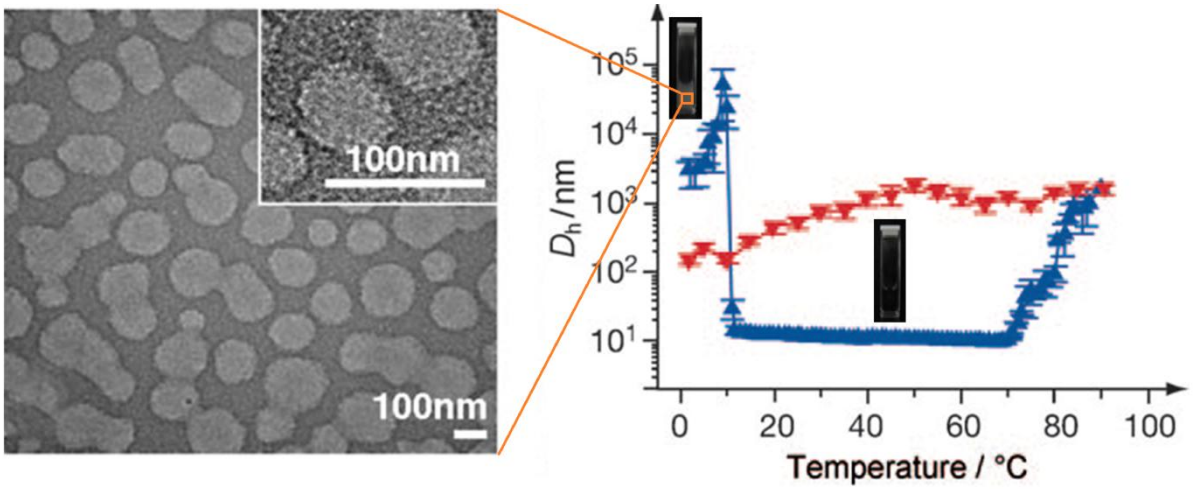


Figure 1.4 Responsive behaviour of Rec1-resilin as a function of temperature, as shown by TEM images and dynamic light scattering data, which demonstrates the change in hydrodynamic diameter with temperature.[43]

1.3.1.2 Physical hydrogels from thermo-responsive synthetic polymers

In addition to the naturally occurring stimuli-responsive polymers, such as resilin and elastin, there are a range of synthetic stimuli-responsive polymers that have been developed. The majority of investigations into synthetic temperature-responsive polymers have focused on poly(N-alkylacrylamide)s, poly(N-vinylcaprolactam) (PVCL), and poly(vinyl methyl ether).[44] This is due to their suitability for biomedical applications as the lower critical solution temperatures (LCST) exhibited by these polymers are in the physiological range.[44, 45] In addition, lactam polymers, such as PVCL, have superior biocompatibility compared to poly(N-isopropylacrylamide) (PNIPAM) due to their stability against hydrolysis.[46, 47] Thus, lactam polymers have been investigated extensively with regard to the development of materials for drug delivery applications[48, 49] and as such have not been attempted for tissue engineering application without modification.

1.3.2 Self-assembling peptide and protein hydrogels

Self-assembly of macromolecules, such as peptides and more complex proteins allows for the development of hydrogels with precisely defined and hierarchical structures.[29] Notably, many biological systems are composed of self-assembling peptides and proteins, including the fibrous protein components of the ECM, actin filaments in the cytoskeleton, and microtubules.[29] The advantages of protein self-assembly include: i) high specificity regulated by molecular recognition and interactions between peptide components; and ii) formation of defined secondary structures that are dictated by the primary amino acid sequence of the protein.[29] As such, protein self-assembly has become of increasing research interest due to the possibilities of exploiting material stimuli-responsiveness to develop new soft materials, such as physically crosslinked hydrogels, that are biologically relevant and can be employed for biomedical applications. A range of synthetically produced polypeptides have been employed to form self-assembled physical hydrogel networks with defined secondary structures, such as β-sheets, β-hairpin, random coils and α-helices.[50-56] The self-assembly process and subsequent hydrogel formation can be controlled by a range of external factors, including temperature, pH, ionic strength and time.[29] The drawback of the use of synthetically produced polypeptides is that time-consuming synthesis procedures are required. Also, the drawback of many self-assembled peptide hydrogels is their lack of mechanical stiffness, which limits their uses in many biomedical applications, such as tissue engineering.

Elastin and resilin are two types of naturally occurring elastomeric self-assembling proteins that assemble in response to changes in temperature, as described above. One particular amino acid that is commonly found in self-assembling proteins present in nature, including elastin and resilin, is proline, which is frequently found as tandem repeats and gives rise to the polyproline II helical structure (PPII).[57] The PPII conformation is highly flexible and is known to have the ability to convert between β-strand and β-turn structures.[58] It has been proposed that this conformational flexibility is responsible for the highly elastic nature of elastin and resilin-based materials.[58] Also, polyproline (PP) homopolymers are known to self-assemble in response to temperature and exhibit an LCST of ~45˚C.[59] The role of the PPII conformation in the thermo-responsive behaviour of protein-based materials, such as elastin and resilin, has not yet been elucidated and a greater understanding of this could lead to the ability to tune the thermo-responsive properties of these materials. In particular, as mentioned above, the dual phase temperature-induced self-assembly of Rec1-resilin above the LCST

(70˚C) and below the UCST (6˚C) is extremely rare and allows for a high level of control over the self-assembly behaviour.[60] This unique property has not yet been harnessed for biomedical applications as the LCST and UCST require tuning to lower values.

Another naturally occurring protein that has been studied extensively and self-assembles to form hydrogels containing a large proportion of β-sheet structures is *Bombyx mori* silk fibroin. Silks are naturally occurring polymers that are produced by lepidopters or spiders.[61] *B. mori* silk fibroin is an abundantly available protein, which is extracted from the raw silk produced by the *Bombyx mori* silkworm. It possesses a number of inherent properties that are particularly suitable for biomedical applications, including biocompatibility, the ability to support cell adhesion and proliferation, superior strength, abundance, ease of processing using aqueous solvents and controllable biodegradation.[62] The different silks that are present in nature differ in their protein structures, which may include β-sheet, α-helix, coiled-coil, triple-helix and polyglycine-II conformations.[38] *B. mori* silk fibroin is composed of a light chain and a heavy chain in a 1:1 ratio, with molecular weights of approximately 26 kDa and 390 kDa, respectively.[38, 63-65] The light and heavy chains are joined together by a single disulphide bond.[63, 64, 66] In addition, silk fibroin is structured as a copolymer with hydrophobic sections that form β-sheet conformations due to hydrophobic interactions, and smaller hydrophilic blocks (Figure 1.2).[63, 65, 66] The asymmetrical β-sheet conformation is due to the dominating hydrophobic crystalline regions containing glycine-X repeats.[63, 65] The X position is occupied by a range of proteins with Ala in 64% of the repeats, Ser in 22%, Tyr in 10%, Val in 3%, and Thr in 1.3% of the repeating units.[64, 65] A range of silk polymorphs have been found through experimental observations. These include: the glandular silk I (random coil) state that occurs prior to crystallization, the silk II state comprising of β-sheet secondary structure, and the helical silk III structure due to an air/water interfacial assembly.[65] The overall structure of silk fibroin is hydrophobic and its ability to self-assemble gives rise to a strong and resilient structure.[63] Figure 1.5 depicts the structure and self-assembly of silk fibroin, which has been observed to result in micelles containing crystalline β-sheet structures that aggregate to form rod-like aggregates and results in a physical hydrogel structure.[67] Notably the random coil to β-sheet transition of silk fibroin is irreversible and forms a permanent physical hydrogel.

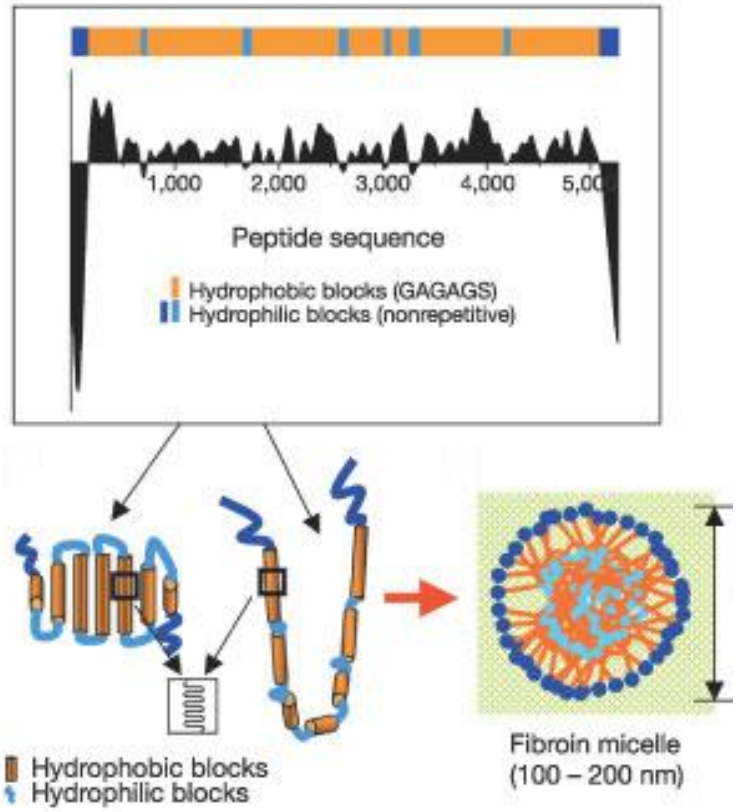


Figure 1.5 Schematic showing sequence of silk fibroin in terms of hydrophobic and hydrophilic segments and how this results in the formation of RSF micelles in solution.[67]

Physically crosslinked regenerated silk fibroin (RSF) hydrogels have been fabricated by inducing the random coil to β-sheet transition using a number of different methods. These include: shear, water evaporation, heat, low pH, solvent exposure, high ionic strength, electric current, and vortex.[65, 68-72] The advantage of physical RSF hydrogels compared to self-assembled polypeptides is their improved mechanical strength due to the large amount of β-sheet structure. RSF gels obtained through β-sheet formation due to low pH had modulus values on the Pa to several kPa range.[69] In addition, vortex induced RSF hydrogels possessed modulus values of ~70 kPa.[72] Kim et al. reported that the compressive modulus of a physically crosslinked RSF hydrogel prepared at 60˚C from a 16 wt% solution was approximately 6 MPa, however the temperature used for preparation is not relevant for *in situ* gelation for biomedical applications.[73] Thus, the majority of RSF physically crosslinked hydrogels demonstrate relatively low modulus values, which limits their use in load-bearing applications.

An overview of the source of various biomimetic proteins derived from silk fibroin, elastin and resilin is presented in Figure 1.6, which shows the synthesis and versatile fabrication routes that may be taken to develop them for biomedical applications, such as tissue engineering and drug delivery.

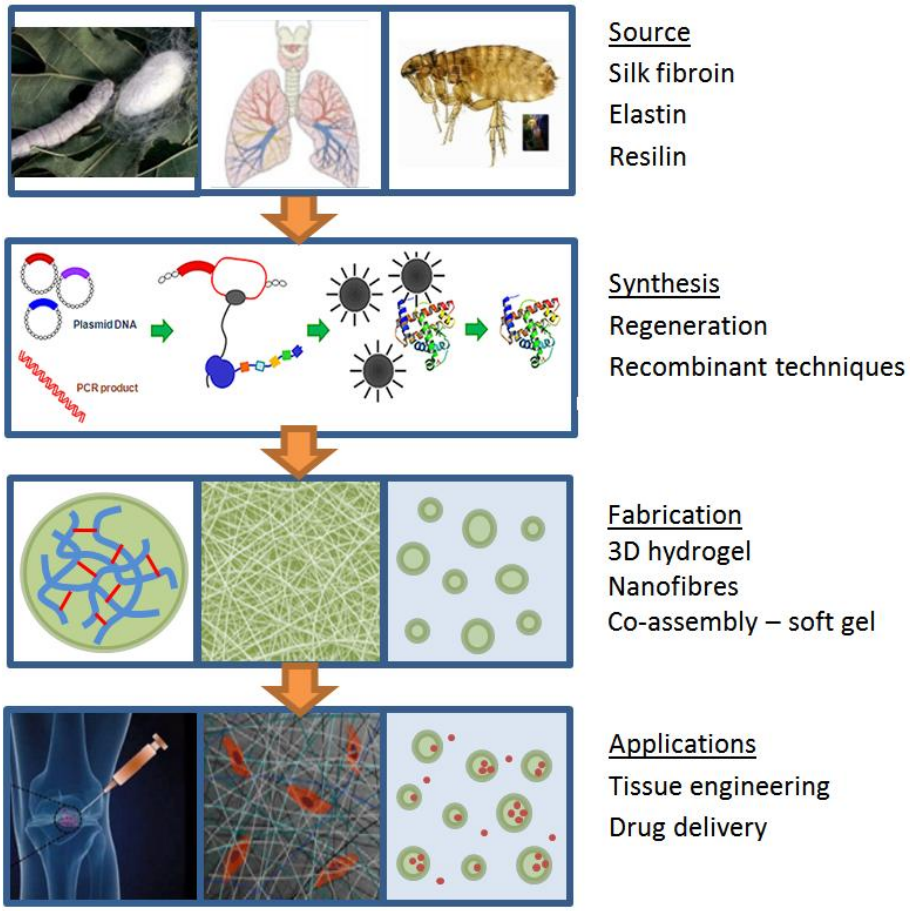


Figure 1.6 Overview of the source, synthesis, fabrication and applications of biomimetic protein-based materials.[43]

1.3.3 Coassembled hydrogels with tuneable responsiveness

As described above self-assembly is a powerful tool for the formation of physical hydrogels with precise control of their interactions and structure. The coassembly of multiple polymer/proteins in solution allows for the development of hydrogels with tuneable properties that can target different biomedical applications. Control over the self-assembly of protein and synthetic polymers materials can be achieved by altering the conformation, which results in an altered distribution of hydrophobic and hydrophilic moieties in the three-dimensional protein structure.[41] For thermo-responsive self-assembling polymers it has been observed that the incorporation of hydrophobic groups lowers the LCST, whereas the

introduction of hydrophilic groups results in an increase in the LCST (Figure 1.7A).[32] Whilst, tailoring the environment of self-assembling proteins and synthetic polymers may be achieved through a number of methods, such as DNA technology and copolymerisation, coassembly provides a facile method for inducing conformational changes due to physical interactions between materials in solution, which can be easily tuned by varying the ratio of constituents in the system.[32] It can be observed from the Kyte-Doolittle hydropathy plot (Figure 1.7B) of elastin, resilin and a spider silk protein that elastin contains predominantly hydrophobic components and resilin is composed of more hydrophilic amino acids.[43, 74] The hydrophilicity/hydrophobicity of proteins will control the interactions and responsiveness when forming coassembled systems. Coassembled systems containing elastin-based materials of different molecular weights and amino acid sequences were employed to tune the LCST of ELPs.[75, 76] Apart from these studies with ELPs, there have been very few reports where the use of coassembly has been employed to tune the LCST of a protein or synthetic polymer through addition of a more hydrophobic protein. A greater understanding of the coassembly process would certainly allow for the use of this facile method to develop coassembled hydrogels for a range of applications.

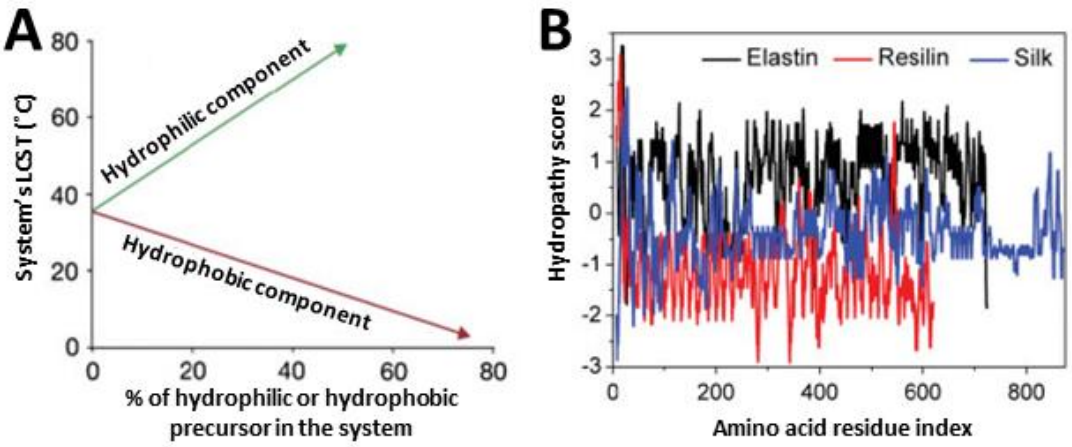


Figure 1.7 A) Effect of the hydrophobic/hydrophilic components in thermo-responsive systems. B) Kyte-Doolittle hydropathy plot of biomimetic proteins elastin, resilin and a spider silk protein.[43]

1.3.3.1 Structural investigation of self- and coassembling protein-based systems

A fundamental understanding of the structural changes occurring during the self- and coassembly processes of protein-based materials is necessary to achieve a high level of control over the material properties. There are a range of methods that can be used to study

the structure and morphology of proteins in solution, including Fourier transform infrared spectroscopy (FTIR), circular dichroism (CD) spectroscopy, small angle X-ray scattering (SAXS) and small angle neutron scattering (SANS). CD spectroscopy is a useful tool to obtain rapid information regarding the secondary structure and folding of proteins in solution.[77] The principles of CD spectroscopy are based on the unequal absorption of left-handed and right-handed circularly polarised light. In particular, different secondary protein structures, including α-helix, random coil, β-sheet and PPII exhibit characteristic CD spectra due to the shift in optical transitions in the backbone that differ when the chain adopts different conformations.[77] As such, CD spectroscopy has been employed to study the structural properties of a range of self-assembling peptide and protein materials.[50, 53, 56, 78, 79]

Small angle scattering (SAS) techniques, such as SAXS and SANS, are useful to study the self- and coassembly behaviour of proteins in solution. This is due to the fact that it allows for the study of samples in the solution state without the need for any sample preparation and over a wide range of length scales (~10 to 500 nm).[80]

SAXS and SANS have been used to study a range of self- and coassembling polypeptide and protein hydrogel systems.[81-83] In addition, recently Balu et al. studied the structure of Rec1-resilin in aqueous solution using SAXS and confirmed that it is an intrinsically disordered protein (IDP), which means that it adopts a structure that is intermediate of a globular protein and a denatured protein.[78] Greving et al. studied the morphology and structure of RSF aqueous solutions using SANS at concentrations ranging from ~12 to 150 mg/mL (Figure 1.8).[84] They observed that the radius of gyration (R_g) of RSF varied from ~20 to 55 Å depending on the molecular weight, solution concentration and RSF dissolution conditions.[84] Nisal et al. observed an average R_g of ~18.2 Å for RSF at 4 wt% in solution, which increased to ~25.5 Å at 15 wt% based on fitting of a Gaussian chain.[85] Furthermore, Rossle et al. reported a somewhat higher R_g of ~68 Å as measured using SAXS.[86] A detailed understanding of the self-assembly process of RSF during gelation using the powerful techniques of neutron scattering is lacking and would allow for the utilisation of RSF in coassembled gel systems with tuneable properties.

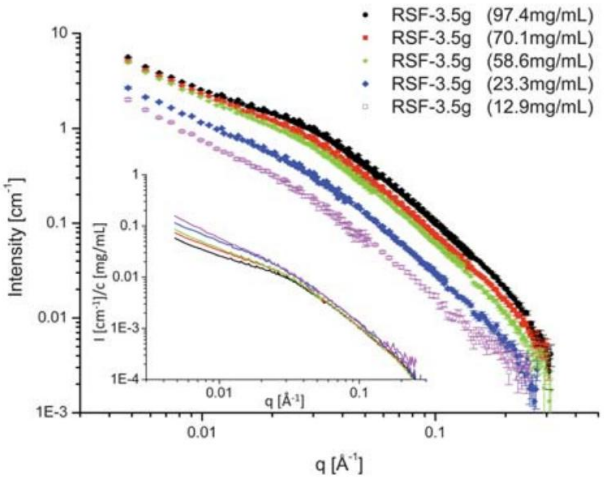


Figure 1.8 The SANS scattering curves of RSF aqueous solutions at different concentrations (in brackets). Inset: SANS curves are normalised for concentration.[84]

1.3.4 Natural and synthetic physically crosslinked hydrogels used for cartilage tissue engineering

Table 1.2 summarises a range of natural and synthetic polymer hydrogels that have been physically crosslinked by thermo-responsive sol-gel transitions or ionic interactions and evaluated for cartilage tissue engineering. Their ability to support the chondrogenesis/differentiation of chondrocytes (cartilage cells) was studied and is detailed in the table. Chondrogenesis of cartilage TE is assessed by measuring the expression of cartilage-related genes, such as collagen type II (Col II), Sox9 and aggrecan, and also synthesis of proteoglycans (PGs) and glycosaminoglycan (GAG) that are constituents of the ECM. Notably the modulus values of the physical gels were low and did not match with that of cartilage (~180 to 2500 kPa).

Table 1.2 Summary of physically crosslinked hydrogels from natural and synthetic polymers that have been evaluated for cartilage tissue engineering *in vitro*.

Polymer	**Crosslinking method**	**Modulus (kPa)**	**Cell type**	**Ability to support chondrogenesis**	**Ref.**
Collagen	Physical – temperature (~37˚C)	~65	Human chondrocytes	*In vitro* – Improved Col II expression compared to alginate hydrogels	[87]
Alginate – RGD functionalised	Ionic – Ca^{2+} ions	~12-127	Bovine chondrocytes	*In vitro* – greater attachment and spreading on RGF-alginate surfaces compared to bare alginate	[88]
Fibrin	Ionic – Ca^{2+} ions	-	Bovine chondrocytes	*In vitro* – synthesis of cartilaginous tissue	[89]
ELP	Physical – temperature (~37˚C)	~0.08	Swine chondrocytes	*In vitro* – maintain cell viability, synthesis of Col and GAG.	[34]
RSF	Physical – sonication	~0.1-0.2	Bovine chondrocytes	*In vitro* – Supported proliferation and Col II and GAG synthesis	[90a]
Chitosan – glycerol-phosphate disodium salt added	Physical – temperature (~37˚C)	-	Bovine chondrocytes	*In vitro* - >80% viability *In vivo* – chondrocytes expressed cartilage specific genes Col II and Agg	[90b]
Methoxy poly(ethylene glycol) (PEG)-polycaprolactone (PCL) diblock copolymer	Physical – sol-gel transition at 37˚C	-	Rabbit chondrocytes	Demonstrated growth and proliferation *in vitro*. Synthesis of GAG, PG and Col II *in vivo*	[91]

1.4 Chemical hydrogels

Chemical hydrogels are another class of hydrogels, which contain covalent crosslinks and may be formed by a number of methods including polymer-polymer reactions, crosslinking of polymeric precursors and crosslinking copolymerisation.[29] The advantage of covalently crosslinked hydrogels is that they are stable and the crosslinking is irreversible, which is unlike many physical hydrogels that demonstrate reversible gelation due to weak secondary

interactions. Hydrogel structural stability is important for tissue engineering applications where mechanical integrity is crucial.[24]

1.4.1 Chemically crosslinked hydrogels from naturally occurring polymers

Biomimetic hydrogels synthesised from naturally occurring polymers, such as proteins and polysaccharides, possess a number of advantages over synthetic polymers including generally low toxicity, biocompatibility and providing a biologically relevant environment for cell growth.[24] The natural polymer hydrogels that have been studied with regard to biological applications include collagen, hyaluronic acid (HA), alginate, agarose, fibrin, chitosan, and RSF.[24] Collagen has been studied extensively for regenerative applications as it is a structural protein that is present in all connective tissues including cartilage, bone, tendon, and skin.[38] Recombinant collagens have the ability to self-assemble and form physical hydrogels; however, despite possessing adequate biocompatibility collagen gels are mechanically weak.[92-95] Thus, chemical crosslinking of collagen has been conducted by several groups; however, the modulus obtained is quite low (kPa range).[96, 97] HA is a type of GAG that contains disaccharide repeat units and is present in joints in the body.[97] Covalently crosslinked HA hydrogels have been synthesised by a number of methods and require chemical modifications.[98, 99] Photo-polymerised methacrylic anhydride HA hydrogels exhibited compressive moduli of ~2-100 kPa.[100, 101] Chitosan hydrogels have been synthesised using physical or chemical crosslinking methods.[102, 103] Table 1.3 summarises the advantages and disadvantages of a range of widely studied natural hydrogels. Notably, the majority of the materials, including collagen, alginate, chitosan, and fibrin possess low mechanical strength and thus there is a significant need for new biomimetic hydrogels with enhanced mechanical properties or elasticity.

Table 1.3 Summary of natural materials and their associated advantages and disadvantages for tissue engineering.

Material	**Advantages for tissue engineering**	**Disadvantages for tissue engineering**	**Reference**
Collagen	• Major component of cartilage ECM	• Inadequate mechanical properties • Fast degradation • Limited availability	[92-95, 104-106]
Alginate	• Ease of gelation	• Unfavourable immunological responses *in vivo* • Inadequate mechanical properties • Slow degradation	[62, 105, 107, 108]
Chitosan	• Controllable biodegradation • Good biocompatibility *in vivo* • Controllable porosity	• Low mechanical strength	[106, 109]
Agarose	• Thermo-responsive gelation • Shown promise from *in vitro* studies	• Poor biocompatibility *in vivo*	[106, 110]
Fibrin	• Injectable • Biodegradable	• Low mechanical strength	[106]
Hyaluronan	• Injectable • Biodegradable • Stimulates chondrogenesis	• Insufficient mechanical strength	[106, 111-113]
RSF	• Biocompatibility • Controllable degradation rates • Excellent mechanical strength • Easily processed using aqueous solvents	• Rigid/Stiff	[62, 106]

In section 1.3 it has been discussed that physically crosslinked RSF hydrogels have been fabricated through a range of methods; however generally the resultant hydrogels exhibit mechanical strength in the kPa range that do not meet the requirements for engineering load-bearing tissue, such as cartilage. While RSF possesses a number of advantageous properties for biomedical applications as shown in Table 1.3, there have been few reports of chemically crosslinked RSF hydrogels in the literature. Several groups have employed Genipin as a chemical crosslinking agent to form RSF hydrogels; however this process was time consuming and took approximately 6 hours to complete.[114-116] Xiao et al. measured the compressive modulus of genipin crosslinked RSF hydrogels to be ~300 kPa, which demonstrates an improvement over the physically crosslinked RSF hydrogels.[115] In another study, enzymatic covalent crosslinking of RSF using tyrosinase has been achieved, however this reaction required ~20 hours to complete.[117] Therefore, significant scope remains to develop new methods for rapid chemical crosslinking of RSF to form hydrogels with tuneable properties that can be applied to a range of tissue engineering applications. In addition, the stiffness of RSF limits its use for applications that require elasticity, such as cartilage regeneration, and thus there is a need to design RSF-based hydrogels with tuneable elasticity and toughness.

Elastomeric proteins, such as elastin and resilin and polypeptides derived from their structure (ELPs and RLPs), have also been chemically crosslinked to form biologically relevant hydrogels. Chemically crosslinked elastin-mimetic polypeptide [(VPGVG)4(VPGXG) where X is Lys (K) 1 and Ile (I) 2] hydrogels were synthesised and demonstrated a thermo-responsive expansion and contraction phase transition at 35˚C.[118, 119] Lee et al. demonstrated two methods of chemically crosslinking of ELPs using dicumyl peroxide and carbodiimide to form hydrogels that possessed tensile moduli on the scale of tens of kPa.[120] Renner et al. fabricated a RLP composed of the repeat sequence $(AQTPSSQYGAP)^{10}$ and one bioactive domain that was chemically crosslinked with tris(hydroxymethyl)phosphine and possessed a compressive modulus of ~22 kPa.[121] Kiick and colleagues synthesised a range of RLPs containing 12 repeats of the resilin consensus motif from exon 1 of the *D. melanogaster* containing different cell-binding domains and crosslinked them via a Mannich-type reaction of lysine residues with β-[tris(hydroxymethyl)-phosphino]propionic acid (THPP).[122-124] The RLPs crosslinked with THPP demonstrated elastic moduli in the range of 1-25 kPa and supported cell growth.[124] Truong et al. demonstrated the rapid Ru(II)-mediated photo-crosslinking of Rec1-resilin to form a hydrogel containing di-tyrosine crosslinks that

possessed tuneable glass transition temperature (T_g) and mechanical properties by adjusting the crosslink density and environment (Figure 1.9).[25] The Rec1-resilin hydrogel is shown to possess outstanding elasticity and superior resilience (~92%) (Figure 1.9B) over any other synthetic or biopolymer hydrogel reported, which is particularly useful for applications where repetitive motion is required.[25] However, the modulus of the Rec1-resilin hydrogel was very low ~2 kPa and this limits its use for tissue engineering applications where toughness and structural integrity is important.[25]

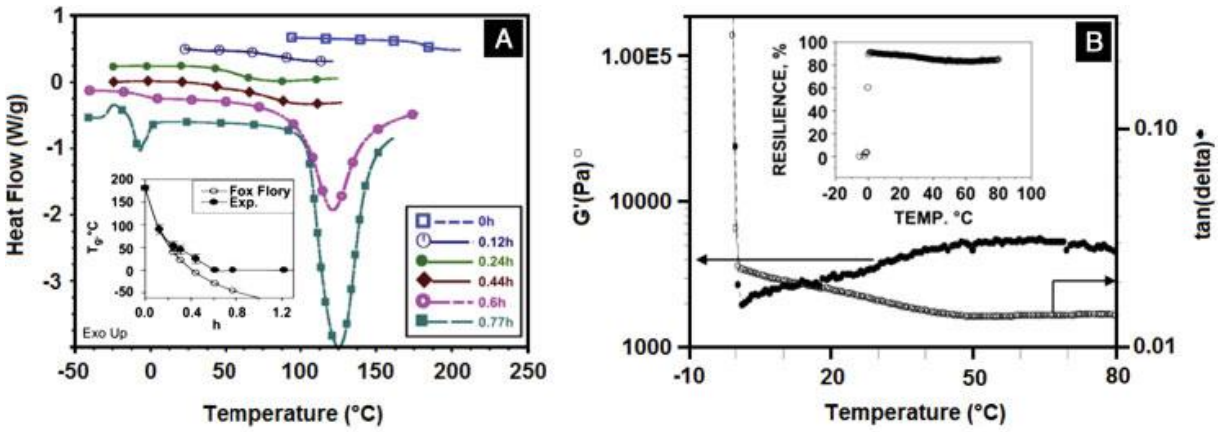


Figure 1.9 Mechanical behaviour of Rec1-resilin photo-crosslinked hydrogel. A) Effect of hydration on the T_g. B) Effect of temperature on the elastic storage modulus (G') and damping tan δ (G"/G') at equilibrium hydration; inset, resilience as a function of temperature.[43]

From the above literature study, it is evident that a range of crosslinked hydrogels have been fabricated from biomimetic polymers. Whilst some of these exhibit excellent properties, such as the high elasticity and resilience of Rec1-resilin and the improved strength and biocompatibility of RSF, there remains significant scope to improve the mechanical properties of natural hydrogels to target tissue engineering applications for more mechanically active tissue environments, such as cartilage, that require modulus values on the MPa scale.

1.4.2 Chemically crosslinked hydrogels based on synthetic polymers

Synthetic polymer-based hydrogels can be fabricated using various chemical methods, including photo- and thermal-initiated polymerisation.[24] In particular, control of the molecular structure and crosslink density allows for hydrogels with tuneable properties, such as mechanical strength, biodegradation, and response to stimuli.[24] Hydrogels based on

poly(ethylene glycol) (PEG), poly(vinyl alcohol) (PVA), poly(hydroxyethyl methacrylate) (PHEMA), poly(lactic acid) (PLA) and poly(glycolic acid) (PGA) have been widely studied for tissue engineering applications. PEG hydrogels have been fabricated using a range of covalent crosslinking methods and are non-toxic and approved for use by the US Food and Drug Administration.[24] West et al. first synthesised photo-polymerised hydrogels using acrylate-terminated PEG monomers.[125] In another study, Bryant et al. synthesised photo-crosslinked PEG-based hydrogels that possessed equilibrium swelling ratios of 9.3 to 4.2 and compressive moduli ranging from 34 to 1370 kPa.[126] The drawback of PEG-based materials is that they prevent protein adsorption and thus require modification with peptide sequences to modify cell adhesion or induce degradation.[24] PVA hydrogels have also been studied extensively for biomedical applications and can be crosslinked by a range of physical and chemical methods. The chemical crosslinking agents that have been used to synthesise PVA hydrogels include glutaraldehyde, acetaldehyde, formaldehyde, and other mono-aldehydes.[24] The use of the aforementioned crosslinking agents in the presence of acetic acid, methanol, or sulphuric acid results in the formation of acetyl crosslinks between the hydroxyl groups of PVA.[24] However, the use of toxic crosslinking agents is not suitable for biomedical applications and the extraction procedures are time consuming. Photo-crosslinked PVA hydrogels have also been synthesised and shown to promote cell adhesion.[127, 128]

Thermo-responsive chemically crosslinked hydrogels have also been fabricated from synthetic thermo-responsive polymers, such as PNIPAM and PVCL, and exhibit a volume change in response to temperature. PNIPAM hydrogels were synthesised by crosslinking with N,N'-methylenebisacrylamide (MBAm) and exhibit swelling and shrinking in response to temperature.[129, 130] Hinkley et al. studied the mechanical properties of PVCL hydrogels, chemically crosslinked with ethylene glycol dimethacrylate, and found that the engineering modulus (E) increased from 30.1 (±6.6) kPa to 940 (±220) kPa at temperatures of 22˚C and 47.5˚C, respectively.[131] In addition, the engineering failure stress (strength) and elongation at break were determined to be 98 (±12) kPa and 239 (±26) %, and 830 (±140) kPa and 500 (±80) % at 22˚C and 47.5˚C, respectively.[131] The use of thermo-responsive polymers for tissue engineering applications will allow for additional functions such as therapeutic molecule delivery.

Chemically crosslinked hydrogels synthesised from synthetic polymers exhibit a range of advantageous properties including precise control over the hydrogel structure and properties;

however, they do not provide a biomimetic environment to induce cellular differentiation, and thus require chemical modification with peptide-based sequences.

1.4.3 Natural and synthetic chemically crosslinked hydrogels used for cartilage tissue engineering

Table 1.4 summarises a range of natural and synthetic polymer hydrogels that have been chemically crosslinked by a range of methods and evaluated for cartilage tissue engineering. Their ability to support the chondrogenesis/differentiation of chondrocytes and mesenchymal stem cells (MSCs) was studied and is detailed in the table. Notably the natural polymer hydrogels did not possess modulus values that were close to that of cartilage (~180 to 2500 kPa). Also, a number of the synthetic polymer hydrogels have been modified with cell binding sequences to improve their biocompatibility. Thus it is evident that the current hydrogel materials composed of either natural or synthetic materials do not fulfil all of the characteristic requirements for tissue engineering, including elasticity, toughness, swelling capacity, responsiveness and biocompatibility. Thus, there remains a distinct need to develop hydrogels with improved and tuneable properties to target a range of tissue engineering applications, in particular those that are exposed to active mechanical environments, such as cartilage.

Table 1.4 Summary of chemically crosslinked hydrogels from natural and synthetic polymers that have been evaluated for cartilage tissue engineering *in vitro*.

Polymer	**Crosslinking method**	**Modulus (kPa)**	**Cell type**	**Ability to support chondrogenesis**	**Ref.**
Chitosan modified with Col II or Chondroitin sulphate (CS)	UV irradiation	~5.8-7.0 (with Col II) ~5.0-5.3 (with CS)	Rabbit chondrocytes	*In vitro* (with Col II – enhanced GAG, Aggrecan and Col II production)	[132]
Collagen	Dual chemical crosslinking: photo-crosslinking (Rose Bengal) + 1-ethyl-3-(3-dimethylaminopropyl)carbodiimide and N-hydroxysuccinimide)	~0.118	Swine chondrocytes	*In vitro* - ~96% viability	[133]
Gelatin	Genipin	-	Rat chondrocytes	*In vitro* – synthesis of tissue containing Col II and GAG	[134]
ELP	Enzymatic	~0.28	Swine chondrocytes	*In vitro* – promotes cell viability and ECM synthesis	[135]
RLP – RGD functionalised	Tris(hydroxymethyl) phosphine	~22	hMSCs	*In vitro* – 95% cell viability	[121]
PEO-dimethacrylate/ PEG	Photo-polymerisation	~1-10	Bovine and ovine chondrocytes	*In vitro*	[136]
PEG	Photo-crosslinking	~36-350	Bovine chondrocytes	*In vitro* (Col II and GAG synthesis)	[126]
PEG-co-PLA	Photo-polymerisation	-	Bovine chondrocytes	*In vivo* (Col II and GAG synthesis)	[137]
PEG modified with cleavable RGD binding motif	Photo-polymerisation	-	Human mesenchymal stem cells (hMSCs)	*In vitro* ~80% cell survival, Col II synthesis	[138]
PEG modified with RGD and KLER (binding site from decorin protein binds Col II) motifs	Photo-polymerisation	-	hMSCs	*In vitro* Improved Col II and GAG synthesis	[139]
PNIPAM and PNIPAM-co-AAc	Chemical and physical – polymerisation followed by thermal stabilisation *in vitro*	-	Bovine articular chondrocytes	*In vitro* – formed tissue	[130]

1.5 Hybrid hydrogels

To facilitate cellular infiltration and adequate nutrient transport, hydrogels need to possess a range of properties including appropriate elasticity, toughness, water swelling capability, responsiveness and biocompatibility and emulate the balanced microarchitecture of the native ECM. In general, as can be seen from the previous sections, hydrogels are soft and brittle materials and do not satisfy the mechanical requirements for many tissue engineering applications, including load-bearing tissues such as cartilage that possesses modulus values in the MPa range. To date, it has not been possible to demonstrate all of the aforementioned properties in a hydrogel composed of a single polymer and thus there has been significant research on the formation of hybrid hydrogels, which are composed of more than one polymer, to obtain biomaterials with improved properties. Hybrid hydrogels can be formed through chemical or physical crosslinks, or a combination of both. Notably, biomaterials and hybrid gels are designed to provide multiple structural and functional ECM analogues for cell growth, offering an environment to direct cell migration, proliferation and differentiation.[3] It has been observed that the combination of natural and synthetic polymers is a valuable platform for enhancing material properties. In general, natural polymers are biocompatible and have an ordered secondary structure, whereas synthetic polymers are generally lacking those properties/characteristics but are easily processed and have defined properties.[140]

1.5.1 Hybrid material synthesis

A range of chemical and physical interactions are possible in the synthesis of hybrid materials, including covalent bonds, hydrogen bonding, hydrophobic interaction, van der Waals, electrostatic, solvation and steric forces. In all cases, the free energy of mixing governs the miscibility of blends of more than one polymer or protein material.[141] The blending of two polymer materials to form a hybrid can result in three phases in the system, including miscible phase, metastable phase, and immiscible phase (Figure 1.10A).[141] Figure 1.10A shows the phase diagram of a two component system in which, the miscibility is dictated by the temperature and composition of components. Using differential scanning calorimetry (DSC), a useful thermal analysis technique for measuring the miscibility of polymer hybrids, the glass transition temperature (T_g) can be elucidated.[141] Figure 1.10B shows that a miscible system is demonstrated by a single T_g that is intermediate of the individual component T_gs, whereas, separate T_gs indicate an immiscible system.[141] A number of parameters can affect the miscibility of blend systems including temperature, pH, protein

concentration, etc.[141] Thus, when designing hybrid hydrogel materials, it is important to understand the miscibility of the constituent polymer/or protein components in a particular system.

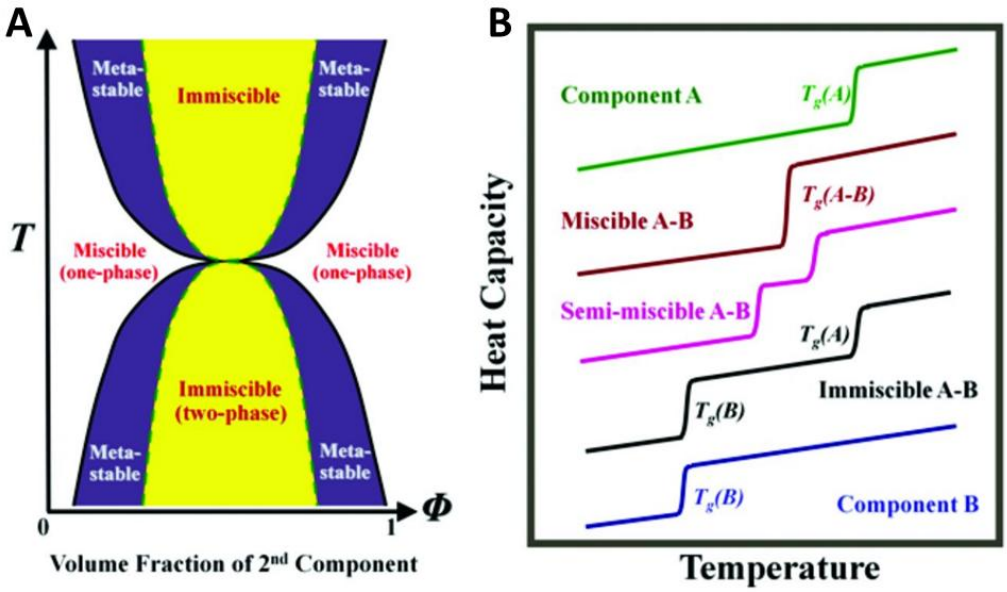


Figure 1.10 A) Schematic phase diagram for a two component hybrid system. B) Schematic DSC thermograms showing the T_g behaviour indicating the type of phase behaviour in a hybrid system.[141]

1.5.2 Methods of fabricating hybrid hydrogels with enhanced properties

There has been significant research in recent years on developing new types of hybrid hydrogels with different structures that result in improved mechanical properties. A number of different methods have been employed to enhance hydrogel performance, including co-crosslinked networks,[142] double network (DN) hydrogels,[143, 144] nanocomposite hydrogels,[145, 146] microgel-reinforced hydrogels,[147, 148] sliding-ring hydrogels,[149] tetra-PEG hydrogels,[150] fibre-reinforced hydrogels,[151-154] and physical interaction enhanced hydrogels.[155-157] Figure 1.11 depicts the structure of a range of different hydrogel types that have been developed to date.[158] Nanocomposite hydrogels are composed of organic and inorganic components, such as polymer and clay, where the clay platelets act as multifunctional crosslinkers and the resultant hydrogels exhibit superior properties.[159] Microgel-reinforced hydrogels contain two phases, where the disperse phase exists in a microgel with DN structure and the continuous phase is the soft gel matrix.[148] Tetra-PEG hydrogels consist of a four-arm PEG network that is prepared by cross-end-coupling two kinds of four-arm PEG structures that possess different functional groups.[160] The advanced mechanical properties of the tetra-PEG hydrogels have

been attributed to their uniform network structure.[160] The structure of the interpenetrating network (IPN) hydrogel (Figure 1.11C) consists of two or more physically entangled polymer networks. The DN hydrogel (Figure 1.11E) is a type of IPN; however there are a number of requirements specific to the DN hydrogel structure. In particular, the first network is rigid and brittle and should be highly crosslinked, whereas the second network must be soft and loosely crosslinked.[158] Also, there is the presence of inter-network crosslinks in addition to intra-network crosslinks. As a result, the DN hydrogel structure has been shown to significantly enhance the toughness of hydrogels and is a versatile method that has the potential to be applied for a range of natural and synthetic rigid and soft polymer materials. Thus, the fabrication and properties of DN hydrogels will be presented in more detail in the following sections.

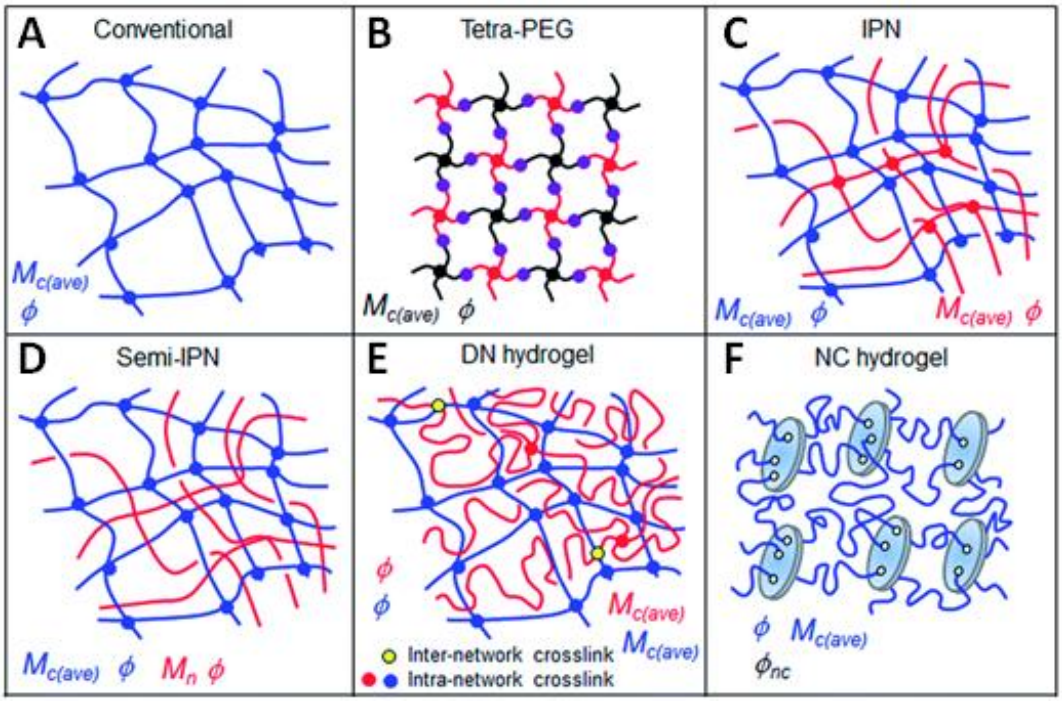


Figure 1.11 Schematic representations of the structures of different types of hydrogels[158]

1.5.3 Fabrication and mechanical properties of DN hydrogels

Gong et al. pioneered the synthesis of a DN hydrogel using a two-step process involving the formation of a highly crosslinked rigid polymer (poly(2-acrylamido-2-methylpropanesulfonic acid) (PAMPS)) in the presence of a softer more loosely crosslinked one (poly(acrylamide) (PAAm)).[143, 161] DN hydrogels have been reported to possess impressive mechanical properties, such as fracture tensile stresses of 1-10 MPa and strains of 1000-2000%, in addition to high toughness that is evident from tearing fracture energies of around 10^2-10^3

J/m^2.[144, 161] These values of strength and toughness are shown to be comparable to cartilage, which demonstrates their suitability for cartilage tissue engineering applications.[162] The enhanced mechanical properties of DN hydrogels have been attributed to the contrast in network structure and strong entanglement.[144] Similarly, other groups have used the DN concept to prepare hydrogels combining bacterial cellulose (BC) with other polymers, including gelatin, polysaccharides and synthetic polymers.[163, 164] Despite this, the fabrication of DN hydrogels is tedious and very time consuming as it takes 1-2 days to complete the hydrogel synthesis.[144] As a result, several groups have reported the synthesis of DN hydrogels using a one-pot method. Chen et al. employed a one-pot approach to synthesise agar-PAAm DN hydrogels that consisted of a hydrogen bonded agar network interpenetrated with a covalently crosslinked PAAm network.[165] These hydrogels exhibit enhanced elastic moduli (123 kPa) and toughness (dissipate energy of 9 MJ/m^3).[165] In addition, Chen et al. synthesised PEG-poly(acrylic acid) (PAA) DN hydrogels using a one-pot method with a first network composed of glutaraldehyde (GA) crosslinked PEG.[166] The one-pot method allows for the facile synthesis of hybrid physically-chemically crosslinked DN hydrogels that can be completed in 1-2 hours.[144, 165]

Most of the classical DN hydrogels are composed of two chemically crosslinked networks, one with a high crosslink density and the other one loosely crosslinked.[144] However, recently there have been some reports of hybrid DN hydrogels containing a combination of physical and chemical crosslinks.[4, 167, 168] The types of physical interactions that occur within the physical network and between the two networks can include different types of non-covalent bonds, such as hydrogen bonds, hydrophobic interactions, van der Waals, and ionic interactions.[144] Sun et al. reported the synthesis of a DN hydrogel composed of ionically crosslinked alginate and covalently crosslinked polyacrylamide, which demonstrated enhanced properties compared to single network hydrogels and possessed a fracture energy of ~9,000 J/m^2 (Figures 1.12A and B).[4] The mechanism behind the toughness of DN hydrogels relates to the sacrificial bond concept.[161, 165, 169, 170] However, the drawback of classical DN hydrogels containing only covalent bonds is that permanent damage occurs due to breakage of the covalent bonds after rupture during the first loading, which cannot be recovered.[165] Figure 1.12C shows a comparison between the toughness of DN hydrogels and other materials, which demonstrates its enhanced properties compared to single network hydrogels. By forming a hybrid physical-chemical DN structure, the physical network, which is formed from reversible non-covalent interactions, enables the formation of hybrid DN hydrogels with

recoverable properties that demonstrate high mechanical strength and toughness.[144] However, there remain only a few reports of physical-chemical DN hydrogels. Furthermore, the formation of a physical-chemical DN hydrogels that takes advantage of the biomimetic properties of RSF and combines it with a softer more elastic protein or synthetic polymer has not been reported to date.

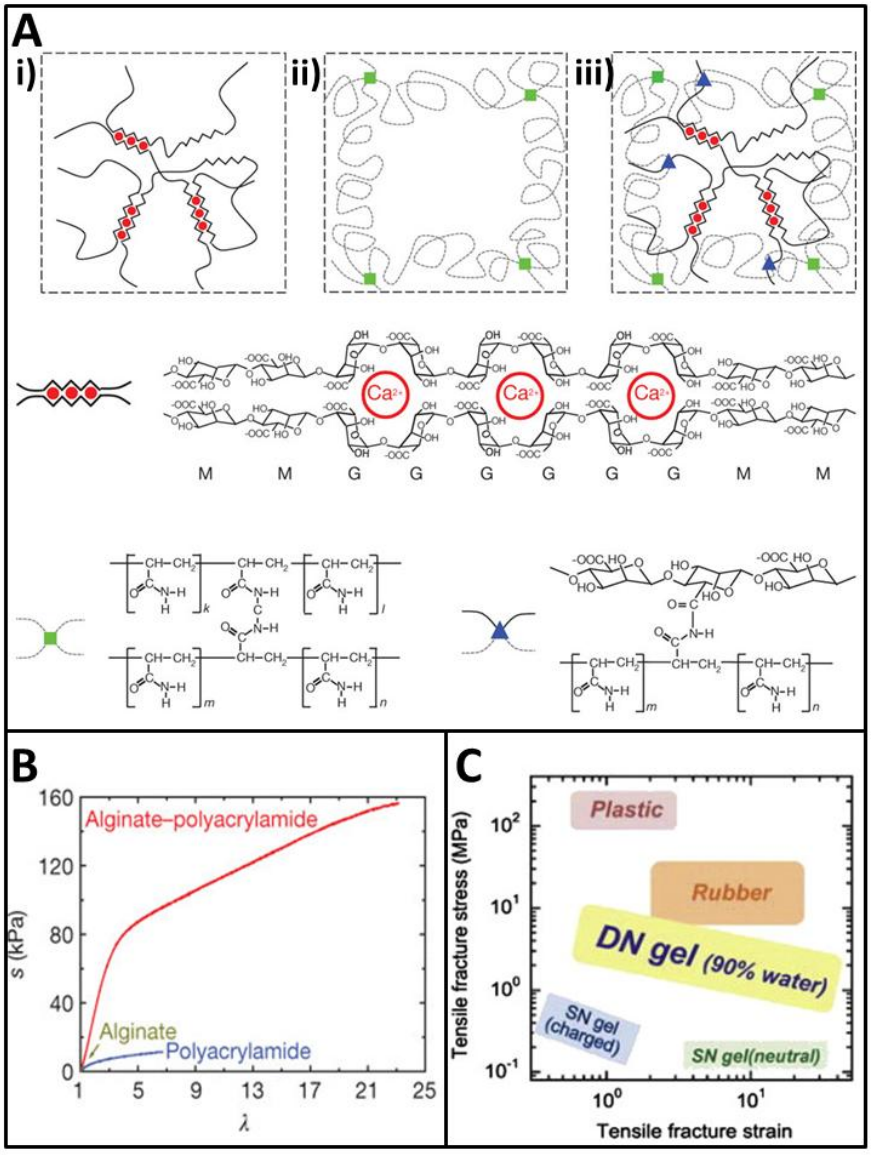


Figure 1.12 A) Schematic of the structure of i) alginate single network gel with ionic crosslinking (red circles); ii) PAAm single network hydrogel with covalent crosslinks through MBAm (green squares); and iii) alginate/PAAm DN hydrogel showing the crosslinks that occur in the single network hydrogels in addition to covalent crosslinks between amine groups on polyacrylamide chains and carboxyl groups on alginate (blue triangles). Detailed chemical structures are shown below.[4] B) Stress-stretch curves of the alginate and PAAm

single network hydrogels compared to the alginate/ PAAm DN hydrogel.[4] C) Comparison of the toughness of DN hydrogels with various types of materials.[161]

1.6 Understanding the microstructure of hydrogels using small angle neutron scattering techniques

Depending on the method of crosslinking used, a gel could be homogeneous or heterogeneous. An understanding of the correlation between the biomaterial structure and observed bulk properties, such as mechanical properties and water swelling capacity, is essential for designing hybrid hydrogels with enhanced properties. Neutron scattering techniques including SANS and ultra-small angle neutron scattering (USANS) are valuable techniques to study the structure and mesh size (ξ) of different types of materials, including hydrogels. An advantage of SANS/USANS for investigating the hydrogel structure compared to other microscopic techniques, such as scanning electron microscopy (SEM), is that the samples can be studied in the fully hydrated state, which is highly relevant for these types of materials. Also, by combining SANS and USANS, it is possible to obtain structural information covering four orders of magnitude in size (~10 Å to 10 μm).[171] The structure of hydrogels is complex and consists of a range of heterogeneities that are introduced by the formation of physical or chemical crosslinks between polymer chains.[172] Generally, the scattering from hydrogels on the nanoscale can be described as a combination of a dynamic component, due to the mobile network polymer chains, and a static component, that is due to crosslinking heterogeneities and leads to regions of different polymer density on the molecular scale.[173, 174] Thus, SANS and USANS are ideal and can be used to provide information relating to the crosslink density and porosity of hydrogels, which is directly related to the mechanical properties and water swelling capacity.

SANS has been employed to study the microstructure of a range of different types of physically and chemically crosslinked hydrogels, predominantly from synthetic polymers.[173, 175-178] However, there are less examples where a combination of SANS and USANS has been employed to study the hydrogel structure over a large size range.[179-181] Crompton et al. employed SANS and USANS to unravel the microstructure (~10 to 10,000 Å) of thermo-responsive chitosan-glycerophosphate (GP) hydrogels.[181] From SANS they observed a polymer-rich domain of ~350 Å and polymer-poor regions with a correlation length of ~120 Å, which conformed to classical gel theory.[181] In addition, the observation of 1-2 μm sized particles from USANS correlated well with their observations from laser scanning confocal

microscopy.[181] In another study, Mangiapia et al. used SANS to study chemically crosslinked chitosan and chitosan-poly(vinylpyrrolidone) (PVP) hydrogels.[175] It was observed that the hydrogel was composed of dense and less dense polymer regions with a correlation distance that increased in the presence of PVP.[175] Furthermore, the crosslinked domains had a mesh size of ~90 Å, which did not change significantly with the addition of PVP.[175] Iannuzzi et al. employed USANS to study the porosity of PHEMA hydrogels and how this changes in the dry and swollen states.[182] They observed micron-sized pores for the swollen hydrogels that disappeared upon drying, which was in agreement with SEM observations.[182] Furthermore, Tominaga et al. used SANS to study the structure of a PAMPS/PAAm DN hydrogel in the deformed and undeformed states to elucidate the origin of toughness.[183] A deformation induced structure of ~1.5 μm was observed for the PAMPS/PAAm DN hydrogel and SANS confirmed the existence of molecular interactions between PAMPS and PAAm in the DN hydrogel.[183]

Despite the extensive research on methods of forming physically crosslinked RSF hydrogels, to date there has not been any reports of using neutron scattering to understand the microstructure of physically or chemically crosslinked RSF hydrogels. However, Greving et al. have used SANS to study the morphology of RSF in aqueous solutions of different concentrations.[84] Also, Dandu et al. synthesised a series of silk-elastin-like protein polymers (SELPs) containing silk-like (GAGAGS) repeats, and elastin-like (GVGVP) units, that were physically crosslinked to form hydrogels.[176] By correlating the results from SANS and dynamic mechanical analysis (DMA) they observed that the correlation length was inversely proportional to the storage modulus.[176] Thus, it is clear that USANS and SANS are valuable techniques for studying the structure of hydrogels over a large size range. A major advantage of neutron scattering techniques is that no preparation procedures, other than swelling in deuterated water (D_2O), are required, which is unlike other techniques such as SEM that requires the use of chemical drying agents that can affect the hydrogel structure.

1.7 Evaluation of hybrid hydrogels for tissue engineering applications

As discussed above, hybrid hydrogels formed through DN structure and co-crosslinking, among others, have been identified as promising methods to form hydrogels with enhanced properties. In this section, a detailed discussion of the current types of hybrid hydrogels and their application for tissue engineering is presented.

Amongst many studies, the recent study of Yu et al. presented a unique way of fabrication of an injectable HA/PEG hydrogel that was crosslinked via a combination of enzymatic and Diels-Alder click chemistry.[184] The resultant HA/PEG hydrogel possessed a storage modulus of ~27 kPa and compressive strain of up to 81.9%.[184] The cell lines that are commonly used for *in vitro* cartilage tissue engineering studies are chondrocytes, from human or animal origin, and MSCs. In the study by Yu et al., a mouse pre-chondrocyte cell line (ATDC5) was encapsulated in the HA/PEG hydrogels and cell viability and proliferation was demonstrated *in vitro*.[184] The main drawback of this method is that it is a two-step process and is quite time consuming. In another study DeKosky et al. synthesised IPN hydrogels composed of agarose and PEG-diacrylate by photo-polymerisation.[185] The agarose-PEG IPN hydrogels demonstrated improved shear modulus values (~40 kPa) compared to the individual networks.[185] Furthermore, *in vitro* encapsulation of chondrocytes in the agarose-PEG hydrogels resulted in the production of GAG and demonstrated the cytocompatibility of the hydrogels.[185] However, the modulus remains quite low compared to that of native cartilage. Park et al. developed injectable, biodegradable hybrid hydrogels composed of oligo(poly(ethylene glycol) fumarate) (OPF) with transforming growth factor-β1 (TGF-β1) loaded gelatin microparticles (MPs).[186, 187] The OPF-MP hydrogels demonstrated elastic moduli ranging from ~20 to 60 kPa and swelling ratios of between 1.2 and 3.3.[187] MSCs were encapsulated in the OPF-MP TGF-β1 loaded hydrogels and demonstrated a significant increase in Col II and aggrecan compared to the hydrogels that were not loaded with TGF-β1.[186] In another study, Tan et al. used composite hydrogels fabricated using *in situ* approach from chitosan and hyaluronic acid that possessed compressive modulus values of ~12-28 kPa.[188] In addition, the chitosan-hyaluronic hydrogels were shown to support chondrocyte adhesion; however, the use of these materials is limited due to their low modulus values.[188] Mirahmadi et al. synthesised thermo-responsive chitosan (CS)/GP hydrogels reinforced with electrospun RSF fibres and observed increased compressive and Young's modulus values with the incorporation of RSF electrospun fibres.[189] In addition, they observed a significant increase in the accumulation of PG and Col II content in the RSF electrospun fibre reinforced CS/GP hydrogels after 21 days of culture, indicating a correlation between enhanced mechanical properties and the expression of cartilage-like markers.[189] A recent study by Yodmuang et al. demonstrated the formation of RSF hydrogels reinforced with RSF microfibres that exhibited improved modulus properties (Figure 1.13A).[151] Furthermore, the RSF fibre reinforced hydrogels demonstrated chondrocyte compatibility and supported the synthesis of Col II and GAG, whilst producing cartilage constructs that displayed similar

modulus values to cartilage.[151] However, the method of fabrication of the RSF fibre reinforced hydrogels is particularly time consuming (~1-2 days) and the identification of a rapid method to produce RSF hydrogels with improved elasticity and stiffness is required. Thus, it has been observed that despite the ability of RSF-based hydrogels to support the chondrocyte attachment and synthesis of cartilage ECM, improvement of the mechanical properties is necessary to successfully synthesise optimal load-bearing biomaterials.[151] The current methods of enhancing hydrogel properties through hybrid hydrogel formation and via co-crosslinked and DN gel systems may provide a promising way to develop novel RSF-based materials with enhanced properties for cartilage tissue engineering.

The DN method of hydrogel formation has resulted in hydrogels that possess enhanced toughness compared to conventional IPN hydrogels. Yasuda et al. reported the use of a DN hydrogel composed of PAMPS and poly(N,N'-dimethylacrylamide) (PDMAAm) as a plug to induce spontaneous hyaline cartilage regeneration *in vivo*.[191] The results showed that the PAMPS/PDMAAm DN gel surface enhanced the expression of cartilage-related genes (Col II, Sox9 and aggrecan) compared to tissue culture polystyrene (TCP) *in vitro*.[191] Furthermore, the cells of the regenerated tissue also exhibited a high expression of Col II, Sox9 and aggrecan, which is promising for their use in cartilage regeneration.[191] In another study, Ronken et al. demonstrated the ability to tune the stiffness of PAMPS/PAAm DN hydrogels by modifying the ratios of both networks, which lowered the water content.[192] It was observed that by reducing the water content to 61%, the modulus value was close to that of articular cartilage.[192] DN hydrogels composed of gellan gum methacrylate (GGMA) as the first network and gelatin methacrylamide (GelMA) for the second network were fabricated by Shin et al. (Figure 1.13B).[190] The GGMA/GelMA DN hydrogel exhibited a compressive modulus of ~110 kPa and a compressive failure stress of ~6.9 MPa, which indicates its suitability for cartilage tissue engineering.[190] An i*n vitro* cell culture study of fibroblasts encapsulated in the GGMA/GelMA DN hydrogels demonstrated their cytocompatibility.[190] However, the method for synthesising classical DN hydrogels, such as the PAMPS/PAAm hydrogel, is time consuming and significant scope remains to develop a rapid and facile approach to fabricate hydrogels with tuneable stiffness and a fundamental understanding of the structure and performance of these materials.

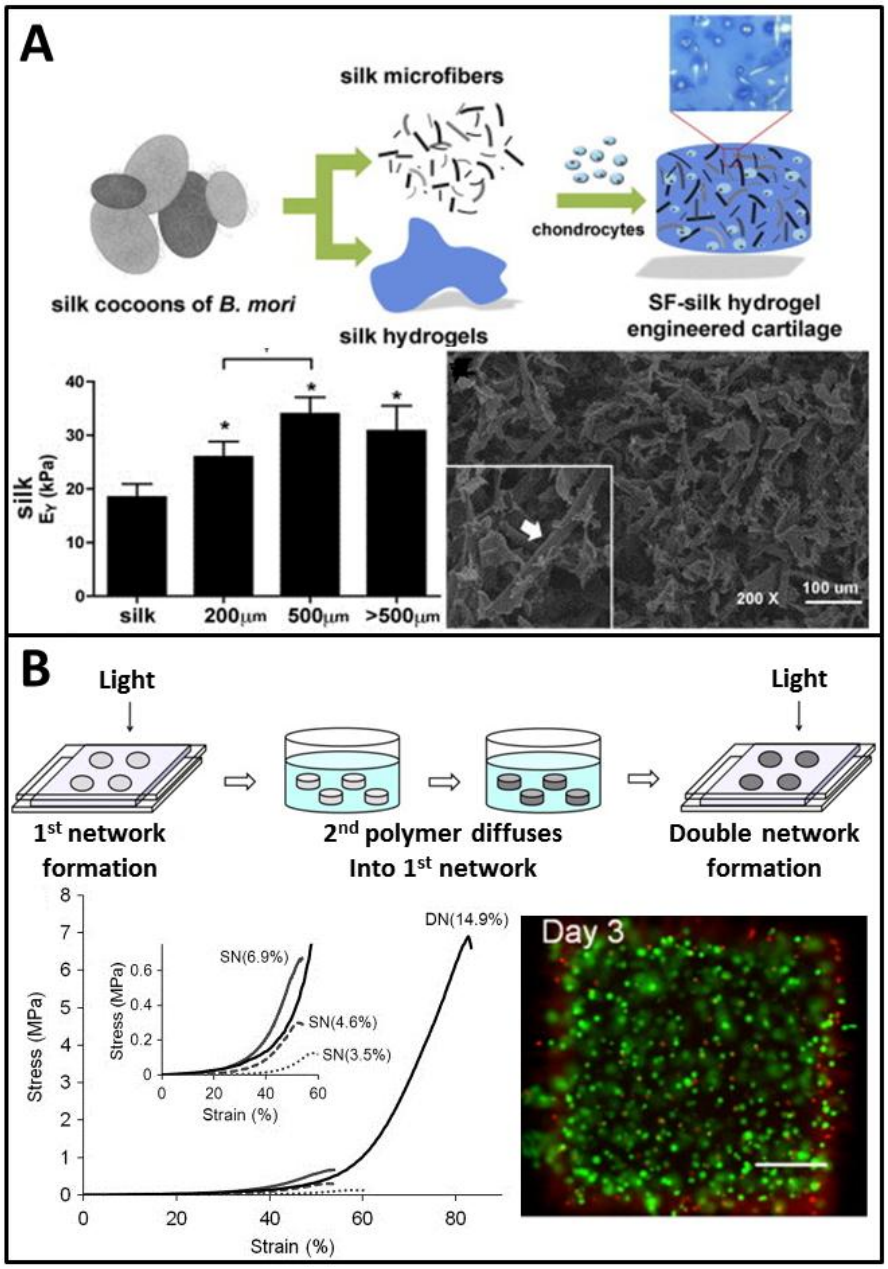


Figure 1.13 A) Clockwise from top: Schematic of the formation of RSF hydrogels reinforced with RSF microfibres; scanning electron micrograph of RSF hydrogel reinforced with RSF microfibres; Equilibrium modulus values of RSF hydrogels reinforced with RSF microfibres. Adapted from [151] with permission. B) Clockwise from top: Schematic depicting the synthesis of DN hydrogels by photo-polymerisation; Fluorescence image of live/dead stained NIH-3T3 fibroblasts encapsulated in GGMA/GelMA DN hydrogels; Stress-strain curves of GGMA/GelMA single network (SN) and DN hydrogels with the same mass ratio (GelMA/GGMA=8.2). Adapted from [190] with permission.

1.8 Biomimetic fabrication of nanofibrous materials by electrospinning

A variety of techniques, such as solution crosslinking, lyophilisation and solvent casting-leaching etc., have been used for hydrogel fabrication to incorporate control of bulk porosity and mechanical properties that can be tuned to match those of native tissue. Electrospinning is an attractive method for fabricating fibrous mats composed of continuous fibres with diameters from a few nanometres to microns, which can be applied for a wide range of applications, including water filtration, biotechnology, nano-sensors, drug delivery, and tissue engineering, as it is economical, easily scalable and versatile.[193-196] The large surface areas, high porosity, ability to easily functionalise the fibres and increased mechanical properties associated with nanofibrous materials has resulted in increasing interest for their use as biomimetic materials for tissue engineering scaffolds and drug delivery vehicles.[197, 198]

In addition, three-dimensional scaffolds are ideal for tissue engineering applications as they have been shown to increase cell adhesion and proliferation.[193] The porosity and pore size of the nanostructure determine whether it is viewed as a two- or three-dimensional structure and are therefore important for ensuring that cells are able to migrate and infiltrate through the scaffold.[199] In particular, larger pore sizes allow for diffusion of nutrients and waste products.[196] Research has shown that an increase in the width of fibres results in an increase in the mean pore radius.[199] Thus it is not ideal to decrease the fibre width less than 100 nm, as the pores will be too small and the cells will be unable to migrate into the scaffold.[199]

1.8.1 Electrospinning to form nanofibrous mats for tissue engineering

A number of synthetic and naturally occurring polymers have been employed to fabricate electrospun mats for tissue engineering. Toyokawa et al. synthesised poly(D,L-lactide-co-glycolide) (PLG) scaffolds and studied their ability to repair osteochondral defects *in vivo*.[200] They observed the formation of fibrous tissue at the surface of the scaffold after two weeks and was maintained at 24 weeks.[200] Li et al. fabricated electrospun PCL three-dimensional nanofibrous scaffolds and evaluated their potential for cartilage tissue engineering.[201, 202] *In vitro* cell culture studies with fetal bovine chondrocytes cultured on PCL electrospun scaffolds resulted in the expression of cartilage-specific ECM genes, including Col II and aggrecan.[202] Further to this, the PCL electrospun scaffolds were seeded with hMSCs and supplemented with chondrogenic media containing TGF-β1 and it was observed that treatment with TGF-β1 for 21 days resulted in the expression of aggregan and Col II and the

formation of cartilaginous tissue *in vitro*.[201] Shields et al. reported the synthesis of electrospun Col II nanofibres crosslinked with glutaraldehyde that demonstrated fibre diameters ranging from 0.14 to 3.51 μm.[203] The Col II nanofibres were culture with adult human articular chondrocytes and it was observed that the cells adhered to and infiltrated into the scaffold.[203]

The combination of natural and synthetic polymers in one material offers a number of advantages, in particular improved biocompatibility as materials like PCLs do not possess the biological cues to direct cell differentiation. Bhattarai et al. fabricated chitosan nanofibres by electrospinning solutions of chitosan containing PEO to lower the high viscosity of chitosan solutions and improve the electrospinnability.[204] The chitosan-based nanofibres were stable in aqueous systems and supported the adhesion of chondrocytes.[204] PCL and starch-compounded PCL (SPCL) were electrospun by Da Silva et al. to form nanofibrous mats with fibre sizes ranging from 0.4 to 1.4 μm and 0.3 to 20 μm, respectively.[205] The PCL and SPCL nanofibrous mats were evaluated *in vitro* with bovine articular chondrocytes and cell proliferation and ECM formation and GAG synthesis was observed, indicating their suitability for cartilage regeneration.[205] In another study, Chen et al. synthesised poly(L-lactic acid) (PLLA) electrospun nanofibres modified with cationized gelatin (CG) to improve their biocompatibility.[206] *In vitro* cell culture studies with rabbit articular chondrocytes indicated that the culturing on CG-PLLA nanofibres enhanced cell viability, proliferation and differentiation compared to pristine PLLA nanofibres.[206] In addition, the cells cultured on CG-PLLA nanofibres maintained expression of cartilage-related markers, Col II, aggrecan and Sox9.[206] Furthermore, *in vivo* studies by subcutaneous implantation of the cell-CG-PLLA constructs resulted in the formation of cartilage tissue after 28 days.[206] It can be observed that synthetic polymers are predominantly employed for electrospinning but they require modification with natural materials in order to provide a biomimetic environment for cell growth. Thus, there is a significant need to develop methods for facile fabrication of electrospun mats that combine the advantages of natural and synthetic materials.

1.8.2 Co-axial electrospinning to form core/shell nanofibrous mats

One method which allows for the facile electrospinning of two different polymer solutions to form core/shell fibres is known as co-axial electrospinning. Core/shell fibres are advantageous for tissue engineering and drug delivery applications as there is the potential to combine mechanical support, biocompatibility, and delivery of therapeutic compounds in one

material.[207] The co-axial setup consists of two separate concentric capillaries and the core and shell solutions are introduced individually using separate syringes (Figure 1.14).[199, 208] The stresses generated by the applied potential on the sheath solution results in viscous dragging of the core solution and the formation of a compound co-axial jet at the tip of the capillary.[207] This process is expected to occur fast enough to limit any mixing of the core and shell solutions and thus results in fibres with core/shell morphology.[209, 210]

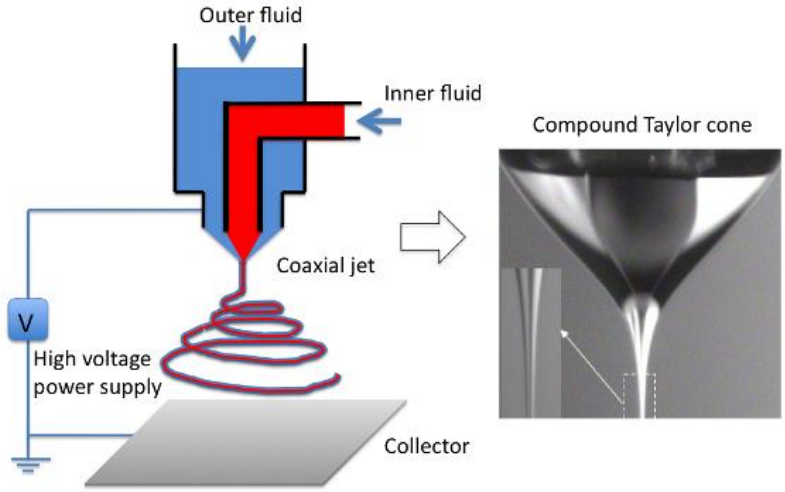


Figure 1.14 Schematic of the formation of core/shell fibres by co-axial electrospinning.

1.8.3 Core/shell electrospun fibres/mats for tissue engineering

In recent years, the co-axial configuration has been employed to electrospin a range of synthetic and natural polymer materials to obtain core/shell fibres and mats.[194, 210-213] As mentioned, the co-axial electrospinning method is useful to fabricate fibres containing drugs or bioactive components in the core, whilst the shell protects the core components and provides mechanical support for cell growth. In a recent study by Man et al., co-axial electrospinning was employed to synthesise core/shell nanofibres of ~700 nm in diameter containing TGF-β1 to stimulate chondrogenic differentiation of bovine MSCs (BMSCs).[214] The core solution contained PVP, bovine serum albumin (BSA) and TGF-β1, whilst the shell solution was composed of PCL.[214] In addition, a BMSC-specific affinity peptide (E) was conjugated to the PCL shell to facilitate cell-scaffold interactions as PCL is hydrophobic and has no recognition sites for cell attachment.[214] Transmission electron microscopy (TEM) showed the morphology of the PVP/PCL core/shell fibres containing TGF-β1 (CBrhT) and

demonstrated the hollow core after release of the TGF-β1 (Figures 1.15A and B).[214] It was observed that the core/shell fibres released TGF-β1 in a controlled manner and stimulated the attachment and differentiation of BMSCs, with greater expression of Col II and aggrecan observed for scaffolds containing TGF-β1 and the binding peptide (CBrhTE) compared to those without (CB and CBE) (Figure 1.15C).[214] In a recent study, Tian et al. prepared RSF/Poly(lactic acid) core/shell nanofibres with nerve growth factor encapsulated in the core with RSF that demonstrated suitable properties (cell attachment and proliferation) for nerve tissue engineering.[215]

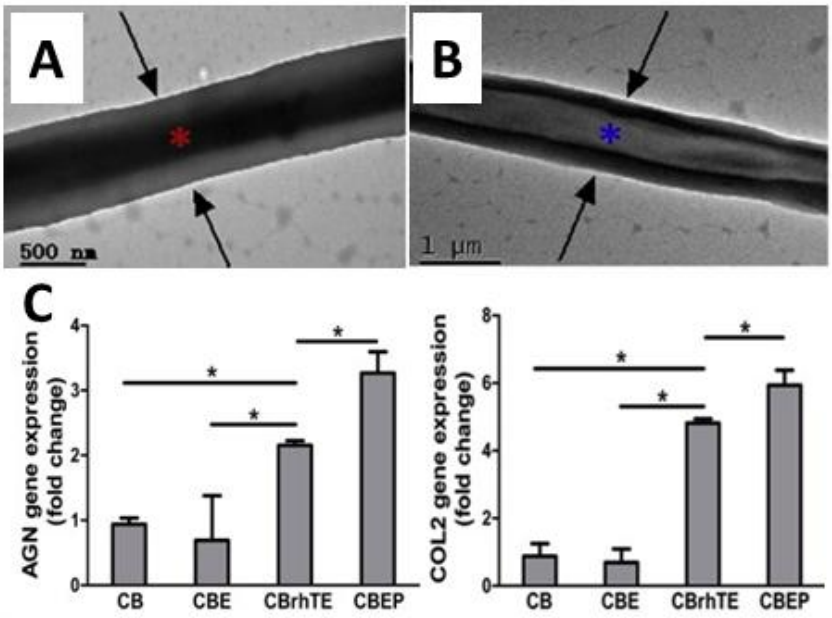


Figure 1.15 A) TEM images showing the morphology of PVP/PCL core/shell fibres containing TGF-β1 in the core (CBrhTE). B) TEM of PVP/PCL core/shell fibres after release of TGF-β1. C) Relative expression levels of aggrecan (AGN) and Col II for BMSCs cultured on different scaffolds after 14 days of incubation. Adapted from [214] with permission.

The use of stimuli-responsive polymers in core/shell nanofibres also offers a useful way of designing drug delivery vehicles that enable triggered release as a result of change in environmental conditions, such as temperature or pH.[216] Chen et al. fabricated temperature-responsive core/shell nanofibres composed of PNIPAM and PCL and demonstrated the thermo-responsiveness with contact angle measurements.[217] In addition, there has not been much work on thermo-responsive core/shell electrospun fibres and thus there is scope for the development of new materials in this area that combine the features of tissue engineering supports and drug delivery.

1.9 Effect of elasticity, stiffness and swelling capacity on cellular interaction and differentiation

The principle of tissue engineering is to develop a scaffold that mimics the ECM and can act as a mechanical support whilst encouraging cell proliferation and differentiation to stimulate the natural tissue growth. The native ECM environment is complex and consists of proteins, proteoglycans, and other soluble molecules.[218] The composition, structure and mechanical properties of the ECM of different tissues vary somewhat depending on their location and function in the body. Table 1.1 that was presented in section 1.1.1 gives an overview of the different mechanical properties of human tissues. Research has shown that a number of ECM physical factors, such as elasticity/stiffness and nanoscale geometry, play a role in dictating the fate of cells.[219] This is in addition to other factors, such as molecular interactions.[219] On attachment to a substrate, cells are known to exert contractile forces, which results in tensile stresses in the cytoskeleton (Figure 1.16).[219, 220] It has been observed that the correlation between the mechanical elasticity/stiffness of a substrate and the aforementioned cell forces dictates cell behaviour, such as growth, proliferation and differentiation.[219] Cells can sense the local mechanical property of the matrix environment and convert the mechanical signal to a chemical signal, which in turn alters gene expression.[221]

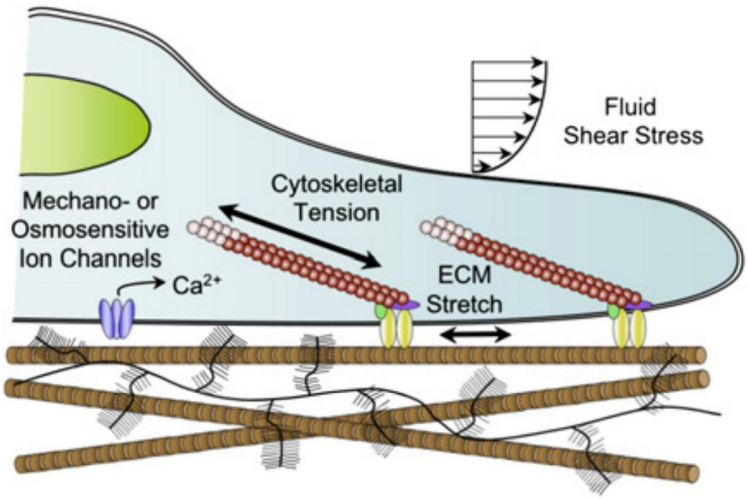


Figure 1.16 Transduction of mechanical factors (tensile, compressive, shear) and the regulation of stem cell growth and differentiation.[219]

Early studies by Emerman et al. demonstrated that mouse mammary epithelial cells grown on soft collagen gels showed increased differentiation compared with TCP.[222] More recently, Engler et al. investigated the growth of MSCs on polyacrylamide gels of different stiffness

and observed that the stiffness dictated the differentiation lineage of the cells.[223] It was found that soft substrates induced the formation of neurogenic cells, substrates with intermediate stiffness that was similar to muscle resulted in myogenic cell behaviour, and stiff substrates induced the osteogenic phenotype.[223] Also, the expression of cartilage-related genes, Col II, Sox9, aggrecan and fibronectin was significantly higher for hMSCs grown on electrospun RSF nanofibrous mats of relatively reduced stiffness (~4.8 GPa) compared to stiffer mats (~7.8 GPa).[224] Bovine articular cartilage is known to contain ~80% water and demonstrates a modulus of ~180 to 2500 kPa and thus matrix swelling capacity and modulus contribute to the differentiation of chondrocyte cells *in vitro* and *in vivo*.[7-9] Bryant et al. investigated the differentiation of chondrocytes photo-encapsulated in a range of PEG hydrogels with different swelling ratios and compressive moduli (~30 to 960 kPa).[126] It was observed that maximum Col II production occurred for samples with intermediate moduli (360 kPa); however the gels with maximum swelling ratio allowed for homogeneous GAG diffusion throughout the gels.[126] They addressed this by designing degradable linkages into the network that allowed for an initial modulus of ~350 kPa and an increased swelling ratio after degradation of the linkages. Wang et al. observed that chondrocytes grown on gelatin-hydroxyphenypropionic acid (Gtn-HPA) hydrogels with intermediate storage modulus (~1000 Pa) maintained their chondrogenic phenotype better than gels of lower or higher modulus.[93] In another study, Hopkins et al. demonstrated that neurite growth was greater on RSF hydrogels of medium stiffness (~7.4 to 22.4 kPa) compared to softer (~4.8 kPa) and stiffer (33.1 kPa) hydrogels for neural tissue engineering.[225] Furthermore, in a very recent study, Chaudhuri et al. demonstrated that the stress relaxation of hydrogels also has an effect on the cell response.[226] In particular, it was observed that the spreading, proliferation and osteogenic differentiation of MSCs were enhanced when cells were cultured in hydrogels with faster relaxation rates.[226] In addition to mechanical cues, the swelling behaviour also dictates cell viability and differentiation as it is related to the diffusion of nutrient and cell transport.[126] Park et al. demonstrated that significantly higher expression of Col II and aggrecan from MSCs cultured in oligo(poly(ethylene glycol) fumarate) (OPF)-gelatin microparticle hydrogel composites of higher swelling ratios.[227] This is attributed to the fact that swelling ratio is proportional to the mesh size, which influences nutrient transport and thus influences cell proliferation and differentiation.[227]

Thus, during tuning hydrogel elasticity/rigidity by varying the constituent composition, it is important to ensure that other important properties are not affected or compromised, such as cell-gel interactions, protein transport etc., which alters cell function.

1.10 Aims and Scope of the Project

In light of the above discussion it is obvious that extensive work has been carried out in the area of physical and chemical hydrogels for tissue engineering applications. Physical hydrogels from protein-based materials that self-assemble due to a range of stimuli, including temperature, pH, time etc. possess several advantages, such as effectiveness in forming a biomimetic environment and lack of toxic crosslinking agents. However, they generally demonstrate poor mechanical characteristics due to their reversible interactions and are not ideal for tissue engineering that requires scaffolds with high mechanical integrity. Thus, coassembly with other protein-based materials provides a method for the development of scaffolds with tuneable properties and there is a significant need for developing a greater understanding of the role of coassembly in dictating bulk properties. On the other hand, the majority of the chemically crosslinked hydrogels synthesised to date are soft and brittle and do not meet the requirements for mechanically active tissue environments, such as cartilage. Furthermore, the use of synthetic materials requires chemical modification with biological molecules to induce the desired cellular response. Thus, the approach of forming hybrid hydrogels containing natural, synthetic or a combination of both materials to form hydrogels with enhanced properties has been investigated extensively in recent years. Despite great improvements in the elasticity and toughness properties of hybrid hydrogels that have been fabricated to date, generally the methods are time consuming, they do not provide a biomimetic environment, or the mechanical properties are not sufficient for load-bearing tissues, such as cartilage. Therefore, there is a significant need to develop hydrogels that provide a biomimetic environment for cell growth and differentiation, whilst possessing the desired elasticity, toughness and responsive properties.

RSF from the *Bombyx mori* silkworm is a remarkable natural protein material and has many advantageous properties, as discussed above. However, despite the extensive work on the physical gelation of RSF, the rapid formation of chemically crosslinked RSF hydrogels with tuneable elasticity and stiffness is lacking. Also, its rigidity limits its use for tissue engineering applications where repetitive motion is required. Thus, there is a distinct need to

achieve facile and rapid formation of novel RSF-based hybrid hydrogel materials that possess tuneable properties.

The hypothesis of this work is engineered silk-based hybrid hydrogels will provide a biomimetic environment for cell growth. Therefore, the specific aims of this research include:

- To investigate the formation of a three-dimensional coassembled protein-based hydrogel with tuneable responsiveness.
- Identification and understanding of a facile and rapid method for the photo-chemical crosslinking of RSF.
- Fabrication of RSF-based physical and chemical hydrogels with tuneable elasticity and in-depth understanding of the microstructure of the gels.
- To understand cell-gel interactions and investigate the role of RSF hybrid hydrogel environment to direct cell growth, differentiation and tissue engineering.

The scope of this work has been shown schematically in Figure 1.17. Summarily, three types of biomimetic hybrid hydrogels have been developed based on physical interactions, chemical crosslinking and chemical crosslinking in the presence of non-covalent interactions. An in-depth understanding of the structure-property-performance relationship is established and the best system is indentified.

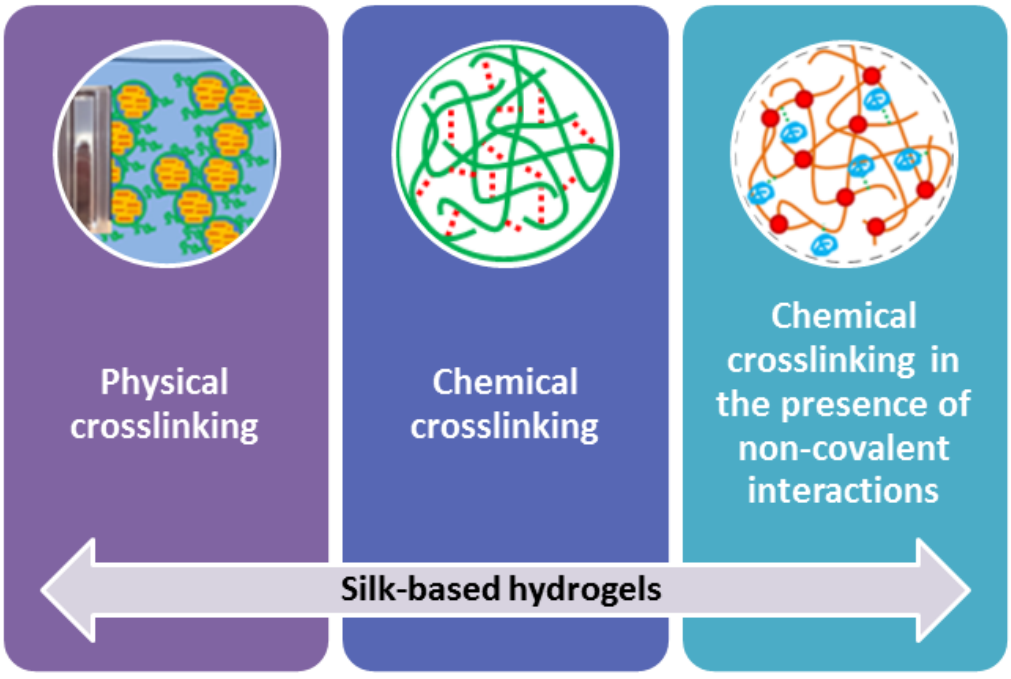


Figure 1.17 Scope of the work.

1.11 References

1. Zhu, J.; Marchant, R. E., *Expert Rev. Med. Devices* **2011,** *8* (5), 607-626.
2. Wu, Y.; Li, C.; Boldt, F.; Wang, Y.; Kuan, S. L.; Tran, T. T.; Mikhalevich, V.; Fortsch, C.; Barth, H.; Yang, Z.; Liu, D.; Weil, T., *Chem. Commun.* **2014,** *50* (93), 14620-14622.
3. Jia, X.; Kiick, K. L., *Macromol. Biosci.* **2009,** *9* (2), 140-156.
4. Sun, J.-Y.; Zhao, X.; Illeperuma, W. R. K.; Chaudhuri, O.; Oh, K. H.; Mooney, D. J.; Vlassak, J. J.; Suo, Z., *Nature* **2012,** *489* (7414), 133-136.
5. Zhang, L.; Hu, J.; Athanasiou, K. A., *Crit. Rev. Biomed. Eng.* **2009,** *37* (1-2).
6. Drury, J. L.; Mooney, D. J., *Biomaterials* **2003,** *24* (24), 4337-4351.
7. Armstrong, C. G.; Mow, V. C., *J. Bone Jt. Surg.* **1982,** *64* (1), 88-94.
8. Setton, L. A.; Mow, V. C.; Howell, D. S., *J. Orthop. Res.* **1995,** *13* (4), 473-482.
9. Zhu, W.; Mow, V. C.; Koob, T. J.; Eyre, D. R., *J. Orthop. Res.* **1993,** *11* (6), 771-781.
10. Sabir, M.; Xu, X.; Li, L., *J. Mater. Sci.* **2009,** *44* (21), 5713-5724.
11. Webb, A. R.; Yang, J.; Ameer, G. A., *Expert Opin. Biol. Ther.* **2004,** *4* (6), 801-812.
12. Liang, X.; Boppart, S. A., *IEEE Trans. Biomed. Eng.* **2010,** *57* (4), 953-959.
13. Gallagher, A. J.; Ni Anniadh, A.; Bruyere, K.; Ottenio, M.; Xie, H.; Gilchrist, M. D. In *Dynamic tensile properties of human skin*, International Research Council on the Biomechanics of Injury, Dublin, Ireland, Dublin, Ireland, 2012.
14. Prescott, V.; Health, A. I. o.; Welfare; Health, A. D. o.; Ageing; Arthritis, B.; Program, O. C.; Australia, A., *A picture of osteoarthritis in Australia*. Australian Institute of Health and Welfare: Canberra, 2007.
15. ABS, Arthritis and Osteoporosis. Australian Bureau of Statistics: 2012.
16. Kandel, R.; Roberts, S.; Urban, J. G., *Eur. Spine J.* **2008,** *17* (4), 480-491.
17. Keeney, M.; Lai, J. H.; Yang, F., *Curr. Opin. Biotechnol.* **2011,** *22* (5), 734-740.
18. Stevens, M. M.; Marini, R. P.; Martin, I.; Langer, R.; Shastri, V. P., *J. Orthop. Res.* **2004,** *22* (5), 1114-1119.
19. Indrawattana, N.; Chen, G.; Tadokoro, M.; Shann, L. H.; Ohgushi, H.; Tateishi, T.; Tanaka, J.; Bunyaratvej, A., *Biochem. Biophys. Res. Commun.* **2004,** *320* (3), 914-919.
20. Altunbas, A.; Pochan, D., Peptide-Based and Polypeptide-Based Hydrogels for Drug Delivery and Tissue Engineering. In *Peptide-Based Materials*, Deming, T., Ed. Springer Berlin Heidelberg: 2012; Vol. 310, pp 135-167.

21. Kundu, J.; Poole-Warren, L. A.; Martens, P.; Kundu, S. C., *Acta Biomater.* **2012,** *8* (5), 1720-1729.
22. Nicodemus, G. D.; Bryant, S. J., *Tissue Eng. Part B Rev.* **2008,** *14* (2), 149-165.
23. El-Sherbiny, I. M.; Yacoub, M. H., *Glob. Cardiol. Sci. Pract.* **2013,** *2013* (3), 38.
24. Peppas, N. A.; Hilt, J. Z.; Khademhosseini, A.; Langer, R., *Adv. Mater.* **2006,** *18* (11), 1345-1360.
25. Truong, M. Y.; Dutta, N. K.; Choudhury, N. R.; Kim, M.; Elvin, C. M.; Nairn, K. M.; Hill, A. J., *Biomaterials* **2011,** *32* (33), 8462-8473.
26. Wang, Y.; Ameer, G. A.; Sheppard, B. J.; Langer, R., *Nat. Biotech.* **2002,** *20* (6), 602-606.
27. Krongauz, V., *J. Therm. Anal. Calorim.* **2010,** *102* (2), 435-445.
28. Djordjevic, I.; Choudhury, N. R.; Dutta, N. K.; Kumar, S., *Polymer* **2009,** *50* (7), 1682-1691.
29. Kopeček, J.; Yang, J., *Acta Biomater.* **2009,** *5* (3), 805-816.
30. Tang, Y.; Heaysman, C. L.; Willis, S.; Lewis, A. L., *Expert Opin. Drug Delivery* **2011,** *8* (9), 1141-1159.
31. Ward, M. A.; Georgiou, T. K., *Polymers* **2011,** *3* (3), 1215.
32. Cordeiro, A. L., Stimuli-Responsive Polymer Nanocoatings. In *Nanotechnologies for the Life Sciences*, Wiley-VCH Verlag GmbH & Co. KGaA: 2007.
33. Gibson, M. I.; O'Reilly, R. K., *Chem. Soc. Rev.* **2013,** *42* (17), 7204-7213.
34. Betre, H.; Setton, L. A.; Meyer, D. E.; Chilkoti, A., *Biomacromolecules* **2002,** *3* (5), 910-916.
35. Mithieux, S. M.; Weiss, A. S., Elastin. In *Advances in Protein Chemistry*, David, A. D. P.; John, M. S., Eds. Academic Press: 2005; Vol. Volume 70, pp 437-461.
36. Rodriguez-Cabello, J. C.; Reguera, J.; Girotti, A.; Alonso, M.; Testera, A. M., *Prog. Polym. Sci.* **2005,** *30* (11), 1119-1145.
37. van Eldijk, M. B.; McGann, C. L.; Kiick, K. L.; van Hest, J. C. M., *Top. Curr. Chem.* **2012,** *310*, 71.
38. Werkmeister, J. A.; Ramshaw, J. A. M., *Biomed. Mater.* **2012,** *7* (1), 012002.
39. Elvin, C. M.; Carr, A. G.; Huson, M. G.; Maxwell, J. M.; Pearson, R. D.; Vuocolo, T.; Liyou, N. E.; Wong, D. C. C.; Merritt, D. J.; Dixon, N. E., *Nature* **2005,** *437*, 999-1002.
40. Dutta, N. K.; Choudhury, N. R.; Truong, M. Y.; Kim, M.; Elvin, C. M.; Hill, A. J., *Biomaterials* **2009,** *30* (28), 4868-4876.

41. Löwik, D. W. P. M.; Leunissen, E. H. P.; van den Heuvel, M.; Hansen, M. B.; van Hest, J. C. M., *Chem. Soc. Rev.* **2010,** *39* (9), 3394-3412.
42. Truong, M. Y.; Dutta, N. K.; Choudhury, N. R.; Kim, M.; Elvin, C. M.; Hill, A. J.; Thierry, B.; Vasilev, K., *Biomaterials* **2010,** *31* (15), 4434-4446.
43. Whittaker, J.; Balu, R.; Choudhury, N. R.; Dutta, N. K., *Polym. Int.* **2014,** *63* (9), 1545-1557.
44. Crespy, D.; Golosova, A.; Makhaeva, E.; Khokhlov, A. R.; Fortunato, G.; Rossi, R., *Polym. Int.* **2009,** *58* (11), 1326-1334.
45. Vihola, H.; Laukkanen, A.; Hirvonen, J.; Tenhu, H., *Eur. J. Pharm. Sci.* **2002,** *16* (1-2), 69-74.
46. Laukkanen, A.; Wiedmer, S. K.; Varjo, S.; Riekkola, M. L.; Tenhu, H., *Colloid Polym. Sci.* **2002,** *280* (1), 65-70.
47. Kozanoglu, S.; Ozdemir, T.; Usanmaz, A., *J. Macromol. Sci., Part A: Pure Appl. Chem.* **2011,** *48* (6), 467-477.
48. Srivastava, A.; Kumar, A., *J. Mater. Sci.: Mater. Med.* **2010,** *21* (11), 2937-2945.
49. Destarac, M.; Marty, J.-D.; Beija, M., *Chem. Commun.* **2011,** *47* (1), 2826-2828.
50. Yokoi, H.; Kinoshita, T.; Zhang, S., *Proc. Natl. Acad. Sci. U. S. A.* **2005,** *102* (24), 8414-8419.
51. Collier, J. H.; Hu, B. H.; Ruberti, J. W.; Zhang, J.; Shum, P.; Thompson, D. H.; Messersmith, P. B., *Journal of the American Chemical Society* **2001,** *123* (38), 9463.
52. West, M. W.; Hecht, M. H., *Protein Science : A Publication of the Protein Society* **1995,** *4* (10), 2032-2039.
53. Yoon, Y.-R.; Lim, Y.-b.; Lee, E.; Lee, M., *Chemical Communications* **2008,** (16), 1892-1894.
54. Pochan, D. J.; Schneider, J. P.; Kretsinger, J.; Ozbas, B.; Rajagopal, K.; Haines, L., *J. Am. Chem. Soc.* **2003,** *125* (39), 11802-11803.
55. Veerman, C.; Rajagopal, K.; Palla, C. S.; Pochan, D. J.; Schneider, J. P.; Furst, E. M., *Macromolecules* **2006,** *39* (19), 6608-6614.
56. Xu, C.; Kopeček, J., *Pharm. Res.* **2008,** *25* (3), 674-682.
57. Creasey, R. G.; Voelcker, N. H.; Schultz, C. J., *BBA - Proteins Proteom.* **2012,** *1824* (5), 711.
58. Bochicchio, B.; Pepe, A., *Chirality* **2011,** *23* (9), 694-702.
59. Lorusso, M.; Pepe, A.; Ibris, N.; Bochicchio, B., *Soft Matter* **2011,** *7* (13), 6327-6336.

60. Dutta, N. K.; Truong, M. Y.; Mayavan, S.; Choudhury, N. R.; Elvin, C. M.; Kim, M.; Knott, R.; Nairn, K. M.; Hill, A. J., *Angew. Chem., Int. Ed.* **2011,** *50* (19), 4428-4431.
61. Alessandrino, A.; Marelli, B.; Arosio, C.; Fare, S.; Tanzi, M. C.; Freddi, G., *Eng. Life Sci.* **2008,** *8* (3), 219-225.
62. Wang, Y.; Kim, H.-J.; Vunjak-Novakovic, G.; Kaplan, D. L., *Biomaterials* **2006,** *27* (36), 6064-6082.
63. Rockwood, D. N.; Preda, R. C.; Yucel, T.; Wang, X. Q.; Lovett, M. L.; Kaplan, D. L., *Nat. Protoc.* **2011,** *6* (10), 1612-1631.
64. Zhou, C. Z.; Confalonieri, F.; Jacquet, M.; Perasso, R.; Li, Z. G.; Janin, J., *Proteins: Struct., Funct., Bioinf.* **2001,** *44* (2), 119-122.
65. Vepari, C.; Kaplan, D. L., *Prog. Polym. Sci.* **2007,** *32* (8), 991-1007.
66. Sell, S. A.; Wolfe, P. S.; Garg, K.; McCool, J. M.; Rodriguez, I. A.; Bowlin, G. L., *Polymers* **2010,** *2* (4), 522-553.
67. Jin, H.-J., *Nature* **2003,** *424* (6952), 1057-1061.
68. Matsumoto, A.; Chen, J.; Collette, A. L.; Kim, U.-J.; Altman, G. H.; Cebe, P.; Kaplan, D. L., *J. Phys. Chem. B* **2006,** *110* (43), 21630.
69. Nagarkar, S.; Nicolai, T.; Chassenieux, C.; Lele, A., *Phys. Chem. Chem. Phys.* **2010,** *12* (15), 3834.
70. Lu, Q.; Huang, Y.; Li, M.; Zuo, B.; Lu, S.; Wang, J.; Zhu, H.; Kaplan, D. L., *Acta Biomater.* **2011,** *7* (6), 2394-2400.
71. Kojic, N.; Panzer, M. J.; Leisk, G. G.; Raja, W. K.; Kojic, M.; Kaplan, D. L., *Soft Matter* **2012,** *8* (26), 2897-2905.
72. Yucel, T.; Cebe, P.; Kaplan, D. L., *Biophys. J.* **2009,** *97* (7), 2044-2050.
73. Kim, U.-J.; Park, J.; Li, C.; Jin, H.-J.; Valluzzi, R.; Kaplan, D. L., *Biomacromolecules* **2004,** *5* (3), 786-792.
74. Kyte, J.; Doolittle, R. F., *J. Mol. Biol.* **1982,** *157* (1), 105-132.
75. Fernandez-Trillo, F.; van Hest, J. C. M.; Thies, J. C.; Michon, T.; Weberskirch, R.; Cameron, N. R., *Chem. Commun.* **2008,** (19), 2230-2232.
76. Ge, X.; Hoare, T.; Filipe, C. D. M., *Langmuir* **2010,** *26* (6), 4087.
77. Greenfield, N. J., *Nat. Protoc.* **2007,** *1* (6), 2876-2890.
78. Balu, R.; Knott, R.; Cowieson, N. P.; Elvin, C. M.; Hill, A. J.; Choudhury, N. R.; Dutta, N. K., *Sci. Rep.* **2015,** *5*.
79. Reiersen, H.; Clarke, A. R.; Rees, A. R., *J. Mol. Biol.* **1998,** *283* (1), 255-264.
80. Guilbaud, J.-B.; Saiani, A., *Chem. Soc. Rev.* **2011,** *40* (3), 1200-1210.

81. Malik, L.; Nygaard, J.; Christensen, N. J.; Streicher, W. W.; Thulstrup, P. W.; Arleth, L.; Jensen, K. J., *J. Pept. Sci.* **2013,** *19* (5), 283-292.
82. Schneider, J. P.; Pochan, D. J.; Ozbas, B.; Rajagopal, K.; Pakstis, L.; Kretsinger, J., *J. Am. Chem. Soc.* **2002,** *124* (50), 15030-15037.
83. Cousin, F.; Gummel, J.; Ung, D.; Boué, F., *Langmuir* **2005,** *21* (21), 9675-9688.
84. Greving, I.; Dicko, C.; Terry, A.; Callow, P.; Vollrath, F., *Soft Matter* **2010,** *6* (18), 4389-4395.
85. Nisal, A.; Kalelkar, C.; Bellare, J.; Lele, A., *Rheol. Acta* **2013,** *52* (10-12), 833-840.
86. Rössle, M.; Panine, P.; Urban, V. S.; Riekel, C., *Biopolymers* **2004,** *74* (4), 316-327.
87. Yamaoka, H.; Asato, H.; Ogasawara, T.; Nishizawa, S.; Takahashi, T.; Nakatsuka, T.; Koshima, I.; Nakamura, K.; Kawaguchi, H.; Chung, U.-i.; Takato, T.; Hoshi, K., *J. Biomed. Mater. Res., Part A* **2006,** *78A* (1), 1-11.
88. Genes, N. G.; Rowley, J. A.; Mooney, D. J.; Bonassar, L. J., *Arch. Biochem. Biophys.* **2004,** *422* (2), 161-167.
89. Eyrich, D.; Brandl, F.; Appel, B.; Wiese, H.; Maier, G.; Wenzel, M.; Staudenmaier, R.; Goepferich, A.; Blunk, T., *Biomaterials* **2007,** *28* (1), 55-65.
90a. Chao, P.-H. G.; Yodmuang, S.; Wang, X.; Sun, L.; Kaplan, D. L.; Vunjak-Novakovic, G., *J. Biomed. Mater. Res., Part B* **2010,** *95B* (1), 84-90.
90b. Chenite, A.; Chaput, C.; Wang, D.; Combes, C.; Buschmann, M. D.; Hoemann, C. D.; Leroux, J. C.; Atkinson, B. L.; Binette, F.; Selmani, A., *Biomaterials* **2000,** *21* (21), 2155-2161.
91. Kwon, J. S.; Yoon, S. M.; Kwon, D. Y.; Kim, D. Y.; Tai, G. Z.; Jin, L. M.; Song, B.; Lee, B.; Kim, J. H.; Han, D. K.; Min, B. H.; Kim, M. S., *J. Mater. Chem. B* **2013,** *1* (26), 3314-3321.
92. Zhong, S. P.; Zhang, Y. Z.; Lim, C. T., *Wiley Interdiscip. Rev.: Nanomed. Nanobiotechnol.* **2010,** *2* (5), 510-525.
93. Wang, L.-S.; Du, C.; Toh, W. S.; Wan, A. C. A.; Gao, S. J.; Kurisawa, M., *Biomaterials* **2014,** *35* (7), 2207-2217.
94. Kwon, H.; Sun, L.; Cairns, D. M.; Rainbow, R. S.; Preda, R. C.; Kaplan, D. L.; Zeng, L., *Acta Biomater.* **2013,** *9* (5), 6563-6575.
95. Chung, C.; Burdick, J. A., *Adv. Drug Delivery Rev.* **2008,** *60* (2), 243-262.
96. Lee, C. R.; Grodzinsky, A. J.; Spector, M., *Biomaterials* **2001,** *22* (23), 3145-3154.
97. Lee, C. R.; Grodzinsky, A. J.; Spector, M., *Tissue Eng.* **2003,** *9* (1), 27-36.

98. Vercruysse, K. P.; Marecak, D. M.; Marecek, J. F.; Prestwich, G. D., *Bioconjugate Chem.* **1997,** *8* (5), 686-694.
99. Prestwich, G. D.; Marecak, D. M.; Marecek, J. F.; Vercruysse, K. P.; Ziebell, M. R., *J. Controlled Release* **1998,** *53* (1–3), 93-103.
100. Burdick, J. A.; Chung, C.; Jia, X.; Randolph, M. A.; Langer, R., *Biomacromolecules* **2005,** *6* (1), 386-391.
101. Gamini, A.; Paoletti, S.; Toffanin, R.; Micali, F.; Michielin, L.; Bevilacqua, C., *Biomaterials* **2002,** *23* (4), 1161-1167.
102. Francis Suh, J. K.; Matthew, H. W. T., *Biomaterials* **2000,** *21* (24), 2589-2598.
103. Ishihara, M.; Nakanishi, K.; Ono, K.; Sato, M.; Kikuchi, M.; Saito, Y.; Yura, H.; Matsui, T.; Hattori, H.; Uenoyama, M.; Kurita, A., *Biomaterials* **2002,** *23* (3), 833-840.
104. Meinel, L.; Hofmann, S.; Karageorgiou, V.; Zichner, L.; Langer, R.; Kaplan, D.; Vunjak-Novakovic, G., *Biotechnol. Bioeng.* **2004,** *88* (3), 379-391.
105. Kim, I. L.; Mauck, R. L.; Burdick, J. A., *Biomaterials* **2011,** *32* (34), 8771-8782.
106. Athanasiou, K. A.; Darling, E. M.; Hu, J. C., *Synthesis Lectures on Tissue Engineering* **2009,** *1* (1), 1-182.
107. Fragonas, E.; Valente, M.; Pozzi-Mucelli, M.; Toffanin, R.; Rizzo, R.; Silvestri, F.; Vittur, F., *Biomaterials* **2000,** *21* (8), 795-801.
108. Hunziker, E. B., *Osteoarthr. Cartilage* **2002,** *10* (6), 432-463.
109. Madihally, S. V.; Matthew, H. W. T., *Biomaterials* **1999,** *20* (12), 1133-1142.
110. Hunter, C. J.; Levenston, M. E., *Tissue Eng.* **2004,** *10* (5-6), 736.
111. Kujawa, M. J.; Caplan, A. I., *Dev. Biol.* **1986,** *114* (2), 504-518.
112. Grigolo, B.; Roseti, L.; Fiorini, M.; Fini, M.; Giavaresi, G.; Nicoli Aldini, N.; Giardino, R.; Facchini, A., *Biomaterials* **2001,** *22* (17), 2417-2424.
113. Stoddart, M. J.; Grad, S.; Eglin, D.; Alini, M., *Regener. Med.* **2008,** *4* (1), 81-98.
114. Vasconcelos, A.; Gomes, A. C.; Cavaco-Paulo, A., *Acta Biomater.* **2012,** *8* (8), 3049.
115. Xiao, W.; Liu, W.; Sun, J.; Dan, X.; Wei, D.; Fan, H., *J. Bioact. Compat. Polym.* **2012,** *27* (4), 327-341.
116. Silva, S. S.; Maniglio, D.; Motta, A.; Mano, J. F.; Reis, R. L.; Migliaresi, C., *Macromol. Biosci.* **2008,** *8* (8), 766-774.
117. Kang, G.; Lee, K.; Ki, C.; Park, Y., *Fiber Polym.* **2004,** *5* (3), 234-238.
118. McMillan, R. A.; Caran, K. L.; Apkarian, R. P.; Conticello, V. P., *Macromolecules* **1999,** *32* (26), 9067-9070.

119. McMillan, R. A.; Conticello, V. P., *Macromolecules* **2000,** *33* (13), 4809-4821.
120. Lee, J.; Macosko, C. W.; Urry, D. W., *Biomacromolecules* **2001,** *2* (1), 170-179.
121. Renner, J. N.; Cherry, K. M.; Su, R. S. C.; Liu, J. C., *Biomacromolecules* **2012,** *13* (11), 3678-3685.
122. Li, L. Q.; Teller, S.; Clifton, R. J.; Jia, X. Q.; Kiick, K. L., *Biomacromolecules* **2011,** *12* (6), 2302-2310.
123. Li, L.; Tong, Z.; Jia, X.; Kiick, K. L., *Soft Matter* **2013,** *9* (3), 665-673.
124. Charati, M. B.; Ifkovits, J. L.; Burdick, J. A.; Linhardt, J. G.; Kiick, K. L., *Soft Matter* **2009,** *5* (18), 3412-3416.
125. West, J. L.; Hubbell, J. A., *React. Polym.* **1995,** *25* (2–3), 139-147.
126. Bryant, S. J.; Anseth, K. S., *J. Biomed. Mater. Res.* **2002,** *59* (1), 63-72.
127. Schmedlen, R. H.; Masters, K. S.; West, J. L., *Biomaterials* **2002,** *23* (22), 4325-4332.
128. Nuttelman, C. R.; Henry, S. M.; Anseth, K. S., *Biomaterials* **2002,** *23* (17), 3617-3626.
129. Pong, F. Y.; Lee, M.; Bell, J. R.; Flynn, N. T., *Langmuir* **2006,** *22* (8), 3851-3857.
130. Stile, R. A.; Burghardt, W. R.; Healy, K. E., *Macromolecules* **1999,** *32* (22), 7370-7379.
131. Hinkley, J. A.; Morgret, L. D.; Gehrke, S. H., *Polymer* **2004,** *45* (26), 8837-8843.
132. Choi, B.; Kim, S.; Lin, B.; Wu, B. M.; Lee, M., *ACS Appl. Mater. Interfaces* **2014,** *6* (22), 20110-20121.
133. Omobono, M. A.; Zhao, X.; Furlong, M. A.; Kwon, C.-H.; Gill, T. J.; Randolph, M. A.; Redmond, R. W., *J. Biomed. Mater. Res., Part A* **2015,** *103* (4), 1332-1338.
134. Lien, S.-M.; Li, W.-T.; Huang, T.-J., *Mater. Sci. Eng., C* **2008,** *28* (1), 36-43.
135. McHale, M.; Setton, L.; Chilkoti, A., *Tissue Eng.* **2005,** *11* (11-12), 1768-1779.
136. Elisseeff, J.; McIntosh, W.; Anseth, K.; Riley, S.; Ragan, P.; Langer, R., *J. Biomed. Mater. Res.* **2000,** *51* (2), 164-171.
137. Bryant, S. J.; Durand, K. L.; Anseth, K. S., *J. Biomed. Mater. Res., Part A* **2003,** *67A* (4), 1430-1436.
138. Salinas, C. N.; Anseth, K. S., *J. Tissue Eng. Regener. Med.* **2008,** *2* (5), 296-304.
139. Salinas, C. N.; Anseth, K. S., *J. Biomed. Mater. Res., Part A* **2009,** *90A* (2), 456-464.
140. Carlsen, A.; Lecommandoux, S., *Curr. Opin. Colloid Interface Sci.* **2009,** *14* (5), 329-339.

141. Wang, F.; Yang, C.; Hu, X., Advanced Protein Composite Materials. In *Lightweight Materials from Biopolymers and Biofibers*, American Chemical Society: 2014; Vol. 1175, pp 177-208.
142. Jalani, G.; Rosenzweig, D. H.; Makhoul, G.; Abdalla, S.; Cecere, R.; Vetrone, F.; Haglund, L.; Cerruti, M., *Macromol. Biosci.* **2015,** *15* (4), 473-480.
143. Gong, J. P.; Katsuyama, Y.; Kurokawa, T.; Osada, Y., *Adv. Mater.* **2003,** *15* (14), 1155-1158.
144. Chen, Q.; Chen, H.; Zhu, L.; Zheng, J., *J. Mater. Chem. B* **2015,** *3* (18), 3654-3676.
145. Haraguchi, K.; Takehisa, T., *Adv. Mater.* **2002,** *14* (16), 1120-1124.
146. Lin, W.-C.; Fan, W.; Marcellan, A.; Hourdet, D.; Creton, C., *Macromolecules* **2010,** *43* (5), 2554-2563.
147. Hu, J.; Hiwatashi, K.; Kurokawa, T.; Liang, S. M.; Wu, Z. L.; Gong, J. P., *Macromolecules* **2011,** *44* (19), 7775-7781.
148. Hu, J.; Kurokawa, T.; Nakajima, T.; Wu, Z. L.; Liang, S. M.; Gong, J. P., *Macromolecules* **2014,** *47* (11), 3587-3594.
149. Okumura, Y.; Ito, K., *Adv. Mater.* **2001,** *13* (7), 485-487.
150. Sakai, T.; Matsunaga, T.; Yamamoto, Y.; Ito, C.; Yoshida, R.; Suzuki, S.; Sasaki, N.; Shibayama, M.; Chung, U.-i., *Macromolecules* **2008,** *41* (14), 5379-5384.
151. Yodmuang, S.; McNamara, S. L.; Nover, A. B.; Mandal, B. B.; Agarwal, M.; Kelly, T.-A. N.; Chao, P.-h. G.; Hung, C.; Kaplan, D. L.; Vunjak-Novakovic, G., *Acta Biomater.* **2015,** *11*, 27-36.
152. Marshall, D. B.; Cox, B. N.; Evans, A. G., *Acta Metall.* **1985,** *33* (11), 2013-2021.
153. Coburn, J.; Gibson, M.; Bandalini, P. A.; Laird, C.; Mao, H.-Q.; Moroni, L.; Seliktar, D.; Elisseeff, J., *Smart Struct. Syst.* **2011,** *7* (3), 213-222.
154. Hannouche, D.; Terai, H.; Fuchs, J.; Terada, S.; Zand, S.; Nasseri, B.; Petite, H.; Sedel, L.; Vacanti, J., *Tissue Eng.* **2007,** *13* (1), 87-100.
155. Tuncaboylu, D. C.; Sari, M.; Oppermann, W.; Okay, O., *Macromolecules* **2011,** *44* (12), 4997-5005.
156. Henderson, K. J.; Zhou, T. C.; Otim, K. J.; Shull, K. R., *Macromolecules* **2010,** *43* (14), 6193-6201.
157. Song, G.; Zhang, L.; He, C.; Fang, D.-C.; Whitten, P. G.; Wang, H., *Macromolecules* **2013,** *46* (18), 7423-7435.
158. Richtering, W.; Saunders, B. R., *Soft Matter* **2014,** *10* (21), 3695-3702.
159. Haraguchi, K., *Curr. Opin. Solid State Mater. Sci.* **2007,** *11* (3–4), 47-54.

160. Matsunaga, T.; Sakai, T.; Akagi, Y.; Chung, U.-i.; Shibayama, M., *Macromolecules* **2009,** *42* (4), 1344-1351.
161. Gong, J. P., *Soft Matter* **2010,** *6* (12), 2583-2590.
162. Simha, N. K.; Carlson, C. S.; Lewis, J. L., *J. Mater. Sci.: Mater. Med.* **2004,** *15* (5), 631-639.
163. Nakayama, A.; Kakugo, A.; Gong, J. P.; Osada, Y.; Takai, M.; Erata, T.; Kawano, S., *Adv. Funct. Mater.* **2004,** *14* (11), 1124-1128.
164. Hagiwara, Y.; Putra, A.; Kakugo, A.; Furukawa, H.; Gong, J., *Cellulose* **2010,** *17* (1), 93-101.
165. Chen, Q.; Zhu, L.; Zhao, C.; Wang, Q.; Zheng, J., *Adv. Mater.* **2013,** *25* (30), 4171-4176.
166. Chen, P.; Wu, R.; Wang, J.; Liu, Y.; Ding, C.; Xu, S., *J. Polym. Res.* **2012,** *19* (3), 1-4.
167. Stevens, L.; Calvert, P.; Wallace, G. G.; Panhuis, M. i. h., *Soft Matter* **2013,** *9* (11), 3009-3012.
168. Bakarich, S. E.; Panhuis, M. i. h.; Beirne, S.; Wallace, G. G.; Spinks, G. M., *J. Mater. Chem. B* **2013,** *1* (38), 4939-4946.
169. Haque, M. A.; Kurokawa, T.; Gong, J. P., *Polymer* **2012,** *53* (9), 1805-1822.
170. Chen, Q.; Zhu, L.; Huang, L.; Chen, H.; Xu, K.; Tan, Y.; Wang, P.; Zheng, J., *Macromolecules* **2014,** *47* (6), 2140-2148.
171. Rehm, C.; Brule, A.; Freund, A. K.; Kennedy, S. J., *J. Appl. Crystallogr.* **2013,** *46* (6), 1699-1704.
172. Okay, O., General Properties of Hydrogels. In *Hydrogel Sensors and Actuators*, Gerlach, G.; Arndt, K.-F., Eds. Springer Berlin Heidelberg: 2010; Vol. 6, pp 1-14.
173. Norisuye, T.; Masui, N.; Kida, Y.; Ikuta, D.; Kokufuta, E.; Ito, S.; Panyukov, S.; Shibayama, M., *Polymer* **2002,** *43* (19), 5289-5297.
174. Geissler, E.; Hecht, A.-M.; Rochas, C.; Horkay, F.; Basser, P. J., *Macromol. Symp.* **2005,** *227* (1), 27-38.
175. Mangiapia, G.; Frielinghaus, H.; Derrico, G.; Ortona, O.; Sartorio, R.; Paduano, L., *Phys. Chem. Chem. Phys.* **2007,** *9* (46), 6150-6158.
176. Dandu, R.; Cresce, A. V.; Briber, R.; Dowell, P.; Cappello, J.; Ghandehari, H., *Polymer* **2009,** *50* (2), 366-374.
177. Helminger, M.; Wu, B.; Kollmann, T.; Benke, D.; Schwahn, D.; Pipich, V.; Faivre, D.; Zahn, D.; Cölfen, H., *Adv. Funct. Mater.* **2014,** *24* (21), 3187-3196.

178. Shibayama, M.; Sakai, T., Chapter 2. Fabrication, Structure, Mechanical Properties, and Applications of Tetra-PEG Hydrogels. In *Polymeric and Self Assembled Hydrogels: From Fundamental Understanding to Applications*, The Royal Society of Chemistry: 2013; pp 7-38.
179. Helgeson, M. E.; Gao, Y.; Moran, S. E.; Lee, J.; Godfrin, M.; Tripathi, A.; Bose, A.; Doyle, P. S., *Soft Matter* **2014,** *10* (17), 3122-3133.
180. Hudson, S. D.; Hutter, J. L.; Nieh, M.-P.; Pencer, J.; Millon, L. E.; Wan, W., *The J. Chem. Phys.* **2009,** *130* (3), 034903.
181. Crompton, K. E.; Forsythe, J. S.; Horne, M. K.; Finkelstein, D. I.; Knott, R. B., *Soft Matter* **2009,** *5* (23), 4704-4711.
182. Iannuzzi, M. A.; Reber Iii, R.; Lentz, D. M.; Zhao, J.; Ma, L.; Hedden, R. C., *Polymer* **2010,** *51* (9), 2049-2056.
183. Tominaga, T.; Tirumala, V. R.; Lin, E. K.; Gong, J. P.; Furukawa, H.; Osada, Y.; Wu, W.-l., *Polymer* **2007,** *48* (26), 7449-7454.
184. Yu, F.; Cao, X.; Li, Y.; Zeng, L.; Yuan, B.; Chen, X., *Polym. Chem.* **2014,** *5* (3), 1082-1090.
185. DeKosky, B. J.; Dormer, N. H.; Ingavle, G. C.; Roatch, C. H.; Lomakin, J.; Detamore, M. S.; Gehrke, S. H., *Tissue Eng., Part C* **2010,** *16* (6), 1533-1542.
186. Park, H.; Temenoff, J. S.; Tabata, Y.; Caplan, A. I.; Mikos, A. G., *Biomaterials* **2007,** *28* (21), 3217-3227.
187. Holland, T. A.; Tabata, Y.; Mikos, A. G., *J. Controlled Release* **2003,** *91* (3), 299-313.
188. Tan, H.; Chu, C. R.; Payne, K. A.; Marra, K. G., *Biomaterials* **2009,** *30* (13), 2499-2506.
189. Mirahmadi, F.; Tafazzoli-Shadpour, M.; Shokrgozar, M. A.; Bonakdar, S., *Mater. Sci. Eng.: C* **2013,** *33* (8), 4786-4794.
190. Shin, H.; Olsen, B. D.; Khademhosseini, A., *Biomaterials* **2012,** *33* (11), 3143-3152.
191. Yasuda, K.; Kitamura, N.; Gong, J. P.; Arakaki, K.; Kwon, H. J.; Onodera, S.; Chen, Y. M.; Kurokawa, T.; Kanaya, F.; Ohmiya, Y.; Osada, Y., *Macromol. Biosci.* **2009,** *9* (4), 307-316.
192. Ronken, S.; Wirz, D.; Daniels, A. U.; Kurokawa, T.; Gong, J. P.; Arnold, M. P., *Biomech. Model Mechanobiol.* **2013,** *12* (2), 243-248.
193. Teo, W.-E.; Inai, R.; Ramakrishna, S., *Sci. Technol. Adv. Mater.* **2011,** *12* (1), 013002.

194. Zhang, Y. Z.; Huang, Z. M.; Xu, X. J.; Lim, C. T.; Ramakrishna, S., *Chem. Mater.* **2004,** *16* (18), 3406-3409.
195. Teo, W. E.; Ramakrishna, S., *Nanotechnology* **2006,** *17* (14), R89-R106.
196. Ashammakhi, N.; Ndreu, A.; Yang, Y.; Ylikauppila, H.; Nikkola, L., *Eur. J. Plast. Surg.* **2012,** *35* (2), 135-149.
197. Agarwal, S.; Wendorff, J. H.; Greiner, A., *Polymer* **2008,** *49* (26), 5603-5621.
198. Min, B.-M.; Lee, G.; Kim, S. H.; Nam, Y. S.; Lee, T. S.; Park, W. H., *Biomaterials* **2004,** *25* (7-8), 1289-1297.
199. Sill, T. J.; von Recum, H. A., *Biomaterials* **2008,** *29* (13), 1989-2006.
200. Toyokawa, N.; Fujioka, H.; Kokubu, T.; Nagura, I.; Inui, A.; Sakata, R.; Satake, M.; Kaneko, H.; Kurosaka, M., *Arthroscopy: J. Arthroscopic Rel. Surg.* **2010,** *26* (3), 375-383.
201. Li, W.-J.; Tuli, R.; Huang, X.; Laquerriere, P.; Tuan, R. S., *Biomaterials* **2005,** *26* (25), 5158-5166.
202. Li, W.-J.; Danielson, K. G.; Alexander, P. G.; Tuan, R. S., *J. Biomed. Mater. Res., Part A* **2003,** *67A* (4), 1105-1114.
203. Shields, K. J.; Beckman, M. J.; Bowlin, G. L.; Wayne, J. S., *Tissue Eng.* **2004,** *10* (9-10), 1510.
204. Bhattarai, N.; Edmondson, D.; Veiseh, O.; Matsen, F. A.; Zhang, M., *Biomaterials* **2005,** *26* (31), 6176-6184.
205. Da Silva, M. A.; Crawford, A.; Mundy, J.; Martins, A.; Araújo, J. V.; Hatton, P. V.; Reis, R. L.; Neves, N. M., *Tissue Eng. Part A* **2009,** *15* (2), 377.
206. Chen, J.-P.; Su, C.-H., *Acta Biomater.* **2011,** *7* (1), 234-243.
207. Elahi, M. F.; Lu, W.; Guoping, G.; Khan, F., *J. Bioeng. Biomed. Sci.* **2013,** *3* (121).
208. Bellan, L. M.; Craighead, H. G., *Polym. Adv. Technol.* **2011,** *22* (3), 304-309.
209. Wang, M.; Yu, J. H.; Kaplan, D. L.; Rutledge, G. C., *Macromolecules* **2006,** *39* (3), 1102-1107.
210. Sun, Z.; Zussman, E.; Yarin, A. L.; Wendorff, J. H.; Greiner, A., *Adv. Mater.* **2003,** *15* (22), 1929-1932.
211. Zhang, Y. Z.; Venugopal, J.; Huang, Z. M.; Lim, C. T.; Ramakrishna, S., *Biomacromolecules* **2005,** *6* (5), 2583-2589.
212. Huang, Z.-M.; Zhang, Y.; Ramakrishna, S., *J. Polym. Sci., Part B: Polym. Phys.* **2005,** *43* (20), 2852-2861.
213. Sun, B.; Duan, B.; Yuan, X., *J. Appl. Polym. Sci.* **2006,** *102* (1), 39-45.

214. Man, Z.; Yin, L.; Shao, Z.; Zhang, X.; Hu, X.; Zhu, J.; Dai, L.; Huang, H.; Yuan, L.; Zhou, C.; Chen, H.; Ao, Y., *Biomaterials* **2014,** *35* (19), 5250-5260.
215. Tian, L.; Prabhakaran, M. P.; Hu, J.; Chen, M.; Besenbacher, F.; Ramakrishna, S., *RSC Adv.* **2015,** *5* (62), 49838-49848.
216. Amler, E.; Mickova, A.; Buzgo, M., *Nanomedicine* **2013,** *8* (4), 509-512.
217. Chen, M.; Dong, M.; Havelund, R.; Regina, V. R.; Meyer, R. L.; Besenbacher, F.; Kingshott, P., *Chem. Mater.* **2010,** *22* (14), 4214-4221.
218. Geckil, H.; Xu, F.; Zhang, X.; Moon, S.; Demirci, U., *Nanomedicine (London, England)* **2010,** *5* (3), 469-484.
219. Guilak, F.; Cohen, D. M.; Estes, B. T.; Gimble, J. M.; Liedtke, W.; Chen, C. S., *Cell Stem Cell* **2009,** *5* (1), 17-26.
220. Ingber, D., *Mech. Chem. Biosyst.* **2004,** *1*, 53-68.
221. Miller, C. J.; Davidson, L. A., *Nat. Rev. Genet.* **2013,** *14* (10), 733-744.
222. Emerman, J. T.; Burwen, S. J.; Pitelka, D. R., *Tissue and Cell* **1979,** *11* (1), 109-119.
223. Engler, A. J.; Sen, S.; Sweeney, H. L.; Discher, D. E., *Cell* **2006,** *126* (4), 677-689.
224. Ghosh, S.; Laha, M.; Mondal, S.; Sengupta, S.; Kaplan, D. L., *Biomaterials* **2009,** *30* (33), 6530-6540.
225. Hopkins, A. M.; De Laporte, L.; Tortelli, F.; Spedden, E.; Staii, C.; Atherton, T. J.; Hubbell, J. A.; Kaplan, D. L., *Adv. Funct. Mater.* **2013,** *23* (41), 5140-5149.
226. Chaudhuri, O.; Gu, L.; Klumpers, D.; Darnell, M.; Bencherif, S. A.; Weaver, J. C.; Huebsch, N.; Lee, H.; Lippens, E.; Duda, G. N.; Mooney, D. J., *Nature Materials* **2015,** doi: 10.1038/nmat4489.
227. Park, H.; Guo, X.; Temenoff, J. S.; Tabata, Y.; Caplan, A. I.; Kasper, F. K.; Mikos, A. G., *Biomacromolecules* **2009,** *10* (3), 541-546.

Chapter 2: Experimental methodology

This chapter is presented in four sections: (a) chemicals and materials; (b) synthesis and fabrication methods; (c) background to the instrumental techniques and (d) cell culture methods that have been used in this research. In the first part the main materials used in the work are included, while chapter specific materials are highlighted in each chapter. The second part of the chapter details the synthesis of the natural and synthetic polymers and also the fabrication methods for the hydrogels and electrospun mats. In the third part, details of various experimental techniques that are used for the characterisation of the materials fabricated in this study. The fourth part describes the cell culture methods employed to analyse the ability of the hydrogels to support cell adhesion, growth and differentiation.

2.1 Chemicals, solvents and materials

Table 2.1 summarises the details of the chemicals, solvents and materials used to prepare the RSF, Rec1-resilin and PVCL containing hydrogels and electrospun mats and to perform all chemical, physical and biological characterisations. All chemicals are of laboratory and/or analytical grade and were used as received.

Table 2.1 List of chemicals, solvents and materials used in this research work

Name	Supplier
Solvents and chemicals for synthesis of regenerated silk fibroin (RSF) solution	
Bombyx mori raw silk	Beautiful Silks, Australia
Water-soluble (BMWS) freeze dried regenerated silk fibroin powder	Dr. Anja Glisovic, Germany
Sodium carbonate (Na_2CO_3)	Chem Supply, Australia
Calcium chloride ($CaCl_2$)	Chem Supply, Australia
Ethanol	Sigma-Aldrich, Australia
Solvents and chemicals for synthesis of poly(N-vinylcaprolactam) (PVCL)	
N-vinylcaprolactam	Sigma-Aldrich, Australia
2,2'-azoisobutyronitrile (AIBN)	Sigma-Aldrich, Australia
Toluene	Sigma-Aldrich, Australia

Name	Supplier
Solvents and chemicals for synthesis of poly(N-vinylcaprolactam) (PVCL)	
Diethyl ether	Sigma-Aldrich, Australia
Acetone	Sigma-Aldrich, Australia
Chemicals for preparation of Rec1-resilin based coassemblies	
Phosphate buffered saline	Sigma-Aldrich, Australia
Poly-L-proline	Sigma-Aldrich, Australia
Chemicals for RSF-based hydrogel fabrication	
Tris(2,2-bipyridyl)dichlororuthenium(II) ($Ru(II)(bpy)_3^{2+}$)	Sigma-Aldrich, Australia
Ammonium peroxodisulfate (APS)	Sigma-Aldrich, Australia
Solvents and chemicals for conventional and co-axial electrospinning	
Tannic acid (TA)	Sigma-Aldrich, Australia
N,N-dimethylformamide (DMF)	Sigma-Aldrich, Australia
Hexafluoroisopropanol (HFIP)	CovaChem, United States
Cell culture reagents	
Alpha modified minimum medium (α-MEM)	Sigma-Aldrich, Australia
Sterile Phosphate buffered saline (PBS)	Sigma-Aldrich, Australia
L-Glutamine 200 mM	Invitrogen, Australia
Penicillin Streptomycin Solution	Invitrogen, Australia
Fetal Calf Serum	MultiSer, Australia
Transforming growth factor beta 1 (TGF-β1)	ThermoFisher Scientific, Australia
0.05% Trypsin	ThermoFisher Scientific, Australia
L-ascorbic acid	Invitrogen, Australia
Sodium pyruvate	ThermoFisher Scientific, Australia
Cell Fixation Reagents	
1.25% Glutaraldehyde, 4% Paraformaldehyde, 4% Sucrose	Sigma-Aldrich, Australia
2% Osmium Tetraoxide	Sigma-Aldrich, Australia
Hexamethyldisilazane (HMDS)	Sigma-Aldrich, Australia
Reagents for WST-1 Assay	
Tetrazolium salt [2-(4-iodophenyl)-3-(4-nitrophenyl)-5-(2,4-disulfophenyl)-2H-tetrazolium]	Roche, Australia
Reagents for RNA extraction, cDNA synthesis and Real-time Polymerase Chain Reaction	
TRIzol	Invitrogen, Australia
RNase free Glycogen	ThermoFisher Scientific, Australia
RNase free water	ThermoFisher Scientific, Australia

Name	Supplier
Cell culture reagents	
Superscript III kit	ThermoFisher Scientific, Australia
SYBR Green PCR Mastermix	ThermoFisher Scientific, Australia

2.2 Synthesis and fabrication methods

2.2.1 Preparation of regenerated silk fibroin solution

Raw silk (Beautiful Silks, Australia) was degummed by boiling in aqueous 0.02 M Na_2CO_3 for 30 minutes, rinsed in distilled water (DW) three times and allowed to dry at room temperature overnight. The fibroin was then dissolved in a calcium chloride, water, and ethanol solution ($CaCl_2/H_2O$/EtOH 1/8/2 molar ratio), with a liquor ratio of 1:20, at 70°C for 3 hours.[1] Following this, the solution was dialysed using SnakeSkin dialysis tubing (3.5 kDa molecular weight cut-off) (ThermoFisher Scientific) for several days and centrifuged at 10,000 rpm and 20°C for 20 minutes. Figure 2.1 shows a schematic of the process for the preparation of RSF solutions. The RSF solution obtained was ~2 wt% and was concentrated by evaporation at room temperature to obtain more concentrated solutions for hydrogel synthesis and electrospinning.

Water-soluble freeze dried regenerated silk fibroin (BMWS) powder was supplied by Dr Anja Glasovic and was used for the hydrogel formation by photo-chemical crosslinking in Chapter 4 as a comparison to the RSF solutions to verify the versatility of the method. Solutions of BMWS silk fibroin of varying concentrations were prepared by slowly adding the silk fibroin powder to distilled water (DW) whilst sonicating. Sonication was conducted for less than one hour to prevent beta-sheet formation. The solution was filtered using a non-sterile pre-filter (Minisart-GF 17824) with a pore size of approximately 1.2 microns.
All RSF and BMWS solutions were stored at 4°C to prevent gelation.

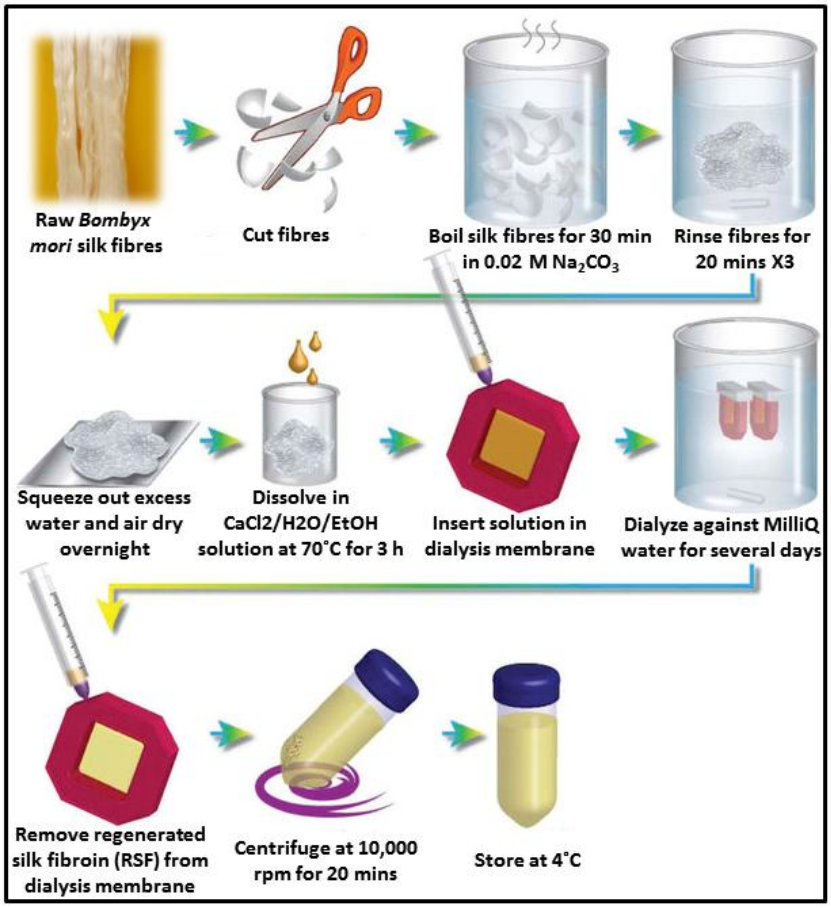


Figure 2.1 Schematic depicting the procedure to prepare regenerated silk fibroin solution (adapted with permission from Ref. 2).[2]

Figure 2.2 shows the repeat sequence that makes up the majority of the RSF sequence.

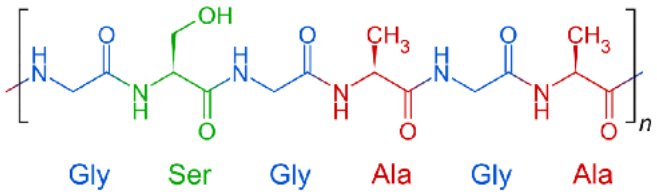


Figure 2.2 Structure showing the primary amino acid repeat sequence of RSF.

2.2.2 Synthesis and purification of Rec1-resilin

Rec1-resilin was synthesised as a water soluble protein by cloning, expression in *Escherichia coli*, and purification of exon 1 of the fruit fly *Drosophila melanogaster* gene CG15920, as reported previously.[3, 4] Figure 2.3 shows a general schematic for the synthesis of recombinant proteins.

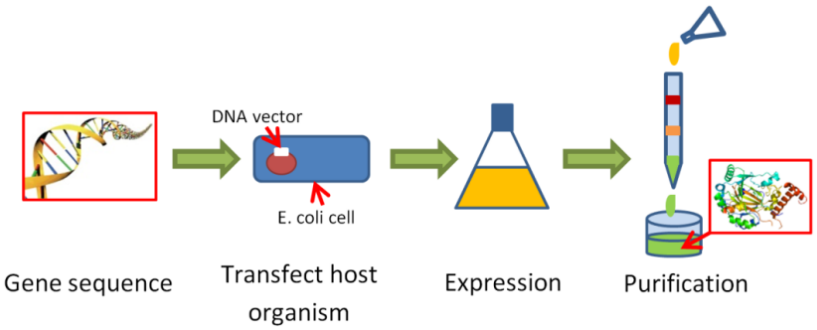


Figure 2.3 Schematic representation of the key steps involved in the synthesis of recombinant proteins.[5]

The Rec1-resilin protein was extracted by cell disruption with a yield of ~300 mg/L of culture. A three step purification process involved salt precipitation (using 20% ammonium sulphate) followed by overnight dialysis at 4˚C (in excess phosphate buffered saline, PBS) and heating at 80˚C for 10 minutes with stirring. The denatured proteins were removed by centrifugation at 12,000 g for 15 minutes at 20˚C and the resulting protein solution in supernatant was used for the synthesis of coassemblies and hydrogels. Figure 2.4 shows the consensus repeat sequence for Rec1-resilin, which is composed of 310 amino acids and has a molecular weight of 28.4 kDa.[6]



Figure 2.4 Alignment of the amino acid repeat in the Rec1-resilin sequence using the one-letter amino acid code.[6]

2.2.3 Synthesis of Poly(N-vinylcaprolactam) by free radical polymerisation

Poly(N-vinylcaprolactam) (PVCL) was prepared via free radical polymerisation of the N-vinylcaprolactam (VCL) monomer with 2,2'-azoisobutyronitrile (AIBN) as the initiator and toluene as the solvent (Figure 2.5). The reaction proceeded for 24 hours under nitrogen atmosphere at 70˚C. The polymer was recovered through precipitation in diethyl ether and purified by redissolving PVCL in a mixture of acetone and water (3:7) at room temperature, followed by precipitation by heating the solution to 80˚C. This process was repeated twice, and the polymer was then dried at room temperature and finally vacuum dried at 50˚C for 3 hours to remove any residual moisture.

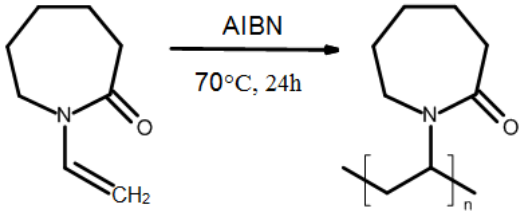


Figure 2.5 Reaction scheme depicting synthesis of PVCL by free radical polymerisation.

2.2.4 Hydrogel formation by photo-chemical crosslinking

An aqueous RSF, BMWS, Rec1-resilin/RSF and RSF/PVCL solutions were photo-chemically crosslinked to form hydrogels, using Tris(2,2-bipyridyl) dichloro ruthenium (II) hexahydrate ($Ru(II)(bpy)_3^{2+}$) as the catalyst and ammonium persulphate (APS) as the electron acceptor. Figure 2.6 shows a schematic representation of the hydrogel preparation process and also the reaction mechanism for the formation of dityrosine crosslinks. Predefined amounts of $Ru(II)(bpy)_3^{2+}$, APS, and silk fibroin solution were mixed, whilst preventing exposure to light. The solutions were then transferred to a Teflon mould and exposed to a 250W light source for 120 seconds, and then the gels were turned over and exposed to the light source for a further 60 seconds to ensure full crosslinking of the sample. The hydrogel was subsequently immersed in distilled water (DW) for several days to remove the un-reacted material. The water was changed daily. The gels were dried for three days in the fume hood at room temperature and subsequently for 3 hours in the vacuum oven at 40˚C to a constant weight.

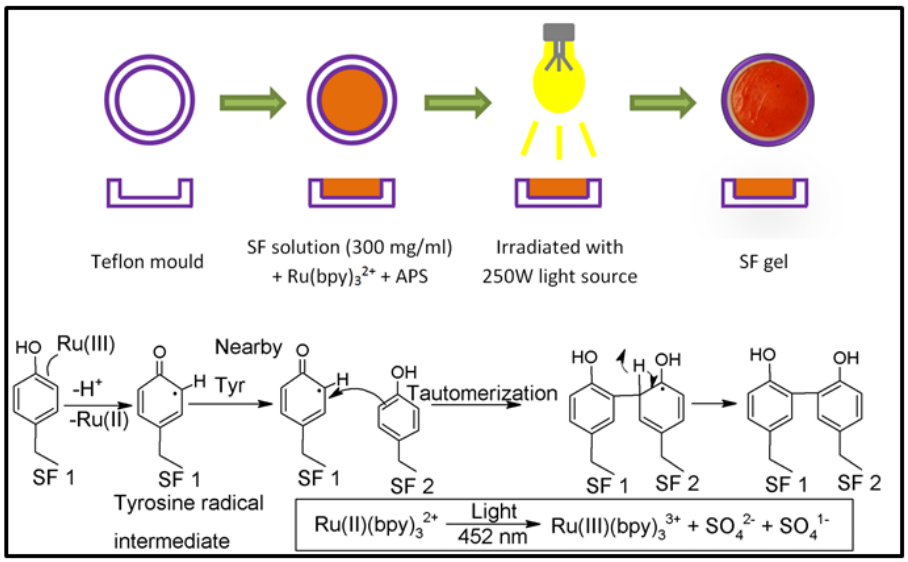


Figure 2.6 Schematic of the process to form crosslinked RSF-based hydrogels and the proposed reaction mechanism.[6]

2.2.5 Electrospinning of RSF and PVCL (conventional and co-axial)

Electrospinning is a versatile method that allows for the production of thin fibres ranging in size from nanometer to microns that possess high porosity and surface area.[7, 8] The principle of electrospinning involves the injection of a positive or negative charge from a high voltage source into a polymer solution or melt.[9] The solution particles become charged and are subsequently attracted to an oppositely charged collector.[9] In addition to the attraction for the collector, the particles in the polymer solution or melt also undergo repulsion from one another.[9] This leads to the formation of a cone at the edge of the solution, which is known as the Taylor cone. As the electric field strength exceeds the surface tension of the solution, a jet of polymer is forced through the atmosphere and towards the collector plate.[9-12] During this process the solvent evaporates, which leads to the formation of dry polymer fibres on the collector.[9] A chaotic bending instability is experienced during acceleration of the fibre.[9, 10] This increases the time prior to fibre deposition, and allows for thinning of the fibres and increased solvent evaporation.[9, 12]

Figure 2.7 shows a schematic of a typical electrospinning setup.[9] A syringe pump is commonly used to force the solution through a capillary at a nominated flow rate. The metal capillary is connected to a high voltage source, which transfers charge into the solution.[9] It is important that the capillary or needle has a small orifice in order to concentrate the charge on a small drop of solution.[13] A number of collector types may be employed, including a

stationary plate, a rotating disk, a moving platform or a solvent such as water.[9, 13] The choice of collector will depend on the required characteristics for the material being produced. A stationary collector is typically used to form a randomly oriented mat of fibres, whereas a rotating collector will result in the generation of uniform mats or aligned fibres.[9]

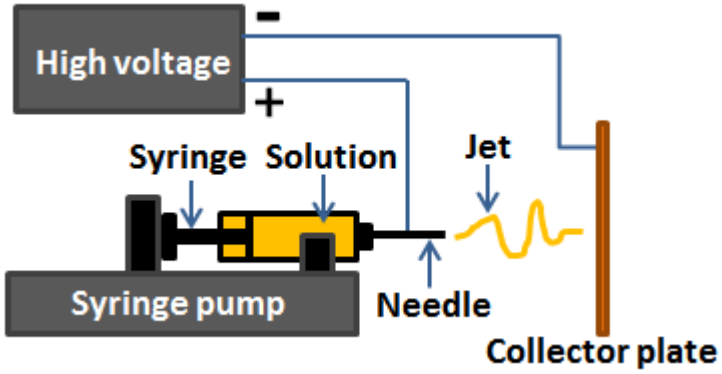


Figure 2.7 Schematic of a typical electrospinning setup.

Coaxial electrospinning follows the same principles as conventional electrospinning; however two needles are present in a concentric conformation and on the injection of two different materials in the outer and inner needles core/shell fibres are produced. The co-axial setup consists of two separate concentric capillaries and the core and shell solutions are introduced individually using separate syringes (Figure 2.8).[9, 14] The stresses generated by the applied potential on the sheath solution results in viscous dragging of the core solution and the formation of a compound co-axial jet at the tip of the capillary.[15] This process is expected to occur fast enough to limit any mixing of the core and shell solutions and thus results in fibres with core/shell morphology.[16, 17]

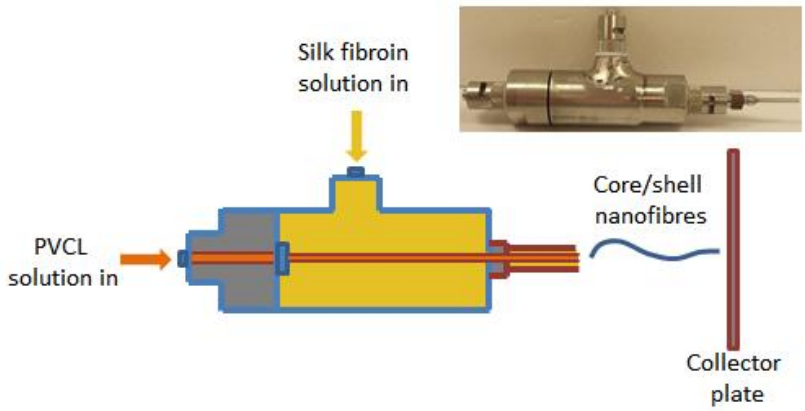


Figure 2.8 Schematic depicting co-axial electrospinning setup used to produce core/shell fibres. Inset: Photograph of co-axial electrospinning device.

Fibrous mats of RSF, PVCL, TA/PVCL nanofibres and core/shell PVCL/RSF nanofibres were prepared by electrospinning using a range of different solvents, including water, DMF and HFIP. A high voltage DC power supply was used to generate potential differences ranging from 4 to 20 kV. Both conventional and co-axial electrospinning were employed using a horizontal conformation. Solution concentrations and experimental parameters for each system can be found in Chapter 6.

2.3 Characterisation techniques

2.3.1 Spectroscopic techniques

2.3.1.1 Circular dichroism (CD) spectroscopy

CD spectroscopy is a useful tool for analysing the secondary structure of proteins in solution. CD is defined as the unequal absorption of left- and right-handed circularly polarised light, which arises due to structural asymmetry.[18] The CD experiment involves measuring the CD of the molecules of interest over a range of wavelengths. The far-UV (~190-250 nm) CD spectrum of proteins can be used to determine the secondary structure content of proteins as it is known that different secondary structures exhibit characteristic CD spectra (Figure 2.9).[18] In this study, far-UV CD spectra were obtained using a Jasco J-815 spectropolarimeter. The measuring range was 190-260 nm. The data pitch was 0.2 nm, with a 50 nm/min scanning speed, bandwidth of 1.0 nm, digital integration time (DIT) of 1 s and accumulation of 10 scans.

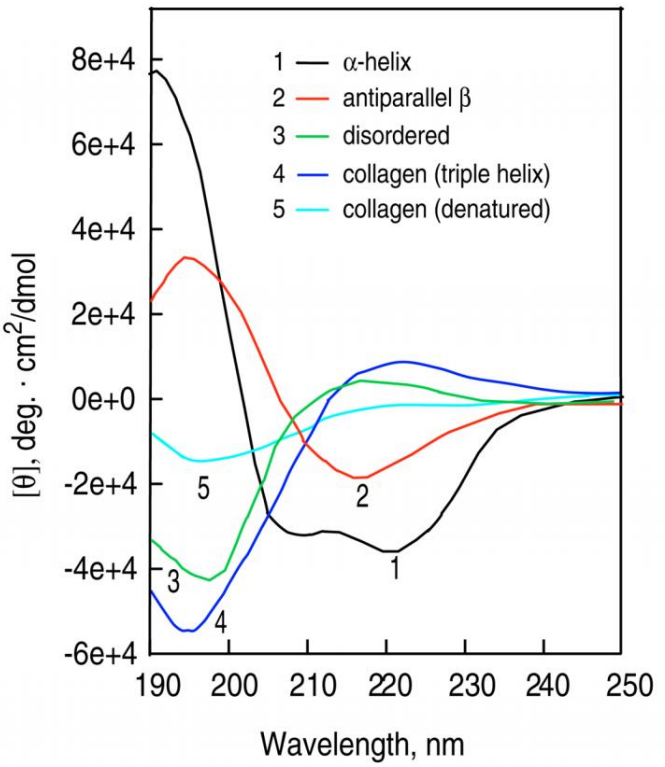


Figure 2.9 CD spectra depicting the characteristic scattering curves of different types of secondary structures.[18]

2.3.1.2 Photo-acoustic Fourier Transform Infrared (PA-FTIR) Spectroscopy

Photo-acoustic spectroscopy is based on the photo-acoustic effect, which was discovered by Alexander Graham Bell in 1880. The photo-acoustic effect is when intermittent light is irradiated onto a substrate, which then emits waves of the same frequency as the light pulse frequency. The analysis of solid samples by PA-FTIR is conducted by placing a sample in a sealed chamber with a microphone attached (Figure 2.10). An IR light beam is irradiated on and absorbed by the sample, which then releases heat that causes a pressure change in the surrounding gas (Helium) and this is detected by the highly sensitive microphone. Acoustic interference waves that are generated from this measurement and Fourier transformation is applied to produce a spectrum. In this study, experiments were conducted using the Nicolet Magna-IR Spectrometer 750 in photo-acoustic mode using a carbon black reference. Spectra were obtained in the range 400 to 4000 cm^{-1} and the data was processed using the Omnic computer program.

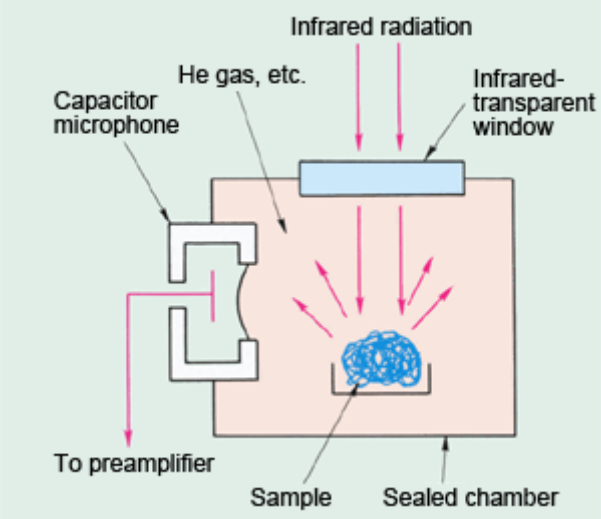


Figure 2.10 Principle of PA-FTIR spectroscopy.[19]

2.3.1.3 Nuclear magnetic resonance (NMR) spectroscopy

NMR spectroscopy is a common technique that is used to analyse the properties and chemical environment of molecules by exploiting the magnetic properties of certain atomic nuclei. The principles of the technique is that when a sample is placed in a magnetic field, NMR active nuclei, such as ^{1}H or ^{13}C, absorb electromagnetic radiation at a frequency characteristic of the isotope. Spectra are obtained by excitation of a sample with radio frequency pulse and a NMR response is obtained. A Fourier transform is performed to extract the frequency-domain spectrum and is presented in terms of the chemical shift. The chemical shift provides information about the structure of a molecule. In this study, NMR was used to characterise the RSF, BMWS and PVCL structures. RSF and BMWS were dissolved in deuterated water (D_2O) and PVCL was dissolved in deuterated chloroform ($CDCl_3$) for NMR experiments. ^{1}H NMR spectra were obtained on a 300 MHz Bruker Avance spectrometer operating at 300.138 MHz and the spectra were referenced relative to TMS (0 ppm).

2.3.2 Scattering techniques

2.3.2.1 Dynamic light scattering (DLS)

DLS is a commonly used method to characterise the particle size of different materials, including proteins and polymers in solution. For DLS experiments the sample is irradiated with light (usually a laser), repeatedly at short time intervals and the scattered light due to particles is measured using a detector at a fixed angle over time. The Brownian motion exhibited by particles in solution results in fluctuations in the scattered light intensity and the

velocity of the Brownian motion is measured from this and is then subsequently related to the size distribution by the Stokes-Einstein equation.[20] In this study, the Zetasizer Nano ZS was employed to measure the hydrodynamic radius of RSF, Rec1-resilin, PP, PVCL and coassemblies of these. The measured values were calculated from cumulative analysis (three cycles) using the Zetasizer software and uses an algorithm based up a non-negative least-squares fit. Figure 2.11 depicts the schematic of the DLS technique.

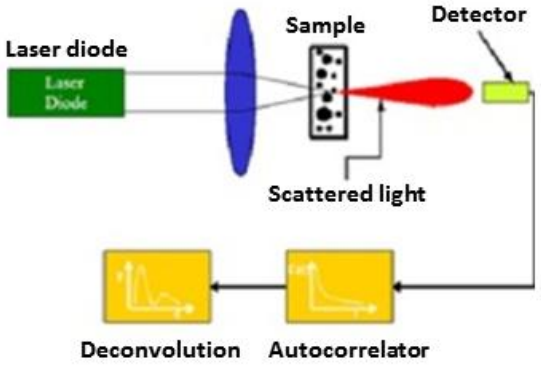


Figure 2.11 Schematic of dynamic light scattering system.

2.3.2.2 Small angle scattering – background

Small angle X-ray scattering (SAXS) and Small angle neutron scattering (SANS) and ultra-small angle neutron scattering (USANS) are valuable techniques for investigating the structure of materials between the nano to micro length scales. These techniques are complementary and when used in combination can provide unique structural information. One major advantage over other characterisation techniques is that the sample is *intact* i.e. very little sample preparation is necessary. This is particularly relevant for the study of hydrogels and hydrogel components since the samples are in a fully hydrated state.

In all three techniques, the scattered intensity, I, is measured as a function of the scattering vector, Q (where $Q=4\pi\sin\theta/\lambda$; 2θ is the scattering angle and λ is the x-ray/neutron wavelength). The I(Q) is proportional to the number of nanometre/micron sized scattering regions (particles, blobs etc) in the sample, and the scattering length density (SLD) of the region and the SLD of the background. The SLD is defined as the sum of the scattering lengths of the region components divided by the molecular volume. To help with experiment planning and interpretation of results, there are online tools to calculate the SLD of materials based on the chemical composition and bulk density (e.g. http://www.ncnr.nist.gov/resources/activation/). Since x-rays are scattered by the atom

electrons the SLD of a region is proportional to the number of electrons. This means any heavy atoms make a greater contribution to the I(Q). For neutron scattering there is no such simple relationship since neutron scattering is a nuclear event. Indeed the neutron SLD for isotopes of the same chemical species can be dramatically different (e.g. hydrogen/deuterium).

This leads to an important concept - that of contrast and contrast variation. Contrast is formally defined as the difference between the SLD of the region and the background matrix. For SAXS the contrast is determined by the inherent chemical composition and bulk density and there is very little one can do to change the natural contrast. For SANS and USANS on the other hand, there exists the unique possibility to manipulate the contrast by exchanging the hydrogen atoms for deuterium without significantly changing the chemistry of the system. This can have a dramatic effect on the contrast and hence on the I(Q).

In the case of hydrogels, the sample should appear as regions of increased SLD (caused by such effects as cross linking, hydrogen bonding, hydrophobic interactions, chain collapse etc.) in a matrix of reasonably uniform SLD consisting of polymer chains dissolved in water. Since the hydrogels were prepared from a solution, the regions of increased SLD will be randomly distributed; however will most likely be polydispersed in size and shape. This must be taken into consideration when analysing the I(Q) data.

The experimental I(Q) is collected in Q (or reciprocal) space and, in general, it is not possible to directly back transform to give an image in real space (i.e. the equivalent of focussing in microscopy is not possible). Therefore a number of techniques have been developed to overcome this problem. There are a number of model independent procedures (e.g. Guinier approximation, indirect Fourier transform) that provide useful structural parameters (e.g. radius of gyration, maximum dimension) without making any assumptions about the structure. The next level of data analysis is to fit theoretic models to the I(Q) data and hence obtain a more detailed description of the structure on the nano/micro length scale. This usually requires some prior knowledge to be able to select from the enormous number of theoretical models (e.g. chains, spheres, cylinders etc). The challenge is to establish that the selected model is the most appropriate. Supporting information from other techniques and/or published data can be valuable. In the present study, it was reasonably assumed that the RSF, Rec1-resilin and PVCL were essentially chains in solution, and the hydrogels had structural characteristics similar to other well-characterised hydrogels. The soundness of these assumptions will be discussed in more detail in Chapter 7.

2.3.2.3 Small angle X-ray scattering (SAXS)

SAXS in a technique used to analyse the size and morphology of a range of materials including polymers and proteins. A beam of X-rays is irradiated through a sample and the elastic scattering pattern is recorded by a 2D detector that is positioned behind the samples. Figure 2.12 illustrates the general schematic for small angle scattering experiments. For SAXS, the source is a rotating Cu anode with a beam size of about 1 mm diameter. The intensity and angle of the scattered X-rays are collected over time and used to give information regarding the microstructure of the given sample. For this study, the NanoSTAR II SAXS instrument (Bruker AXS, Karlsruhe) at the Australian Nuclear Science and Technology Organisation (ANSTO), Lucas Heights, Sydney was employed. Detailed experimental parameters and procedures for each study are discussed in detail in Chapters 3 and 7.

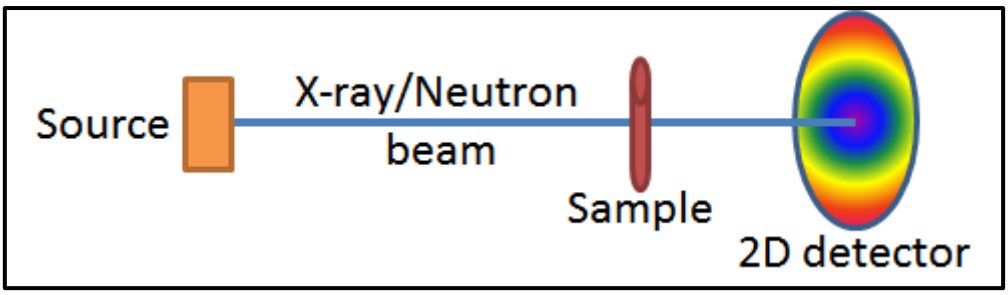


Figure 2.12 General schematic of small angle scattering.

2.3.2.4 Small angle neutron scattering (SANS)

Small angle neutron scattering (SANS) is a technique used to study the nanostructure of different materials and can be used to obtain information of structural heterogeneities on the nanometre scale.[21] A sample is irradiated with a monochromatic beam of neutrons and the scattering pattern of neutrons is recorded at very low angles (typically 0.1 – 10˚) by a 2D detector that is situated behind the sample and is perpendicular to the primary beam. For SANS, the source is a large cold neutron source that provides a rather large beam; usually about 10 mm diameter to give approximately the same flux at the sample position as for SAXS. For experiments into the structure of hydrogels, D_2O was employed to swell the hydrogel and provide enhanced contrast and reduced background. In this study, SANS measurements were performed on RSF, Rec1-resilin and PVCL solutions and hydrogels using the QUOKKA SANS instrument at ANSTO. More detailed experimental parameters and procedures are discussed in detail in Chapter 7.

2.3.2.5 Ultra small angle neutron scattering (USANS)

USANS extends the range of length scales obtained from SANS experiments by two orders of magnitude into the micrometre size range.[22] This allows for the study of materials with large structural order, such as hydrogels. The KOOKABURRA USANS instrument at ANSTO is based on the Bonse-Hart method (Figure 2.13).[22, 23] In this system, two multiple-reflection crystal systems are employed in a nondispersive geometry.[22] This allows for the detection of very small angular deviations of the neutron beam from scattering of a sample that is placed between two channel-cut crystals.[22] USANS was employed to study the structure of RSF, Rec1-resilin/RSF and RSF/PVCL hydrogels swollen in D_2O. In the same way as SANS, the intensity of scattered neutrons is measured as a function of the scattering vector. Furthermore, model functions were fitted to describe the structure on the molecular scale. More detailed experimental parameters and procedures are discussed in detail in Chapter 7.

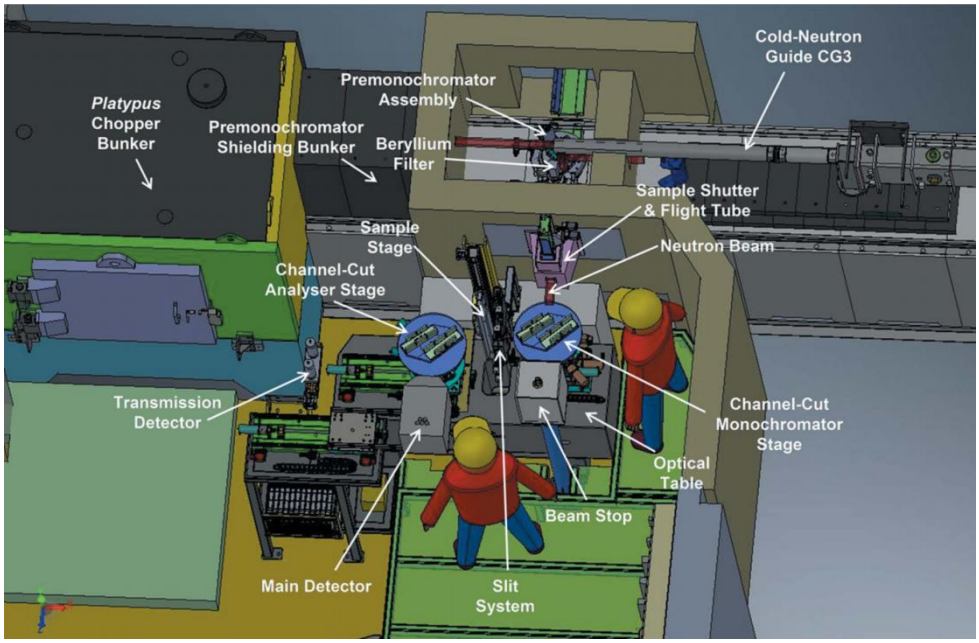


Figure 2.13 Schematic of layout of Kookaburra USANS instrument.[22]

2.3.3 Microscopic techniques

2.3.3.1 Scanning electron microscopy (SEM)

SEM is widely used to obtain images of a range of different sample types to provide information of their surface topology. SEM experiments are conducted by scanning a focused beam of electrons (primary electrons) over a sample surface and the secondary electrons,

backscattered electrons, X-rays and Auger electrons generated by the atoms of the sample are collected by a detector and an image of the surface is created (Figure 2.14).[24] Typical SEM experiments are conducted in vacuum to avoid the collision of electrons with air molecules; however low vacuum is possible in some types of SEM equipment. In this study, the secondary electron detector was employed to image samples, including the hydrogel morphology, electrospun fibres and cells cultured on the hydrogels. Several different instruments were employed during the course of this thesis including the Philips XL30 FEG SEM (USA), FEI Quanta 450 FEG ESEM and the on-axis in-lens secondary electron detector on a Zeiss MERLIN with GEMINI II column.

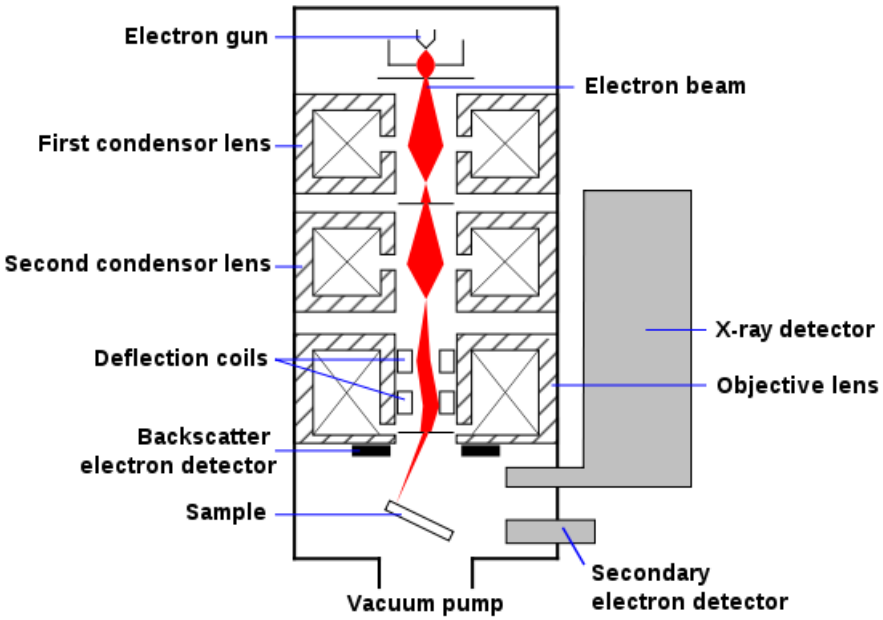


Figure 2.14 Schematic representation of a SEM instrument.

2.3.3.2 Transmission electron microscopy (TEM)

TEM is an electron microscopy technique that is widely used to examine the morphology of a wide range of different materials. TEM operates by transmitting an electron beam through a vacuum, which is then focused using electromagnetic lenses and is transmitted through a thin sample of interest (Figure 2.15).[24] The density of the material dictates whether the electrons are scattered or disappear from the beam. At the bottom of the microscope the unscattered electrons hit a fluorescent screen, which generates an image that can be captured with a camera.[24] The contrast between different materials in the TEM micrograph is due to the differences in composition, with thicker regions or samples regions with a higher atomic number appear darker. In this study, the morphology of electrospun core/shell PVCL/RSF

nanofibres was examined using a JEOL-2100F TEM (JEOL, MA, USA) operated at 200 kV. The analysis was performed using the 'Digital Micrograph' software (Gatan Inc.). Details of the sample preparation are detailed in Chapter 6.2.

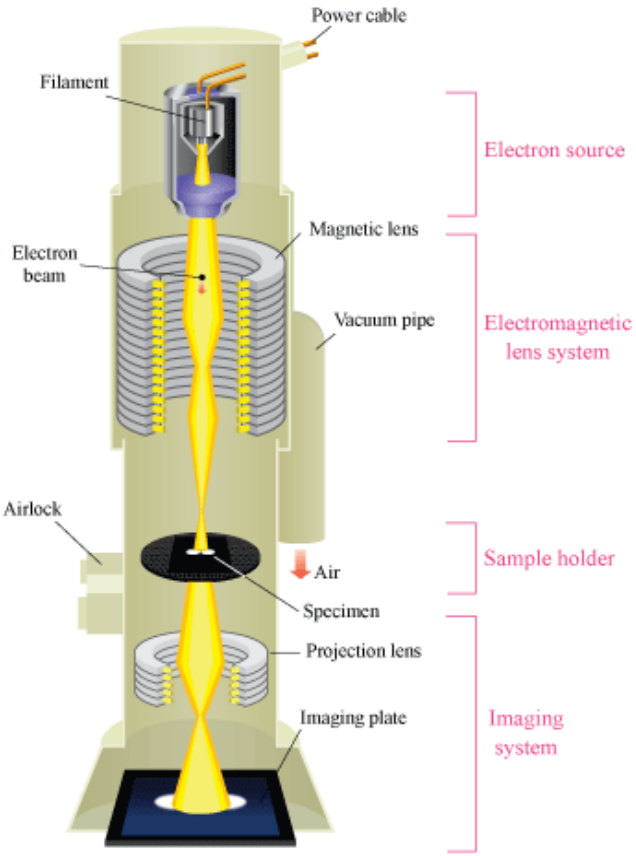


Figure 2.15 Schematic representation of TEM setup.[25]

2.3.3.3 Atomic force microscopy (AFM)

AFM is a high resolution scanning probe microscopy and demonstrates resolution on the order of fractions of a nanometre. AFM consists of a sharp tipped cantilever that is used to scan the sample surface (Figure 2.16). The forces between the tip and the sample when they are in close proximity leads to a deflection of the cantilever, which follows Hooke's law. These forces include mechanical contact force, van der Waals forces, electrostatic forces, chemical bonding, capillary forces, etc. The deflection of the cantilever is measured using a laser spot that is reflected from the top surface of the cantilever into an array of photodiodes, which creates electrical pulses that are sent to the computer and transformed into an image.[26] The operating mode of AFM employed in this study is tapping mode in which the cantilever oscillates and is only in contact with the surface for a short period of time. This oscillation is

controlled by a small piezoelectric element that is mounted in the tip holder. The oscillation amplitude, phase, and resonance frequency are controlled by the interactions between the sample and tip, including van der Waals forces, dipole-dipole interactions and electrostatic forces, which cause the amplitude of oscillation to decrease as the tip approaches the sample. The force of the intermittent contact between the tip and sample surface is used to produce an image of the sample surface. Tapping mode lessens the damage done to the surface and is gentle enough to visualise polymer molecules adsorbed on surfaces.

In this study, tapping mode AFM was conducted with a JPK NanoWizard III (JPK Instruments, Berlin) and was used to study the morphology of Rec1-resilin/PP and Rec1-resilin/RSF coassembled systems. The probe used for the experiments was an AppNano ACT uncoated silicon cantilever, with a spring constant (k) of 25-75 N/mA. Sample preparation details can be found in the experimental section of Chapter 3. The topographic and phase images were analysed using the JPKSPM data-processing software.

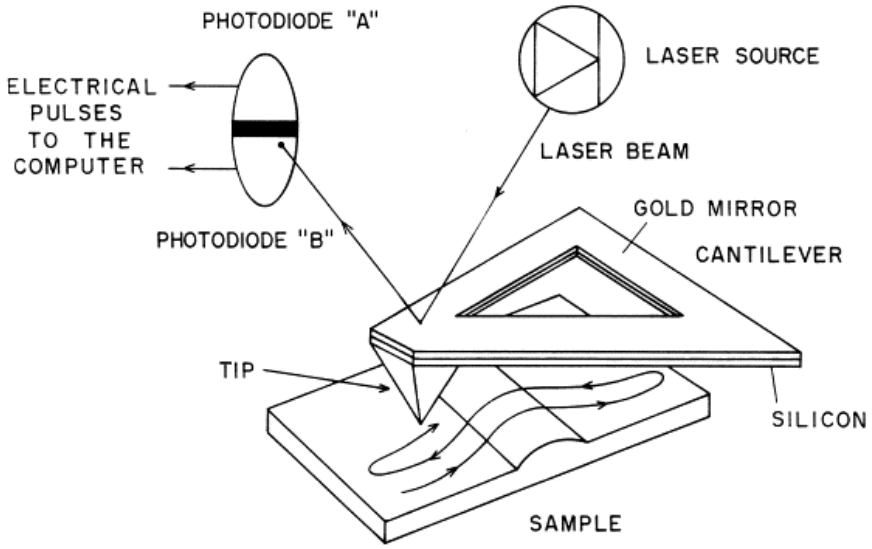


Figure 2.16 Schematic depicting the working principle of the AFM instrument.[26]

2.3.4 Thermal analysis techniques

2.3.4.1 Differential scanning calorimetry (DSC)

DSC is a thermoanalytical technique that is commonly employed to investigate the thermal phase transitions of polymer materials, such as glass transition, crystallisation, and decomposition. The phase transitions of materials are accompanied by changes in heat flow that are measured by the DSC instrument. The instrument measures the difference in heat

flow between a sample and reference, which provides information about the exothermic or endothermic reaction occurring at that particular temperature range.[27] Figure 2.17A shows the experimental setup for a DSC instrument. In this study, the thermal transitions, such as glass transition temperature (T_g) and enthalpy, were measured for the RSF, Rec1-resilin and PVCL hydrogels and electrospun mats using a Discovery DSC analyser (TA Instruments) (Figure 2.17B). Samples were measured under a controlled nitrogen atmosphere and a constant heating/cooling rate of 10˚C/min. The temperature ranges studied varied depending on the sample and are included in the experimental sections of the corresponding chapters. The data analysis of the transitions was performed using the TRIOS software (TA Instruments).

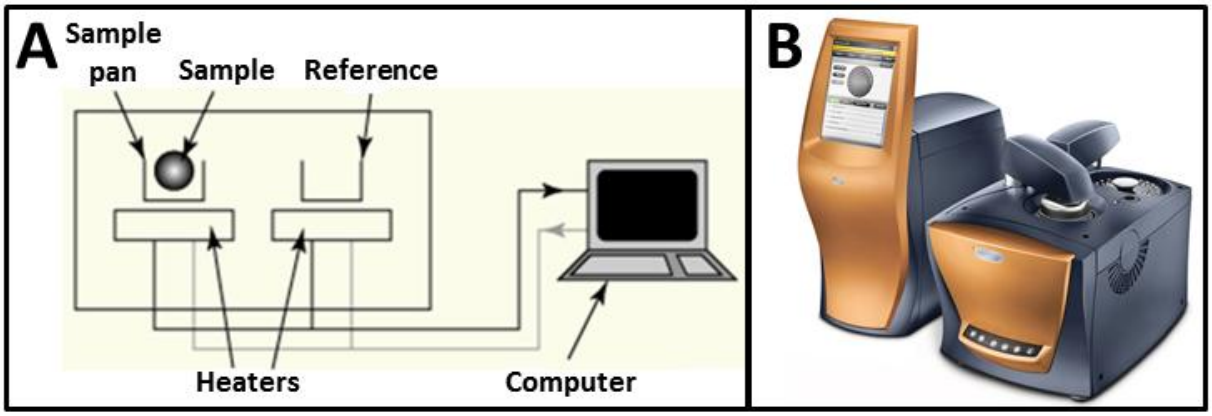


Figure 2.17 A) Schematic representation of a DSC instrument. B) Image of the TA Instruments Discovery DSC.

2.3.4.2 Thermogravimetric analysis (TGA)

TGA is a commonly used thermal analysis technique that can be used to measure the decomposition of a material with respect to temperature. A TGA instrument consists of a high precision balance with a pan attached that may be loaded with the sample, which is located within a furnace and allows for heating at a constant rate and under a controlled atmosphere environment. In this study, a Discovery TGA analyser (TA Instruments) was employed to study the thermal behaviour of RSF, Rec1-resilin, and PVCL biomaterials as a function of temperature. The weight loss and derivative weight loss were measured as a function of increasing temperature (10˚C/min) and under nitrogen atmosphere. The analysis was performed using the TRIOS software (TA Instruments).

2.3.5 Mechanical testing

2.3.5.1 Dynamic mechanical analysis (DMA)

DMA is used to analyse the viscoelastic properties of polymer materials. The mechanical properties of a sample are measured as a function of time, temperature and frequency. The DMA applies a sinusoidal stress to a sample and measures the resulting strain. For a perfectly elastic material, the resulting strain and stress will be perfectly in phase; however for a purely viscous material, there will be a phase lag (δ) of strain with respect to stress of 90 degrees. Viscoelastic materials display characteristics somewhere in between and thus when the strain is applied there is some lag in the stress. DMA measurements determine the storage and loss modulus of a material, where the storage modulus is a measure of the stored energy and represents the elastic portion, and the loss modulus measures the energy dissipated as heat and represents the viscous portions. Tan δ is measured as the ratio of the loss modulus to storage modulus and is a measure of the viscoelasticity of a material.

In this study, DMA of the swollen RSF-based hydrogels was performed in tension mode using the DMA Q800 (TA Instruments) equipped with a humidity accessory. The equilibrium swollen samples were mounted and run at ambient temperature, 50 %RH increment, with an amplitude of 10 μm and a preload force of 0.010 N.

2.3.5.2 Tensile testing

Tensile testing is a fundamental test employed in materials science where a sample undergoes a controlled tension until failure. Tensile testing provides information about the strength of a material, its elongation and ultimate tensile strength (point of breakage). From these measurements, other properties can be determined including Young's modulus, yield strength, and toughness. The test is undertaken by placing a sample between to clamps and slowly stretching the sample at a controlled rate until it breaks. The force and elongation are measured and used to calculate the stress and strain using the equations given below.

$$\sigma = \frac{F}{A} \quad (1)$$

where σ = stress, F = force and A = area of the sample.

$$\varepsilon = \frac{\Delta L}{L} \quad (2)$$

where ε = strain, ΔL = change in sample length and L = initial sample length.

The toughness is calculated from the area under the stress-strain curve and has units of Pa/m^3.

In this study, tensile testing of the equilibrium swollen RSF and RSF/PVCL hydrogels was performed in extension mode using a Hounsfield Universal Tensiometer equipped with a 1 kN load cell. Samples were mounted and tested until breakage at room temperature with a constant velocity of 10 mm/min.

2.3.6 Contact angle measurement - sessile drop technique

The sessile drop method is used for the characterisation of wettability of the surface, which is relevant for biological applications. A liquid droplet is placed on a sample and the contact angle (θ_c), which is the angle made by the intersection of the liquid/solid interface and the liquid/air interface (Figure 2.18), is measured. When using water as the liquid, a high contact angle is indicative of a hydrophobic surface and a low degree of wetting, whereas a low contact angle indicates that the surface is hydrophilic and there is a high degree of wetting. The sessile drop experiment is performed with a goniometer, which allows for measurement of the contact angle visually. A droplet of liquid is deposited on the sample surface using a syringe and a high resolution captures the image. In this study, the contact angles of electrospun surfaces were calculated using the SCA20 software.

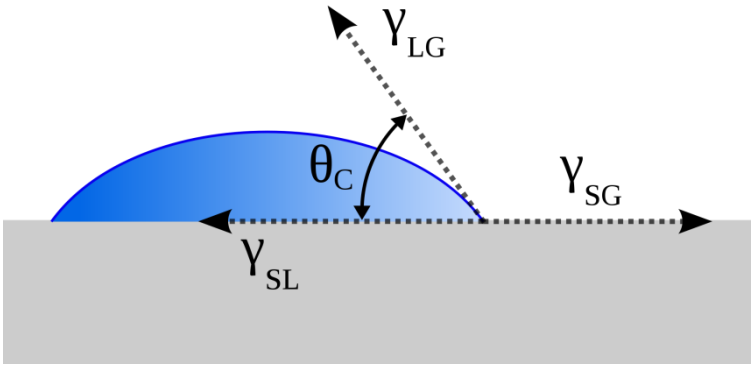


Figure 2.18 Schematic showing the sessile drop technique to determine the contact angle ($\theta_{c)}$.

2.3.7 X-ray diffraction (XRD)

XRD is an analytical technique used to obtain structural information about crystalline solids. The experiment involves the irradiation of a sample with a continuous beam of x-rays and the diffracted x-rays are collected by a detector (Figure 2.19).

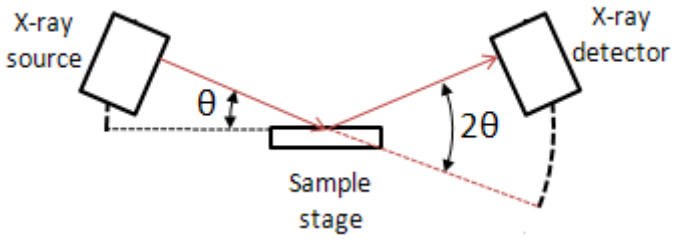


Figure 2.19 Schematic representation of an x-ray diffraction system.

The diffraction pattern is then analysed to determine the relation between the angle of diffraction and the distance between the adjacent crystal planes (d), which is given by Bragg's Law.[28]

$$2d\sin\theta = n\lambda \ldots \quad (3)$$

where, n is a positive integer, λ is the wavelength of the x-ray and θ is the angle of diffraction. In this study, XRD was used to examine the structure of the BMWS powder, film and hydrogel. The experiments were performed with an XRD analyser (Scintag/Thermo-electron ARL X'Tra XRD) using copper Kα radiation (1.542 Å). The X-ray tube was run at 40 kV and 30 mA. Scans were performed from 5 to 90˚ 2θ in steps of 0.02˚ at a rate of 1.2˚ per minute.

2.3.8 Photophysical characterisation

2.3.8.1 UV-vis absorption spectroscopy

UV-vis spectroscopy is a common absorption technique used to measure molecules undergoing electronic transitions in the ultraviolet-visible spectral region. The instrument operates by irradiating a sample with light (near-UV and near-infrared wavelength ranges) and the transmitted light is measured and compared to the intensity of the light before it passes through the sample to determine the absorbance. The difference between the incident and transmitted light at a particular wavelength provides information about the electronic states in the sample. In this study, UV-vis absorption spectra of the RSF-based hydrogels were acquired using a spectrophotometer (Evolution 201, Thermo Scientific) with a quartz cuvette of 10 mm path length. The analysis was performed using the INSIGHT software (Thermo Scientific).

2.3.8.2 Fluorescence spectroscopy

Fluorescence spectroscopy is a type of electromagnetic spectroscopy that is commonly used to analyse the fluorescence emission from samples undergoing electronic transitions. The instrument operates by irradiating a sample with a beam of light (near-UV and near-infrared wavelength ranges) and the fluorescence emitted from the sample upon excitation is measured using a detector that is positioned at 90˚ to the incident light. Molecules possess various states referred to as energy levels, and upon irradiation the electrons in the molecules within the sample get excited (absorb photon) from the ground state to one of higher energy states. Collisions with other molecules in the sample cause the molecule to lose energy and drop down to the ground electronic state, which results in the emission of a photon.[29] This can give information on the molecular states of the molecules in the sample. In this study, a Cary Eclipse fluorometer (Varian Inc.) with a quartz cuvette of 10 mm path length was used to confirm the formation of dityrosine crosslinks in the RSF hydrogels. The analysis was performed using the Eclipse SCAN software.

2.4 Cell culture study

2.4.1 ATDC5 pre-chondrocyte cell line

The ATDC5 pre-chondrocyte cell line (Riken laboratories, Japan) was employed to examine the potential of the RSF-based hydrogels for cartilage tissue engineering.[30, 31] The cells were plated in monolayer in T-75 tissue culture flasks and cultured to confluence in α-MEM culture medium containing 10% fetal calf serum (FCS) as previously described.[32] Prior to seeding the cells onto the hydrogels and tissue culture polystyrene (TCP), the cells were detached with 0.05% trypsin, enumerated using a hemocytometer and the cell concentration adjusted to suit the experiment.

2.4.2 Assessment of ATDC5 cell adhesion on BMWS-based hydrogels

The dried hydrogel discs (6 x 6 mm) were sterilised in 70% ethanol for 2 hours followed by overnight drying. Following this, the hydrogels were immersed in sterile PBS for 24 hours and transferred to individual wells of a 96 well plate. The cell concentration was adjusted so that each well received 12 x 10^4 cells/cm^2 and were cultured overnight. The Ru5APS28 hydrogel/cell constructs were cultured overnight, washed with PBS to remove non-adherent cells, fixed with paraformaldehyde (4%) solution for 1 hour, washed with PBS and immersed

in PBS for imaging. Phase-contrast micrographs were captured using a Nikon Eclipse Ti microscope through a 10X objective and recorded with a Qi1 Monochrome camera.

2.4.3 Culture of ATDC5 cells on RSF-based hydrogels

The dried hydrogel samples (6 x 6 mm) and tissue culture polystyrene (TCP) control samples (6 x 6 mm) were sterilised in 70% ethanol for 2 hours followed by overnight drying. Following this, the hydrogels were immersed in sterile PBS for 24 hours and the hydrogels and TCP were transferred to individual wells of a 48 well plate. A 20 µL droplet of the cell suspension was placed in the centre of each hydrogel/TCP control and allowed to adhere for 30 mins (Figure 2.20). Following this, the wells were topped up with 300 µL of media. The cells were cultured on the RSF-based hydrogels for up to 1 week and were fixed at different time points for analysis.

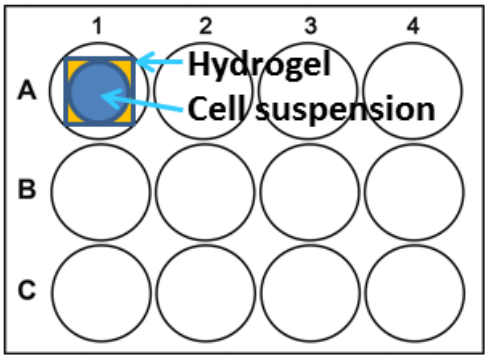


Figure 2.20 Schematic of cell plating method.

2.4.4 Cell fixation and SEM analysis to assess cell adhesion and proliferation

The cells were fixed with a biological fixation agent (glutaraldehyde/paraformaldehyde) for 30 minutes, washed with PBS for 5 minutes and post-fixed with 2% osmium tetroxide for 30 minutes. The hydrogel/ATDC5 cell constructs were serially dehydrated with 70%, 90% and 10% ethanol for 10 minutes each cycle and followed by rinsing with hexamethyldisilazane (HMZ) diluted with an equal volume of ethanol for 10 minutes, then undiluted HMZ for 10 minutes and left to dry overnight. The hydrogel/ATDC5 cell constructs were sputter coated with platinum and analysed using a SEM (Philips XL30 FEGSEM) at an accelerating voltage of 10 kV as previously described.[33]

2.4.5 Assessment of cell proliferation and viability

The WST-1 cell proliferation assay (Roche) is a simple colorimetric assay to measure the proliferation rate of cells. The principle is based on the conversion of the tetrazolium salt, WST-1 [2-(4-iodophenyl)-3-(4-nitrophenyl)-5-(2,4-disulfophenyl)-2H-tetrazolium], to a coloured dye by mitochondrial dehydrogenase enzymes. The soluble salt is released into the media and within a given time period a colour change is observed that is proportional to the amount of mitochondrial dehydrogenase in a given culture. Thus, the WST-1 assay is a measure of the metabolic activity of the cells.

For the proliferation studies, samples were prepared as described in section 2.4.3. The cells were allowed to proliferate for up to 1 week and the relative amount of viable, metabolically active ATDC5 cells on each hydrogel type was quantified using the WST-1 (water soluble tetrazolium salts) viability assay at allocated time points assay using an established protocol.[34] The WST-1 reagent (-20˚C) was transferred to a water bath (37˚C) to thaw for 10 minutes, followed by dilution to 1:10 with phenol red free α-MEM/10% FCS. Following this the hydrogel/cell constructs were transferred to adjacent empty wells to avoid false readings. 200 μL of the diluted WST-1 reagent was added to the wells containing the hydrogel/cell constructs and were incubated for 2 hours at 37˚C / 5% CO_2. 100 μL from each well was transferred to a flat bottom 96 well plate (including blank) for absorbance measurements on an ELISA plate reader with a wavelength of 490 nm. Triplicate experiments were performed for each sample type and TCP was used as the control.

2.4.6 Evaluation of the chondrogenic differentiation of ATDC5 cells cultured on RSF-based hydrogels

Cells regulate the expression of genes by turnover of gene transcripts (messenger RNA), which can be measured by the number of copies of an mRNA transcript of that particular gene that is present in a sample. The mRNA is first reverse-transcribed to complementary DNA (cDNA), followed by real-time polymerase chain reaction (RT-PCR), which is a laboratory technique used to monitor the amplification of a targeted DNA molecule during PCR. A fluorescence marker is used to monitor the generation rate of the product of interest and quantify the relative expression level. In this study, RT-PCR was used to analyse the expression of cartilage-related genes (Collagen type I (Col I), Collagen type II (Col II) and Sox9), which is a measure of the differentiation of ATDC5 cells cultured on different hydrogel samples. Also, the expression of osteogenic markers (Runx2, osteonectin (Sparc),

osteocalcin (Bglap), osterix (Sp7), integrin-binding saloprotein (Ibsp), osteopontin (Spp1), and alkaline phosphatase (Alpl)) were analysed.

ATDC5 cells were seeded at 15 x 10^4 cells/mL (8.3 x 10^3 cells/cm^2) as described in section 2.4.3. Samples were incubated under chondrogenic culture conditions in α-MEM supplemented with 10% FCS and TGF-β1 (10 ng/mL). The media was changed twice weekly and after 1, 7 and 14 days, the media was removed from the wells, and the cell/hydrogel constructs were rinsed with PBS and then transferred to new wells prior to the addition of TRIzol reagent for 5 minutes. The TRIzol solubilized cellular extracts were transferred to a fresh tube prior to the addition of 200 μL chloroform. Samples were vortexed briefly for 15 seconds and subsequently incubated for 2-3 minutes at room temperature. The tubes were centrifuged at 12,000 g for 15 minutes at 4˚C and the aqueous layer was extracted and transferred to a new tube. 1 μL of RNase free glycogen (20 mg/mL) was added to the tube, followed by the addition of 150 μL of isopropanol. The tube was gently mixed and incubated at room temperature for 10 minutes. The RNA precipitate was pelleted by centrifugation at 12,000 g for 10 minutes at 4˚C. The supernatant was removed and the pellet washed in 75% ethanol followed by centrifuging at 7,500 g for 5 minutes at 4˚C. The supernatant was removed and the tube spun again, followed by removal of any residual ethanol. The air-dried RNA pellet was dissolved in 20 μL RNase-free water at 55˚C for 10 minutes, and the RNA concentration was quantified using the Nanodrop spectrophotometer.

Complementary DNA (cDNA) was synthesized from 1500 ng of the RNA for each sample using a Superscript III kit. The RT-PCR reactions were conducted with the Bio-Rad CFX Connect Real-Time PCR machine and monitored using the SYBR Green PCR Mastermix. Transcript levels of cartilage-related genes, Col I, Col II, and Sox9 were analysed, with β-Actin as the reference gene. In addition, the expression of osteogenic markers, Runx2, Sparc, Bglap, Sp7, Ibsp, Spp1, and Alpl were analysed. The details of the PCR primers are listed in Table 2.2. Each PCR reaction was performed in a 15 μL reaction mixture containing 2 μL of cDNA, 7.5 μL of SYBR Green, 0.75 μL of primer pair, and 4.75 μL of nuclease free water. RT-PCR was performed according to the following conditions: 50˚C for 2 minutes and 95˚C for 15 minutes, followed by 39 cycles of 95˚C for 15 seconds, 55˚C for 25 seconds and 72˚C for 10 seconds. The samples were kept at 72˚C for 3 minutes and 65˚C for 15 seconds, followed by melt curve analysis (0.5˚C/second increase from 65 to 95˚C) at the end of the cycles to confirm that a single PCR product was obtained. The RT-PCR procedure was performed in the same manner for all genes of interest. For each gene, triplicate PCRs were

conducted for each experimental sample. The C_t value for each gene marker was defined as the cycle number at which the fluorescence intensity reached a certain threshold where amplification of each target gene was within the linear region of the reaction amplification curves. The relative expression for each gene was normalized by the C_t value of the housekeeping gene (β-actin).

Table 2.2 Oligonucleotide sequences used for Real-time PCR

Gene	Forward (5' – 3')	Reverse (5' – 3')	Mw (Da)
β-actin	TTGCTGACACCATGCAGAAG	AAGGGTGTAAAACGCAGCTC	6126.1 /6175.1
Col I	AAAGGGTCCCTCTGGAGAAC	CACCTCTAGAGCCAGGGAGAC	6151.0 /6425.2
Col II	CGAGTGGAAGAGCGGAGACTAC	CCAGTTTTTCCGAGGGACAGT	6858.5 /6437.2
Sox9	ACGGCTCCAGCAAGAACAAG	TTGTGCAGATGCGGGTACTG	6129.0 /6204.1
Runx2	ATGATGACACTGCCACCTCTG	ATGAAATGCTTGGGAACTGC	6366.2 /6181.1
Sparc	ACTACATCGGACCATGCAAATAC	CGTACAAGGTGACCAGGACAT	6985.6 /6464.3
Bglap	AAGCAGGAGGGCAATAAGGT	TCAAGCCATACTGGTCTGATAGC	6264.2 /7023.7
Sp7	ATGGCGTCCTCTCTGCTTG	GTCCATTGGTGCTTGAGAAGG	5761.8 /6517.3
Ibsp	CAGTCCAGGGAGGCAGTG	GGAAAGTGTGGAGTTCTCTG	5589.7 /6228.1
Spp1	AGCAAGAAACTCTTCCAAGCAA	GATTCGTCAGATTCATCCGAGT	6705.4 /6725.4
Alpl	GCCTTACCAACTCTTTTGTGC	GGCTACATTGGTGTTGAGCTT	6323.2 /6483.3

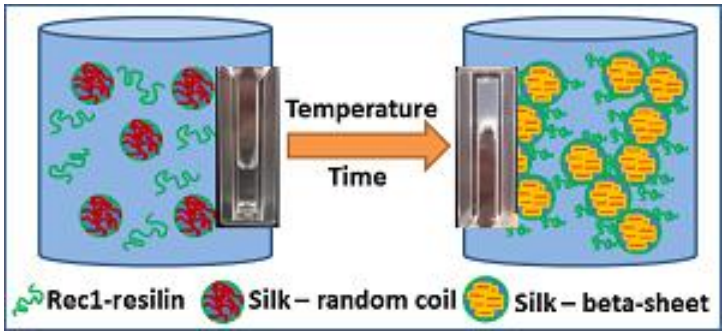
2.5 References

1. Cho, H. J.; Ki, C. S.; Oh, H.; Lee, K. H.; Um, I. C., *Int. J. Biol. Macromol.* **2012,** *51* (3), 336.
2. Rockwood, D. N.; Preda, R. C.; Yucel, T.; Wang, X. Q.; Lovett, M. L.; Kaplan, D. L., *Nat. Protoc.* **2011,** *6* (10), 1612-1631.
3. Elvin, C. M.; Carr, A. G.; Huson, M. G.; Maxwell, J. M.; Pearson, R. D.; Vuocolo, T.; Liyou, N. E.; Wong, D. C. C.; Merritt, D. J.; Dixon, N. E., *Nature* **2005,** *437*, 999-1002.
4. Kim, M.; Elvin, C.; Brownlee, A.; Lyons, R., *Protein Expression Purif.* **2007,** *52* (1), 230-236.
5. Whittaker, J.; Balu, R.; Choudhury, N. R.; Dutta, N. K., *Polym. Int.* **2014,** *63* (9), 1545-1557.
6. Truong, M. Y.; Dutta, N. K.; Choudhury, N. R.; Kim, M.; Elvin, C. M.; Nairn, K. M.; Hill, A. J., *Biomaterials* **2011,** *32* (33), 8462-8473.
7. Agarwal, S.; Wendorff, J. H.; Greiner, A., *Polymer* **2008,** *49* (26), 5603-5621.
8. Min, B.-M.; Lee, G.; Kim, S. H.; Nam, Y. S.; Lee, T. S.; Park, W. H., *Biomaterials* **2004,** *25* (7-8), 1289-1297.
9. Sill, T. J.; von Recum, H. A., *Biomaterials* **2008,** *29* (13), 1989-2006.
10. Teo, W. E.; Ramakrishna, S., *Nanotechnology* **2006,** *17* (14), R89-R106.
11. Alessandrino, A.; Marelli, B.; Arosio, C.; Fare, S.; Tanzi, M. C.; Freddi, G., *Eng. Life Sci.* **2008,** *8* (3), 219-225.
12. Ma, P. X., *Adv. Drug Delivery Rev.* **2008,** *60* (2), 184-198.
13. Teo, W.-E.; Inai, R.; Ramakrishna, S., *Sci. Technol. Adv. Mater.* **2011,** *12* (1), 013002.
14. Bellan, L. M.; Craighead, H. G., *Polym. Adv. Technol.* **2011,** *22* (3), 304-309.
15. Elahi, M. F.; Lu, W.; Guoping, G.; Khan, F., *J. Bioeng. Biomed. Sci.* **2013,** *3* (121).
16. Wang, M.; Yu, J. H.; Kaplan, D. L.; Rutledge, G. C., *Macromolecules* **2006,** *39* (3), 1102-1107.
17. Sun, Z.; Zussman, E.; Yarin, A. L.; Wendorff, J. H.; Greiner, A., *Adv. Mater.* **2003,** *15* (22), 1929-1932.
18. Greenfield, N. J., *Nat. Protoc.* **2007,** *1* (6), 2876-2890.

19. Shimadzu ABC's of Photoacoustic Spectroscopy. http://www.shimadzu.com/an/ftir/support/ftirtalk/talk7/intro.html (accessed 17 September 2015).
20. Miller, C. C., *Proc. R. Soc. A* **1924,** *106* (740), 724-749.
21. Hammouda, B., Probing Nanoscale Structures - The SANS Toolbox. 2012. http://www.ncnr.nist.gov/staff/hammouda/the_SANS_toolbox.pdf (accessed 10 January 2015).
22. Rehm, C.; Brule, A.; Freund, A. K.; Kennedy, S. J., *J. Appl. Crystallogr.* **2013,** *46* (6), 1699-1704.
23. Bonse, U.; Hart, M., *Appl. Phys. Lett.* **1965,** *7* (9), 238-240.
24. Goodhew, P. J.; Humphreys, F. J.; Beanland, R., *Electron Microscopy and Analysis*. 3rd Ed.; Taylor and Francis: London, 2000.
25. Department of Physics, The Chinese University of Hong Kong. Basic principle of transmission electron microscope. http://www.hk-phy.org/atomic_world/tem/tem02_e.html (accessed 18 September 2015).
26. Pereira, R. d. S., *Biochem. Pharmacol.* **2001,** *62* (8), 975-983.
27. Höhne, G. W. H.; Hemminger, W. F.; Flammersheim, H.-J.; SpringerLink, *Differential Scanning Calorimetry*. 2nd ed.; Springer Berlin Heidelberg : Imprint: Springer: Berlin, Heidelberg, 2003.
28. Bragg, W. H.; Bragg, W. L., *Proc. R. Soc. A* **1913,** *88* (605), 428-438.
29. Sharma, A.; Schulman, S. G., *Introduction to Fluorescence Spectroscopy*. Wiley: 1999.
30. Shukunami, C.; Ohta, Y.; Sakuda, M.; Hiraki, Y., *Exp. Cell Res.* **1998,** *241* (1), 1-11.
31. Shukunami, C.; Ishizeki, K.; Atsumi, T.; Ohta, Y.; Suzuki, F.; Hiraki, Y., *J. Bone Miner. Res.* **1997,** *12* (8), 1174-1188.
32. Vandyke, K.; Fitter, S.; Zannettino, A. C. W., *Blood Cancer J.* **2011,** *1*, e2.
33. Ahmed, F.; Choudhury, N. R.; Dutta, N. K.; Zannettino, A.; Knott, R., *Biomacromolecules* **2013,** *14* (11), 3850-3860.
34. Vandyke, K.; Dewar, A. L.; Diamond, P.; Fitter, S.; Schultz, C. G.; Sims, N. A.; Zannettino, A. C. W., *J. Bone Miner. Res.* **2010,** *25* (8), 1759-1770.

Chapter 3: Tunable thermo-responsiveness of Resilin via coassembly with rigid biopolymers

This chapter of the thesis is presented as a research article "J. L. Whittaker, N. K. Dutta, R. Knott, G. McPhee, N. H. Voelcker, C. M. Elvin, A. Hill and N. R. Choudhury. Tunable thermoresponsiveness of Resilin via Coassembly with Rigid Biopolymers. Langmuir, 2015, 31 (32), 8882-8891", published and reproduced by permission of the American Chemical Society, Copyright 2015.



Langmuir

Article

pubs.acs.org/Langmuir

Tunable Thermoresponsiveness of Resilin via Coassembly with Rigid Biopolymers

Jasmin L. Whittaker,[†] Naba K. Dutta,*[,†] Robert Knott,[‡] Gordon McPhee,[§] Nicolas H. Voelcker,[§] Chris Elvin,[∥] Anita Hill,[⊥] and Namita Roy Choudhury*[,†]

[†]Ian Wark Research Institute, University of South Australia, Mawson Lakes Boulevard, Adelaide, South Australia 5095, Australia

[‡]Bragg Institute, ANSTO, Lucas Heights, New South Wales 2234, Australia

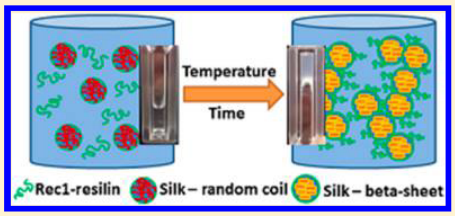
[§]Mawson Institute, University of South Australia, Mawson Lakes Boulevard, Adelaide, South Australia 5095, Australia

[∥]CSIRO Agriculture, Queensland Bioscience Precinct, 306 Carmody Road, St. Lucia, Queensland 4067, Australia

[⊥]CSIRO Manufacturing, Bayview Avenue, Clayton, Victoria 3168, Australia

Supporting Information

ABSTRACT: The ability to tune the thermoresponsiveness of recombinant resilin protein, Rec1-resilin, through a facile coassembly system was investigated in this study. The effects of change in conformation and morphology with time and the responsive behavior of Rec1-resilin in solution were studied in response to the addition of a rigid model polypeptide (poly-L-proline) or a hydrophobic rigid protein (*Bombyx mori* silk fibroin). It was observed that by inducing more ordered conformations and increasing the hydrophobicity the lower critical solution temperature (LCST) of the system was tuned to lower values. Time and temperature were found to be critical parameters in controlling the coassembly behavior of Rec1-resilin in both the model polypeptide and more complex protein systems. Such unique properties are useful for a wide range of applications, including drug delivery and soft tissue engineering applications.



INTRODUCTION

The coassembly of multiple self-assembling proteins and peptides in a single gel offers significant opportunities to prepare a unique class of materials with tunable properties. Native resilins are a class of highly resilient, elastic proteins that are found in all insects and likely in all arthropods. In particular, Rec1-resilin is a recombinant form of resilin that is derived from the first exon of the *Drosophila melanogaster* CG15920 gene.[1] It exhibits responsiveness to multiple stimuli, including temperature, pH, and light, which allows for precise control of the self-assembly behavior.[2] Rec1-resilin exhibits dual-phase transition behavior (DPB), with both a lower critical solution temperature (LCST) and an upper critical solution temperature (UCST). Below the UCST (~6 °C) and above the LCST (~70 °C) the protein undergoes phase separation in solution, whereas between these temperatures the protein is soluble with a hydrodynamic diameter of ~11 nm.[2] While the DPB is an outstanding property of Rec1-resilin, both the UCST and LCST are outside the physiological temperature range, which limits the use of this unique behavior for biomedical applications. In general, a number of methods can be used to tailor the stimuli-responsive behavior of polymer materials, including altering the self-assembly behavior or hydrophobic/hydrophilic balance of the material.[3] Control over the self-assembly of polypeptide systems can be achieved by altering the conformation, which causes a change in the distribution of the hydrophobic and hydrophilic amino acid residues in the material at the 3D level.[4] In general, it has been found that the LCST is lowered by incorporating hydrophobic moieties and raised through the introduction of hydrophilic groups.[3,5] Tailoring the environment of the stimuli-responsive polymer materials may be achieved through a number of strategies. These include: copolymerization, DNA technology, or forming hybrid materials through chemical and physical interactions.[3] Urry et al. tuned the LCST of elastin-like peptides (ELPs) with structure (VPGVG) by substituting the fourth valine residue with another amino acid residue.[6] Another method that has been employed to tune the LCST of ELPs is to form coassembled structures with the introduction of mixtures of elastin-based materials of different molecular weights and amino acid sequences, where the LCST could be tuned by varying the composition of the system;[7,8] however, there are very few reports to tune the LCST of a synthetic polymer or biological polymer through coassembly with a material of more hydrophobic nature.

The need to lower the LCST of Rec1-resilin has stimulated our interest into investigating its coassembly with other proteins/peptides. Therefore, in this investigation, the coassembly of Rec1-resilin through the addition of two different polypeptides has been investigated in relation to the phase

Received: March 19, 2015
Revised: July 15, 2015
Published: July 15, 2015

ACS Publications © 2015 American Chemical Society

DOI: 10.1021/acs.langmuir.5b01014
Langmuir 2015, 31, 8882–8891

transition behavior, conformation, and morphology of the system. The materials that have been chosen for this study are (i) the synthetic polypeptide poly-L-proline (PP) and (ii) the native protein *Bombyx mori* silk fibroin. We have chosen to add PP as a model rigid polypeptide system, which constitutes 14 mol % of the structure of Rec1-resilin.[9] Proline is a unique amino acid because it is the only one that contains a pyrrolidine ring, which introduces steric constraints and results in the rigid polyproline type II (PPII) helix that it forms in aqueous solutions.[10−12] PP also exhibits temperature responsiveness with an LCST at ∼45 °C.[13] This is attributed to the stable PPII conformation that is present in polyproline-rich environments and results in self-assembly by coacervation.[13] A more complex biomolecule is predominantly hydrophobic silk protein, fibroin, which is dominated by the repeat sequence GAGAGS. Silk fibroin can exist in the silk I or silk II state, which corresponds to the soluble random coil and insoluble beta-sheet conformations, respectively. As previously mentioned, the addition of hydrophobic components has been shown to lower the LCST. Thus, silk fibroin, with its propensity to self-assemble into rigid structures, has been identified as a promising candidate to tune the behavior of Rec1-resilin. Xia et al. investigated tunable self-assembling silk-elastin-like polypeptides, which showed tunable LCST characteristics on the addition of silk fibroin functional groups;[14] however, the ability to tune the responsiveness of resilin-based materials through the addition of silk fibroin was not studied.

The influence of the polypeptides (PP and silk fibroin) on the coassembly behavior of Rec1-resilin was examined in this work. The addition of PP served as a simple model system to determine whether the addition of rigid structures with increased hydrophobicity resulted in tuning temperature-responsive behavior of Rec1-resilin. Following this, the addition of silk fibroin was studied to gain an understanding of the effect of coassembly with a complex rigid molecule. Both systems were investigated using dynamic light scattering (DLS) by probing the changes in the LCST and phase behavior. In addition, circular dichroism (CD) was employed to examine the changes in secondary structure due to the coassembly of the proteins. Finally, the morphological changes in the system were examined by means of atomic force microscopy (AFM). A comprehensive small-angle X-ray scattering (SAXS) study of the Rec1-resilin/silk fibroin system was also undertaken to gain insights into the structure and morphological evolution of this system.

EXPERIMENTAL SECTION

Materials. Rec1-resilin was synthesized by cloning, expression, and purification of exon 1 of the *Melanogaster* gene CG15920 as a water-soluble protein, as described elsewhere.[1,15] The primary structure of Rec1-resilin comprises 310 amino acids with 18 copies of a 15 amino acid sequence (GGRPSDSYGAPGGGN) with a molecular mass of 28.5 kDa (Supporting Information, S1).

PP was purchased from Sigma-Aldrich (MW(vis) = 10 700 g/mol). *Bombyx mori* silk was purchased as raw silk from Beautiful Silks, Australia. The raw silk was degummed by boiling in aqueous 0.02 M Na_2CO_3 for 30 min, rinsed in distilled water (DW) three times, and allowed to dry at room temperature overnight. The fibroin was then dissolved in a calcium chloride, water, ethanol solution ($CaCl_2/H_2O$/EtOH 1/8/2 molar ratio), with a liquor ratio of 1:20, at 70 °C for 3 h. Following this, the solution was dialyzed using SnakeSkin dialysis tubing (3.5 kDa molecular weight cutoff) (ThermoFisher Scientific) for several days and centrifuged at 10 000 rpm and 20 °C for 20 min. The solution was diluted using DW to obtain the concentrations required for the experiments. The main amino acid constituents of the regenerated silk fibroin (RSF) were confirmed through nuclear magnetic resonance (NMR) (Supporting Information S2). In addition, the molecular weight range was measured through SDS-PAGE experiments and was found to be from ∼37 to 200 kDa, which is common for RSF solutions (Supporting Information S3).[16,17]

Hydrophobicity by Kyte−Doolittle Plot. The Kyte−Doolittle hydrophobicity plot is a measure of the hydrophobicity of a protein by analyzing the hydrophobicity and hydrophilicity of the amino acid sequence.[18] The prediction of the hydrophobicity of Rec1-resilin, PP, and RSF was determined using a web-based calculator (http://web.expasy.org/protscale/). The full protein sequences of the materials were input, and a window size of 9 was employed.

Size Analysis by DLS. Solutions of Rec1-resilin, PP, and RSF with concentrations of 10 mg/mL were prepared in 5 mM phosphate-buffered saline (PBS) (pH 7.4). The PP and RSF solutions were individually added to Rec1-resilin (50:50 volumetric ratio), and the combined solutions were sonicated for several minutes to allow adequate distribution of particles. The solutions were transferred into low volume cuvettes for analysis using the Malvern Zetasizer NanoZS. The Rec1-resilin/PP (Rec1-resilin/PP) system was studied with time at room temperature and also with increasing temperature. The Rec1-resilin/RSF coassembled system was aged over 0 to 6 days and the particle size distribution in the system was monitored daily over a range of temperatures. The samples were equilibrated at each temperature for 5 min. Photographs of the Rec1-resilin/RSF samples at different temperatures were taken to evaluate the change in appearance as the phase transitions took place.

Secondary structure study by CD. Rec1-resilin/PP coassemblies with different volume ratios were prepared with a total concentration of 0.1 mg/mL. In addition, Rec1-resilin and RSF were coassembled in solution at a 50:50 volume ratio with a total concentration of 0.1 mg/mL. The solutions were prepared with 0.5 mM PBS as higher concentrations of PBS resulted in noisy spectra. The Rec1-resilin/RSF solutions were aged to examine the structural changes over time. Far-UV CD spectra of the coassembled systems were obtained using a Jasco J-815 spectropolarimeter. The temperature was maintained at 25 °C throughout the experiments using a Peltier-type heating/cooling system. The measuring range was 190−260 nm. The data pitch was 0.2 nm, with a 50 nm/min scanning speed, bandwidth of 1.0 nm, DIT of 1 s, and accumulation of 10 scans. The HT value was maintained below 600 V for all spectra.

Structure and Morphology Study Using AFM and SAXS. Tapping mode AFM was conducted with a JPK NanoWizard III (JPK Instruments, Berlin) and was used to study the morphology of the Rec1-resilin/PP and Rec1resilin/RSF system. The probe used for the experiments was an AppNano ACT, uncoated silicon cantilever, with a spring constant (k) 25−75 N/mA. The AFM samples were prepared by depositing 10 μL of sample solution (Rec1-resilin/PP and Rec1-resilin/RSF) of concentration 10 μg/mL onto a cleaned silicon wafer substrate and incubated at room temperature for 30 min under controlled atmosphere. The samples were then rinsed with DW and dried with a stream of nitrogen gas. The topographic and phase images were collected at 0 and 6 days and analyzed using the JPKSPM data-processing software.

SAXS was employed to analyze the structure and morphology of the Rec1-resilin/RSF assembly with time. The Rec1-resilin and Rec1-resilin/RSF solutions were prepared at a concentration of 10 mg/mL in 5 mM PBS, while the RSF solution was 10 mg/mL in DW. Data were collected on a NanoSTAR II SAXS instrument (Bruker AXS, Karlsruhe Germany).[19] For each sample, the 2D SAXS data were collected for 3600 s as a function of the scattering vector Q (where $Q = 4\pi \sin(\theta)/\lambda$; 2θ the scattering angle; λ the X-ray wavelength) over the range $0.011 < Q < 0.33$ Å^{-1}. The samples were loaded into 2 mm ID quartz capillaries (using a gel-tip pipette) and the temperature was maintained at 23 °C. The 2D data were corrected for detector spatial effect and variation in sensitivity and reduced to 1D data using routines in the Bruker software. The 1D data were analyzed using Igor Pro software (Wavemetrics, Portland, OR) and macros developed at NIST.[20]

DOI: 10.1021/acs.langmuir.5b01014
Langmuir 2015, 31, 8882−8891

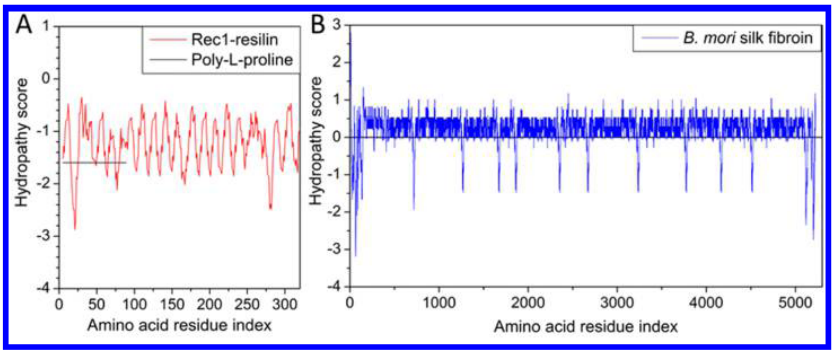


Figure 1. Kyte–Doolittle hydropathy plot of (a) Rec1-resilin and PP and (b) *B. mori* silk fibroin.

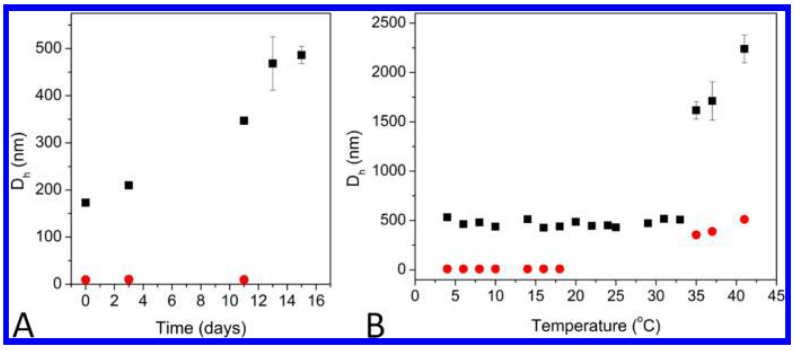


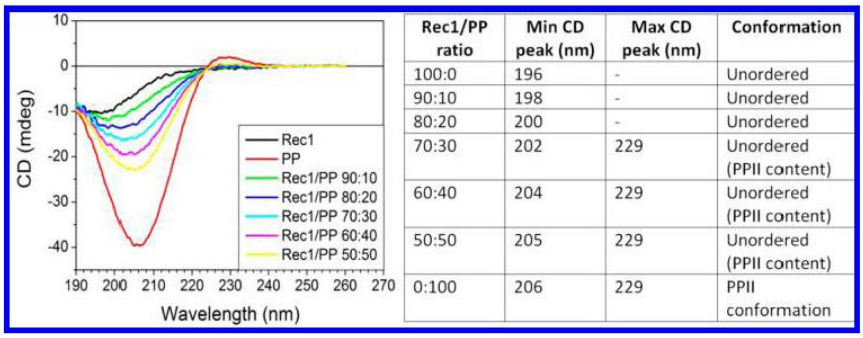
Figure 2. Hydrodynamic diameter (D_h) of Rec1-resilin/PP (50:50) coassembly over (A) time at 20 °C and (B) increasing temperature measured at day 16 (red dot: small particles; black dot: large particles).

RESULTS AND DISCUSSION

Hydrophobicity/Hydrophilicity by Kyte–Doolittle Hydropathy Plot. Kyte–Doolittle hydropathy plots indicating the relative hydrophobicity/hydrophilicity of residues constituting the Rec1-resilin, PP, and RSF structures are shown in Figure 1.[18] The mean hydrophobic index of the amino acids within a given window was calculated, and this value was plotted for each position. In general terms, a score of 4.6 constitutes the most hydrophobic value and a score of −4.6 the most hydrophilic. The scores for Rec1-resilin are between −0.5 and −3, and PP has a score of −1.6, indicating that both are hydrophilic in nature (Figure 1A); however, the Kyte–Doolittle hydropathy plots do not take into account the secondary structure of the peptide. The rigid PPII structure that PP exhibits in solution results in exposure of the nonpolar methylene groups.[10] Therefore, while the hydrophobicity of the individual PP amino acid is small, Yoon et al. have shown that PP peptide blocks behave as slightly hydrophobic rigid structures that result in microphase separation when self-assembled with hydrophilic segments.[10] RSF is predominantly hydrophobic but contains short hydrophilic segments at the C- and N-terminal ends and distributed throughout the sequence. The hydropathy scores range between 0 and 1 for the hydrophobic segments and −1.5 to −3 for the smaller hydrophilic regions (Figure 1B). These scores were used to probe the mechanism behind the phase behavior and morphology of the coassemblies, as examined in the following sections.

Effect of Model Rigid Peptide Addition on the Phase Transition Behavior of Rec1-Resilin. To examine whether the system results in homogeneous or heterogeneous assemblies, we have used two types of precursor materials. The first is a low-molecular-weight (10.7 kDa) rigid homopolypeptide (polyproline (PP)) and the second is a rigid regenerated silk protein (RSF). Poly-L-proline was chosen as the steric constraints present in the structure that results in the PPII helix are shown to be important for temperature-induced coacervation.[13] The purpose was to investigate the effect of a model system (PP) on inducing structural changes of the coassembly, in this case induction of PPII helix formation. The molecular weight, 10.7 kDa, was chosen because the size is appropriate for interactions with Rec1-resilin of molecular weight 28.4 kDa. The influence of the addition of 50 wt % PP to Rec1-resilin on the phase behavior of the mixture was studied using DLS (Figure 2A). Initially, two intensity peaks at 173 and 9.3 nm were observed. These values closely match those of the individual components in solution, with the hydrodynamic diameters (D_h) of Rec1-resilin and PP being 10.4 ± 0.1 and 146.5 ± 1.4 nm, respectively (Supporting Information S4). Incubation for 3 and 11 days at 4 °C results in an increase in the larger particle size, while the smaller particle remains between 9 and 10 nm; however, by day 13 the appearance of a single peak (468.4 ± 56.8 nm) indicates a state of homogeneity of the coassembly (Supporting Information S5). These results show that with time a miscible coassembled system between Rec1-resilin and PP was formed. The proposed mechanism of the self-assembly involves the formation of a core–shell structure with the more hydrophobic PP molecules in the center surrounded by hydrophilic Rec1-resilin molecules. We evaluated this mechanism by means of AFM (vide infra).

DOI: 10.1021/acs.langmuir.5b01014
Langmuir 2015, 31, 8882–8891



Rec1/PP ratio	Min CD peak (nm)	Max CD peak (nm)	Conformation
100:0	196	-	Unordered
90:10	198	-	Unordered
80:20	200	-	Unordered
70:30	202	229	Unordered (PPII content)
60:40	204	229	Unordered (PPII content)
50:50	205	229	Unordered (PPII content)
0:100	206	229	PPII conformation

Figure 3. CD spectra of Rec1-resilin, PP, and Rec1-resilin/PP coassembly at different mass ratios after 1 day of incubation and at room temperature. The table shows the maximum and minimum peaks in the CD spectra for the different mass ratios and how this translates to secondary conformations.

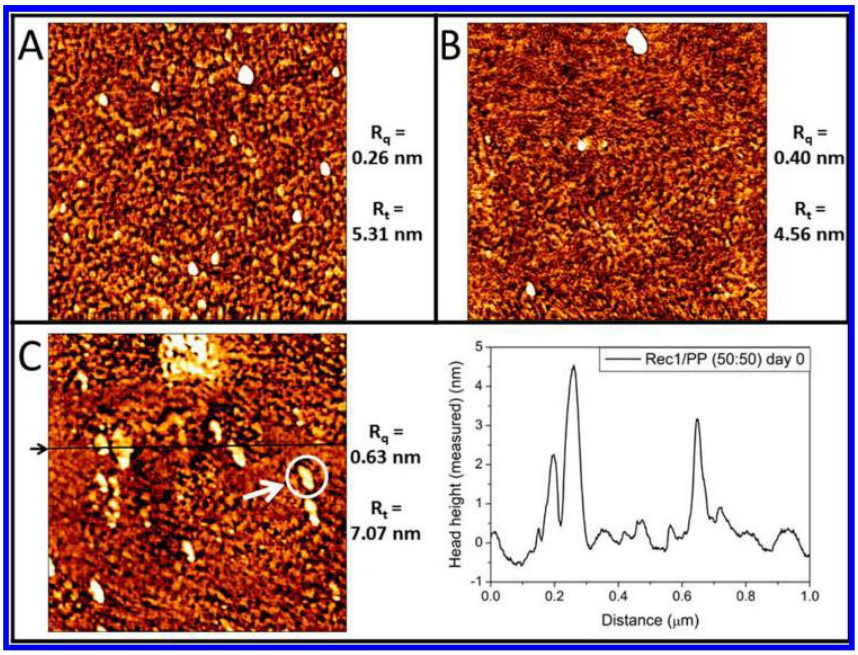


Figure 4. AFM phase images of A) Rec1-resilin and B) PP adsorbed on flat silicon and corresponding roughness data and (B) PP. AFM phase image obtained on flat silicon, roughness data and line curve of (C) Rec1-resilin 50:50 Day 0 (R_q: RMS roughness; R_t: peak-to-valley roughness). Width of image: 1 μm.

On day 16, the particle size distribution of the blend was studied with respect to temperature (Figure 2B). Initially at 4 °C the sample appeared transparent and two distinct intensity peaks (9.3 and 533.0 nm) were observed. At 35 °C the particle size increased dramatically with a broad intensity peak featuring two maximum values of 354.6 ± 18.2 and 1616.0 ± 88.6 nm. At 41 °C the Rec1-resilin/PP coassembly appeared turbid, with peak values of 511.9 ± 28.5 and 2239.0 ± 140.7 nm (Supporting Information S6). DLS measurements above ~1600 nm would lead to sedimentation effects, and thus the measurements for large structures are not quantitatively reliable; however, the dramatic increase in particle size and the turbidity of the sample are certainly indicative of phase separation of the blend and coassembly and of loss of solubility. The phase behavior of Rec1-resilin alone has been extensively studied in our previous work.[2] Rec1-resilin has been shown to exhibit dual temperature-responsive behavior, with a UCST of 6 °C and a LCST of 70 °C.[2] PP solutions have been shown to exhibit an LCST phase transition above ~45 °C.[13] The observed phase transition at 41 °C indicates that the LCST of Rec1-resilin can be lowered by adding PP. In addition, the UCST of Rec1-resilin is not observed in this temperature range in the presence of PP. We ascribed the higher propensity for the self-assembling coacervation process of the Rec1-resilin/PP system to the stability of the PPII conformation and studied this by means of CD spectroscopy.

Secondary Structure Changes Due to Addition of PP. CD was used to examine the influence of PP on the co/self-assembly of Rec1-resilin and to gain an understanding into the changes in responsive behavior that are observed with DLS. Figure 3 shows the CD spectra of Rec1-resilin, PP, and the Rec1-resilin/PP coassembly, measured at room temperature after 1 day of incubation (4 °C). In addition the peak values and corresponding predominant secondary structures are

DOI: 10.1021/acs.langmuir.5b01014
Langmuir 2015, 31, 8882−8891

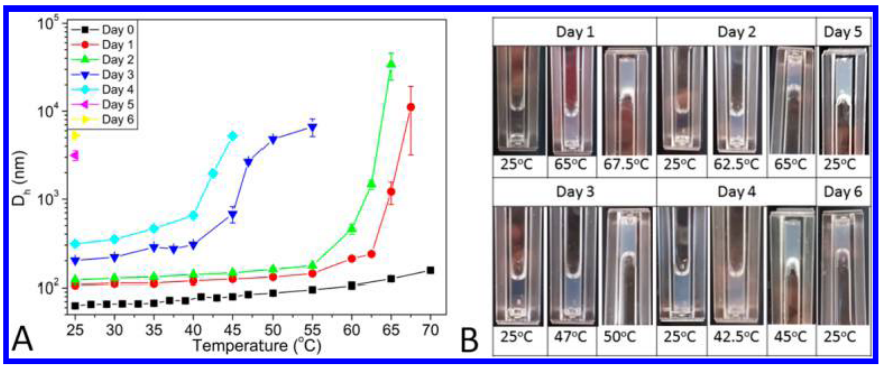


Figure 5. (A) DLS data demonstrating the shift in LCST of the Rec1-resilin/RSF system with time (0 to 6 days) by measuring changes in hydrodynamic diameter (D_h). (B) Photographs of Rec1-resilin/RSF system aged for 1 to 6 days and at specific temperatures showing the temperatures where the phase transition occurs leading to gelation of the system. Cuvettes were inverted to indicate physical gelation of the system.

reported. It is difficult to detect PPII structure from curve fitting of CD spectra using libraries that are derived from nonglobular proteins;[21,22] however, PPII structure can be confirmed by the presence of a strong negative peak at approximately 190−206 nm and a unique weaker positive peak around 220−230 nm.[11−13,21−23] The spectrum of PP in Figure 3 depicts a strong negative peak at 206 nm and a weak positive peak at 229 nm, indicating a stable PPII conformation. The PPII helix is a left-handed helix and forms when residues adopt (φ, ψ) backbone dihedral angles of (−75°, 150°) and have trans isomers of their peptide bonds.[11] It is not confined to structures that contain PP but can also be adopted by sequences that contain polyglycine and polylysine, among others.[23] The PPII helices are also known to be induced at low temperature, and if not stabilized by a strong hydrogen-bonding pattern they have the ability to convert between other conformations such as random coil and beta-strand;[24] however, conformational freedom is restricted for structures that contain proline due to the pyrrolidine ring in the structure.[25] The spectrum for the Rec1-resilin sample shows a relatively weak negative band at 196 nm, which is similar to that of previous reports and is indicative of disordered structures.[22] Coassemblies containing Rec1-resilin and PP with an increasing PP content of 10 to 50 wt % were measured after 1 day of incubation at room temperature (Figure 3). As the PP content increased, the negative peak systematically shifted from 196 to 205 nm, while the intensity of the peak also increased, suggesting a larger contribution from the PPII conformation. In addition, the evolution of a maximum at 229 nm also confirms the increase in proportion and stability of the PPII conformation due to the presence of PP above 30 wt %. The systematic shift of the spectra indicates that Rec1-resilin and PP form a compatible system. Curve deconvolution using the MagicPlot software was employed to examine the contributions from the unordered and PPII conformations exhibited by Rec1-resilin and PP, respectively. Gaussian curve fitting was applied with the peaks set at 196 nm for the predominantly unordered Rec1-resilin contribution and 206 nm for the PPII helical contribution of PP. The results showed that the PPII content was increased in comparison with the PP content in the coassembly, suggesting that PP is driving the structural change of Rec1-resilin to a more stable PPII conformation (Supporting Information, Figure S8). Lorusso et al. reported that proline-rich domains that form stable PPII structures are responsible for the self-assembling coacervation process of the tropoelastin molecule.[13] Therefore, the higher propensity for coacervation and lower LCST observed for the Rec1-resilin/PP coassembly can be attributed to the achievement of a more stable PPII conformation.

Coassembly and Morphological Study of the Model Rec1-Resilin/PP System. To complement the phase and structural information obtained from DLS and CD, we employed tapping mode AFM at room temperature to provide morphological information on the coassembly of Rec1-resilin and PP. Figure 4 shows the phase images of freshly prepared Rec1-resilin, PP, and Rec1-resilin/PP (50:50) coassembly. On examination of the Rec1-resilin AFM images it was found that the protein was arranged in an isolated "island-like" morphology with particle sizes of 24 ± 3 nm and R_q of 0.26 nm, which is similar to the behavior of Rec1-resilin in our previous work (Figure 4A).[26] The PP molecules had uniform morphology and they appear connected, with a small number of larger aggregates (Figure 4B). This is consistent with the study by Lorusso et al. that reported the morphology of PP on silicon wafer to be globular aggregates that evolve into protofibrils.[13] The Rec1-resilin/PP system showed increased roughness values and larger elongated PP aggregates distributed throughout the Rec1-resilin matrix (Figure 4C), which is in agreement with the DLS data that revealed structures of increasing size and the two distinct peaks of smaller individual particles and larger aggregated groups (Supporting Information S5,S6). The line curve indicates that the larger aggregates have a height of approximately 2 to 5 nm, which is in agreement with the known behavior of PP (Figure 4C).[13] The average size of the aggregates on the silicon was measured to be 40 ± 14 nm in diameter and 93 ± 29 nm in length. This was less than the particle sizes measured through DLS, which is ascribed to the fact that AFM has been conducted on dehydrated samples.

Therefore, it is evident that the coassembly of Rec1-resilin and PP results in a system in which larger homogeneous coassembled aggregates form over time that adopt a stable PPII conformation contributing to a lowering of the LCST. Yoon et al. have shown that the exposure of the nonpolar methylene groups when the polypeptide adopts the PPII structure would be conducive to hydrophobic effects.[10] In addition, hydrogen bonding between the backbone carbonyl oxygen atoms in PP and side chains of Rec1-resilin is possible. Thus, the DLS, CD, and AFM results support the mechanism of aggregating PP molecules interacting with each other due to hydrophobic interactions, while hydrogen bonding with the more hydro-

DOI: 10.1021/acs.langmuir.5b01014
Langmuir 2015, 31, 8882−8891

philic Rec1-resilin side chains occurs and stabilizes the coassembled structures.

The study of PP addition on the behavior of Rec1-resilin has shown that a simple model rigid peptide system changes the self-assembly and structural behavior, which results in tuning of the temperature-responsiveness. Because of this, the study of the addition of the more complex rigid silk fibroin protein was studied in depth.

Effect of RSF on the Coassembly and Phase Transition Behavior. Following the study of the addition of a low-molecular-weight rigid polypeptide on the behavior of Rec1-resilin, the effect of a more complex rigid biomacromolecule (silk fibroin) was investigated. DLS was used to study the phase-transition behavior of the Rec1-resilin/RSF system as a function of increasing temperature (Supporting Information S7). The Rec1-resilin/RSF coassembly solutions were prepared and allowed to age while being stored at 4 °C. Aliquots were taken at different time points (0 to 6 days), and the particle size was measured at various temperatures (Figure 5A). The particle size of individual components was measured as 70 nm for RSF and 11 nm (Supporting Information S4) for Rec1-resilin, which is consistent with reported values.[2,27] The particle size of the fresh Rec1-resilin/RSF coassembly (day 0) did not markedly increase with temperature up to 70 °C, suggesting that there was insufficient time for self-assembly to occur; however, from day 1 onward, a phase transition occurred below 70 °C. The phase transition involved an increase in the particle size by several orders of magnitude, accompanied by a change in the sample appearance from transparent to opaque (Figure 5B). The LCST of the Rec1-resilin/RSF solution shifted to 42.5 °C when the coassembly was incubated for 4 days. It should be noted that the phase transition was irreversible on cooling the solution and a permanent physical gel formed. The photographs of the inverted cuvettes indicate the gelation of the solution (Figure 5B). In addition, after 5 and 6 days of incubation the coassembly formed an opaque weak physical gel at room temperature, which is confirmed by measured particle size values of 3000 and 5000 nm, respectively. We therefore suggest that the aggregation of the Rec1-resilin/RSF coassembly is influenced by a combination of time and temperature, which is similar for the model Rec1-resilin/PP system. It should be noted that the RSF solution was stable for up to several weeks and did not form a physical gel in the time frame of the Rec1-resilin/RSF coassembly. Therefore, the hydrophobicity of the coassembly is increased due to the addition of RSF, and this contributes to a lowering of the phase-transition temperature. The results show that the value of the LCST depends on the interaction time between Rec1-resilin and RSF and is tuned accordingly.

Along with the dramatic increase in particle size due to temperature, the particle size of the Rec1-resilin/RSF coassembly increased with time from ~60 nm to several microns (Figure 5A). It has been reported that silk fibroin molecules form micellar structures in aqueous systems, with the hydrophobic repeat segments in the core and the terminal hydrophilic portions as the outer regions.[28,29] In a study by Xia et al., self-assembly of temperature-responsive silk-elastin-like polymers (SELPs) was tuned by varying the silk-like content.[14] The morphology of the SELPs was similar to silk fibroin alone, with micellar-like structures containing the silk blocks in the core and more soluble elastin segments as the corona.[14] With increasing silk content above a certain threshold, the self-assembly occurring at the LCST became irreversible. This is similar to our case where irreversible coassembly was observed in the Rec1-resilin/RSF system. Therefore, our results show that the aggregation of the Rec1-resilin/RSF coassembly is induced by time with increasing temperature accelerating the process. Study into the behavior of Rec1-resilin above its LCST shows that the increase in temperature induces the formation of aggregates due to the dominating hydrophobic interactions and the subsequent expulsion of water from the system.[2] In addition, it has been reported that the loss of water from the silk micellar structure results in the formation of ordered structures within the micelles.[29] Therefore, we propose that an increase in temperature results in the formation of dominating hydrophobic interactions for Rec1-resilin, and the expulsion of water from the system leads to more ordered conformations in the silk structure. The secondary structure and morphological aspects of the Rec1-resilin/RSF coassembly were further investigated by CD spectroscopy, AFM, and SAXS.

Structural Changes of the Rec1-Resilin/RSF Coassembly by CD Spectroscopy. The changes in secondary structure of the Rec1-resilin/RSF coassembly were investigated using CD spectroscopy to understand the mechanism of the coassembly as a function of incubation time. The spectra for the individual Rec1-resilin and RSF solutions were obtained in addition to the coassembly incubated for 1 to 6 days. The spectra of Rec1-resilin, RSF, and Rec1-resilin/RSF days 1 and 6 are shown in Figure 6. The spectrum for the Rec1-resilin sample shows a

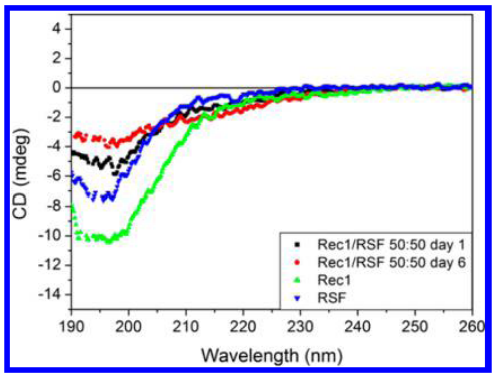


Figure 6. CD spectra of Rec1-resilin/RSF system (50:50) measured at days 1 and 6.

negative band at 196 nm, consistent with previous reports and indicative of unordered structures.[22] A negative minimum at 196 nm is also present in the spectrum of RSF. This observation is consistent with previous reports of RSF solutions that display negative minima in this region and indicates the protein has a random-coil conformation in solution.[30,31] The coassembled Rec1-resilin/RSF solutions at days 1 and 6 also showed negative bands in the same region (~196 nm); however, the intensity of this peak decreased with increasing incubation time. In addition, the negative intensity in the 210 to 220 nm region increased with time. Study of a SELP system by Xia et al. reported that a weakening of the signal at 197 nm and an increase in the magnitude of the signal at 210 nm is indicative of the induction of a type II beta-turn conformation.[14] Other groups have reported that the decrease in intensity of the peak at 196 nm and increase in the 210 to 220 nm region suggests a random-coil to beta-sheet transition, which is responsible for the physical gelation of silk fibroin.[27,31]

DOI: 10.1021/acs.langmuir.5b01014
Langmuir 2015, 31, 8882−8891

In general, a negative peak in the 210 to 220 nm region is characteristic of beta-sheet structures.[30,32] The spectra were fitted using the CCA+ program with the Lincomb (linear combination least-squares) method to analyze, semiquantitatively, the contribution of different secondary structures on the Rec1-resilin/RSF system. The data indicate an initial beta-sheet content of ~22% that increases to ~30% from day 4 onward, where it remained at this value. Thus, the evidence indicates that more ordered structures formed over time in the Rec1-resilin coassembly. This was reflected in the physical gelation that was observed with DLS measurements and was found to be irreversible.

Morphology Evolution of the Rec1-Resilin/RSF Coassembly by AFM. AFM was employed to study the morphology of the Rec1-resilin/RSF coassembly with time and correlate with the observed changes in particle size and structure obtained by DLS and CD spectroscopy. The AFM phase and height images, along with the roughness data for the Rec1-resilin/RSF system are shown in Figure 7. Discrete

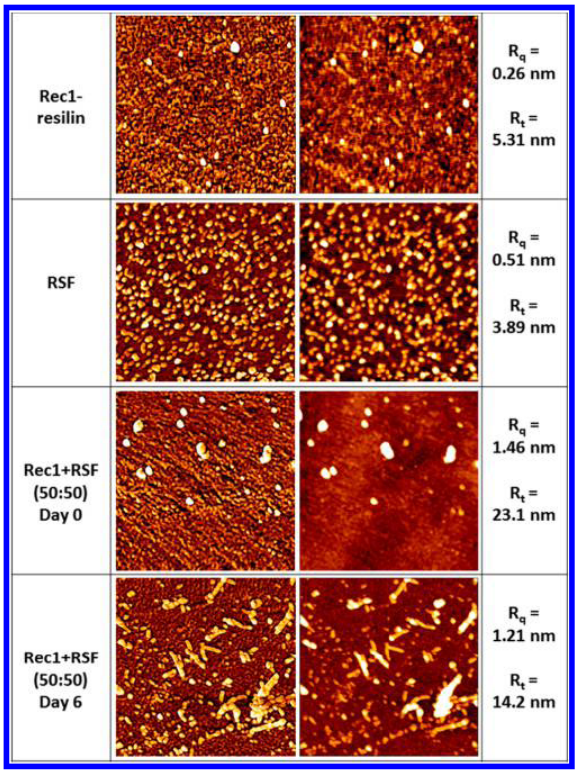


Figure 7. AFM phase (left) and height (right) images of Rec1-resilin/RSF (50:50) adsorbed on flat silicon and corresponding roughness values of coassembly at different time points.

spherical RSF particles with particle sizes ranging from 22 to 47 nm were observed, which were somewhat smaller than the particles measured by DLS (~70 nm). This is attributed to the fact that the molecules are in a dehydrated state for AFM. The Rec1-resilin/RSF system when initially combined (day 0) shows a homogeneous network of brighter particles surrounded by darker features. Some small rod-like structures were observed that are composed of spherical particles; however, after 6 days of incubation the AFM images depict larger rod-like aggregates made up of aggregated spherical particles. The rod-like structures are 80 to 260 nm in length and 26 ± 4 nm in width. The rod-like component was distributed homogeneously throughout the matrix, which was determined by imaging a number of regions on the samples. The increased R_t and R_q values of the coassembly, when compared with the individual proteins, indicate that larger aggregates had formed. Larger aggregates and rod-like structures made up of aggregated spherical particles are consistent with the reported behavior of silk fibroin, which involves the formation of micelles that aggregate over time to form nanofilament structures.[28,33] Therefore, the evidence suggests the formation of aggregated structures containing an RSF core and Rec1-resilin shell region that increase in size with time. This is in agreement with the DLS data showing increases in particle size with time; however, in the case of AFM analysis, the solution was more dilute and thus the growth was expected to occur at a slower rate. The AFM images support the model of the RSF micelles aggregating to form rod-like structures with the outer hydrophilic residues of RSF interacting with the hydrophilic Rec1-resilin molecules. The morphology of the coassembly with time was further evaluated using SAXS.

Size and Morphology of the Rec1-Resilin/RSF Coassembly by SAXS. The size and morphology of the Rec1-resilin/RSF coassembly in solution was further examined over time using SAXS. The RSF and Rec1-resilin/RSF samples were measured immediately after mixing (day 0) and monitored closely for up to 48 h, followed by measurements at 3, 7, and 15 days. The Rec1-resilin protein was measured after aging for 26 days to confirm that the structure is stable. Using the Guinier approximation, the radius of gyration, R_g, of Rec1-resilin in H_2O is 42.6 ± 1.0 Å, which is in agreement with previous values for resilin proteins.[34,35] Therefore, the protein was essentially an intrinsically disordered protein (IDP). The data closely agree with the DLS measurement for the D_h of Rec1-resilin (11 nm) and indicate that the structure is stable over a period of time.

A Guinier−Porod function was fitted to the RSF solution data (Figure 8A).[36] The RSF solution was measured at days 0, 1, 3, and 7 with no observed change, and thus only day 0 is shown. The measured R_g at day 0 was 28.1 ± 0.8 Å and the Porod exponent was 1.98 ± 0.01. The RSF has a wide MW distribution (30 to 200 kDa), which is common for regenerated silk proteins, and thus the calculated R_g is a size average for the system.[16,17] A study by Greving et al. on small-angle scattering of RSF solutions found that the R_g value varied greatly (~20 to 55 Å) depending on the processing conditions, molecular weight, and concentration of the solution;[37] however, another report of the R_g of RSF proteins determined from SAXS measurements is ~6.8 nm.[38] It is well known that the size and structure of RSF proteins is very much dependent on the dissolution conditions used for the silk fibroin, thus accounting for the differences observed in the literature. The Porod exponent suggests scattering from a random coil in solution.[36] It is known that silk fibroin forms micellar structures in solution that transform from internal random coil conformation to beta-sheet structures with time.[28,29] Therefore, this conforms to the reported behavior of silk fibroin in the initial solution state. Against this background, the conformations of the RSF observed by the SAXS technique were for RSF prepared under the conditions outlined in the Experimental Section. Care was taken to ensure that the RSF in the native and Rec1-resilin/RSF solutions were directly comparable.

DOI: 10.1021/acs.langmuir.5b01014
Langmuir 2015, 31, 8882−8891

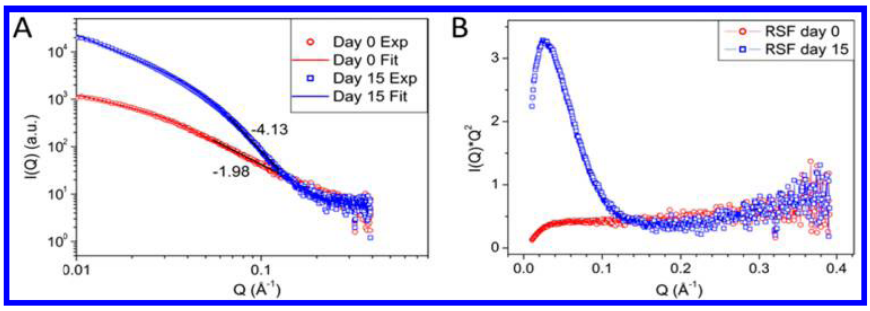


Figure 8. SAXS analysis of RSF solutions measured at 0 and 15 days. (A) SAXS data fitted with Guinier−Porod function. (B) Kratky plot from SAXS data.

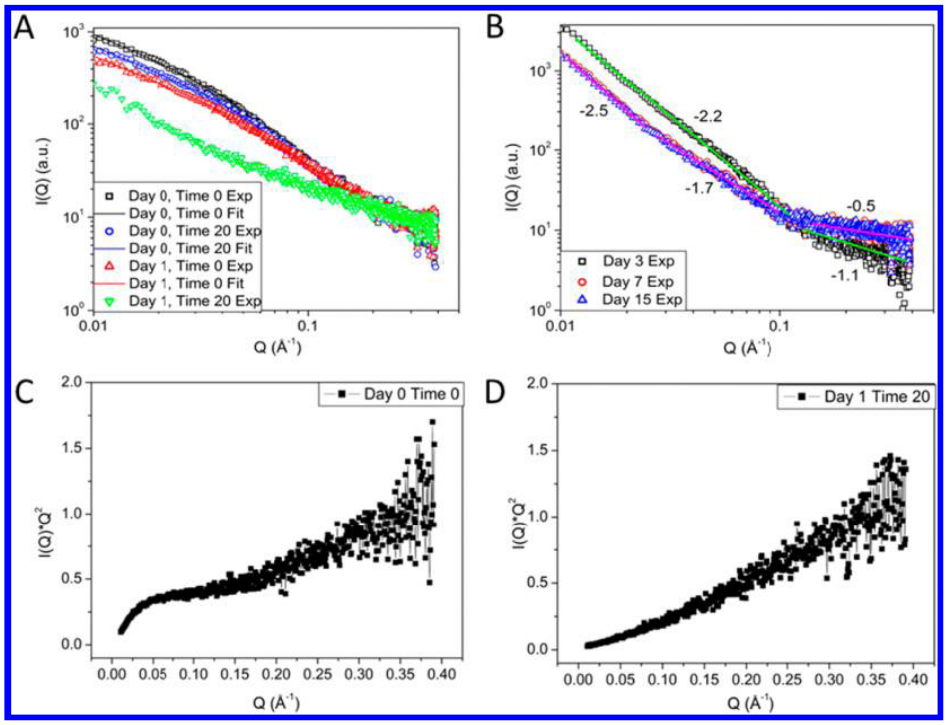


Figure 9. SAXS analysis of Rec1-resilin/RSF solutions measured from 0 to 15 days. (A) SAXS data fitted with Guinier-Porod function. (B) SAXS data for 3 to 15 days. (C) and (D) Kratky plot from SAXS data at days 0 and 1.

Note that the DLS results gave a larger diameter (~70 nm) for the RSF solutions, which is attributed to the aggregation of a number of silk fibroin molecules and is consistent with the known behavior of this protein in solution.

The measured R_g and Porod exponent for the RSF solution at day 15 were measured as 20.90 ± 0.07 Å and 4.13 ± 0.01, respectively. The lower R_g indicates that the silk structure is collapsing, attributable to the change in secondary structure from random coil to beta-sheet structures. The Porod exponent suggests scattering from a diffuse surface, which is consistent with a partially collapsed structure with an R_g less than 20 Å and is in agreement with the AFM results. In addition, the intensity of the scattering at low Q increases with time, indicating the presence of aggregated structures, which is expected behavior for silk fibroin, where micelles aggregate to larger structures that result in gelation of silk solutions.

A Kratky plot (Figure 8B) was employed to qualitatively examine the structure of RSF with time.[39] At day 0, the Kratky plot shows an initial increase at low Q, followed by a plateau in the mid Q range and a slight increase at high Q. This behavior is indicative of a random-coil protein structure, which is in agreement with the results from the CD measurements; however, the Kratky plot at day 15 is quite different with a distinct peak at low Q, followed by a plateau at mid Q and a gentle increase at higher Q values. The well-defined maximum suggests a more collapsed conformation and is attributed to an ordering of the secondary structure as interchain hydrogen bonding develops and is reported in other studies on silk fibroin.[38]

The behavior of the Rec1-resilin/RSF coassembly was studied with time to understand the effect of the addition of RSF and how the behavior differed from that of RSF alone. The SAXS data for the Rec1-resilin/RSF samples from day 0 to 15

DOI: 10.1021/acs.langmuir.5b01014
Langmuir 2015, 31, 8882−8891

are shown in Figure 9A and Figure 9B. A Guinier-Porod function was fitted to the Rec1-resilin/RSF solution at day 0 and the initial measurement of day 1; however, with increasing aggregation observed after day 1 the function was not suitable to fit the data (Figure 9A).[36] The R_g for the Rec1-resilin/RSF solution shifted from 20.41 ± 0.64 to 13.28 ± 0.58 Å from the initial measurement to the first measurement of day 1. The decrease in R_g indicates rearrangement and compaction of the coassembly with time. This is different from the behavior of Rec1-resilin in solution, which displays a much larger R_g, indicating a more open structure. The Porod exponent was measured as 1.96 ± 0.02, initially indicating the presence of random-coil structures. This shifted to 1.70 ± 0.03, which suggests the presence of swollen chains. From the measurement at the end of day 1, the nature of the curve is altered and shows an increasing slope in the low Q region and reveals the presence of aggregated structures. A decrease in intensity with time at the low Q region and slight increase at high Q was observed indicating the presence of smaller structures that are aggregating. This was also observed in the AFM results that showed larger aggregates due to silk fibroin that were present at day 0 that had altered by day 6 to smaller aggregated micelle structures. At day 3 there was a low Q slope of 2.2 and a high Q slope at 1.1. The SAXS measurements were stable from day 7 to 15, with a low Q dependence of 2.5 and high Q of 0.5. The slope of the low Q region decreased from day 3 to 7 and subsequently increased in the high Q region due to a further rearrangement of the proteins. In addition, the increasing slope at low Q indicates the presence of larger structures that are outside of the SAXS range. This correlates well with the AFM data that demonstrated compact micellar structures aggregating with time and also the DLS data that showed increasing size with time (Figure 5A and Figure 7).

A Kratky plot was employed to qualitatively examine the structure of the Rec1-resilin/RSF coassembly with time.[39] Representative plots are shown for days 0 and 1 that monitor the change in structure of the Rec1-resilin/RSF coassembly with time (Figure 9C and Figure 9D). Initially, the Kratky plot shows a steady increase at higher Q, indicating random conformations, as observed in CD measurements. At the end of day 1 the plot altered to show an increasing slope, indicative of rod-like structures.[40] Thus, the SAXS time study indicates that the Rec1-resilin/RSF undergoes a number of morphological changes in the coassembly process. This ultimately led to more ordered conformations in the SAXS size range that contributes to larger aggregates, as observed by DLS and AFM.

CONCLUSIONS

This study demonstrates that the self-assembly behavior of Rec1-resilin can be controlled through the addition of either a rigid synthetic polypeptide or a rigid native protein, to form coassembled structures with tuned phase behavior. The addition of PP results in conformational changes of the coassembly from a more random structure to a more stable PPII helical structure. AFM analysis indicates that stable coassembled structures formed over time that contained a core structure of PP molecules surrounded by a more hydrophilic Rec1-resilin molecules. The addition of the hydrophobic RSF also resulted in changes in the phase behavior, structure, and morphology of Rec1-resilin with the LCST shifting to 42.5 °C for the self-assembled structure on the 4th day, after which it undergoes sol−gel transition and forms a stable gel without the requirement of any enzyme or chemical mediated cross-linking.

The results from this study indicate that the phase-transition behavior of Rec1-resilin can be tuned to more physiologically relevant temperatures through coassembly with rigid biomolecules. The knowledge from this study is useful for the development of facile coassembled systems that can be applied to drug-delivery applications where the responsive behavior is advantageous or as injectable biomaterials.

ASSOCIATED CONTENT

Supporting Information

Consensus repeat structure of Rec1-resilin, NMR data and SDS-PAGE confirming the identity and molecular weight range of the RSF, and the size distribution curves from DLS and CD curve fitting. The Supporting Information is available free of charge on the ACS Publications website at DOI: 10.1021/acs.langmuir.5b01014.

AUTHOR INFORMATION

Corresponding Authors

*N.R.C.: E-mail: namita.choudhury@unisa.edu.au. Tel: +61883023719.

*N.K.D.: E-mail: naba.dutta@unisa.edu.au. Tel: +61883023546.

Notes

The authors declare no competing financial interest.

ACKNOWLEDGMENTS

This research has been financially supported by the Australian Research Council (ARC) through Discovery Grant funding (DP1092678 and DP120103537). We thank the Australian Institute of Nuclear Science and Engineering (AINSE) for their support in carrying out the SAXS work. We thank Dr Emma Parkinson-Lawrence, School of Pharmacy and Medical Sciences, University of South Australia for assistance with the SDS-PAGE experiments.

REFERENCES

(1) Elvin, C. M.; Carr, A. G.; Huson, M. G.; Maxwell, J. M.; Pearson, R. D.; Vuocolo, T.; Liyou, N. E.; Wong, D. C. C.; Merritt, D. J.; Dixon, N. E. Synthesis and properties of crosslinked recombinant pro-resilin. *Nature* **2005**, *437*, 999−1002.

(2) Dutta, N. K.; Truong, M. Y.; Mayavan, S.; Roy Choudhury, N.; Elvin, C. M.; Kim, M.; Knott, R.; Nairn, K. M.; Hill, A. J. A Genetically Engineered Protein Responsive to Multiple Stimuli. *Angew. Chem., Int. Ed.* **2011**, *50*, 4428−4431.

(3) Cordeiro, A. L. Stimuli-Responsive Polymer Nanocoatings. In *Nanotechnologies for the Life Sciences*; Wiley Interscience: New York, 2007.

(4) Löwik, D. W. P. M.; Leunissen, E. H. P.; van den Heuvel, M.; Hansen, M. B.; van Hest, J. C. M. Stimulus responsive peptide based materials. *Chem. Soc. Rev.* **2010**, *39* (9), 3394−3412.

(5) Kozanoglu, S.; Ozdemir, T.; Usanmaz, A. Polymerization of N-Vinylcaprolactam and Characterization of Poly(N-Vinylcaprolactam). *J. Macromol. Sci., Part A: Pure Appl.Chem.* **2011**, *48*, 467−477.

(6) Urry, D. W.; Luan, C. H.; Parker, T. M.; Gowda, D. C.; Prasad, K. U.; Reid, M. C.; Safavy, A. Temperature of polypeptide inverse temperature transition depends on mean residue hydrophobicity. *J. Am. Chem. Soc.* **1991**, *113*, 4346−4348.

(7) Fernandez-Trillo, F.; van Hest, J. C. M.; Thies, J. C.; Michon, T.; Weberskirch, R.; Cameron, N. R. Fine-tuning the transition temperature of a stimuli-responsive polymer by a simple blending procedure. *Chem. Commun.* **2008**, 2230−2232.

(8) Ge, X.; Hoare, T.; Filipe, C. D. M. Protein-based aqueous-multiphasic systems. *Langmuir* **2010**, *26*, 4087.

(9) Truong, M. Y.; Dutta, N. K.; Choudhury, N. R.; Kim, M.; Elvin, C. M.; Nairn, K. M.; Hill, A. J. The effect of hydration on molecular chain mobility and the viscoelastic behaviour of resilin-mimetic protein-based hydrogels. *Biomaterials* **2011**, *32*, 8462−8473.
(10) Yoon, Y.-R.; Lim, Y.-b.; Lee, E.; Lee, M. Self-assembly of a peptide rod-coil: a polyproline rod and a cell-penetrating peptide Tat coil. *Chem. Commun.* **2008**, 1892−1894.
(11) Tooke, L.; Duitch, L.; Measey, T. J.; Schweitzer-Stenner, R. Kinetics of the self-aggregation and film formation of poly-L-proline at high temperatures explored by circular dichroism spectroscopy. *Biopolymers* **2010**, *93*, 451−457.
(12) Creasey, R. G.; Voelcker, N. H.; Schultz, C. J. Investigation of self-assembling proline- and glycine-rich recombinant proteins and peptides inspired by proteins from a symbiotic fungus using atomic force microscopy and circular dichroism spectroscopy. *Biochim. Biophys. Acta, Proteins Proteomics* **2012**, *1824*, 711.
(13) Lorusso, M.; Pepe, A.; Ibris, N.; Bochicchio, B. Molecular and supramolecular studies on polyglycine and poly-l-proline. *Soft Matter* **2011**, *7*, 6327−6336.
(14) Xia, X.-X.; Xu, Q.; Hu, X.; Qin, G.; Kaplan, D. L. Tunable Self-Assembly of Genetically Engineered Silk−Elastin-like Protein Polymers. *Biomacromolecules* **2011**, *12*, 3844−3850.
(15) Kim, M.; Elvin, C.; Brownlee, A.; Lyons, R. High yield expression of recombinant pro-resilin: Lactose-induced fermentation in E. coli and facile purification. *Protein Expression Purif.* **2007**, *52*, 230−236.
(16) Wang, H.-Y.; Zhang, Y.-Q. Effect of regeneration of liquid silk fibroin on its structure and characterization. *Soft Matter* **2013**, *9*, 138−145.
(17) Vasconcelos, A.; Freddi, G.; Cavaco-Paulo, A. Biodegradable Materials Based on Silk Fibroin and Keratin. *Biomacromolecules* **2008**, *9*, 1299−1305.
(18) Kyte, J.; Doolittle, R. F. A simple method for displaying the hydropathic character of a protein. *J. Mol. Biol.* **1982**, *157*, 105−132.
(19) Pedersen, J. A flux- and background-optimized version of the NanoSTAR small-angle X-ray scattering camera for solution scattering. *J. Appl. Crystallogr.* **2004**, *37*, 369−380.
(20) Kline, S. Reduction and analysis of SANS and USANS data using IGOR Pro. *J. Appl. Crystallogr.* **2006**, *39*, 895−900.
(21) Tamburro, A. M.; Panariello, S.; Santopietro, V.; Bracalello, A.; Bochicchio, B.; Pepe, A. Molecular and Supramolecular Structural Studies on Significant Repetitive Sequences of Resilin. *ChemBioChem* **2010**, *11*, 83−93.
(22) Lyons, R. E.; Nairn, K. M.; Huson, M. G.; Kim, M.; Dumsday, G.; Elvin, C. M. Comparisons of Recombinant Resilin-like Proteins: Repetitive Domains Are Sufficient to Confer Resilin-like Properties. *Biomacromolecules* **2009**, *10*, 3009−3014.
(23) Bochicchio, B.; Tamburro, A. M. Polyproline II structure in proteins: Identification by chiroptical spectroscopies, stability, and functions. *Chirality* **2002**, *14*, 782−792.
(24) Mansiaux, Y.; Joseph, A. P.; Gelly, J.-C.; de Brevern, A. G. Assignment of PolyProline II conformation and analysis of sequence−structure relationship. *PLoS One* **2011**, *6*, e18401.
(25) Adzhubei, A. A.; Sternberg, M. J. E.; Makarov, A. A. Polyproline-II Helix in Proteins: Structure and Function. *J. Mol. Biol.* **2013**, *425*, 2100−2132.
(26) Dutta, N. K.; Choudhury, N. R.; Truong, M. Y.; Kim, M.; Elvin, C. M.; Hill, A. J. Physical approaches for fabrication of organized nanostructure of resilin-mimetic elastic protein rec1-resilin. *Biomaterials* **2009**, *30*, 4868−4876.
(27) Chen, P.; Kim, H.; Park, C.-Y.; Kim, H.-S.; Chin, I.-J.; Jin, H.-J. pH-Triggered transition of silk fibroin from spherical micelles to nanofibrils in water. *Macromol. Res.* **2008**, *16*, 539−543.
(28) Lu, Q.; Zhu, H.; Zhang, C.; Zhang, F.; Zhang, B.; Kaplan, D. L. Silk self-assembly mechanisms and control from thermodynamics to kinetics. *Biomacromolecules* **2012**, *13*, 826−832.
(29) Jin, H.-J.; Kaplan, D. L. Mechanism of silk processing in insects and spiders. *Nature* **2003**, *424*, 1057−1061.
(30) Matsumoto, A.; Chen, J.; Collette, A. L.; Kim, U.-J.; Altman, G. H.; Cebe, P.; Kaplan, D. L. Mechanisms of silk fibroin sol-gel transitions. *J. Phys. Chem. B* **2006**, *110*, 21630.
(31) Lin, Y.; Xia, X.; Wang, M.; Wang, Q.; An, B.; Tao, H.; Xu, Q.; Omenetto, F.; Kaplan, D. L. Genetically Programmable Thermoresponsive Plasmonic Gold/Silk-Elastin Protein Core/Shell Nanoparticles. *Langmuir* **2014**, *30*, 4406−4414.
(32) Schneider, J. P.; Pochan, D. J.; Ozbas, B.; Rajagopal, K.; Pakstis, L.; Kretsinger, J. Responsive Hydrogels from the Intramolecular Folding and Self-Assembly of a Designed Peptide. *J. Am. Chem. Soc.* **2002**, *124*, 15030−15037.
(33) Shulha, H.; Po Foo, C. W.; Kaplan, D. L.; Tsukruk, V. V. Unfolding the multi-length scale domain structure of silk fibroin protein. *Polymer* **2006**, *47*, 5821−5830.
(34) Nairn, K. M.; Lyons, R. E.; Mulder, R. J.; Mudie, S. T.; Cookson, D. J.; Lesieur, E.; Kim, M.; Lau, D.; Scholes, F. H.; Elvin, C. M. A synthetic resilin is largely unstructured. *Biophys. J.* **2008**, *95*, 3358−3365.
(35) Balu, R.; Knott, R.; Cowieson, N. P.; Elvin, C. M.; Hill, A. J.; Choudhury, N. R.; Dutta, N. K. Structural ensembles reveal intrinsic disorder for the multi-stimuli responsive bio-mimetic protein Rec1-resilin. *Sci. Rep.* **2015**, *5*, 10896.
(36) Hammouda, B. A new Guinier-Porod model. *J. Appl. Crystallogr.* **2010**, *43*, 716−719.
(37) Greving, L.; Dicko, C.; Terry, A.; Callow, P.; Vollrath, F. Small angle neutron scattering of native and reconstituted silk fibroin. *Soft Matter* **2010**, *6*, 4389−4395.
(38) Rössle, M.; Panine, P.; Urban, V. S.; Riekel, C. Structural evolution of regenerated silk fibroin under shear: Combined wide- and small-angle x-ray scattering experiments using synchrotron radiation. *Biopolymers* **2004**, *74*, 316−327.
(39) Receveur-Bréchot, V.; Durand, D. How Random are Intrinsically Disordered Proteins? A Small Angle Scattering Perspective. *Curr. Protein Pept. Sci.* **2012**, *13*, 55−75.
(40) Hammouda, B. Probing Nanoscale Structures - The SANS Toolbox, 2012. http://www.ncnr.nist.gov/staff/hammouda/the_SANS_toolbox.pdf (accessed 10 January 2015).

DOI: 10.1021/acs.langmuir.5b01014
Langmuir 2015, 31, 8882−8891

3.2 Supplementary information

S3.2.1 Consensus sequence of Rec1-resilin

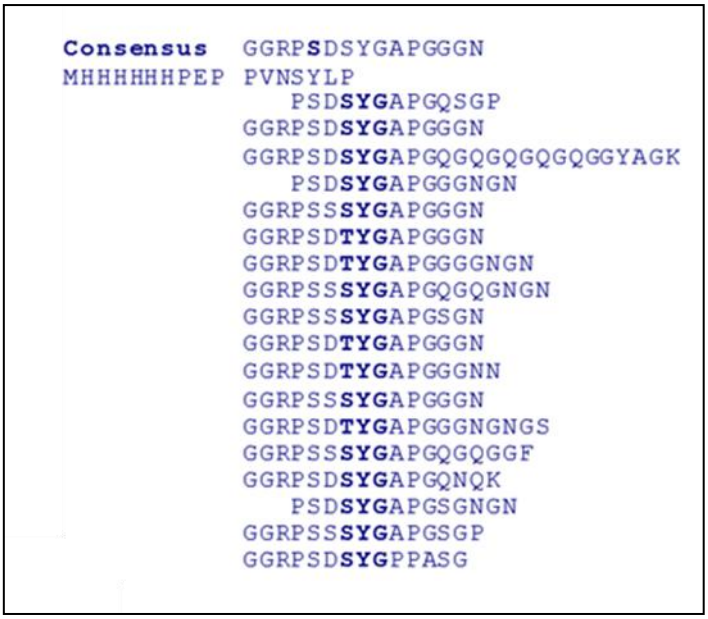


Figure S3.1 Structural consensus and alignment of amino acid repeat sequence in Rec1-resilin. Single-letter code is used.

S3.2.2 NMR analysis of RSF

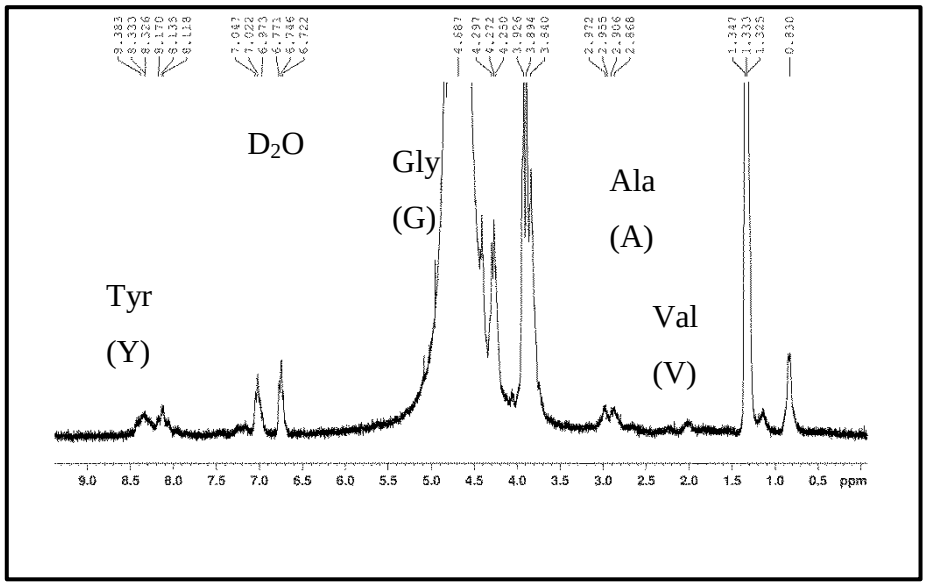


Figure S3.2 NMR spectra of RSF in D_2O.

S3.2.3 SDS-PAGE

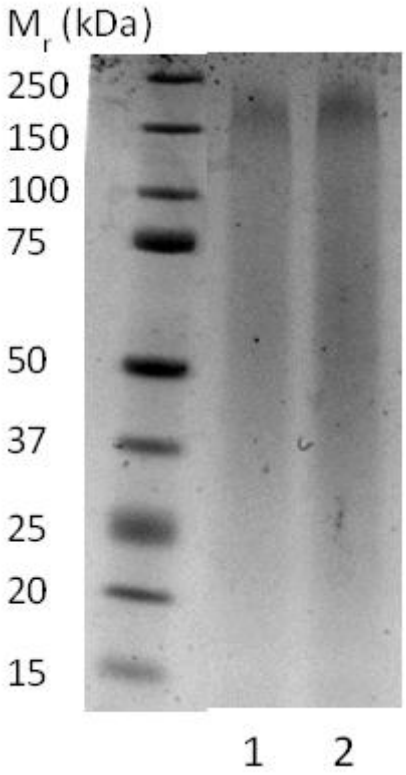


Figure S3.3 SDS-page of freeze dried silk fibroin (BMWS) lanes 1 and 2, and regenerated silk fibroin (RSF) lanes 3 and 4.

S3.2.4 Dynamic light scattering (DLS)

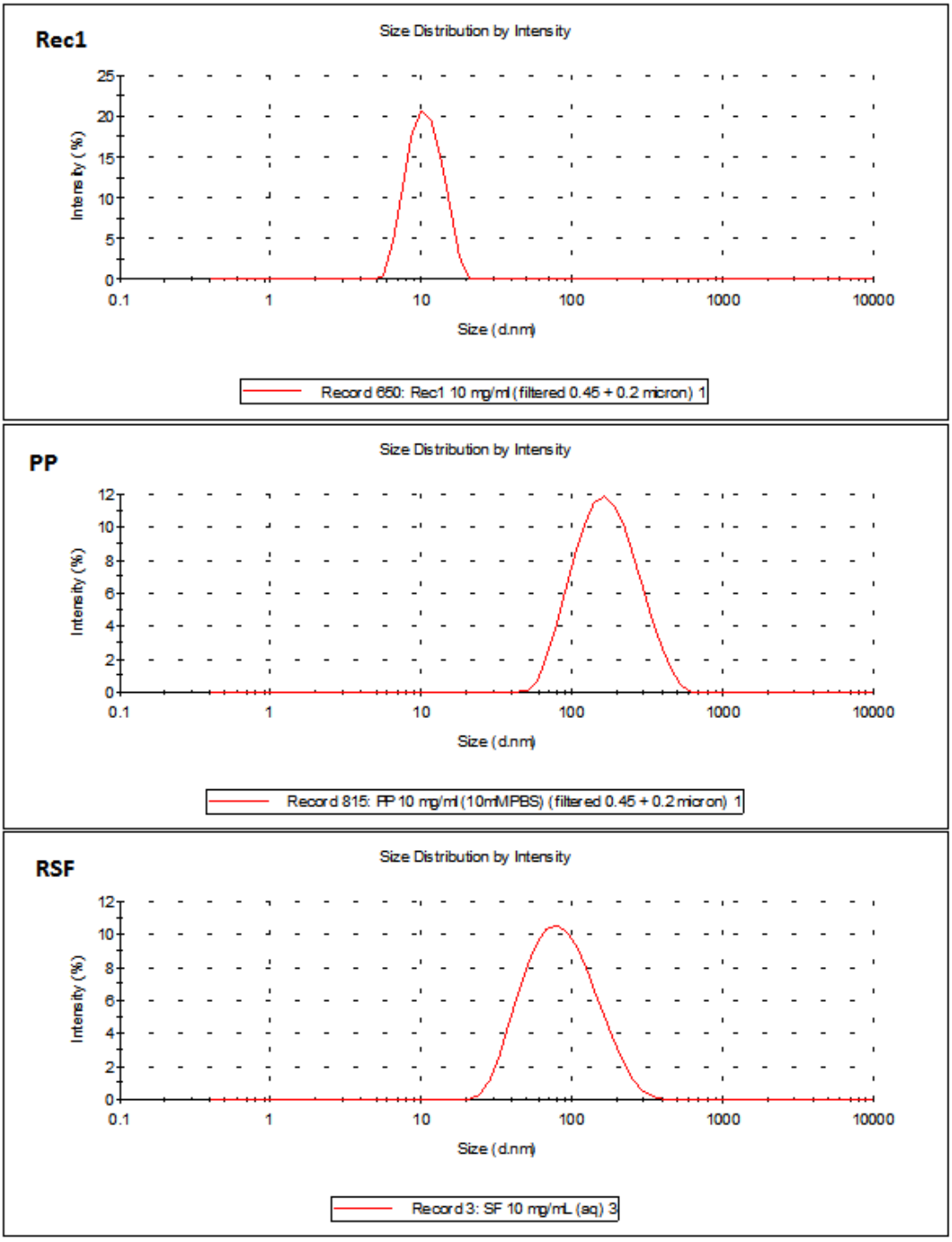


Figure S3.4 Size distribution curves from DLS measurements of Rec1, PP and RSF at 10 mg/mL and 25˚C.

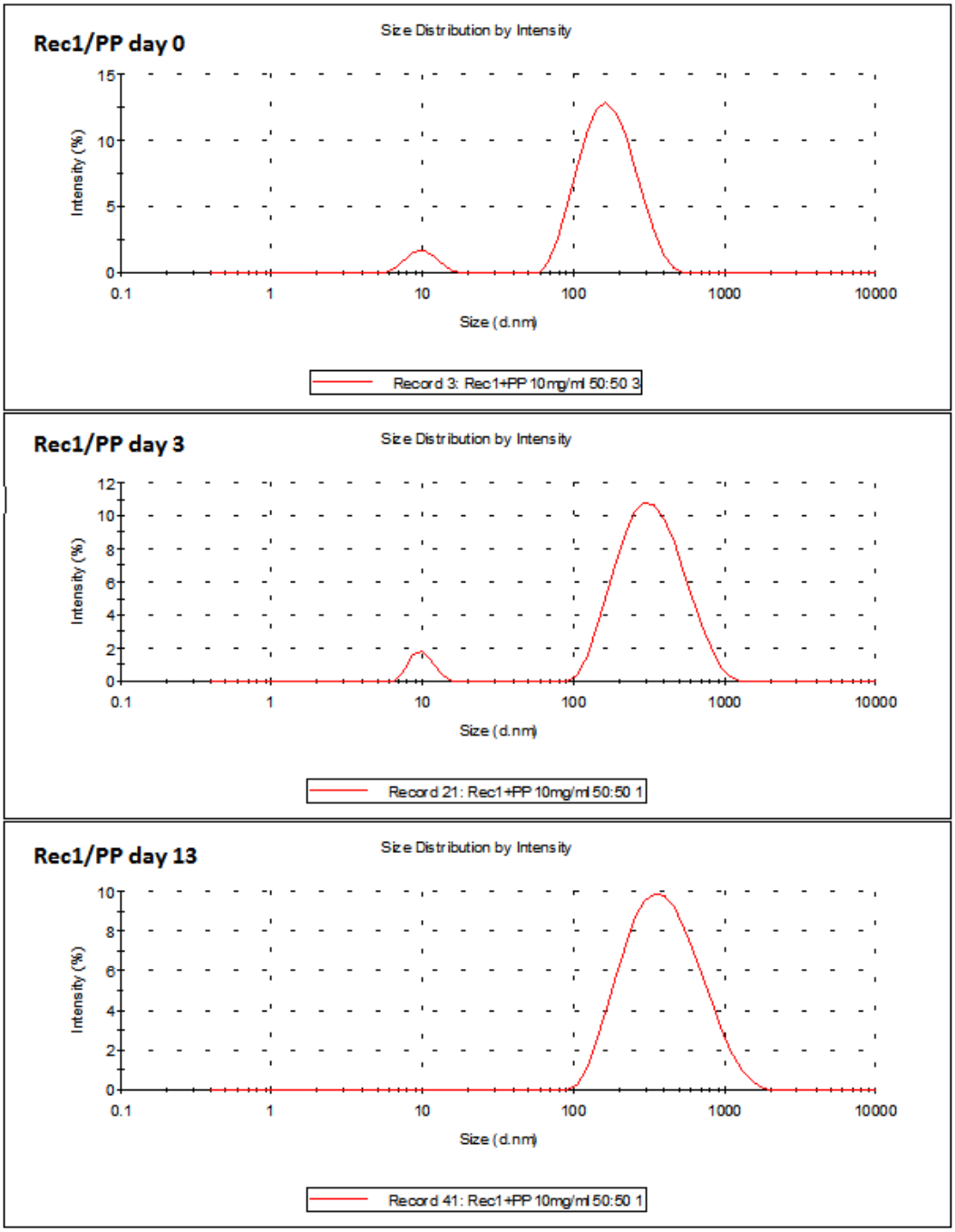


Figure S3.5 Size distribution curves from DLS measurements of Rec1/PP co-assembly (10 mg/mL) at day 0, 3 and 13 at 25˚C.

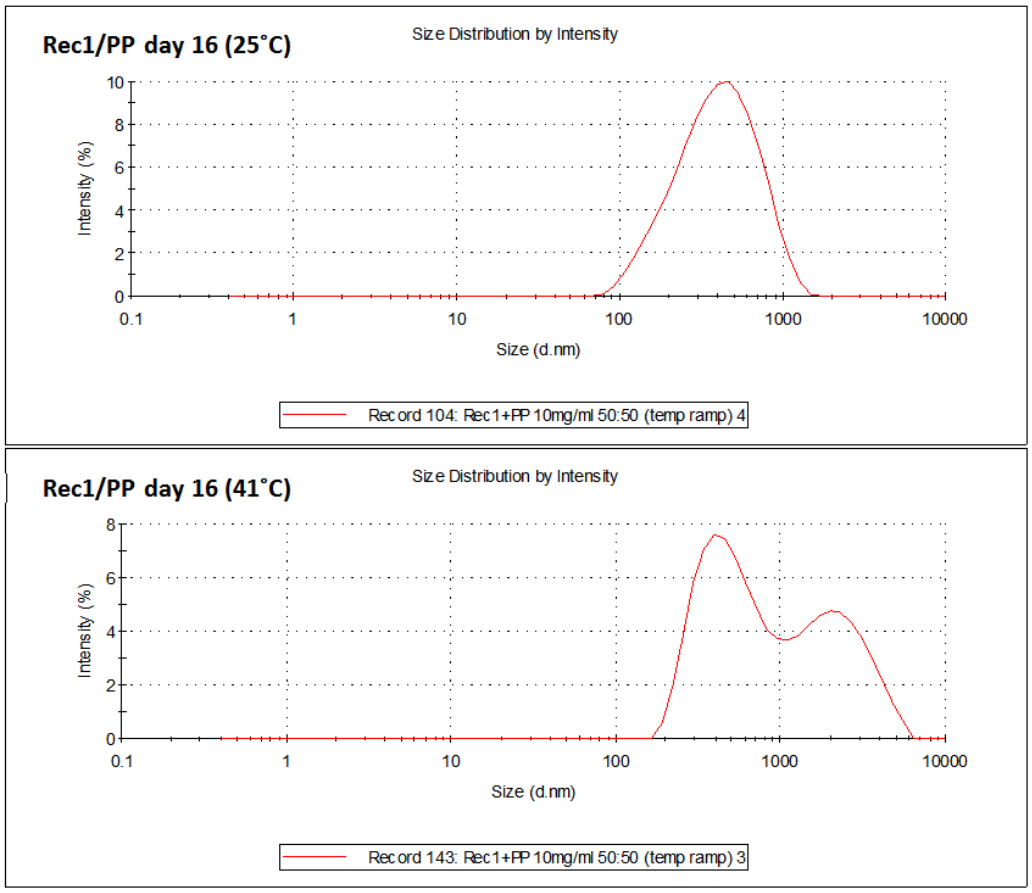


Figure S3.6 Size distribution curves from DLS measurements of Rec1/PP co-assembly (10 mg/mL) after 16 days incubation at 25˚C and 41˚C.

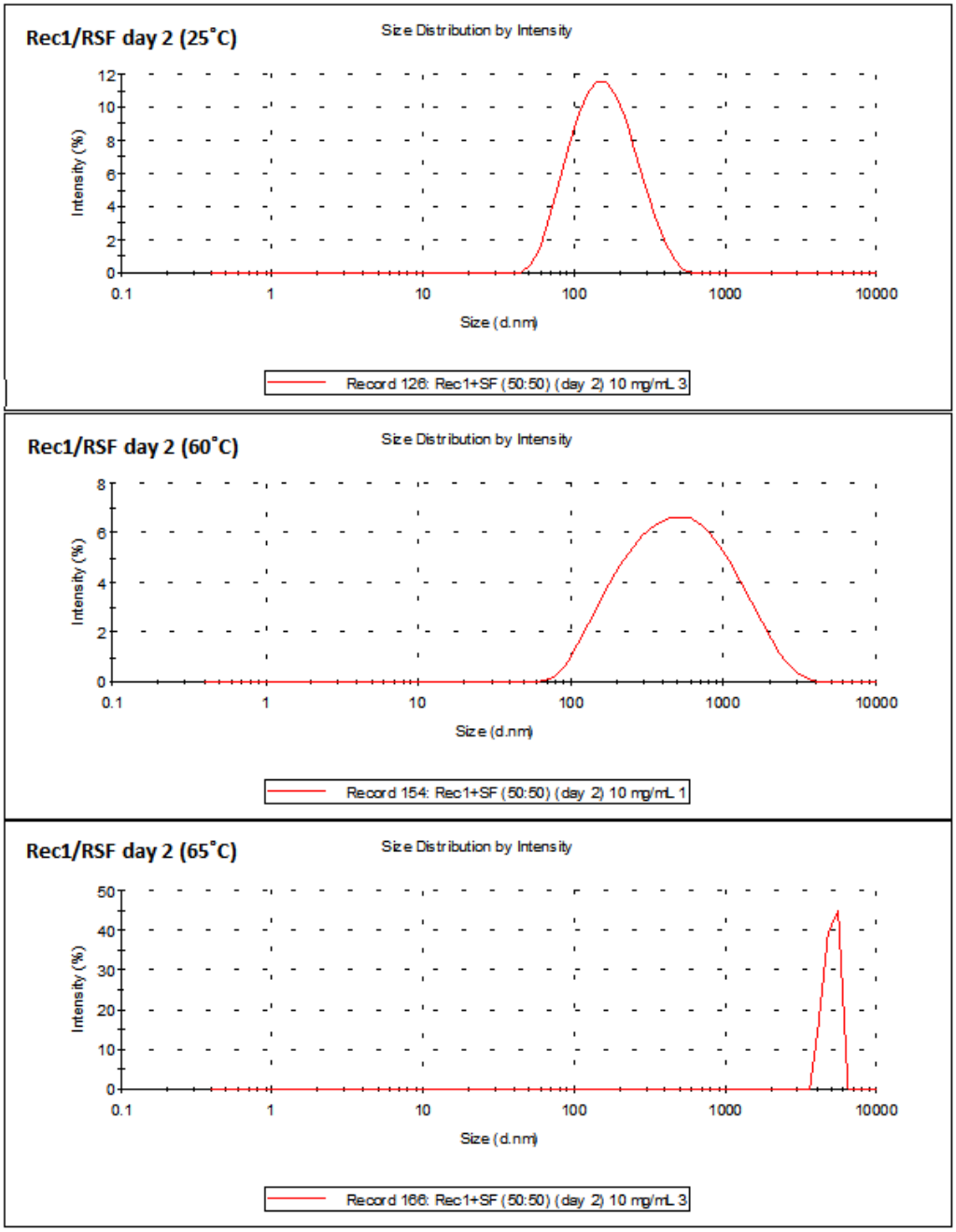
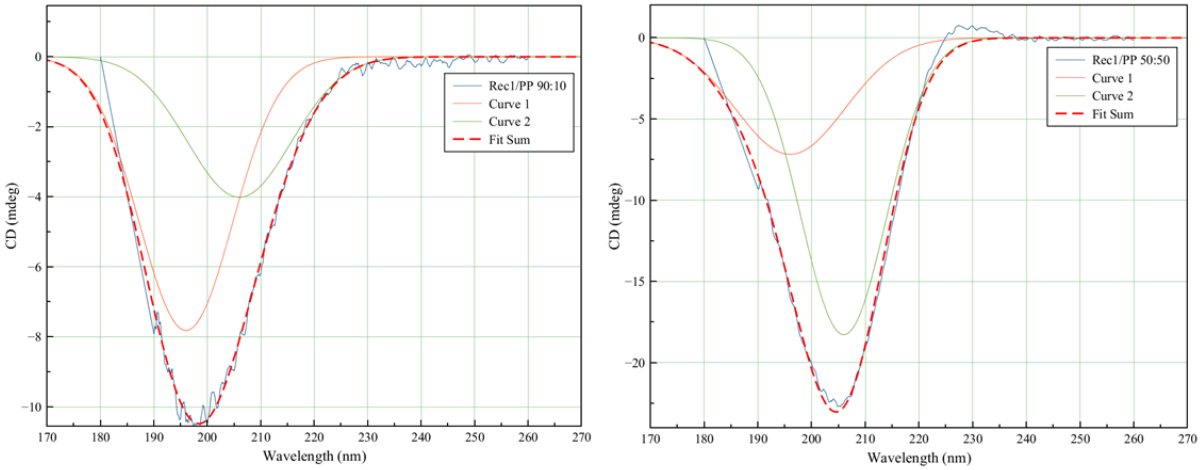


Figure S3.7 Size distribution curves from DLS measurements of Rec1/RSF co-assembly (10 mg/mL) on day 2 at 25˚C, 60 and 65˚C.

S3.2.5 Circular dichroism (CD) fitting

Curve deconvolution of the CD spectra to examine the structural changes through addition of PP and was conducted using the MagicPlot software. Gaussian curve fitting was applied to the curves with the peaks fixed at 196 nm for Rec1, which exhibits a predominantly unordered conformation, and 206 nm for PP, which exhibits a PPII conformation. Figure S3.8 depicts two of the fit curves generated, with the % contributions due to Rec1 and PP shown in the table. It was observed that the proportion of PPII structure increased compared to the PP content in the co-assembly. This indicates that the addition of PP is driving the structural changes of the Rec1/PP co-assembly to an increasing PPII helical conformation.

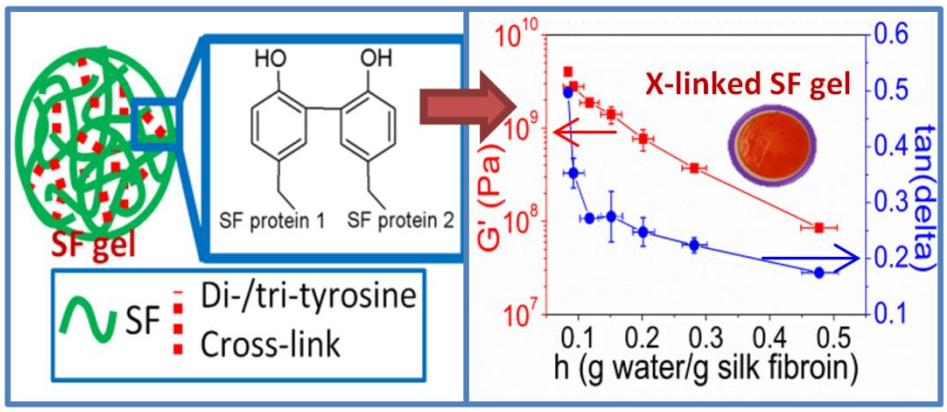


Sample	Rec1-resilin unordered (196 nm) % contribution	PPII helical (206 nm) % contribution
Rec1/PP 90:10	64	36
Rec1/PP 80:20	54	46
Rec1/PP 70:30	46	54
Rec1/PP 60:40	39	61
Rec1/PP 50:50	34	66

Figure S3.8 Example CD fit curves for Rec1/PP 90:10 and 50:50 co-assemblies. % contribution of unordered and PPII structures determined through curve fitting.

Chapter 4: Facile and rapid ruthenium mediated photo-crosslinking of Bombyx mori silk fibroin

This chapter of the thesis is presented as a research article "Jasmin L. Whittaker, Namita R. Choudhury, Naba K. Dutta and Andrew Zannettino. Facile and rapid ruthenium mediated photo-crosslinking of *Bombyx mori* silk fibroin. Journal of Materials Chemistry B, 2014, 2, 6259-6270", published and reproduced by permission of the Royal Society of Chemistry, Copyright 2014.



4.1 Research Article

Journal of Materials Chemistry B

PAPER

View Article Online
View Journal | View Issue

Facile and rapid ruthenium mediated photo-crosslinking of *Bombyx mori* silk fibroin†

Jasmin L. Whittaker,[a] Namita R. Choudhury,*[a] Naba K. Dutta*[a] and Andrew Zannettino[b]

Cite this: *J. Mater. Chem. B*, 2014, **2**, 6259

Received 2nd May 2014
Accepted 17th June 2014

DOI: 10.1039/c4tb00698d

www.rsc.org/MaterialsB

A facile and rapid ruthenium catalysed photo-crosslinking method was employed to prepare *Bombyx mori* silk fibroin hydrogels for the first time that may be used for biomedical applications. The gels have been characterised by differential scanning calorimetry (DSC), dynamic mechanical analysis (DMA), photo-acoustic Fourier transform infrared spectroscopy (PA-FTIR), and X-ray diffraction (XRD). We have reported the tuning of the properties of the chemically crosslinked gels through hydration level. DSC and DMA measurements have shown that the molecular chain dynamics and mechanical properties are dependent on the moisture/water content. The structural changes upon gelation were examined through the use of DSC, PA-FTIR and XRD, which confirmed that the gels were less crystalline than the original silk powder. Finally, the biocompatibility and hence, the potential tissue engineering application of the silk fibroin hydrogel was also assessed by culturing chondrocyte progenitor cells for up to one week on the engineered fibroin surfaces.

Introduction

Hydrogels are three-dimensional, insoluble structures composed of physically or chemically crosslinked materials and find applications in the field of regenerative medicine/tissue engineering.[1] The design requirements for scaffolds are extensive and include biocompatibility, mechanical integrity, controlled degradability, cell signaling, *etc.* Also, tissue stiffness plays a central role in the adhesion and cytoskeletal organisation by acting as an informational template to the cells. Therefore, it is important to engineer the environment of the scaffolds by tuning their properties. One method to enhance the strength of gels is through crosslinking. A number of different natural and synthetic polymers, including collagen, elastin, poly(acrylic acid) (PAA), and poly(vinyl alcohol) (PVA), among many others, have been used to form hydrogels. Due to its superior strength, biocompatibility, biodegradability, and good oxygen and water vapour permeability, *Bombyx mori* (*B. mori*) silk fibroin has excellent potential for biomedical materials development.[2,3] In addition, the processing methods related to silk fibroin are flexible in that an aqueous or organic solvent may be used.[4] As a result, silk fibroin has been investigated with regard to applications for tissue engineered blood vessels, skin, bone, and cartilage.[5]

In order to improve the strength, *B. mori* silk fibroin has been crosslinked *via* a number of methods in recent years. Physically crosslinked silk fibroin hydrogels have been produced through the induction of the beta-sheet structure in silk fibroin solutions.[6] A number of different parameters can result in the sol–gel transition of silk fibroin through the formation of beta-sheet stabilised structures. These have been studied extensively and include: shearing, water evaporation, heating, solvent exposure, low pH, high ionic strength, and electric current.[6–10] Chemically crosslinked silk fibroin hydrogels have also been studied, however to a lesser extent. Vasconcelos *et al.* employed the natural covalent crosslinking agent genipin to form solid structures.[11] In a study by Xiao *et al.*, silk fibroin was crosslinked by first performing ultrasonication to induce gelation through beta-sheet formation.[12] Following this, the silk was chemically crosslinked using genipin. The advantage of using a natural crosslinking agent such as genipin is reduced cytotoxicity when compared to synthetic crosslinkers, such as glutaraldehyde.[11] However, the use of genipin as a crosslinker is time consuming and requires 6 hours to achieve maximum crosslinking.[11] This is due to the fact that it has been reported that genipin reacts mainly with lysine and arginine in protein structures.[13] The lysine and arginine amino acids make up a low percentage of the total silk fibroin composition with approximately 0.6 mol% for each.[13] The enzymatic covalent crosslinking of silk fibroin using tyrosinase was reported by Kang *et al.*[14] This reaction was

[a]*Ian Wark Research Institute, University of South Australia, Mawson Lakes, Adelaide, SA 5095, Australia. E-mail: namita.choudhury@unisa.edu.au; naba.dutta@unisa.edu.au; Tel: +61883023719; +61883023546*

[b]*Myeloma Research Laboratory, School of Medical Sciences, University of Adelaide, Adelaide, SA, Australia*

† Electronic supplementary information (ESI) available: This includes the NMR data confirming the identity of the silk powder, the full crosslinking reaction schematic, fluorescence and UV-vis spectra of the gels, and the determination of the minimum $Ru(II)(bpy)_3^{2+}$ concentration required for crosslinking. See DOI: 10.1039/c4tb00698d

also time consuming, with approximately 20 hours required.[14] Therefore, it would be extremely important and useful to identify a facile and rapid crosslinking method to develop chemically crosslinked silk fibroin gels.

In our earlier work, a recombinant form of the elastic protein resilin, rec1-resilin, was photo-dynamically crosslinked using tris(2,2′-bipyridyl)dichlororuthenium(II) as the catalyst and ammonium peroxodisulfate as the electron acceptor.[15] In this method, the tyrosine residues in the protein structure were employed to form di-tyrosine crosslinks. Stable rec1-resilin gels with tuneable crosslink densities and mechanical properties were achieved. Recently, Schacht and Scheibel have used this method to photo-chemically crosslink a recombinant spider silk protein.[16] *B. mori* silk fibroin contains 4.98 mol% of tyrosine in its overall structure, which is slightly less than that of the recombinant resilin protein.[17] Therefore, it is hypothesised that this method will provide a rapid and simple process for crosslinking of *B. mori* silk fibroin.[4] Successful achievement in the processing of *B. mori* silk fibroin gels *via* this method would increase its uses in a range of applications and provide opportunities for conjugation with other materials. It has been confirmed that ruthenium and APS concentrations used for this method of crosslinking are not cytotoxic and thus this method could be employed for *in situ* crosslinking through a photodynamic approach, increasing its uses for different applications.[18]

In this study, silk fibroin solutions were photo-dynamically crosslinked to form gels through covalent interactions between tyrosine residues. The physical properties, including crosslink density, of these gels were determined using water uptake studies. The structural characteristics of the gels were investigated using Fourier transform infrared (FTIR) spectroscopy and differential scanning calorimetry (DSC). The mechanical properties of the gels were studied under different humidity levels using dynamic mechanical analysis (DMA). Finally, the biocompatibility of the silk fibroin hydrogels was demonstrated through cell culture studies using a pre-chondrocyte cell line, ATDC5. This method provides a basis for simple crosslinking of silk fibroin for the creation of more complex biomaterials with tuneable moduli through chemical crosslinking with other systems.

Experimental

Silk fibroin

Bombyx mori silk was purchased as raw silk from Beautiful Silks, Australia from which silk fibroin was regenerated. Also, water-soluble (BMWS) freeze dried regenerated silk fibroin powder was given by Dr Anja Glisovic, Germany. The structural components of the silk fibroin from the raw silk and BMWS powder have been confirmed through nuclear magnetic resonance (NMR) (ESI S1†).

Solution preparation

The raw silk was degummed by boiling in aqueous 0.02 M Na_2CO_3 for 30 minutes. The silk was rinsed with distilled water three times and allowed to dry at room temperature overnight. The fibroin was then dissolved in a calcium chloride–water–ethanol solution ($CaCl_2$–H_2O–EtOH 1/8/2 molar ratio), with a liquor ratio of 1 : 10, at 70 °C for 24 hours. Following this, the solution was cooled and filtered using a non-sterile pre-filter (Minisart-GF 17824) with a pore size of approximately 1.2 microns. The concentration of the silk fibroin in the solution was determined to be approximately 140 mg mL ^{1}.

Solutions of BMWS silk fibroin of varying concentrations were prepared by slowly adding the silk fibroin powder to distilled water (DW) whilst sonicating (Table 1). Sonication was conducted for less than one hour to prevent beta-sheet formation. The solution was filtered using a non-sterile pre-filter (Minisart-GF 17824) with a pore size of approximately 1.2 microns.

All silk fibroin solutions were stored at 4 °C to prevent silk fibroin gelation.

Photochemical crosslinking

Table 1 shows the various compositions that are used for photochemical crosslinking of regenerated silk solution and solution made from BMWS at different concentrations. An aqueous silk fibroin solution was photo-chemically crosslinked to form a gel, using tris(2,2-bipyridyl) dichloro ruthenium(II) hexahydrate ($Ru(II)(bpy)_3^{2+}$) as the catalyst and ammonium persulphate (APS) as the electron acceptor (see Fig. S2† for full reaction schematic). Predefined amounts of $Ru(II)(bpy)_3^{2+}$, APS, and silk fibroin solution were mixed, whilst preventing exposure to light (Table 1). The solutions were then transferred to a Teflon mould and exposed to a 250 W light source for 120 seconds, and then the gels were turned over and exposed to the light source for a further 60 seconds to ensure full crosslinking of the sample (Fig. 1). The mass of the crosslinked gel was measured and the gel was subsequently immersed in distilled water (DW) for several days to remove the un-reacted material. The water was changed daily. Samples were prepared in duplicate. The gels were dried for three days in the fume hood at room temperature and subsequently for 3 hours in the vacuum oven at 40 °C to a constant weight. The dry weight (w_d) and dimensions of the gels were measured using digital callipers. The BMWS dry and swollen gels were further examined by spectroscopic, thermal and X-ray analyses.

Water and water vapour uptake studies

For water uptake studies, the gels were immersed in DW and the weight was taken at different time intervals to monitor the water uptake and determine the equilibrium swelling weight (w_s). Vapour sorption experiments were conducted by placing the gels in a controlled humidity chamber (ESPEC, SH-241 temperature & humidity chamber, Espec Corp., Japan) under specific conditions including temperature and percent relative humidity (%RH). The weight of the samples was monitored at different time intervals using an accurate microbalance capable of measuring four decimal places. The swelling ratio (Q) and water uptake (h) for the bulk water and water vapour uptake studies were determined using the eqn (1) and (2).

This journal is © The Royal Society of Chemistry 2014

Table 1 Water uptake and crosslink density values of gels under different conditions

Sample	Silk fibroin (mg mL^{-1})	Ru(II)(bpy)$_3^{2+}$ (mM)	Molar ratio Ru(II)(bpy)$_3^{2+}$: APS	Q (swelling ratio)	h (water uptake)	$v_e \times 10^{-3}$ (mol cm^{-3})
Ru0.16APS20	300	0.16	1 : 125	1.64	0.638	0.374
Ru0.5APS20	300	0.5	1 : 40	1.54	0.538	0.380
Ru1APS20	300	1	1 : 20	1.59	0.592	0.377
Ru5APS20	300	5	1 : 4	1.57	0.574	0.378
Ru10APS20	300	10	1 : 2	1.59	0.589	0.377
Ru5APS28	300	5	1 : 5.6	1.60	0.599	0.376
Regenerated SF solution	140	5	1 : 5.6	1.64	0.636	0.374
Ru5APS100	300	5	1 : 20	1.59	0.587	0.377
BMWS150	150	5	1 : 5.6	1.61	0.606	0.376

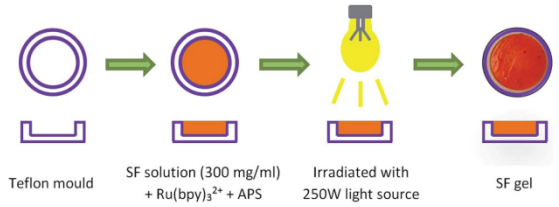


Fig. 1 Method for photodynamic crosslinking of *B. mori* silk fibroin.

$$Q = \frac{w_s}{w_d} \quad (1)$$

$$h = \frac{w_s - w_d}{w_d} \quad (2)$$

where, w_s is the weight of the swollen silk fibroin gel at varying time intervals and conditions, and w_d is the dry weight of the crosslinked silk fibroin gel.

Determination of crosslink density of silk fibroin gels

The crosslink densities of the gels were determined through equilibrium swelling experiments conducted in DW at room temperature. After drying, the gels were immersed in DW and the weight of the gel was monitored until the equilibrium weight ($w_{T,s}$) was reached. The crosslink density of the silk gel samples was calculated using eqn (3) and (4).[15] The Flory–Huggins interaction parameter (χ) between silk fibroin and water was taken as 0.95.[19] The densities of the dry silk fibroin gel (ρ_P) and water at room temperature (ρ_2) are 1.421 g cm^{-3} and 0.997 g cm^{-3}, respectively.[15,20] The molar volume of water (V_2) is 18 cm^3 mol^{-1}.[15]

$$v_{1,s} = \frac{w_p/\rho_p}{\frac{w_{T,s} - w_p}{\rho_2} + w_p/\rho_p} \quad (3)$$

$$v_e = \frac{\rho_p}{M_c} = \frac{-\ln(1 - v_{1,s}) + v_{1,s} + \chi v_{1,s}}{V_2\left(v_{1,s} - \frac{1}{2}v_{1,s}\right)} \quad (4)$$

Porosity of the hydrogel from scanning electron microscopy (SEM)

The internal microstructure of the representative Ru5APS28 hydrogels was analysed using Environmental SEM (ESEM) with the Quanta FEG 450, FEI. The gels were immersed in DW until equilibrium swelling was reached. The hydrogels were cut to expose cross-sections and were examined using ESEM mode under an accelerating voltage of 30 kV. The ESEM experiments were conducted with a pressure of 900 Pa, temperature of 2 °C, and at 100% humidity. The pore size and distribution were examined using the Image J software.

Glass transition behaviour of gel by differential scanning calorimetry (DSC)

DSC measurements of the representative Ru5APS28 (Table 1) gel prepared from BMWS silk fibroin powder were conducted using the TA Instruments Discovery DSC. The instrument was calibrated for baseline and cell constant prior to running the experiments. The samples were sealed in hermetic aluminium pans for use in the DSC experiment, and an empty pan was used as the reference. The temperature range of the experiment was from −80 °C to 300 °C, with a heating rate of 10 °C min^{-1} and under a controlled nitrogen gas flow rate of 50 mL min^{-1}.

Mechanical properties of the silk fibroin gels by dynamic mechanical analysis

DMA was conducted on the Ru5APS28 sample using the TA Instruments Q800 DMA equipped with a humidity accessory. The storage and loss moduli of the sample were determined under controlled humidity. The samples of rectangular geometry were immersed in DW initially for 24 hours to reach equilibrium water uptake before clamping. Then the samples were mounted using the tension clamp and run at ambient temperature with an amplitude of 10 μm and a preload force of 0.010 N. The DMA run was conducted with the humidity ramped to 50% and held for the duration of an hour with isothermal temperature. The sample weight was measured at the beginning and end of each run to determine the water content, which changed over time as the sample dried. This was conducted for six consecutive runs as the sample continued to dry. The sample weights were correlated with the measured modulus values.

Structural analysis of silk fibroin gels

In order to investigate the chemical structure, infrared spectra of the silk fibroin powder, film, and representative gel were acquired using Nicolet Magna-IR Spectrometer 750 in photoacoustic mode using a carbon black reference. The spectra were obtained in the range 400 to 4000 cm^{-1} and the data was processed *via* the Omnic computer program. The amide I region was selected for investigation as it is commonly used to elucidate the secondary structure components of silk fibroin as it corresponds to the C=O stretching bonds in the peptide backbone.[21–23] Curve deconvolution of this region was conducted to analyse the secondary structure content of the samples. This was done using the Magic Plot software by applying the Gaussian curve fitting to the amide I region (1600–1700 cm^{-1}).

X-ray diffraction (XRD) was also employed to examine the structure of the silk fibroin powder, filtered film, and the Ru5APS28 gel from filtered solution. The experiments were performed with an X-ray diffractometer (Scintag/Thermo-electron ARL X'Tra XRD) using copper Kα radiation (1.542 Å). An X-Ray tube was run at 40 kV, 30 mA. Scans were performed from 5 to 90° 2Θ in steps of 0.02° at a rate of 1.2° per min (1 second count per data point).

Assessment of ATDC5 cell adhesion and proliferation

The ability of the swollen hydrogel (Ru5APS28) to support adhesion and proliferation of ATDC5 pre-chondrocyte cells (Riken laboratories, Japan) was examined.[24,25] The dried hydrogel discs of 6 mm in diameter were sterilized in 70% ethanol for 2 hours followed by overnight drying. Following this, the gels were swollen in sterile phosphate buffered saline (PBS) to the equilibrium swelling level for cell culture experiments. The sterilized, swollen gels were then transferred to individual wells of a 96 well plate (Corning, USA) in preparation for cell culture. The ATDC5 cell line was culture expanded in Dulbecco's Modified Eagle Medium (DMEM) supplemented with 10% fetal calf serum (FCS) as previously described.[26] Prior to seeding the cells onto the hydrogels and tissue culture plastic (TCP), the cells were detached with 0.05% trypsin, enumerated using a hemocytometer and the cell concentration was adjusted so that each well received 12×10^4 cell per cm^2. After incubation for 3 hours, an inverted light microscope (Olympus) was used to assess initial attachment and adhesion. The cells were incubated overnight, washed with PBS several times to remove non-adherent cells, fixed with paraformaldehyde (4%) solution for 1 hour, washed with PBS, and finally immersed in PBS for imaging. Phase-contrast micrographs were captured on the Nikon Eclipse Ti microscope through a 10× objective and recorded with a Qi1 Monochrome camera. Proliferation of the ATDC5 cells on the Ru5APS28 hydrogel samples was quantified using the WST-1 assay as previously described.[27] Briefly, ATDC5 cells were seeded onto Ru5APS28 hydrogels and TCP controls at a concentration of 3×10^4 cells per cm^2. Cell proliferation was evaluated at day 1, 3, 5 and 7. All experiments were performed in triplicate and the results were presented as mean ± standard deviation (SD). Data were analysed using a Two-way ANOVA with a Sidak's multiple comparisons test. A p-value less than 0.05 was considered statistically significant.

Results and discussion

Photodynamic crosslinking

Photo-chemical crosslinking of *B. mori* silk fibroin with $Ru(II)(bpy)_3^{2+}$ catalyst was conducted using both regenerated silk fibroin solution and solution made from BMWS powder to study the versatility of the method (Table 1). In both cases, the formation of a solid gel structure was observed. The gel was brittle when dry and swelled macroscopically when exposed to aqueous environments. The structure of the gels is shown in Fig. 2a, which shows the photo-induced crosslinking of silk through di-tyrosine links (see Fig. S2† for full reaction mechanism). The nature of the di-tyrosine crosslinks has been confirmed through the fluorescence of an ultraviolet irradiated sample shown in Fig. 2b (see ESI S3† for fluorescence spectra). In addition, tri-tyrosine crosslinks are also possible, but cannot be distinguished from di-tyrosine in the fluorescence spectra. For a successful crosslinking reaction, a silk fibroin concentration of approximately 150 mg mL^{-1} or more was required. At a concentration of 150 mg mL^{-1} of BMWS, the gel was quite fragile and difficult to remove from the mould. In addition, the regenerated SF solution (~140 mg mL^{-1}) also formed a hydrogel; however this was also relatively fragile. Therefore, a concentration of ~300 mg mL^{-1} was deemed to be the optimum concentration for processing. Table 1 shows the conditions of crosslinking of the silk fibroin solution. The concentrations of the catalyst ($Ru(II)(bpy)_3^{2+}$) and electron acceptor (APS) were varied to understand the effect on the crosslink density and also to determine the effect of water swelling on the gel property. A minimum $Ru(II)(bpy)_3^{2+}$ concentration of 0.16 mM was required to obtain a gel that was strong enough to support itself when removed from the mould, however the gel was quite fragile at this low $Ru(II)(bpy)_3^{2+}$ concentration (see ESI S5†). For ease of handling, a $Ru(II)(bpy)_3^{2+}$ concentration of 0.5 mM or greater was required. A sample of silk solution without $Ru(II)(bpy)_3^{2+}$ and APS was exposed to light and no gelation occurred, indicating the requirement of $Ru(II)(bpy)_3^{2+}$ and APS for successful crosslinking. This was also repeated individually with $Ru(II)(bpy)_3^{2+}$ and APS, where no gelation was observed. This observation certainly confirms the tyrosine mediated

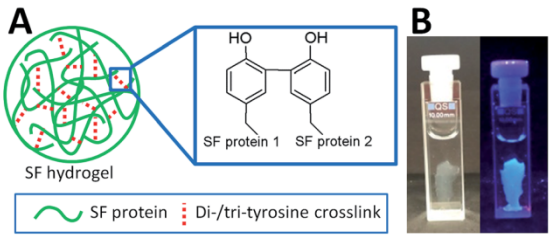


Fig. 2 (A) Schematic of the crosslinked silk fibroin gel showing di-tyrosine crosslink. (B) Photographs of a thin piece of photo-crosslinked silk fibroin under white and ultraviolet light.

This journal is © The Royal Society of Chemistry 2014

photodynamic crosslinking of fibroin solution, which has also been indicated through fluorescence and UV-vis spectroscopy measurements (see ESI S3 and S4†). Fig. 3 shows optical photographs of the various BMWS silk fibroin gels at different stages of processing. The diameter of the gels reduced ~25% after leaching and ~60% of the initial diameter once fully dried. The average dimensions of the gels are also provided in Fig. 3 and did not vary greatly between the different samples. There was a 10- to 12-fold decrease in the mass of the hydrogels from when they were formed to the dry gels, which was due to the loss of water and the unreacted silk fibroin, Ru(II)$(bpy)_3^{2+}$, and APS.

Water uptake (h) and crosslink density

Various silk gels prepared with different Ru(II)$(bpy)_3^{2+}$ and APS concentrations were investigated through water uptake studies to determine their effects on the crosslink density of the gels (Table 1). The equilibrium water uptake (h) value is a common measurement used to study the properties of proteins. In water immersion–sorption studies this value can be related to the crosslink density in that a lower absorption value is related to a highly crosslinked sample as it exists as a denser network. The values for the equilibrium water uptake of the BMWS gels were determined and varied minimally from 0.538 to 0.599 for the samples with Ru(II)$(bpy)_3^{2+}$ concentration greater than 0.5 mM, however the uptake was slightly higher (0.638) for the sample with Ru(II)$(bpy)_3^{2+}$ concentration of 0.16 mM (Table 1). The water uptake curves for the gels were very similar to values close to each other and thus the water uptake of a representative sample (Ru5APS28) over time is shown in Fig. 4A.

A comparison with rec1-resilin shows the level of water uptake to be quite low compared to the equilibrium h values reported for rec1-resilin gels, which were prepared through the same crosslinking method (ranged from approximately 2 to 4.5).[15] When protein gels are immersed in aqueous solutions, the water molecules initially interact with the polar residues followed by filling the voids. The water molecules interacting with the polar groups of the protein are non-crystallisable bound water molecules, whereas once these sites have been occupied, extra water present in the voids is crystallisable water.[15] In rec1-resilin, 46% of the residues are polar, whereas 19% are polar in silk fibroin.[15,17] Therefore, due to the significantly lower proportion of polar residues present in silk fibroin structure, it is not unexpected that the silk fibroin gels took up less water than the rec1-resilin gels.

The equilibrium water content was used to calculate the crosslink density of the gels prepared from different reactant concentrations, as described in our previous work.[15] The maximum crosslink density was determined to be 0.380 mol cm^{-3} and the conditions corresponding to this value were Ru(II)$(bpy)_3^{2+}$ and APS concentrations of 0.5 mM and

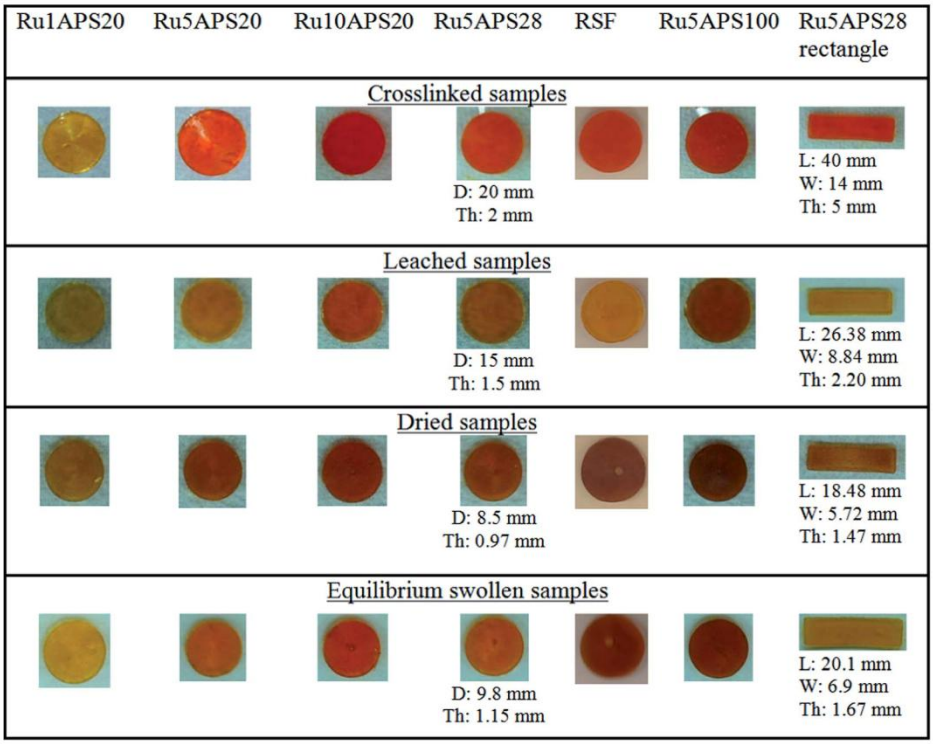


Fig. 3 Photographs of silk fibroin gels from BMWS and regenerated SF (RSF) at different stages of processing. Sizes of round samples are average values under all different conditions as samples did not vary greatly in size. (*D*: diameter; Th: thickness; *L*: length; *W*: width).

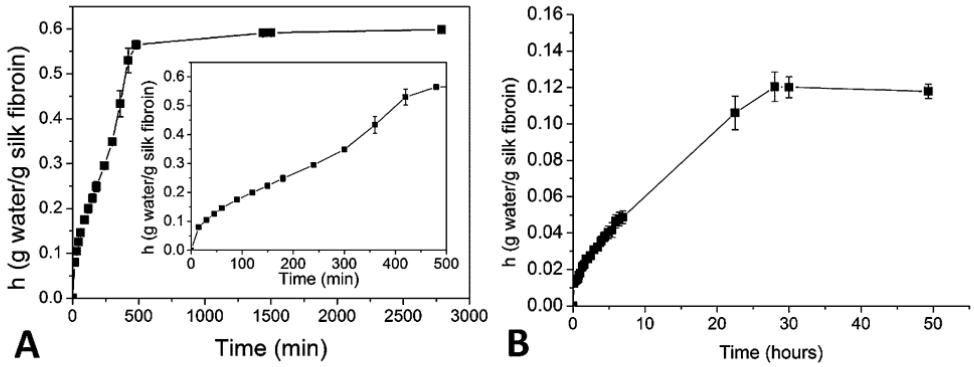


Fig. 4 (A) Plot of water uptake, *h*, as a function of time for sample Ru5APS28 when immersed in DW. Inset: shows initial water uptake to 500 minutes. (B) Plot of water vapour uptake, *h*, with time for sample Ru5APS28 at $T = 37$ °C and $a_w = 0.9$.

20 mM, respectively (Table 1). However, when the standard deviation for the sets of values was taken into account the crosslink density did not vary with the different conditions. The exception to this was the sample with a $Ru(II)(bpy)_3^{2+}$ concentration of 0.16 mM, which had a slightly lower crosslink density of 0.374 that did not overlap with the other values. Therefore, above a $Ru(II)(bpy)_3^{2+}$ concentration of 0.5 mM, the concentrations of the catalyst and electron acceptor did not have a significant effect on the crosslink density of the silk fibroin within the experimental range. Following this, the variables of crosslinking time, silk fibroin concentration, and interaction time of silk fibroin and reactants prior to crosslinking, were also investigated to determine their role in governing the crosslinking density. From the results in Table 1, it can be seen that the water uptake and crosslink density of the samples with extended crosslinking time, lower silk concentration, and a prolonged incubation time of reactants prior to exposure to light, had slightly higher values to the original gel at the same reactant concentrations (0.599). The values of water uptake were 0.620, 0.609, and 0.594 for the samples with less crosslinking time, lower silk fibroin concentration, and extended incubation time, respectively. However, when these values were used to calculate the crosslink densities, the values obtained were 0.375, 0.376, and 0.377 mol cm^{-3}, for less crosslinking time, lower protein concentration, and extended incubation time, respectively (Table 1). These crosslink densities were very similar to the original gel (Ru5APS28) prepared with the same $Ru(II)(bpy)_3^{2+}$ and APS concentrations (0.376 mol cm^{-3}). Thus, it is evident that these factors also did not markedly affect the crosslink density. When compared to the water uptake of the sample prepared under the same conditions using the regenerated silk fibroin solution (~140 mg mL^{-1}), the water uptake value (0.636) was slightly higher than the sample with a BMWS concentration of 150 mg mL^{-1}. This correlated with a crosslink density of 0.374 mol cm^{-3}, which matches closely with the data obtained for the BMWS gel with a similar concentration (0.376 mol cm^{-3}). This confirms that the ruthenium-mediated photo-crosslinking method is versatile and can be applied to silk fibroin solutions prepared from different methods.

When compared to other methods of silk fibroin crosslinking, the maximum crosslinking degree of genipin crosslinked silk fibroin with 24 hour reaction time was 29.4% as determined by the ninhydrin assay.[11] In addition, the water uptake (h) of the genipin crosslinked silk fibroin scaffolds when immersed in aqueous solution was approximately 29 at neutral pH.[11] This is much higher than the water uptake for the photodynamically crosslinked silk fibroin gels (0.599). This observation indicates that our system has a higher crosslinking degree and less swelling was observed.

Considering the insignificant role of the above parameters, a representative photo-crosslinked silk fibroin sample (Ru5APS28) prepared from BMWS powder under intermediate condition of crosslinking was selected for further analysis of the chemical and physical properties.

ESEM assessment of pore morphology of the silk fibroin hydrogels

The internal morphology of the representative Ru5APS28 hydrogel in the equilibrium-swollen state was examined on cross-sections of the hydrogel using ESEM. Fig. 5 shows two different areas highlighting the porous nature of the hydrogels. The average pore size was determined to be 2.49 ± 1.69 μm. In addition, the pore size distribution varied considerably, ranging from 1.15 μm to 7.67 μm, a phenomenon observed with other silk fibroin hydrogel systems.[12] The pores were interconnected by larger flat areas, which aid in the impressive mechanical strength properties that the hydrogels exhibit.[11] The porosity of hydrogels in the swollen state is related to their water uptake capacity and rate of water uptake.[28,29] In comparison with other silk fibroin hydrogels,[11,12] the hydrogels described here possess lower porosity (Fig. 5), and this lower porosity correlates with the decreased capacity to take up water, as measured during the water uptake study. Thus, we have demonstrated that the silk fibroin hydrogels prepared by photodynamic crosslinking are porous in nature, which has important implication for their use in tissue engineering applications.[11]

This journal is © The Royal Society of Chemistry 2014

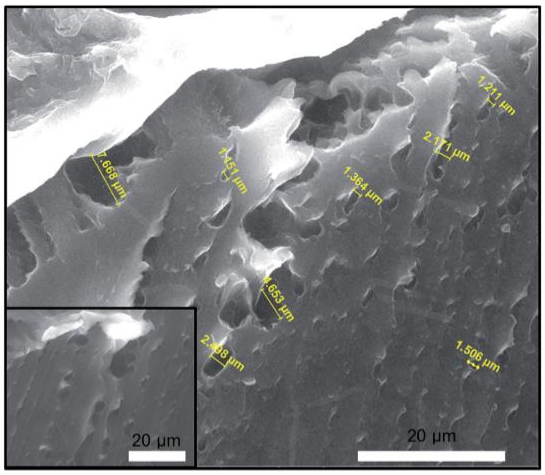


Fig. 5 The SEM image of two representative regions of the Ru5APS28 hydrogels showing pore size distribution.

Effect of hydration on the silk fibroin gel chain dynamics

DSC was used to measure the thermal behaviour of the silk fibroin powder, film and Ru5APS28 gel. Initially the glass transition temperatures (T_g) of the silk fibroin powder and film were determined and reported in Table 2. The dehydrated silk fibroin powder and the film show T_g values of 205 °C (the heat capacity change, $\Delta C_p = 0.47$ J g^{-1} °C) and 158 °C ($\Delta C_p = 0.84$ J g^{-1} °C), respectively. The film shows lowest T_g, which indicates the presence of amorphous silk fibroin with a random coil conformation. On the other hand, the silk powder has a less hydrophilic interaction and an amorphous random coil conformation exhibiting a high T_g value characteristic of the rigid structure.[30] However, from the T_g values it is clear that in both cases the intra- and intermolecular hydrogen bonds are broken leading to increased molecular motion. The change in heat capacity (ΔC_p) associated with the glass transition is a good indicator of the rigidity of the sample. In particular, Hu *et al.* have found a negative correlation between the ΔC_p and the crystalline beta-sheet content of silk fibroin films.[30] The highest T_g value and lowest ΔC_p values of silk fibroin powder certainly reveal the presence of a rigid β form of fibroin. This is attributed to the fact that during drying the powder has undergone thermally induced conformational transition from random coil to the β form of fibroin. Moreover, it is evident that the silk solution contained predominantly the amorphous part of the silk as the film prepared from it exhibits the lowest T_g and the highest associated ΔC_p.

The DSC thermogram of the dehydrated Ru5APS28 gel displays two major thermal events: a shift of the baseline related to an increase in the specific heat capacity indicating the glass transition, and a more complex endothermic peak arising above 250 °C due to chemical degradation of silk. Table 2 shows a summary of the T_gs of the Ru5APS28 gel under different hydration conditions. The dehydrated Ru5APS28 gel ($h = 0$) shows a glass transition temperature of approximately 110 °C ($\Delta C_p = 1.2$ J g^{-1} °C) (Fig. 6). Thus, the thermal behaviour of the gel is significantly different from that of the film, and dry silk fibroin powder. When comparing the T_g value of the dried silk gel to the dried film (158 °C), the gel has a lower value and also a higher ΔC_p. This observation indicates that the film is more rigid in structure than the gel as more thermal energy is required for the glassy to plastic conversion. Therefore, the amorphous portion of the silk solution comprised of the more random coil form of fibroin took part in the crosslinking reaction. It is noteworthy that upon drying, the silk fibroin crosslinked gels become very brittle.

It is well known that moisture/water plays an important role in governing the chain dynamics and mechanical properties of the silk fibroin gel. Investigation into the behaviour of the gels when exposed to moisture/water gave us information about their stability, hydration capabilities, and the tunability of the

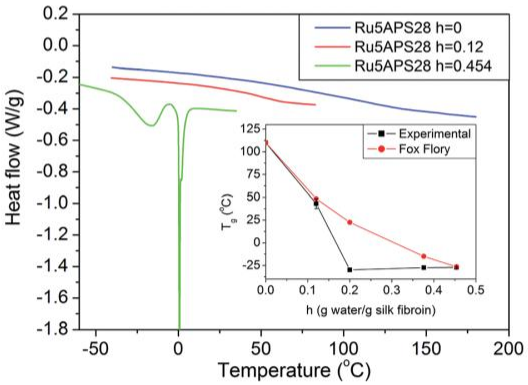


Fig. 6 DSC thermograms of Ru5APS28 gel samples at different levels of hydration. Inset: comparison of experimental T_g to the predicted Fox–Flory values with different h values.

Table 2 T_g and ΔC_p values of BMWS silk fibroin samples under different conditions

Sample	Processing conditions	h (g water per g silk fibroin)	T_g (°C)	ΔC_p (J g^{-1} °C)
Powder	Dehydrated	0	205	0.47
Un-crosslinked filtered film	Dehydrated	0	158.3	0.84
Ru5APS28	Dehydrated	0	110	1.2
Ru5APS28	Equilibrium vapour sorption	0.12	43	—
Ru5APS28	Liquid water uptake	0.454	−27.2	—

mechanical properties with different water uptake. The water vapour sorption was studied in addition to the immersion water uptake (h). The liquid water uptake and vapour sorption isotherms (37 °C and 90% RH) for the crosslinked Ru5APS28 silk fibroin gel are shown in Fig. 4A and B, respectively. The equilibrium h value for vapour sorption was determined to be 0.12 g water per g silk fibroin. In vapour sorption, water molecules were adsorbed and interacted with sites containing polar groups.[15] This is unlike immersion sorption where water also fills the voids after interacting with the polar groups. Therefore, as expected the water uptake was much less for vapour adsorption experiments. In addition, the equilibrium h value for the vapour sorption (0.12 g water per g silk fibroin) was lower than the value for the rec1-resilin gel under the same conditions which was approximately 0.25 g water per g rec1-resilin.[15] Our earlier work has shown that rec1-resilin gels, crosslinked through the same method, are highly elastic and resilient (>92%).[15] It has been reported that elastomeric proteins must exist in a hydrated or polar solvent environment in order to exhibit rubber-like elasticity.[31–33] This is because the internal chain dynamics and interactions of the proteins with water are responsible for the elasticity and resilience of the proteins.[34,35] The lowered propensity for the silk fibroin gels to take up moisture/water when compared to the rec1-resilins can thus be related to differences in their structure, degree of hydrophobicity and hence resultant elasticity. Silk fibroin possesses a structure comprising of flexible and hydrophilic glycine residues (G-44.6 mol%) that alternate with the rigid hydrophobic alanine residue (A-29.4 mol%) based repeat units as represented by (–G–A–G–A–G–S–) along with a variety of other amino acids, the most abundant of which are serine (S-12 mol%), Tyr (Y-4.98 mol%), Asp (D), Arg (R), *etc.* Depending on the conformational transition and processing conditions, the tyrosine residue could either be buried with its phenolic hydroxyl group being a strong hydrogen bond donor, or the tyrosine group is exposed to surface in aqueous solution with its phenolic hydroxyl group being both donor and acceptor. Therefore, although rec1-resilin and silk have some common features, silk differs significantly in the fact that the overall structure is hydrophobic, whereas rec1-resilin is predominantly hydrophilic.

DSC was used to study the effect of hydration on the molecular dynamics of the Ru5APS28 silk fibroin gel samples. The DSC thermogram showed a dramatic change in the T_g of the Ru5APS28 silk fibroin gel to 43 °C for the sample at equilibrium vapour sorption ($h = 0.12$) under the conditions of 90 %RH at 37 °C (Fig. 6). When the protein gel was in the dehydrated state, the intermolecular interactions were strong, and high temperatures were required for cooperative segmental motions (higher T_g).[15] However, in the presence of water, alternate hydrogen bonding donors and acceptors were available which results in a decrease in the energy barrier required for the plasticization of the system, and thus a lower T_g was exhibited.[15] The effect of water on the T_g has also been reported for silk fibroin films, with a systematic decrease in T_g as the relative humidity increased.[36] The absence of an endothermic peak centred at 0 °C related to the melting of bulk water, confirmed that the water uptake at the equilibrium vapour sorption state is bound non-crystallisable water. Thus, the presence of non-crystallisable water was shown to act as a plasticizer for the silk fibroin gel system.

The thermal behaviour of the Ru5APS28 silk fibroin gel under immersion sorption conditions ($h = 0.454$) was also examined (Fig. 6). The existence of an endothermic peak centred at 0 °C that remained with thermal cycling was due to the melting of bulk crystallisable water in the system. The T_g of the silk fibroin gel at this condition was observed at −27 °C. Thus at room temperature, the protein gel was in a flexible state.

The amount of crystallisable and non-crystallisable water was quantified using the endothermic melting of water in the DSC thermograms of Ru5APS28 samples under immersion sorption conditions. The amount of water in the system was initially determined using eqn (5):

$$X_{tw} = 1 - \frac{M_{dry}}{M_{total}} \quad (5)$$

where, X_{tw} is the total water content in the hydrogel, M_{dry} is the mass of the dried gel, and M_{total} is the mass of the swollen gel.

Following this, the amount of non-crystallisable water was calculated from eqn (6):

$$X_{nc} = X_{tw} - \left(\frac{Q_{endo}}{Q_f}\right) \quad (6)$$

where, X_{nc} is the fraction of non-crystallisable water, X_{tw} is the total water fraction of the gel, Q_{endo} is the heat of fusion of the crystallisable water as obtained from the DSC thermogram, and Q_f is the heat of fusion of free water (333 J g^{-1}).[37] It was assumed that the heat of fusion of crystallisable water in the gel was the same as that of ice. The total amount of water (X_{tw}) in the system for the Ru5APS28 gel under immersion sorption conditions ($h = 0.454$) was found to be 0.31. Under this condition, the fractions of crystallisable (X_c) and non-crystallisable (X_{nc}) water were found to be 0.05 and 0.26, respectively. Therefore, from a representative Ru5APS28 gel sample with a total swollen mass of 8.7 mg, there was 2.7 mg of water in total with 2.3 mg of non-crystallisable water occupying the hydrophilic sites and the remaining 0.4 mg being bulk crystallisable water. The amount of bound water present in the sample was calculated to be ~0.38 g water per g silk fibroin, which was less than that of rec1-resilin (~0.54) and was consistent with the lower level of hydrophilic amino acid residues present in silk fibroin.[15]

The effect of the water content (h) on the T_g was predicted using the Fox–Flory equation:

$$\frac{1}{T_{g_{hs}}} = \frac{1 - x_w}{T_{g_s}} + \frac{x_w}{T_{g_w}} \quad (7)$$

where, $T_{g_{hs}}$ is the glass transition of hydrated silk fibroin, T_{g_s} is the glass transition of dehydrated silk fibroin, and T_{g_w} is the glass transition of quenched pure water (estimated as −135 °C).[38] Fig. 5 inset shows the correlation between the experimentally measured T_g values and predicted T_g values of the Ru5APS28 sample with different levels of hydration using both vapour sorption and liquid water uptake. At the equilibrium h level (0.12 g water per g silk fibroin) under vapour

This journal is © The Royal Society of Chemistry 2014

sorption conditions, the T_g value (43 °C) closely agreed with the predicted value. However, when the water content was increased beyond this through immersion sorption the experimental values deviated negatively from the predicted values. A negative deviation is due to the presence of non-bound crystallisable water in addition to the bound water. The presence of crystallisable water was also confirmed from the endothermic peak at 0 °C on the DSC thermogram, which was quantified. Thus, the presence of bound and non-bound water resulted in a decrease in the T_g to approximately −27.2 °C, which did not change when the h value increased above 0.2.

Effect of hydration on the mechanical properties of silk fibroin gels

The effect of hydration on the mechanical properties of the crosslinked silk fibroin gels was examined using DMA with humidity accessory. The storage/loss moduli and tan delta values of the Ru5APS28 samples were measured using samples of rectangular geometry. It was observed that dry samples were too rigid for mounting and thus the samples were mounted after reaching equilibrium swelling in an immersion sorption system for 24 hours. During the run the humidity was ramped to 50% and held for the duration of an hour with isothermal temperature, to prevent rapid dehydration of the system. The sample weight was measured at the beginning and end of each run to determine the actual water content precisely. This was correlated with the measured modulus values (Fig. 7A) and the curves generated for each run are shown in Fig. 7B, where run 1 is the experiment with the equilibrium-swollen gel progressing to run 7 when the gel has the lowest h value. From the graph it can be observed that G' increased as the samples dried and less water was present in this sample. At the highest h value (=0.454 g water per g silk fibroin), G' had a value of 81 MPa, whilst at lower h values (h = 0.08 g water per g silk fibroin) G' increased to a maximum of 4000 MPa. Thus, the presence of water affected the mechanical properties greatly, with a higher water content resulting in an increase in the molecular mobility of the silk fibroin gels and loss of water leading to increased stiffness (higher G'). This has been also confirmed by the DSC experiments where the T_g becomes lower with higher water content. The water acts as a plasticiser to increase the flexibility and extensibility.[21] Dehydrated regenerated silk fibroin films prepared by Motta *et al.* exhibited storage moduli of 1834 MPa and 903 MPa at 0 °C and 37 °C, respectively.[39] The authors also prepared films, which were treated overnight with methanol and under high temperatures to induce physical crosslinking through β-sheet formation.[39] The storage moduli for the dehydrated methanol treated films were 2760 MPa and 2445 MPa at 0 °C and 37 °C, respectively.[39] Whilst the values for the heat treated films were 4840 MPa and 4410 MPa at 0 °C and 37 °C, respectively. The increase in the crystalline content was shown to result in increased stiffness, with highest values due to the high amount of physically crosslinked films due to heat treatment.[39] The uncrosslinked film displayed a significantly lower G' value than that of the crosslinked gel. In addition, the heat treated samples showed comparable values to our dehydrated

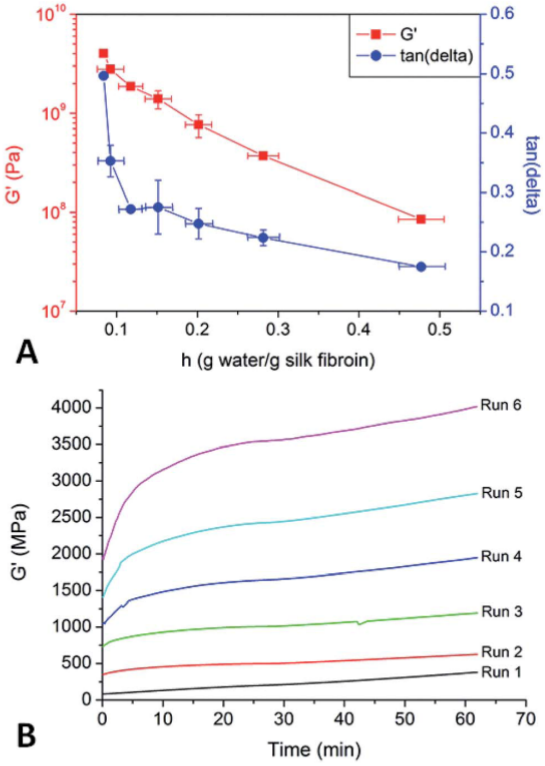


Fig. 7 DMA results for Ru5APS28 samples with different hydration levels. (A) G' and tan(delta). (B) Change in G' with time for each DMA run.

gels, whilst methanol treatment resulted in materials with slightly less stiffness. Therefore, ruthenium-mediated photocrosslinking of silk fibroin is a highly suitable and facile method for the rapid preparation of hydrogels with high strength, the elasticity of which can be tuned through the moisture content as shown here.

Structural analysis of silk fibroin powder, films, and gels

As the extent of silk crosslinking did not change very much using the ruthenium-mediated process with the variables such as time and concentration; we have hypothesised that the nanostructure may be a contributing factor. From the amino acid sequence, it can be observed that the majority of the tyrosine residues reside in the crystalline regions of the silk fibroin sequence.[40] However, on dissolution in water, the tyrosine residue is expected to be exposed to the surface of the protein and air–water interface and hence become accessible for crosslinking. Such rearrangement of the fibroin chain in water is necessary for the tyrosine residues to participate in crosslinking. The silk particles that are removed *via* filtration of the solutions are attributed to the ordered rigid β sheet structure comprising of alanine residues that are insoluble. The dry silk fibroin may also have a β sheet structure, which has been

indicated through DSC experiments. If a fixed fraction of silk is removed during the filtration step, this would explain why the same amount of silk is crosslinked regardless of the conditions. In addition, the flexibility of the gel is attributed to the amorphous and less ordered hydrophilic glycine rich portion of the silk being involved in the tyrosine mediated crosslinking reaction. Photo-acoustic Fourier transform infrared (PA-FTIR) spectroscopy was used to analyse the structural changes of the initial silk fibroin powder, film prepared from filtered solution, and the Ru5APS28 gel prepared from filtered solution that occurred during the different processing steps.

The secondary structure content of the silk fibroin powder, film, and gel was examined using PA-FTIR spectroscopy. The spectra of the samples show the presence of various amide bands corresponding to a number of conformations. Two distinct conformation bands with peak maxima between 1700 and 1600 cm^{-1} (due to amide I) and between 1600 and 1500 cm^{-1} (due to amide II) are observed in the spectra. The amide I band was deconvoluted using the Magic Plot software by applying a Gaussian curve fitting to this region (1600–1700 cm^{-1}).[23,30] The areas under the peaks were determined and the proportion of each secondary structure was calculated from this information to give a semi-quantitative comparison between the samples. Fig. 8A shows the secondary structure content for the samples under different conditions. The beta-sheet content of the powder was calculated from the peak position at 1628–1637 cm^{-1} and was found to be 27 ± 1%.[23,30] Whereas, the films from the filtered solution had a beta-sheet contribution of 18 ± 0.5%. In addition, the Ru5APS28 gel from filtered solutions displayed the lowest beta-sheet contributions of 13 ± 3%. Therefore, there was a significant decrease (~10%) in the beta-sheet content from the powder to the Ru5APS28 gel form. It has been reported earlier that the beta-sheet crystalline structure (silk II) contributes to the rigidity of *B. mori* silk fibroin.[30] Therefore, the decrease in the beta-sheet content is consistent with our hypothesis that the gels contained less ordered silk fibroin when crosslinked.

The PA-FTIR spectra were also examined to confirm the presence of di-/trityrosine crosslinks upon gelation of the silk solutions. There were a number of differences detected between the spectra of the powder and the film to the spectra of the gels in the region of 700–1400 cm^{-1} (Fig. 8B). The strong band at ~821 cm^{-1} in the spectra of the powder and films was assigned to tyrosine as it is in the region of *para*-disubstituted benzenes (800–860 cm^{-1}). However, it was observed that this peak was not present in the spectra of the Ru5APS28 gels, which confirms the crosslinking of tyrosine. In addition, the region from 1170 to 1270 cm^{-1} that is attributed to tyrosine differed between the spectra of the powder and film to the gel.[41] The spectra of the powder and film showed an increase in intensity in this region, however in the gel spectra there was a decrease, indicating a decrease in the presence of tyrosine. Furthermore, a shift in the region of the aliphatic amines (1020–1220 cm^{-1}) for the spectra of the gel when compared to the powder and film indicates changes in the structure on the formation of hydrogels.

XRD experiments were employed to give further information on the nano-structural organisation of the silk fibroin powder,

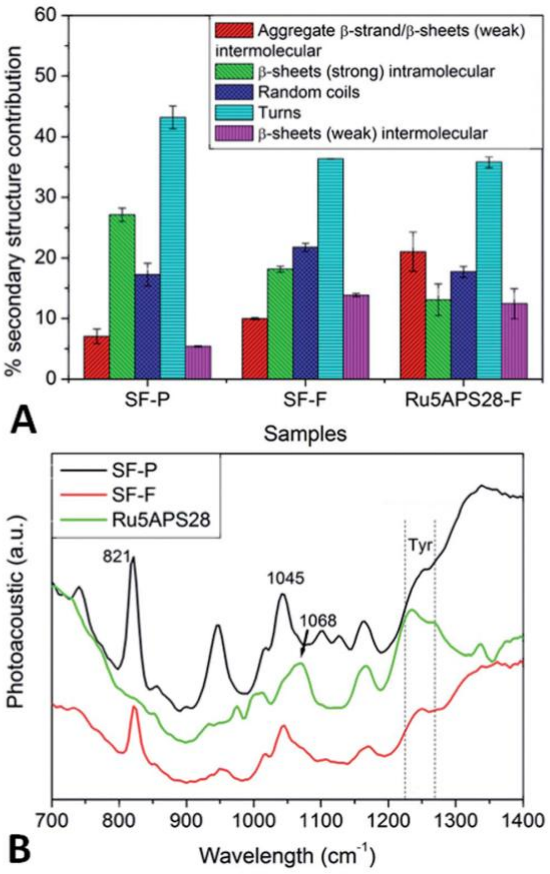


Fig. 8 (A) Secondary structure content of silk fibroin powder, film and Ru5APS28 gel as calculated from PA-FTIR data. (B) FTIR spectra of different forms of silk fibroin. SF-P: silk fibroin powder; SF-F: silk film from filtered solution; Ru5APS28-F: silk gel from filtered solution.

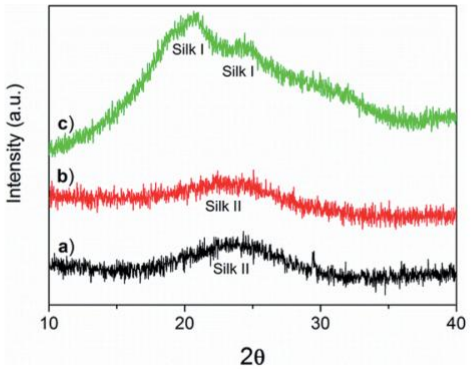


Fig. 9 X-ray diffractograms of (a) silk powder; (b) silk film from filtered solution; (c) Ru5APS28 gel from filtered solution.

This journal is © The Royal Society of Chemistry 2014

film, and the Ru5APS28 gel. Fig. 9 shows the X-ray diffractograms for the aforementioned samples. The *d* spacings for the main peaks were determined and compared to the literature values to obtain information about the structure of the silk fibroin in the different states. The silk powder and film show broad spectra with peaks centred at 23.6 and 23.5°, which correspond to a *d* spacing of ~3.8 Å. From the literature, a *d* spacing of 3.8 Å has been associated with the silk II structure (crystalline beta-sheet).[42] However, as the peaks are so broad and have a low intensity, it is expected that a range of silk I and silk II conformations exist for the silk powder and filtered film. The diffractogram for the Ru5APS28 gel prepared from the filtered solution shows much more intense peaks at 20.4 and 24.4°, which correspond to *d* spacing values of 4.4 and 3.6 Å. These *d* spacings have been attributed to the silk I structure (type II beta-turn), which is the hydrated form.[21,43] Therefore, the silk gels contain the hydrated silk I structure, which allows for the uptake of water. The XRD results correlate with the DSC and PA-FTIR results in that the silk undergoes structural changes from containing more crystalline component in the powder and films to more amorphous when crosslinked to form hydrogels. A summary of the structural information obtained for the different forms of the silk fibroin can be found in Table 3.

Growth of ATDC5 cells on silk fibroin hydrogels

A representative silk fibroin hydrogel (Ru5APS28) was evaluated for its capacity to support cell growth *in vitro*. The pre-chondrocyte cell line ATDC5 was chosen to study the biocompatibility of the hydrogels, as these gels could be suitable for intervertebral disc replacement applications due to the high modulus as determined by DMA. The adhesion and proliferation of the ATDC5 cells, seeded at a density of 12×10^4 cells per cm^2, were assessed using phase-contrast microscopy. Fig. 10a and b shows the morphological characteristics of ATDC5 cells cultured overnight on both TCP and silk fibroin hydrogel, respectively. As seen in Fig. 10a and b, the cells cultured on both TCP and silk fibroin hydrogel displayed a characteristic spread, adherent, elongated morphology. Furthermore, ATDC5 viability and proliferation on the Ru5APS28 hydrogels was assessed over a period of 7 days and cell proliferation was evaluated using the tetrazolium salt, WST-1 [2-(4-iodophenyl)-3-(4-nitrophenyl)-5-(2,4-disulfophenyl)-2*H*-tetrazolium]. As seen in Fig. 10c, the ATDC5s remained viable and expanded in cell number throughout the culture period. However, it should be noted that the ATDC5 cells displayed reduced proliferative capacity

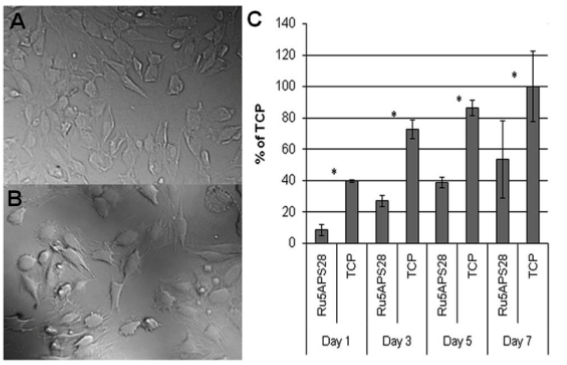


Fig. 10 Phase-contrast micrographs of growth of ATDC5 cells after overnight culture on (A) TCP and (B) Ru5APS28 hydrogels. (C) ATDC5 cell proliferation as assessed using a WST-1 proliferation assay. * represents groups that are statistically different (p value < 0.05).

(p value < 0.0001) on the hydrogels compared to the TCP, at each time point examined. These findings indicate that the silk fibroin photo-crosslinked hydrogels are non-toxic *in vitro*, support cell attachment and cell proliferation and represent promising, biocompatible biomaterials for tissue engineering applications.

Conclusions

In summary, for the first time we have demonstrated successful photo-crosslinking of *B. mori* silk fibroin with Ru(II)$(bpy)_3^{2+}$ as the catalyst and APS as the electron acceptor. The extent of crosslinking depends on the accessibility/availability of the tyrosine residue in the amorphous region to participate in the crosslinking reaction. This has been confirmed through DSC, PA-FTIR, and XRD studies, which show that the gels are less rigid and contain less beta-sheet content than the original silk. In addition, water/moisture has been shown to play a significant role in the molecular chain dynamics. The presence of both crystallisable and non-crystallisable water resulted in a plasticised Ru5APS28 silk fibroin gel at room temperature. In addition, water/moisture was also observed to play an important role in tuning the mechanical properties of the Ru5APS28 gel. The storage modulus (G') values were tuned from 4000 MPa to 81 MPa with hydration levels (h) of 0.08 and 0.454, respectively. The effect of water/moisture on the chain dynamics and mechanical properties is important for understanding the

Table 3 Summary of structural information determined through different experimental methods

Experimental method	BMWS powder	BMWS film from filtered solution	BMWS gel from filtered solution
DSC	Silk II (crystalline)	Predominantly silk I (amorphous)	Silk I (amorphous)
PA-FTIR	Silk II (crystalline) with some silk I (amorphous)	Silk I (amorphous) with some silk II (crystalline)	Predominantly silk I (amorphous)
XRD	Predominantly silk II (crystalline) with some silk I (amorphous)	Silk II (crystalline) with some silk I (amorphous)	Silk I (amorphous)

performance of the hydrogel under different conditions. Thus, we have developed a route for *in situ* photo-crosslinking of silk fibroin to form hydrogels with tuneable modulus values. We have shown through cell culture studies that the hydrogels support the attachment and growth of pre-chondrocyte cells, highlighting their potential suitability as biomaterials for tissue engineering applications.

Acknowledgements

This research has been financially supported by the Australian Research Council (ARC) through Discovery Grant funding.

References

1 J. Kundu, L. A. Poole-Warren, P. Martens and S. C. Kundu, *Acta Biomater.*, 2012, **8**, 1720.
2 A. Alessandrino, B. Marelli, C. Arosio, S. Fare, M. C. Tanzi and G. Freddi, *Eng. Life Sci.*, 2008, **8**, 219–225.
3 B.-M. Min, G. Lee, S. H. Kim, Y. S. Nam, T. S. Lee and W. H. Park, *Biomaterials*, 2004, **25**, 1289–1297.
4 J. A. Werkmeister and J. A. M. Ramshaw, *Biomed. Mater.*, 2012, **7**, 012002.
5 S. Aznar-Cervantes, M. I. Roca, J. G. Martinez, L. Meseguer-Olmo, J. L. Cenis, J. M. Moraleda and T. F. Otero, *Bioelectrochemistry*, 2012, **85**, 36–43.
6 A. Matsumoto, J. Chen, A. L. Collette, U.-J. Kim, G. H. Altman, P. Cebe and D. L. Kaplan, *J. Phys. Chem. B*, 2006, **110**, 21630.
7 S. Nagarkar, T. Nicolai, C. Chassenieux and A. Lele, *Phys. Chem. Chem. Phys.*, 2010, **12**, 3834.
8 C. Vepari and D. L. Kaplan, *Prog. Polym. Sci.*, 2007, **32**, 991–1007.
9 Q. Lu, Y. Huang, M. Li, B. Zuo, S. Lu, J. Wang, H. Zhu and D. L. Kaplan, *Acta Biomater.*, 2011, **7**, 2394–2400.
10 N. Kojic, M. J. Panzer, G. G. Leisk, W. K. Raja, M. Kojic and D. L. Kaplan, *Soft Matter*, 2012, **8**, 2897–2905.
11 A. Vasconcelos, A. C. Gomes and A. Cavaco-Paulo, *Acta Biomater.*, 2012, **8**, 3049.
12 W. Xiao, W. Liu, J. Sun, X. Dan, D. Wei and H. Fan, *J. Bioact. Compat. Polym.*, 2012, **27**, 327–341.
13 S. S. Silva, D. Maniglio, A. Motta, J. F. Mano, R. L. Reis and C. Migliaresi, *Macromol. Biosci.*, 2008, **8**, 766–774.
14 G. Kang, K. Lee, C. Ki and Y. Park, *Fibers Polym.*, 2004, **5**, 234–238.
15 M. Y. Truong, N. K. Dutta, N. R. Choudhury, M. Kim, C. M. Elvin, K. M. Nairn and A. J. Hill, *Biomaterials*, 2011, **32**, 8462–8473.
16 K. Schacht and T. Scheibel, *Biomacromolecules*, 2011, **12**, 2488.
17 M. Mondal, K. Trivedy and S. Nirmal Kumar, *Caspian J. Env. Sci.*, 2007, **5**, 63–76.
18 C. M. Elvin, T. Vuocolo, A. G. Brownlee, L. Sando, M. G. Huson, N. E. Liyou, P. R. Stockwell, R. E. Lyons, M. Kim, G. A. Edwards, G. Johnson, G. A. McFarland, J. A. M. Ramshaw and J. A. Werkmeister, *Biomaterials*, 2010, **31**, 8323–8331.
19 J. Ishikuro, Y. Hirai and T. Nakajima, *Sen'i Gakkaishi*, 1994, **50**, 28–31.
20 S. Fossey and D. Kaplan, in *Polymer Data Handbook*, Oxford University Press, Inc., 1999.
21 C. Zhang, D. Song, Q. Lu, X. Hu, D. L. Kaplan and H. Zhu, *Biomacromolecules*, 2012, **13**, 2148–2153.
22 X. Hu, X. Wang, J. Rnjak, A. S. Weiss and D. L. Kaplan, *Biomaterials*, 2010, **31**, 8121–8131.
23 S. Lin, G. Lu, S. Liu, S. Bai, X. Liu, Q. Lu, B. Zuo, D. L. Kaplan and H. Zhu, *J. Mater. Chem. B*, 2014, **2**, 2622–2633.
24 C. Shukunami, Y. Ohta, M. Sakuda and Y. Hiraki, *Exp. Cell Res.*, 1998, **241**, 1–11.
25 C. Shukunami, K. Ishizeki, T. Atsumi, Y. Ohta, F. Suzuki and Y. Hiraki, *J. Bone Miner. Res.*, 1997, **12**, 1174–1188.
26 K. Vandyke, S. Fitter and A. C. W. Zannettino, *Blood Cancer Journal*, 2011, **1**, e2, DOI: 10.1038/bcj.2011.1.
27 S. Fitter, K. Vandyke, S. Gronthos and A. C. W. Zannettino, *J. Mol. Endocrinol.*, 2012, **48**, 229–240.
28 S. Van Vlierberghe, P. Dubruel, E. Lippens, M. Cornelissen and E. Schacht, *J. Biomater. Sci., Polym. Ed.*, 2009, **20**, 1417–1438.
29 F. Ganji, S. Vasheghani-Farahani and E. Vasheghani-Farahani, *Iran. Polym. J.*, 2010, **19**, 375–398.
30 X. Hu, D. Kaplan and P. Cebe, *Macromolecules*, 2006, **39**, 6161–6170.
31 S. Rauscher and R. Pomès, in *Fuzziness*, ed. M. Fuxreiter and P. Tompa, Springer US, 2012, vol. 725, pp. 159–183.
32 M. Martino, T. Perri and A. M. Tamburro, *Macromol. Biosci.*, 2002, **2**, 319–328.
33 F. Teulé, B. Addison, A. R. Cooper, J. Ayon, R. W. Henning, C. J. Benmore, G. P. Holland, J. L. Yarger and R. V. Lewis, *Biopolymers*, 2012, **97**, 418–431.
34 M. Kim, S. Tang and B. D. Olsen, *J. Polym. Sci., Part B: Polym. Phys.*, 2013, **51**, 587–601.
35 Y. Zhou, S. Wu and V. P. Conticello, *Biomacromolecules*, 2001, **2**, 111–125.
36 N. Agarwal, D. A. Hoagland and R. J. Farris, *J. Appl. Polym. Sci.*, 1997, **63**, 401–410.
37 T. Wang and S. Gunasekaran, *J. Appl. Polym. Sci.*, 2006, **101**, 3227–3232.
38 V. Velikov, S. Borick and C. A. Angell, *Science*, 2001, **294**, 2335–2338.
39 A. Motta, L. Fambri and C. Migliaresi, *Macromol. Chem. Phys.*, 2002, **203**, 1658–1665.
40 C. Z. Zhou, F. Confalonieri, M. Jacquet, R. Perasso, Z. G. Li and J. Janin, *Proteins: Struct., Funct., Bioinf.*, 2001, **44**, 119–122.
41 A. Barth, *Prog. Biophys. Mol. Biol.*, 2000, **74**, 141–173.
42 I. C. Um, H. Y. Kweon, Y. H. Park and S. Hudson, *Int. J. Biol. Macromol.*, 2001, **29**, 91–97.
43 H.-J. Jin, *Nature*, 2003, **424**, 1057–1061.

This journal is © The Royal Society of Chemistry 2014

4.2 Supplementary information

S4.2.1 NMR analysis of BMWS and RSF in D_2O

Regenerated silk fibroin (RSF) from the raw silk and BMWS powder were analysed to confirm the structure of the protein. The RSF in the $CaCl_2/H_2O/EtOH$ solution was dialysed against distilled water for several days and centrifuged at 10,000 rpm for 20 minutes at room temperature. A small amount of solution was dissolved in D_2O. The BMWS powder was dissolved in deuterated water (D_2O) to a concentration of 0.95 %. ^1H NMR spectra were obtained on a 300 MHz Bruker Avance spectrometer operating at 300.138 MHz. Reference relative to 0 ppm for TMS. The predominant presence of glycine (Gly) and alanine (Ala) that makes up the structure of silk fibroin has been confirmed[1]. In addition, the presence of the tyrosine groups required for crosslinking has also been confirmed through the peaks in the spectra, which were correlated with literature values.[1]

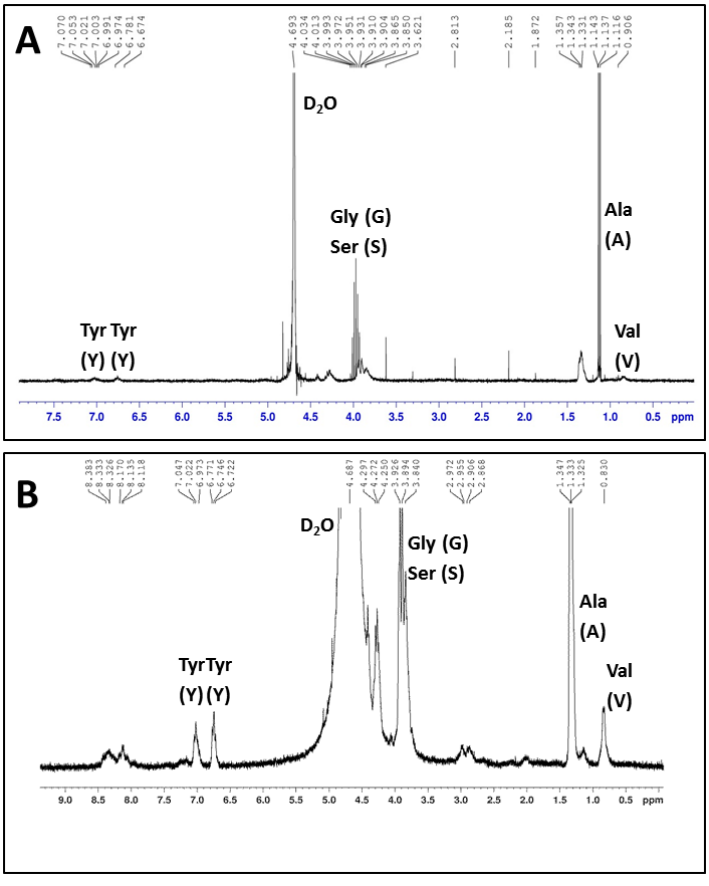


Figure S4.1 NMR spectrum of A) BMWS dissolved in D_2O; B) RSF aqueous solution dissolved in D_2O (peak positions showing individual residues).[1]

S4.2.2 Fluorescence spectra indicating presence of dityrosine crosslinks

A sample gel was prepared with a BMWS concentration of 300 mg/ml, $Ru(II)(bpy)_3^{2+}$ concentration of 0.03 mM, and an APS concentration of 20 mM. A low concentration of $Ru(II)(bpy)_3^{2+}$ was used to prepare a gel that was transparent in order to be suitable for fluorescence measurements using the Cary Eclipse Fluorescence Spectrometer. At this concentration of $Ru(II)(bpy)_3^{2+}$, an extended crosslinking time (~12 hours) was required to form a gel. Figure S4.3 shows the fluorescence spectra of the gel. The peak at ~405 nm in the emission spectra confirms the presence of dityrosine crosslinks in the gel structure.[3]

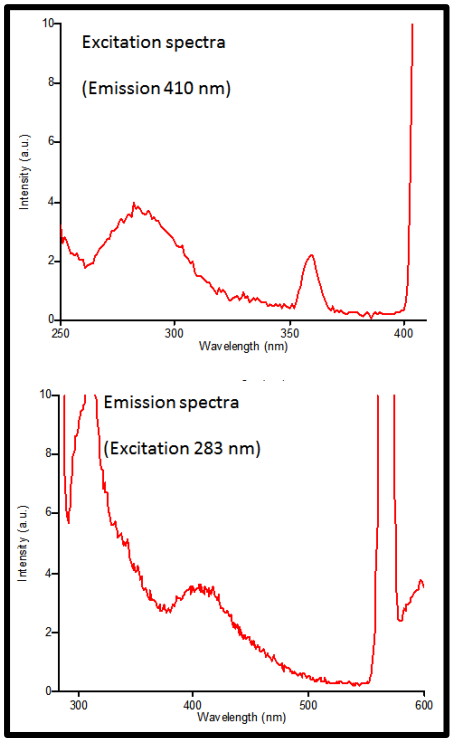


Figure S4.2 Fluorescence spectra of crosslinked gel.

S4.2.3 UV-vis spectrometry of crosslinked dilute solution and gel

A Ru5APS28 gel sample was run in the Evolution 201 UV/VIS Spectrophotometer by cutting a thin strip and vertically placing it in the cuvette to obtain the spectra shown in Figure S4.3A. This was compared to the spectra of the uncrosslinked silk solution. The Tyr present in the silk solution is evident with the peak occurring at 275 nm. The spectra of the gel shows a broad peak ranging from approximately 250 to 350 nm, indicating a range of structures involving tyrosine are present. It is known that the deprotonated absorption of dityrosine occurs at ~315 nm[3]. However, due to the noisy nature of the gel spectra it is difficult to

identify the presence of dityrosine. Thus, a 1% silk solution was mixed with Ru(II)$(bpy)_3^{2+}$ (1 mM) and APS (20 mM) and exposed to light for 180 seconds and the UV-vis spectra was obtained (Figure S4.3 B). It was easier to identify the presence of dityrosine in the solution spectra with a peak evident at 313 nm, along with different forms of tyrosine at 288 nm and 301 nm. In addition, the presence of Ru(II)$(bpy)_3^{2+}$ in the gel and solution was also confirmed due to the peak at 452 nm. As this peak is present in the gel, which has been washed for several days, it indicates that the gel contains Ru(II)$(bpy)_3^{2+}$ that is bound to the silk molecules. This will be investigated further in the future using surface analysis techniques.

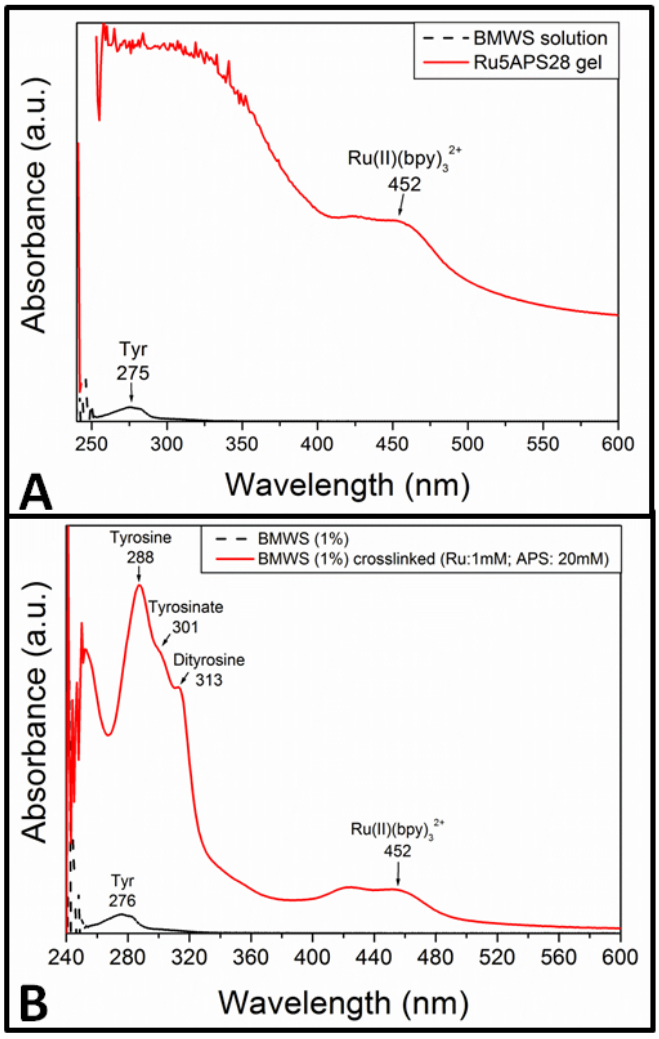


Figure S4.3 UV-vis spectra of A) Ru5APS28 gel and uncrosslinked silk solution; and B) crosslinked and uncrosslinked 1% silk solutions.

S4.2.4 Determination of minimum Ru(II)$(bpy)_3^{2+}$ concentration required for crosslinking

Table S4.1 Ability of BMWS to crosslink at various Ru(II)$(bpy)_3^{2+}$ concentrations (APS concentration remained at 20 mM).

Ru(II)$(bpy)_3^{2+}$ concentration (mM)	Crosslinking observations (crosslinking time: 180 seconds)
0.03	No crosslinking – remained as a solution.
0.105	Partially crosslinked – some gel formation, small portion remained in liquid state.
0.16	Crosslinked – gel fragile but able to be removed from mould after leaching for 1 day.
0.28	Crosslinked – gel fragile but able to be removed from mould after leaching for 1 day.
0.5	Crosslinked – gel remained intact when removed from mould.

From Table S4.1 it can be observed that a minimum Ru(II)$(bpy)_3^{2+}$ concentration of 0.5 mM was required to form a gel that was able to support itself on removal from the mould. Crosslinking was achieved with a Ru(II)$(bpy)_3^{2+}$ concentration of 0.105 mM and above, however gels were flimsy and broke easily upon removal from the mould.

References:

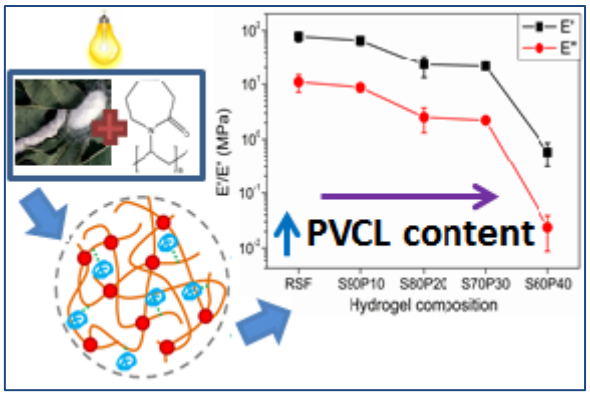
1. Zainuddin; Le, T. T.; Park, Y.; Chirila, T. V.; Halley, P. J.; Whittaker, A. K., *Biomaterials* **2008,** *29* (32), 4268-4274.
2. Truong, M. Y.; Dutta, N. K.; Choudhury, N. R.; Kim, M.; Elvin, C. M.; Nairn, K. M.; Hill, A. J., *Biomaterials* **2011,** *32* (33), 8462-8473.
3. Correia, M.; Neves-Petersen, M. T.; Jeppesen, P. B.; Gregersen, S.; Petersen, S. B., *PLoS ONE* **2012,** *7* (12), e50733.

Chapter 5: Engineering silk-based hybrid hydrogels

This chapter of the thesis is presented in two parts. Part 5.1 is presented as a research article "J. L. Whittaker, N. K. Dutta, C. M. Elvin and N. R. Choudhury. Fabrication of highly elastic resilin/silk fibroin based hydrogel by rapid photo-crosslinking reaction. Journal of Materials Chemistry B. 2015, 3, 6576-6579", published and reproduced by permission of the Royal Society of Chemistry, Copyright 2015.



Part 5.2 is presented as a research manuscript "J. L. Whittaker, N. K. Dutta and N. R. Choudhury. Engineering DN hydrogels from regenerated silk fibroin and Poly(N-vinylcaprolactam)", submitted to *Macromolecules*.



5.1 Fabrication of highly elastic resilin/silk fibroin based hydrogel by rapid photo-crosslinking reaction

5.1.1 Research article

Journal of Materials Chemistry B

COMMUNICATION

View Article Online
View Journal | View Issue

Fabrication of highly elastic resilin/silk fibroin based hydrogel by rapid photo-crosslinking reaction†

J. L. Whittaker,[a] N. K. Dutta,[a] C. M. Elvin[b] and N. R. Choudhury*[a]

Cite this: *J. Mater. Chem. B*, 2015, 3, 6576

Received 21st May 2015,
Accepted 16th July 2015

DOI: 10.1039/c5tb00970g

www.rsc.org/MaterialsB

A new type of hydrogel combining the highly elastic soft phase of Rec1-resilin and the mechanically strong hard phase Bombyx mori Silk fibroin has been reported using a rapid photo-crosslinking method. The improved elasticity and strength through the use of a resilin-based material and silk fibroin has been shown for the first time.

Protein-based hydrogels are crosslinked polypeptide/protein-based networks that have been of interest in biomaterials research due to their high water absorption capacity and resemblance to the extracellular matrix (ECM).[1–3] The advantage of using natural protein-based materials is their ability to support cellular interactions, low toxicity and biocompatibility, which is not the case with many synthetic polymers.[3,4] In particular, resilin-like proteins (RLPs) have gained increasing research attention in recent years as a result of their remarkable elasticity and resilience properties.[5] Previously our group has reported a rapid (~60 seconds) Ruthenium-mediated photo-crosslinking method for Rec1-resilin (Rec1), a recombinant resilin protein, that exploits the tyrosine residues (~6.9 mol%) in the protein structure to form three-dimensional hydrogels.[5,6] Whilst, the hydrophilic Rec1 hydrogel showed impressive resilience (~92%) and water uptake capacity, the softness of the material was indicated by the low storage modulus (~0.002 MPa).[6] In addition, a number of RLP-based hydrogels that also display storage moduli in the tens of kilopascals range have been developed to target a range of soft tissue engineering applications.[7–9] However, in order to exploit the remarkable resilience of Rec1-resilin for tissue engineering applications where higher modulus values are required, it is necessary to improve its strength. Intervertebral disc regeneration is one such application where there is a need to develop materials with high water uptake capacity and mechanical strength.[10] We have recently shown that the Ruthenium-mediated photo-crosslinking method can also be applied to *Bombyx mori* silk fibroin from freeze dried and regenerated silk solutions, which contains 4.9 mol% tyrosine.[11,12] The regenerated silk fibroin (RSF) hydrogel displayed impressive modulus values (~78 MPa) when fully hydrated and was shown to be not cytotoxic when cultured with a mouse pre-chondrocyte cell line.[12] Therefore, in order to target a range of tissue engineering applications where improved modulus values are required, we report on a co-crosslinked Rec1/RSF hybrid hydrogel. We have shown that by combining the water uptake ability and elasticity of Rec1 with the strength and favourable biocompatibility of RSF we are able to develop hydrogels with tuneable properties. To our knowledge this is the first work to combine a resilin-based material with the abundantly available silk fibroin.

Rec1 was synthesised as reported in our previous work, and RSF aqueous solution was prepared *via* established procedures (ESI†).[5,13] The Rec1 and RSF solutions were prepared at concentrations of 20 wt% and 15 wt%, respectively, that correspond to the optimum concentration for this crosslinking reaction as identified for each system.[6,12] The formation of dityrosine crosslinks on irradiation of the Rec1/RSF blend was confirmed using Fluorescence spectroscopy. The presence of excitation and emission peaks at 298 and 406 nm, respectively, indicated the presence of dityrosine in the swollen Rec1/RSF hydrogels (Fig. S4, ESI†).[14–16]

An important property to consider when designing biomaterials for use in tissue regeneration is their water uptake capacity, which is related to their ability for supporting cell growth and also the elasticity and mechanical properties of the material. The water uptake capacity (h) of the RSF and Rec1/RSF hydrogels was calculated by measuring the mass of the dry and swollen gels over a period of time until equilibrium was reached (Fig. 1A). The RSF system reached an equilibrium h value of 0.59 ± 0.05. This was lower than reported for the Rec1 hydrogel, which ranged from 2 to 4.5 depending on the crosslink density.[6] The decreased ability for RSF to uptake water is attributed to the lower amount of polar residues (19%) present in the

[a] *Ian Wark Research Institute, ARC Special Research Centre, Mawson Lakes Campus, University of South Australia, Mawson Lakes, SA 5095, Australia. E-mail: namita.choudhury@unisa.edu.au*
[b] *CSIRO Livestock Industries, Queensland Bioscience Precinct, St Lucia 2067, Queensland, Australia*

† Electronic supplementary information (ESI) available: Synthesis procedures and characterisation data. See DOI: 10.1039/c5tb00970g

This journal is © The Royal Society of Chemistry 2015

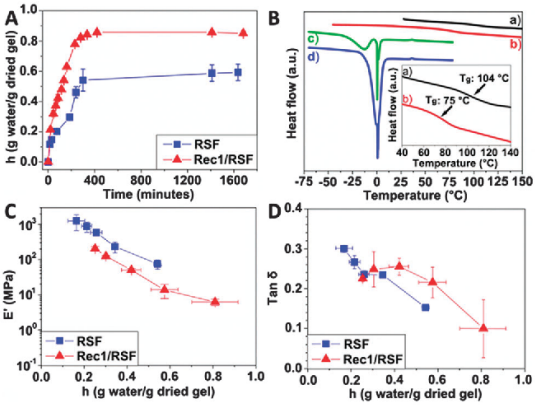


Fig. 1 (A) Plot of water uptake (h) as a function of time for the RSF and Rec1/RSF hydrogels. (B) DSC thermograms of hydrogels: (a) dried RSF, (b) dried Rec1/RSF, (c) RSF (h = 0.52) and (d) Rec1/RSF (h = 0.85). (C) and (D) E' and tan δ values obtained from DMA for RSF and Rec1/RSF hydrogels at different hydration levels. Data is presented as mean ± standard deviation.

structure of silk compared to Rec1 (46%). Therefore, by introducing the more hydrophilic Rec1 it was our aim to improve the water uptake ability of the hydrogel, while maintaining the advantageous properties of RSF, in particular its strength. The Rec1/RSF hydrogel displayed an equilibrium h value of 0.85 ± 0.02. This increase in water uptake is related not only to the increased hydrophilicity through incorporation of Rec1, but is also a result of changes in crosslink density and network structure, which will be investigated further. It also has implications for the elasticity of the hydrogels as water acts as a plasticiser. One-way ANOVA analysis was conducted at a number of time points to analyse the statistical significance of the differences in the water uptake of the RSF and Rec1/RSF hydrogels. It was determined that there were statistically significant differences between the RSF and Rec1/RSF h values at all time points of the water uptake curve as $p < 0.05$ for all time points (ESI†). This confirms that the Rec1/RSF hydrogel had a significant increase in water uptake than the RSF hydrogel, which can be attributed to differences in hydrophilicity. Also, changes in the network microstructure are expected to contribute to changes in the water uptake capacity and an investigation into this is in progress.

Thermogravimetric analysis (TGA) was employed to examine the composition and stability of the hydrogels (ESI†). The derivative of the TGA thermogram of the RSF hydrogel exhibited a single peak (292 °C) (Fig. S5, ESI†). However, the Rec1/RSF hydrogel showed multiple degradation peaks (232 °C and 309 °C), which is consistent with the behaviour of the Rec1 hydrogel.[6] This confirms the presence of Rec1 and RSF in the hybrid hydrogel.

The phase behaviour of the hydrogels is important to understand the molecular dynamics of the material in the dry and swollen states, which relates to the mechanical properties exhibited. The glass transition temperatures (T_g) of the RSF and Rec1/RSF hydrogels in the dehydrated and equilibrium swollen states were examined through the use of differential scanning calorimetry (DSC) (Discovery DSC, TA Instruments) (ESI†). The T_gs of the dehydrated RSF and Rec1/RSF hydrogels were indicated by a shift in the baseline at 104 °C and 75 °C, respectively (Fig. 1B). Determination of the T_g was conducted using the TRIOS software (TA Instruments) (ESI†). The absence of weight loss observed in the TGA curves at these temperatures confirms that this is the T_g as it indicates that this is indeed a physical process. The T_g for the RSF hydrogel is somewhat lower than that of the uncrosslinked silk protein. However, in our previous work we attributed this to the conformation of the hydrogel being predominantly amorphous in nature.[12] The T_g of the Rec1/RSF hydrogel was lower than that of the RSF hydrogel, which is attributed partly to the presence of the more amorphous Rec1. In addition, crosslink density is proportional to T_g, which indicates that a lower crosslink density of the Rec1/RSF hydrogel compared to RSF also contributes to the lower T_g observed.[17] This will be correlated with crosslink density calculations discussed later in the article.

The behaviour of the hydrogels in the swollen state has implications for their use in biomedical applications, such as tissue engineering. The runs for the equilibrium swollen hydrogels (Fig. 1B–D) were started at −75 °C to cover the largest temperature range possible. The T_g for swollen samples is below zero degrees due to plasticisation in the presence of water and thus we started at a lower temperature than for the dry samples to try and capture this. Ribeiro *et al.* and Weska *et al.* have both shown that freezing and low temperatures do not have an effect on the silk conformation for hydrogels or membranes.[18,19] Therefore, we do not expect the use of low temperature will have any effect on the silk structure of our hydrogels. The RSF hydrogel exhibited a shift in the T_g to −24.1 °C due to the plasticizing effect of the water and an exothermic peak due to the melting of ice was observed.[12] When analysing the Rec1/RSF hydrogel, a larger exothermic peak was observed. This is attributed to the increased amount of water present in the Rec1/RSF gel compared to the RSF hydrogel. In addition, the T_g was not observed in the temperature range measured as it was shifted to below the range of detection. This indicates that at room temperature in the swollen state, both hydrogels are elastic in nature, which is supported by the decreased storage modulus and tan δ values observed by DMA at high water uptake values.

In order to evaluate the viscoelastic properties of the co-crosslinked system, dynamic mechanical analysis (DMA) of the hydrogels was performed using the TA Instruments Q800 DMA. Hydrogel samples were studied using the tension clamp at a range of hydration values (ESI†). Fig. 1C and D depict the storage modulus (E') and tan δ values for the RSF and Rec1/RSF gels with increasing levels of hydration. The RSF hydrogel exhibited E' values of 1274.55 ± 594.61 MPa (h = 0.17 ± 0.04) to 78.05 ± 15.91 MPa (h = 0.54 ± 0.02). It was observed that the E' of the Rec1/RSF hydrogel was significantly lower than the RSF hydrogel and the values ranged from 209.65 ± 30.48 MPa (h = 0.25 ± 0.002) to 6.56 ± 1.35 MPa (h = 0.81 ± 0.11). This is several orders of magnitude larger than the E' reported for the Rec1 hydrogel (~0.002 MPa) and indicates that by forming a co-crosslinked system with Rec1 and RSF we are able to tune

the modulus values.[6] One-way ANOVA analysis was carried out to compare the E' values of the RSF and Rec1/RSF hydrogels at the equilibrium swelling water content of each sample (ESI†). The E' value for the equilibrium swollen Rec1/RSF hydrogel was statistically significantly lower than the E' of the equilibrium swollen RSF hydrogel as $p < 0.05$. In addition, the E' values for both samples at h values of ~0.55 and ~0.26 were analysed using the one-way ANOVA to compare the modulus properties of the hydrogels at the same water content. At both of these h values (~0.55 and ~0.26), the E' of the RSF and Rec1/RSF hydrogels were shown to be statistically significantly different ($p < 0.05$). From this it was concluded that the increased water content of the Rec1/RSF hydrogel was not the only factor that led to the decreased modulus when compared to the RSF hydrogel. It is proposed that differences in the crosslink density and network structure of the hydrogels are responsible for the differences in mechanical properties. An investigation into the network structure of the hydrogels using neutron scattering techniques is underway. The Rec1/RSF hydrogel possessed higher modulus values in comparison with a chemically crosslinked hybrid gel composed of chitosan and silk fibroin that reported E' values in the several tens to hundreds of kilopascals.[20] The authors observed that the addition of silk fibroin to chitosan resulted in stiffer materials with increased modulus values.[20] This is in agreement with our results that show that the incorporation of RSF to Rec1 produced a stiffer hydrogel than Rec1 alone. In addition, the modulus values for our Rec1/RSF hydrogel are significantly higher than other RLP-based chemically crosslinked hydrogels that have values in the range of tens of kilopascals.[7,8] This will allow us to apply this hybrid material to such applications where increased stiffness is required.

The presence of water increased the chain mobility of the RSF and Rec1/RSF hydrogel networks as indicated by decreased T_g values. The decreased stiffness was confirmed by the decreasing E' and tan δ values with increasing levels of hydration indicating predominantly elastic behaviour.[21] However, the viscoelastic behaviour was observed as the water content decreased, evident by the increase in tan δ values. The differences in elasticity of the Rec1/RSF and RSF hydrogels is attributed to changes in the microstructure and also the increased hydrophilicity that allows the hydrogel to retain a larger proportion of water.

The crosslink density (n), which quantifies the number of moles of active network chains per unit volume (mol m^{-3}), was calculated for the swollen hydrogels according to the rubber elasticity theory using the expression: $n = E'/3RT = \rho/M_c$.[22–24] M_c represents the molecular weight between crosslinks (g mol^{-1}), E' is the tensile storage modulus (MPa) as measured from DMA experiments, R is the universal gas constant (8.314 J mol K^{-1}), T is the absolute temperature (298 K) and ρ is the density for RSF (1.421 g cm^{-3}) and Rec1/RSF (1.352 g cm^{-3}). The n values for the RSF and Rec1/RSF hydrogels in the swollen state were calculated to be 9545.6 (±3097.6) mol m^{-3} and 840.8 (±240.8) mol m^{-3}, respectively. As the RSF hydrogel exhibited a higher storage modulus value than Rec1/RSF, consequently the RSF hydrogel had a significantly higher crosslink density. Using the density, the M_c values for the RSF and Rec1/RSF hydrogels were calculated as 157.1 (±51.0) g mol^{-1} and 1676.7 (±480.2) g mol^{-1}, respectively. As the M_c is inversely proportional to the E', RSF has a lower molecular weight between crosslinks when compared to the Rec1/RSF hydrogel, which accounts for the higher modulus values for the RSF hydrogel. Elvin *et al.* measured the modulus of ruthenium-crosslinked Rec1 to be 2.5 kPa in the swollen state and thus calculated the M_c of crosslinked Rec1 to be 14 161 g mol^{-1}.[14] This was higher than the predicted value (8500 g mol^{-1}) that was calculated based on the amount of tyrosine present in the chains and relied on the assumption that all di-tyrosine crosslinks are intermolecular. However it is possible that many of the crosslinks formed are intramolecular, which do not contribute to mechanical strength.[14,25] Sando *et al.* also used this method for crosslinking α-keratose extracted from wool with a tyrosine content of 3.8 mol%.[26] The modulus values for the di-tyrosine crosslinked α-keratose gels ranged from 9.5 to 53.5 kPa, depending on the solvent conditions and reactant concentrations.[26] This was reflected in M_c values ranging from 12 200 to 21 400 g mol^{-1}, which is in agreement with the estimated value (17 800 g mol^{-1}) based on the number of tyrosine residues and indicates that the majority of di-tyrosine crosslinks are intermolecular.[26] In comparison with the Rec1 and α-keratose hydrogels, the RSF and Rec1/RSF hydrogels exhibited lower M_c values. This is because the hydrogels containing silk fibroin possess higher modulus values. Furthermore, a higher M_c for the Rec1/RSF system compared to the RSF hydrogel was also reflected in the lower T_g observed for the Rec1/RSF hydrogel. In order to gain a deeper understanding of the microstructure of the hydrogels and how this correlates to the observed behaviour, neutron scattering studies are currently being undertaken.

The secondary structure of the hydrogels was measured using Photoacoustic Fourier Transform Infrared Spectroscopy (PA-FTIR) (Nicolet Magna-IR Spectrometer 750). The Magic Plot software was used to fit the Amide I region to determine the secondary structure content (Fig. S7, ESI†).[27] It was observed that the secondary structure of the Rec1/RSF hydrogels was very similar to that of the measured RSF hydrogel conformations (Table 1). The dominant structure for both hydrogels was β-turn, with smaller contributions from random coil and β-sheet structures. Other RLP hydrogels have also been shown to be dominated by random and β-turn conformations upon covalent crosslinking.[7] It has been shown that β-sheet contents of ~55% were observed for physically gelled silk compared to ~20% for silk fibroin solutions, which is much higher than the

Table 1 Secondary structure content of RSF and Rec1/RSF hydrogels obtained from Amide I region of PA-FTIR spectra

Wavenumber range (cm^{-1})	Secondary structure	RSF (%)	Rec1/RSF (%)
1616–1621	Aggregate β-strand/ β-sheets (weak, intermolecular)	15.9 ± 0.2	13.3 ± 0.8
1628–1637	β-Sheets (strong, intramolecular)	16.7 ± 1.8	16.6 ± 1.2
1638–1655	Random coils	17.7 ± 0.6	20.8 ± 4.0
1663–1685	β-Turns	35.2 ± 0.1	35.5 ± 5.8
1697–1703	β-Sheets (weak, intermolecular)	14.5 ± 1.5	13.7 ± 2.2

This journal is © The Royal Society of Chemistry 2015

values reported here.[20,28] Therefore, this method of photo-crosslinking does not induce the random coil to beta-sheet transition as has been observed in silk fibroin hydrogels that form due to random coil to beta-sheet transitions. Also, from the FTIR analysis it is clear that the RSF and Rec1/RSF hydrogels have no significant differences in terms of secondary protein structure.

Conclusions

In this work we have successfully established a rapid ruthenium-mediated photo-crosslinking method to form hybrid hydrogel materials using Rec1 and RSF for the first time. The Rec1/RSF hydrogel showed improved water uptake capacity compared to the RSF hydrogel, which is important for regenerative medicine applications. In addition, we have shown that by combining the hard and soft phases of RSF and Rec1 we are able to tune the mechanical properties and achieve an E' value of $\sim$6.56 MPa when swollen, which is significantly higher than the Rec1 hydrogel (0.002 MPa). This rapid photo-crosslinking method is a simple way to tune biomaterial properties by taking advantage of the remarkable elastic properties of resilin with the biocompatible and strength properties of silk fibroin. This work serves as a platform for designing biomaterials using resilin and silk based materials with tuneable properties that can potentially be applied to a range of tissue engineering applications. Future work is underway to gain an understanding of the level of tuneability that is possible by varying the ratios of Rec1 and RSF.

Acknowledgements

This work has been financially supported by the Australian Research Council (ARC) through Discovery Grant funding.

Notes and references

1 J. Zhu and R. E. Marchant, *Expert Rev. Med. Devices*, 2011, **8**, 607–626.
2 Y. Wu, C. Li, F. Boldt, Y. Wang, S. L. Kuan, T. T. Tran, V. Mikhalevich, C. Fortsch, H. Barth, Z. Yang, D. Liu and T. Weil, *Chem. Commun.*, 2014, **50**, 14620–14622.
3 X. Jia and K. L. Kiick, *Macromol. Biosci.*, 2009, **9**, 140–156.
4 N. A. Peppas, J. Z. Hilt, A. Khademhosseini and R. Langer, *Adv. Mater.*, 2006, **18**, 1345–1360.
5 C. M. Elvin, A. G. Carr, M. G. Huson, J. M. Maxwell, R. D. Pearson, T. Vuocolo, N. E. Liyou, D. C. C. Wong, D. J. Merritt and N. E. Dixon, *Nature*, 2005, **437**, 999–1002.
6 M. Y. Truong, N. K. Dutta, N. R. Choudhury, M. Kim, C. M. Elvin, K. M. Nairn and A. J. Hill, *Biomaterials*, 2011, **32**, 8462–8473.
7 L. Li, Z. Tong, X. Jia and K. L. Kiick, *Soft Matter*, 2013, **9**, 665–673.
8 C. L. McGann, E. A. Levenson and K. L. Kiick, *Macromol. Chem. Phys.*, 2013, **214**, 203–213.
9 L. Li and K. Kiick, *Front. Chem.*, 2014, 2.
10 S. Chan and B. Gantenbein-Ritter, *Swiss Med. Wkly.*, 2012, **142**, w13598.
11 M. Mondal, K. Trivedy and S. Nirmal Kumar, *Caspian J. Env. Sci.*, 2007, **5**, 63–76.
12 J. L. Whittaker, N. R. Choudhury, N. K. Dutta and A. Zannettino, *J. Mater. Chem. B*, 2014, **2**, 6259–6270.
13 A. Ajisawa, *Sen'i Gakkaishi*, 1968, **24**, 61–64.
14 C. M. Elvin, A. G. Carr, M. G. Huson, J. M. Maxwell, R. D. Pearson, T. Vuocolo, N. E. Liyou, D. C. C. Wong, D. J. Merritt and N. E. Dixon, *Nature*, 2005, **437**, 999–1002.
15 M. Correia, M. T. Neves-Petersen, P. B. Jeppesen, S. Gregersen and S. B. Petersen, *PLoS One*, 2012, **7**, e50733.
16 E. Smail, P. Briza, A. Panagos and L. Berenfeld, *Infect. Immun.*, 1995, **63**, 4078.
17 K. S. Anseth, C. N. Bowman and L. Brannon-Peppas, *Biomaterials*, 1996, **17**, 1647–1657.
18 M. Ribeiro, M. A. de Moraes, M. M. Beppu, F. J. Monteiro and P. M. Ferraz, *Biomatter*, 2014, **4**, e28536.
19 R. F. Weska, W. C. Vieira Jr, G. M. Nogueira and M. M. Beppu, *J. Mater. Res.*, 2009, **12**, 233–237.
20 S. S. Silva, A. Motta, M. T. Rodrigues, A. F. M. Pinheiro, M. E. Gomes, J. F. Mano, R. L. Reis and C. Migliaresi, *Biomacromolecules*, 2008, **9**, 2764–2774.
21 A. Saarai, T. Sedlacek, V. Kasparkova, T. Kitano and P. Saha, *J. Appl. Polym. Sci.*, 2012, **126**, E79–E88.
22 Y. Wang, G. A. Ameer, B. J. Sheppard and R. Langer, *Nat. Biotechnol.*, 2002, **20**, 602–606.
23 V. Krongauz, *J. Therm. Anal. Calorim.*, 2010, **102**, 435–445.
24 I. Djordjevic, N. R. Choudhury, N. K. Dutta and S. Kumar, *Polymer*, 2009, **50**, 1682–1691.
25 C. M. Elvin, A. G. Brownlee, M. G. Huson, T. A. Tebb, M. Kim, R. E. Lyons, T. Vuocolo, N. E. Liyou, T. C. Hughes, J. A. M. Ramshaw and J. A. Werkmeister, *Biomaterials*, 2009, **30**, 2059–2065.
26 L. Sando, M. Kim, M. L. Colgrave, J. A. M. Ramshaw, J. A. Werkmeister and C. M. Elvin, *J. Biomed. Mater. Res., Part A*, 2010, **95A**, 901–911.
27 X. Hu, D. Kaplan and P. Cebe, *Macromolecules*, 2006, **39**, 6161–6170.
28 A. Matsumoto, J. Chen, A. L. Collette, U.-J. Kim, G. H. Altman, P. Cebe and D. L. Kaplan, *J. Phys. Chem. B*, 2006, **110**, 21630.

This journal is © The Royal Society of Chemistry 2015

5.1.2 Supplementary information

S5.1.2.1 Material preparation

Rec1 was synthesised by cloning, expression, and purification of exon 1 of the *Melanogaster* gene CG15920, as a water soluble protein as described elsewhere[1, 2]. Rec1 has a molecular weight of 28.4 kDa with 310 amino acid residues as previously characterised.[1, 2]

Bombyx mori silk was purchased as raw silk from Beautiful Silks, Australia. The raw silk was degummed by boiling in aqueous 0.02 M Na_2CO_3 for 30 minutes. The silk was rinsed in distilled water (DW) three times and allowed to dry at room temperature overnight. The fibroin was then dissolved in a calcium chloride, water, ethanol solution ($CaCl_2/H_2O$/EtOH 1/8/2 molar ratio), with a liquor ratio of 1:20, at 70^{o}C for 3 hours. Following this, the solution was dialysed using SnakeSkin dialysis tubing (3.5 kDa molecular weight cut-off) (ThermoFisher Scientific) for several days and centrifuged at 10,000 rpm and 20^{o}C for 20 minutes. The solution was diluted using DW to obtain the concentrations required for the experiments.

S5.1.2.2 Hydrogel Synthesis

The Rec1 and RSF solutions were prepared at concentrations of 20 wt% and 15 wt%, respectively, that correspond to the optimum concentration for this crosslinking reaction as identified for each system. The RSF solution was added to the Rec1 solution in a 1:1 volumetric ratio giving a mass ratio of 1:0.75 (Rec1:RSF). The catalyst (tris(2,2-bipyridyl) dichloro ruthenium(II) hexahydrate) and electron acceptor (ammonium persulphate) were employed at concentrations of 5 mM and 28 mM, respectively, as established in our previous work.[3] The combined Rec1/RSF solution was exposed to a 250 W light source for 120 seconds, and the gels were turned over and exposed for a further 60 seconds to ensure full crosslinking. Samples were leached in distilled water to remove unreacted material and characterised for water uptake capacity, thermal behaviour, mechanical properties, and secondary structure content.

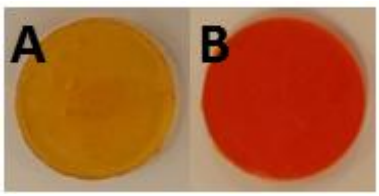


Figure S5.1 Photograph of leached A) RSF hydrogel and B) Rec1/RSF hydrogel

S5.1.2.3 Material characterization

RSF was analysed with nuclear magnetic resonance (NMR) in D_2O. ^1H NMR spectra were obtained on a 300 MHz Bruker Avance spectrometer operating at 300.138 MHz. Reference relative to 0 ppm for TMS. The predominant presence of glycine (Gly) and alanine (Ala) that makes up the structure of silk fibroin has been confirmed (Figure S5.2).[4] In addition, the presence of the tyrosine groups required for crosslinking has also been confirmed through the peaks in the spectra, which were correlated with literature values.[4] Molecular weight range was determined using SDS-PAGE and was found to be from approximately 37 to 200 kDa (Figure S5.3).

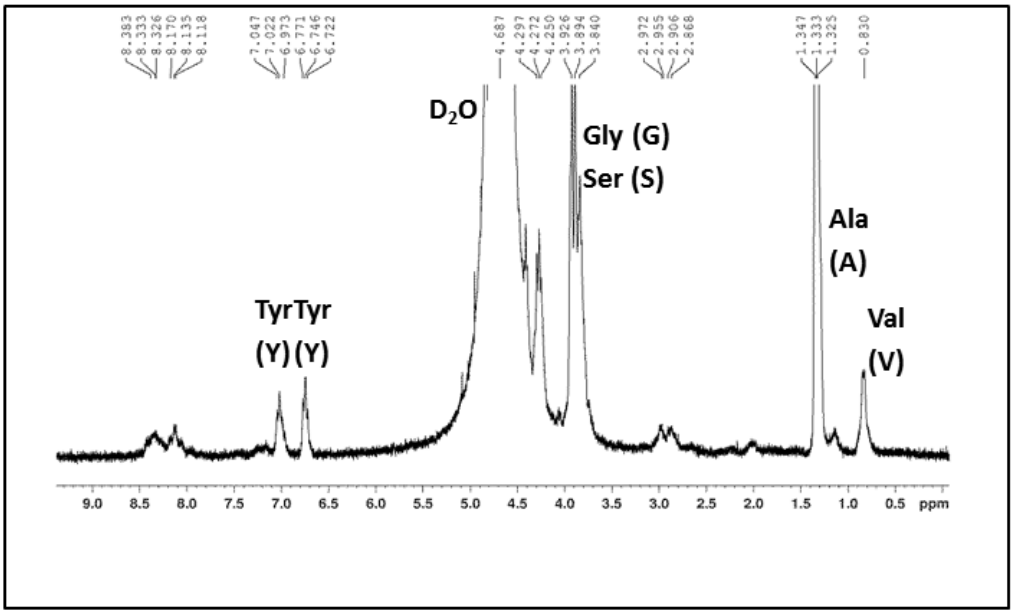


Figure S5.2 NMR of RSF in D_2O.

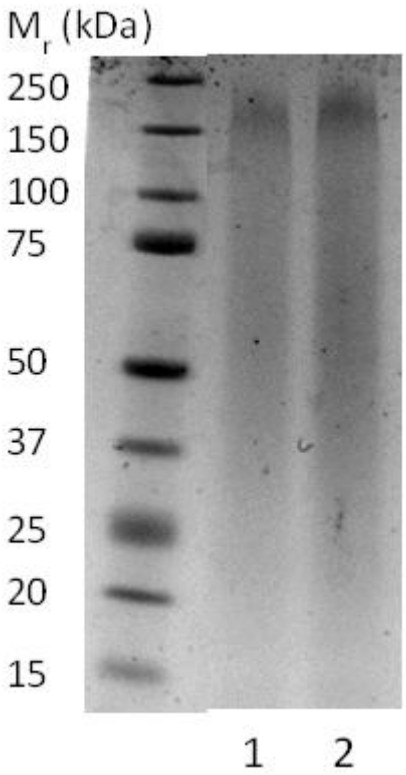


Figure S5.3 SDS-PAGE of RSF at 20 μg/mL (Lane 1) and 40 μg/mL (Lane 2).

Fluorescence measurements using the Cary Eclipse Fluorescence Spectrometer were undertaken to confirm the formation of dityrosine crosslinks in the Rec1/RSF hydrogel. A sample gel was prepared with a Rec1 concentration of 67 mg/mL, RSF concentration of 50 mg/ml, Ru(II)$(bpy)_3^{2+}$ concentration of 0.2 mM, and an APS concentration of 20 mM. Lower concentrations of Rec1, RSF, and Ru(II)$(bpy)_3^{2+}$ were used to prepare a gel that was transparent in order to be suitable for fluorescence measurements using the Cary Eclipse Fluorescence Spectrometer. However, the same ratio of Rec1 to RSF was employed. A corresponding solution of Rec1/RSF at the same concentrations, without Ru(II)$(bpy)_3^{2+}$ and APS was prepared for comparison. Figure S5.4 shows the fluorescence spectra of the hydrogel and solution. The peak at 406 nm in the emission spectra of the Rec1/RSF hydrogel confirms the presence of dityrosine crosslinks in the gel structure that is not exhibited for the Rec1/RSF solution.[1, 5, 6]

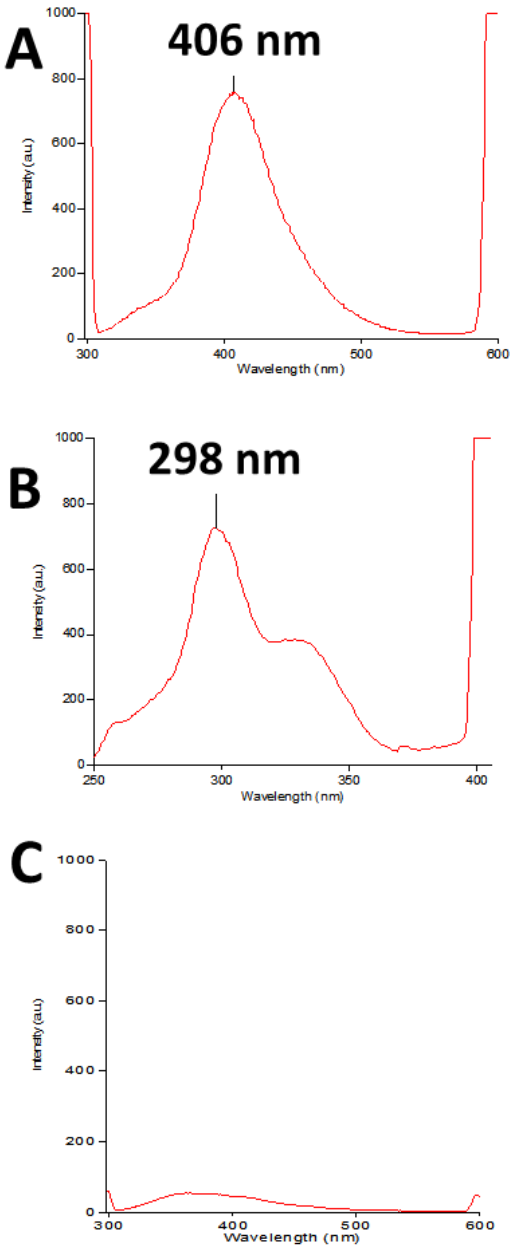


Figure S5.4 A) Fluorescence emission spectra of Rec1/RSF hydrogel (Ru: 0.2 mM and APS: 20 mM), excited at 298 nm. B) Fluorescence excitation spectra of Rec1/RSF hydrogel (Ru: 0.2 mM and APS: 20 mM) measuring with emission at 406 nm. C) Fluorescence emission spectra of corresponding Rec1/RSF solution, excited at 298 nm.

To measure the water uptake capacity of the hydrogels they were first vacuum dried to constant weight, which was measured using a microbalance capable of measuring four decimal places. Then the gels were immersed in DW and the weight was monitored at different time intervals. The water uptake (h) was calculated using equation 1, where w_s and w_d refers to the mass of the swollen and dried gels, respectively.

$$h = \frac{w_s - w_d}{w_d} \quad (1)$$

Thermogravimetric analysis of the vacuum dried RSF and Rec1/RSF hydrogels was conducted using the TA Instruments Discovery TGA. The experiments were run in a nitrogen atmosphere under a heating rate of 10˚C/min.

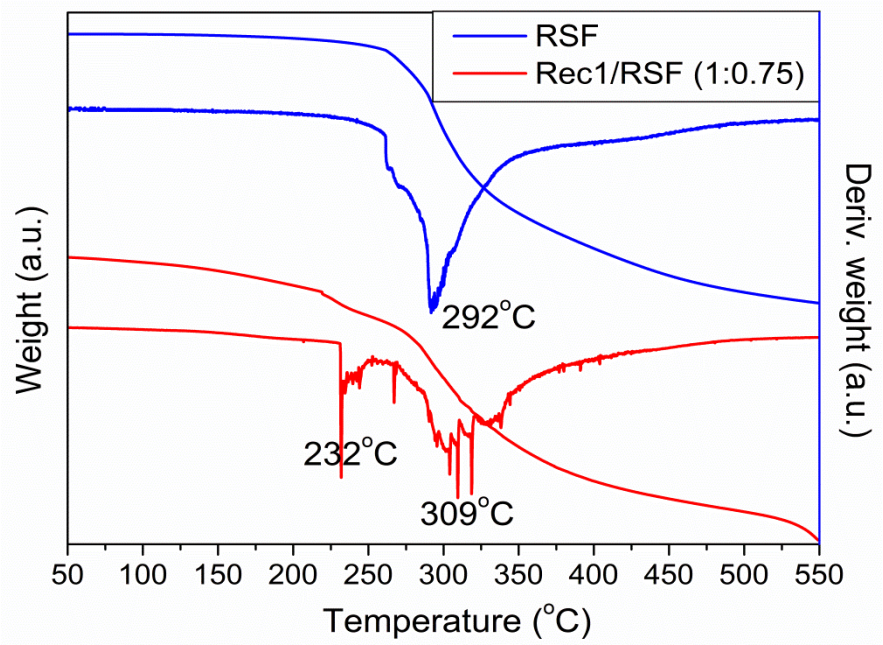


Figure S5.5 TGA thermogram of RSF and Rec1/RSF hydrogels.

The TA Instruments Discovery DSC was used to measure the thermal behaviour of the hydrogels in the dry and swollen states. The instrument was calibrated for baseline and cell constant prior to conducting the experiments. Samples were weighed and sealed in hermetic aluminium pans for measurement with an empty pan used as a reference. Samples were run at a heating rate of 10^{o}C/min under a nitrogen atmosphere (50 mL/min). The TRIOS software was used to determine the T_g of the hydrogels as shown in Figure S5.6.

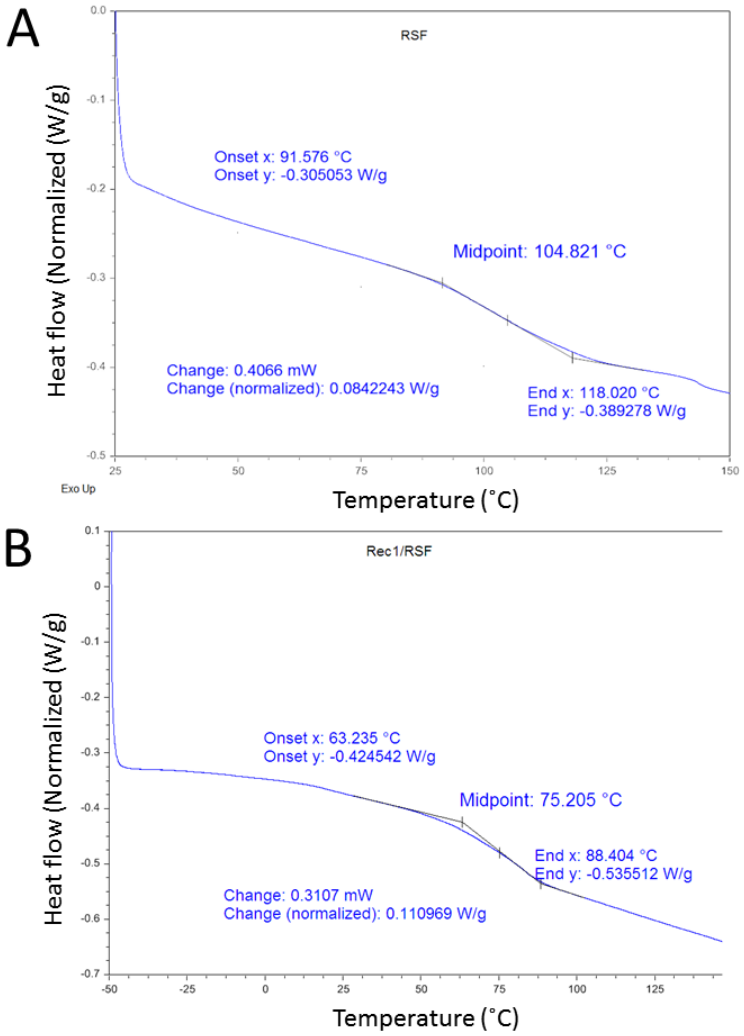


Figure S5.6 Representative DSC thermograms of dried A) RSF and B) Rec1/RSF hydrogels with determination of T_g shown.

The mechanical properties of the hydrogels were measured using the TA Instruments Q800 DMA equipped with humidity accessory. Samples of rectangular geometry were immersed in DW for 24 hours to reach equilibrium water uptake. Samples were mounted using the tension clamp and run at ambient temperature with an amplitude of 10 μm and a preload force of 0.010 N. DMA runs were conducted with humidity ramping to 50% and held for the one hour at isothermal temperature conditions. The samples were run in consecutive runs with the moisture content measured before and after each run to correlate the values with the moisture level, which decreased with time.

Infrared spectra of the RSF and Rec1/RSF hydrogels were acquired using the Nicolet Magna-IR Spectrometer 750 in photo-acoustic mode with a carbon black reference. The range used

was 400 to 4000 cm^{-1} and the data was processed with the Omnic computer program. The amide I region was Gaussian curve fitted to determine the secondary structure components of the hydrogels. This was undertaken using the Magic Plot software (Figure S5.7).

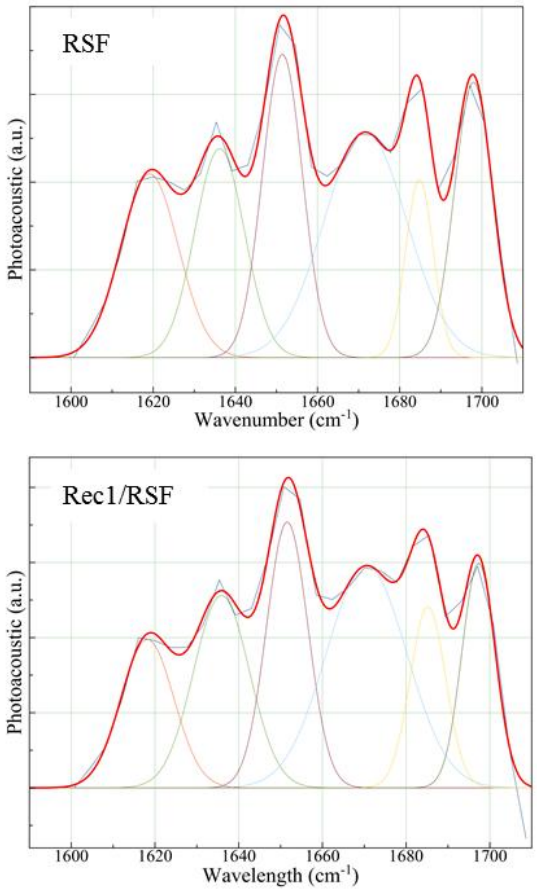


Figure S5.7 PA-FTIR spectra of RSF and Rec1/RSF hydrogels in the amide I region, showing Gaussian fitting to determine the secondary structure content.

S5.1.2.5 Statistical analysis – One-way ANOVA

One-way ANOVA analysis of the water uptake (h) data and E' data was carried out using Microsoft Excel to determine whether there are statistically significant differences between the properties of the RSF and Rec1/RSF hydrogels. The differences between the h values of the RSF and Rec1/RSF hydrogels at time points of 15, 30, 75, 300, 1410 and 1635 minutes was analysed. For all time points the $p<0.05$, which meant that there was statistically significant differences between the water uptake of the RSF and Rec1/RSF hydrogels throughout the water uptake process. An example of the one-way ANOVA analysis at 1635 minutes is shown in Figure S5.8A.

For the E' values, one-way ANOVA analysis was employed to compare between the E' of RSF and Rec1/RSF gels at the equilibrium swelling content of each respective gel (i.e. h=~0.55 for RSF and h=~0.81 for Rec1/RSF). The $p<0.05$ and thus the results were statistically different. We also compared the E' values at the same water contents (h=~0.55 and ~0.26). Also, at h values of 0.55 and 0.26, the $p<0.05$, which indicates that even at the same water content the E' values of the RSF and Rec1/RSF hydrogels are statistically significantly different. An example of the one-way ANOVA analysis for the E' values of the equilibrium swollen RSF and Rec1/RSF hydrogels is shown in Figure S5.8B.

A

Anova: Single Factor

SUMMARY

Groups	Count	Sum	Average	Variance
RSF h (time=1635 mins)	2	1.186578	0.593289	0.002882
Rec1/RSF h (time=1635 mins)	2	1.701418	0.850709	0.000288

ANOVA

Source of Variation	SS	df	MS	F	P-value	F crit
Between Groups	0.066265	1	0.066265	41.80687	0.023094	18.51282
Within Groups	0.00317	2	0.001585			
Total	0.069435	3				

B

Anova: Single Factor

SUMMARY

Groups	Count	Sum	Average	Variance
RSF E' equilibrium swollen	4	312.19	78.0475	253.2083
Rec1/RSF E' equilibrium swollen	3	18.106	6.035333	1.739092

ANOVA

Source of Variation	SS	df	MS	F	P-value	F crit
Between Groups	8889.861	1	8889.861	58.2481	0.000614	6.607891
Within Groups	763.1031	5	152.6206			
Total	9652.964	6				

Figure S5.8 One-way ANOVA analysis of the: A) water uptake (h) data for the RSF and Rec1/RSF hydrogels at time = 1635 minutes; and B) storage modulus (E') data for the equilibrium swollen RSF and Rec1/RSF hydrogels.

References

1. C. M. Elvin, A. G. Carr, M. G. Huson, J. M. Maxwell, R. D. Pearson, T. Vuocolo, N. E. Liyou, D. C. C. Wong, D. J. Merritt and N. E. Dixon, *Nature*, 2005, **437**, 999-1002.
2. M. Kim, C. Elvin, A. Brownlee and R. Lyons, *Protein Expression Purif.*, 2007, **52**, 230-236.
3. J. L. Whittaker, N. R. Choudhury, N. K. Dutta and A. Zannettino, *J. Mater. Chem. B*, 2014, **2**, 6259-6270.
4. Zainuddin, T. T. Le, Y. Park, T. V. Chirila, P. J. Halley and A. K. Whittaker, *Biomaterials*, 2008, **29**, 4268-4274.
5. M. Correia, M. T. Neves-Petersen, P. B. Jeppesen, S. Gregersen and S. B. Petersen, *PLoS ONE*, 2012, **7**, e50733.
6. E. Smail, P. Briza, A. Panagos and L. Berenfeld, *Infect. Immun.*, 1995, **63**, 4078.

5.2 Engineered DN hydrogels from regenerated silk fibroin and poly(N-vinylcaprolactam)

5.2.1 Abstract

The development of novel hydrogels that possess adequate elasticity and toughness to withstand mechanically active environments, along with being biocompatible, remains a significant challenge in the design of materials for tissue engineering applications. In this study, a family of regenerated silk fibroin (RSF) based double network (DN) hydrogels were fabricated for the first time using a rapid one-pot method. The DN hydrogels combine the rigid covalently crosslinked RSF with the softer poly(N-vinycaprolactam) through strong physical interactions. The formation of these DN hydrogels resulted in an improvement of the water uptake capacity, elasticity and toughness compared to the individual RSF hydrogel. The elasticity of the RSF/PVCL DN hydrogels was closer to that of native cartilage, which makes them promising materials for cartilage regeneration applications.

5.2.2 Introduction

Developing hydrogels that possess the combined properties of deformable characteristics, toughness, elasticity, responsiveness and biocompatibility is a grand challenge in the field of tissue engineering. Gels designed for mechanically active environments must be able to withstand environmental forces in addition to serving as a guide of tissue regeneration. Several approaches have been reported to tune gel modulus, including varying the crosslink density and forming different types of hybrid gels.

A new type of hydrogel called a double network (DN) hydrogel was reported by Gong et al. that was formed by a two-step process that resulted in an interpenetrating network containing a highly crosslinked rigid polymer in the presence of a softer more loosely crosslinked one.[1, 2] The proposed mechanism for toughening of the DN hydrogels is due to the high level of heterogeneity in the network and strong network entanglement, combined with energy dissipation as a result of delocalization of the fracture bonds of the first network in the large volume around the crack tip.[2-5] Despite the vast improvement in mechanical properties that have been exhibited by these DN hydrogels, the classical fabrication process is very time consuming and usually takes 1-2 days.[2] To address this, several one-pot methods have been reported.[6-8] In particular, Chen et al. reported a one-pot method to fabricate a hybrid DN hydrogel consisting of a hydrogen bonded agar network and a covalently crosslinked

polyacrylamide (PAAm) network.[7] This DN hydrogel demonstrated superior mechanical properties, however the process still required 1-2 hours to complete.[7] Several other routes for enhancing gel performance through the combination of weak and strong bonds have been recognised, including using particle-filled hydrogels, hydrophobic associations, microgel-reinforced hydrogels and supramolecular chemistry.[2, 9-14]

The synthesis of these gels with tuneable modulus currently attracts considerable attention because of increasing applications in the field of tissue engineering, particularly cartilage and spinal disc repair/regeneration or other repetitive load-bearing applications. The mechanical requirements for tissue replacements vary greatly depending on the location and function of the human tissue. For instance, biomaterials for articular cartilage tissue engineering require a modulus of ~180 to 2500 kPa and thus this must be taken into account when designing biomaterials for this application.[15-17] Despite these recent advances, there is a distinct need to develop more efficient methods to fabricate DN hydrogels that exhibit improved and tuneable mechanical characteristics, as well as gaining a deeper understanding into their structure-property relationship.[2] In addition to the mechanical properties of the hydrogel, such as elasticity and toughness, the water swelling capability and ability to serve as a guide for cell attachment, proliferation and differentiation are all essential to achieve the goal of successful tissue regeneration.

Amongst various synthetic and biosynthetic biomaterials, *Bombyx mori* silk fibroin has been studied extensively due to its remarkable mechanical strength and biocompatibility properties.[18, 19] Regenerated silk fibroin (RSF) that can be extracted from raw silk has been physically and chemically crosslinked by a number of methods to form three-dimensional hydrogels.[20-28] In our recent work, a new, rapid method of photo-crosslinking RSF to form a hydrogel with di-tyrosine crosslinks was identified and the properties of the resultant material were studied.[29] The RSF hydrogel exhibited a storage modulus in the MPa range, and its ability to support cell attachment and growth were established.[29] In addition, this mode of crosslinking using light allows for a minimally invasive injectable delivery of reactants followed by crosslinking on exposure to light, which is advantageous for tissue engineering applications. However, it is important to tune the hydrogel stiffness and improve its water uptake capacity of the hydrogels in order to develop a multi-functional hydrogel.

Poly(N-vinylcaprolactam) (PVCL) is a thermo-responsive synthetic polymer with a lower critical solution temperature (LCST) in the physiological temperature range (~32-35˚C).[30-32]

In addition, lactam polymers, such as PVCL, have superior biocompatibility to poly(N-isopropylacrylamide) (PNIPAM), which is another widely studied thermo-responsive polymer, due to their stability against hydrolysis.[33, 34] Whilst PVCL possesses useful thermo-responsiveness and biocompatibility, it is a relatively soft material, with engineering modulus (E) of 30.1 ± 6.6 kPa and 940 ± 220 kPa at temperatures of 22˚C and 47.5˚C, respectively, which limits its use for tissue engineering applications.[35]

Earlier work by a few authors have shown that RSF and PVCL form stable hydrogen bonding interactions, which have been exploited to fabricate coatings and capsules.[19, 36] So far there has been no study on the effect of RSF on the phase behaviour of PVCL in solution. A range of DN hydrogels containing the combination of covalent and non-covalent interactions were prepared by combining RSF and PVCL in solution, followed by photo-crosslinking the RSF component using the ruthenium-mediated method. This resulted in a hybrid hydrogel with a highly crosslinked rigid phase (RSF) and a physically entrapped soft component (PVCL). By keeping the RSF/PVCL solution at a temperature lower than the LCST (<32˚C) prior to crosslinking, phase separation of PVCL was prevented. However, during crosslinking the solution temperature increased to room temperature, which allowed for the coil-to-globule transition of PVCL and promoted interactions between RSF and PVCL. The advantage of this method is that it is possible to crosslink the hydrogels in a short period of time (~3 minutes), which to our knowledge is much less than any other method reported for DN fabrication to date, and also has the ability to be crosslinked *in situ*. Different compositions were employed to develop an understanding of how the hard and soft components dictate the observed bulk properties of the hydrogels. The RSF/PVCL hydrogels were characterised using a range of swelling, thermal, mechanical and spectroscopic methods to evaluate their potential for use in tissue engineering applications.

5.2.3 Experimental

5.2.3.1 Materials

Bombyx mori silk was purchased as raw silk from Beautiful Silks, Australia. Aqueous regenerated silk fibroin (RSF) solutions were prepared and characterized as described in previous work.[37]

Poly(N-vinylcaprolactam) (PVCL) was prepared via free radical polymerisation of the VCL monomer with 2,2'-azoisobutyronitrile (AIBN) as the initiator and toluene as the solvent. The reaction proceeded for 24 hours under nitrogen atmosphere at 70˚C. The polymer was

recovered through precipitation in diethyl ether and purified by dissolving PVCL in a mixture of acetone and water (3:7), followed by precipitation by heating the solution to 80°C. This process was repeated twice, and the polymer was then dried at room temperature and finally vacuum dried at 50°C for 3 hours to remove any residual moisture. Nuclear magnetic resonance (NMR) spectroscopy was used to confirm the identity and purity of the polymer (S5.2.8.1). Capillary viscometry was employed to determine the molecular weight of the polymer (Figure S5.2.8.2).

5.2.3.2 Dynamic light scattering (DLS)

Solutions of PVCL and RSF with concentrations of 10 mg/ml were prepared in distilled water (DW) and filtered with 0.45 μm syringe filters. RSF/PVCL blends of mass ratio 10:90, 20:80, 30:70, and 40:60 were prepared and sonicated for several minutes to allow adequate distribution of particles. The solutions were transferred into low volume sizing cuvettes for analysis using the Malvern Zetasizer NanoZS. The particle size was measured at temperatures ranging from 4°C to 41°C with 2°C increments. Samples were equilibrated for 10 minutes at each temperature.

5.2.3.3 Hydrogel preparation

Suitable network formation chemistry, combining physical entanglement and association was used to prepare RSF/PVCL solutions with volumetric ratios of 90:10, 80:20, 70:30 and 60:40. Aqueous solutions of PVCL (5%) were added drop wise to solutions of RSF (15%), mixed and kept on ice prior to crosslinking to prevent phase separation. Following this, the RSF/PVCL co-assemblies were photo-crosslinked as previously described, with tris(2,2-bipyridyl)dichlororuthenium(II) ($Ru(II)(bpy)_3^{2+}$) and ammonium peroxodisulfate (APS) concentrations of 5 mM and 28 mM, respectively, at room termperature.[29] The gels were leached in distilled water (DW) for several days and vacuum dried prior to characterisation.

5.2.3.4 Thermogravimetric analysis (TGA)

TGA of the RSF gel, PVCL, and RSF/PVCL 90:10, 80:20, 70:30 and 60:40 gels was performed using the TA Instruments Discovery TGA to examine the composition of the hydrogels. The TGA experiments were run in a nitrogen atmosphere at a heating rate of 10°C/min. The mass ratio of RSF and PVCL in the solid hydrogel after crosslinking was determined from the TGA thermograms. The residual mass due to PVCL was negligible (~1%), therefore it was assumed that the residue was due to the RSF as the individual RSF

hydrogel was shown to have ~40% residue. The proportions of RSF and PVCL were calculated by taking the mass % at the plateau of each derivative.

5.2.3.5 Water uptake studies

For water uptake studies, the gels were vacuum dried to determine the dry weight (w_d) and immersed in DW. The weight of the swollen gel (w_s) was taken at different time intervals to monitor the water uptake and determine the equilibrium value. The weight of the samples was monitored using an accurate microbalance capable of measuring four decimal places. The water uptake (h) was determined using equation 1, where w_s is the weight of the swollen gel at varying time intervals and conditions, and w_d is the dry weight of the crosslinked gel.

$$h = \frac{w_s - w_d}{w_d} \quad (1)$$

5.2.3.6 Differential scanning calorimetry (DSC)

DSC measurement of the RSF/PVCL samples at different ratios was conducted using the TA Instruments Discovery DSC. The instrument was calibrated for baseline and cell constant prior to running the experiments. The samples were sealed in hermetic aluminium pans for use in the DSC experiment, and an empty pan was used as the reference. The temperature range of experiments was from -75°C to 300°C, with a heating rate of 10°C/min and under a controlled nitrogen gas flow rate of 50 ml/min.

5.2.3.7 Dynamic mechanical analysis (DMA)

DMA was conducted on the RSF/PVCL hydrogels using the TA Instruments Q800 DMA. The samples of rectangular geometry were immersed in DW initially for 24 hours to reach equilibrium water uptake before clamping. Then the samples were mounted using the tension clamp and run at ambient temperature with an amplitude of 10 μm and a preload force of 0.010 N to determine the modulus values for each RSF/PVCL hydrogel composition at equilibrium swelling.

5.2.3.8 Tensile testing

Tensile testing was performed in extension mode using a Hounsfield Universal Tensiometer equipped with a 1 kN load cell. Rectangular RSF dehydrated and equilibrium swollen hydrogels and S70P30 equilibrium swollen hydrogel samples were mounted and tested at room temperature with a constant velocity of 10 mm/min. The toughness (work to fracture) was calculated by integrating the stress-strain curve to obtain the area under the curve up to failure.

5.2.3.9 Fourier transform infrared spectroscopy

In order to investigate the secondary structure of the RSF/PVCL hydrogels Fourier Transform infrared (FTIR) spectroscopy was conducted with the Nicolet Magna-IR Spectrometer 750 in photo-acoustic mode using a carbon black reference. The spectra were obtained in the range 400 to 4000 cm^{-1} and the data was processed via the Omnic computer program. The amide I region was selected for investigation as it is commonly used to elucidate the secondary structure components of RSF as it corresponds to the C=O stretching bonds in the peptide backbone.[20,21,22] Curve deconvolution of this region was conducted to analyse the secondary structure content of the samples. This was done using the Magic Plot software by applying Gaussian curve fitting to the amide I region (1600 – 1700 cm^{-1}).

5.2.3.10 Hydrogel degradation in Phosphate buffered saline

The mass loss of RSF and RSF/PVCL hydrogels immersed in 10 mM Phosphate buffered saline (PBS) at 37˚C was measured to determine the degradation profile of the materials. Hydrogel samples were vacuum dried and the dried weight was measured before immersing the samples in PBS for a period of up to 21 weeks. Samples were removed at different time points, rinsed with fresh PBS and vacuum dried to determine the remaining mass. Percent weight loss over time was calculated.

5.2.4 Results and Discussion

5.2.4.1 Effect of RSF on the phase transition behaviour of PVCL

DLS was employed to study the effect of RSF on the phase behaviour of PVCL with temperature to understand how the thermo-responsive behaviour of PVCL will influence the formation of the RSF/PVCL DN hydrogels. Different ratios of RSF and PVCL were employed to alter the hydrophobic/hydrophilic balance of the system. In general, it has been found that the LCST of a polymer is lowered by incorporating hydrophobic moieties, and raised through the introduction of hydrophilic groups.[34, 38] A number of strategies are possible in order to alter the hydrophobic/hydrophilic environment of a polymer, including copolymerization, DNA technology, or forming hybrid materials through chemical and physical interactions.[38] In particular, the formation of blends has been shown to tune the LCST of a number of synthetic and natural polymers, including PNIPAM, PVCL and elastin.[39, 40] Furthermore, our recent work demonstrated that the formation of a co-assembly with RSF and a biomimetic thermo-responsive protein (Rec1-resilin) tuned the LCST to lower values.[37]

The thermo-responsive behaviour of the RSF/PVCL system was therefore studied using DLS in dilute solution (10 mg/mL) with increasing RSF content from 10 to 40 wt% (Figure 5.1). It should be noted that RSF exhibited no change in D_h over the temperature range measured. From the graph it was observed that PVCL exhibited a phase transition above 32˚C as there was a sharp increase in the D_h of several orders of magnitude above this temperature, accompanied by a change in the solution appearance from transparent to turbid. This result was in agreement with other LCST values reported for PVCL that ranged from ~32-35˚C.[30-32] On cooling, the solution became transparent once again and thus the thermo-responsiveness was shown to be a reversible process. The LCST of RSF/PVCL co-assemblies was investigated and it was observed that the onset LCST was inversely proportional to the RSF content. The results showed that when the RSF content was increased from 10 to 40 wt%, the LCST progressively decreased from ~22˚C to ~16˚C (Figure 5.1).

In general, the phase transition observed at the LCST of a polymer is dictated by competing attractive segment-water interactions and segment-segment or hydrophobic interactions.[41] Essentially an increase in the segment-segment interactions results in a lower LCST and vice versa.[41] Other groups have observed the formation of stable hydrogen bonding interactions between RSF and PVCL.[19, 36] Thus, the results suggest that strong hydrogen bonding interactions between RSF and PVCL in the co-assembly lead to a lowering of the LCST. By increasing the proportion of RSF, the extent of hydrogen bonding between RSF and PVCL increases thus further decreasing the LCST. On cooling it was found that the RSF/PVCL solutions became transparent indicating that the incorporation of RSF did not alter the reversibility of the system. Conversely, the Rec1-resilin/RSF co-assembly studied recently demonstrated irreversible phase transitions.[37] Thus, it is evident that by altering the hydrophobic/hydrophilic balance through the addition of RSF it is possible to tune the thermo-responsiveness of PVCL. This has implications for the RSF/PVCL DN gel formation as this confirms that above room temperature physical interactions are present between RSF and PVCL, which allows for the formation of a DN hydrogel containing both chemical and physical interactions.

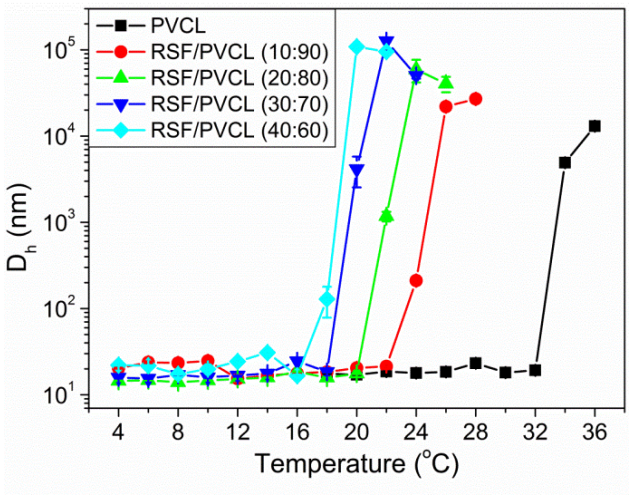


Figure 5.1 Phase transition behaviour of PVCL and RSF/PVCL solutions measured by DLS. Measurements are presented as mean ± standard deviation.

5.2.4.2 Compositional analysis of the RSF/PVCL DN hydrogels from TGA

The investigation into the phase transition behaviour of RSF and PVCL in dilute solutions provided an understanding of their interactions in solution and formed a basis for the fabrication of more complex DN hydrogels. A series of unique DN hydrogels combining the hard phase of RSF with the soft phase of PVCL were fabricated combining chemical crosslinking with non-covalent interactions. TGA was employed to determine the thermal stability and compare the theoretical and experimental mass compositions of the RSF/PVCL DN hydrogels. Figure 5.2 shows the TGA thermograms and corresponding derivative curves for the RSF hydrogel, PVCL and the RSF/PVCL DN hydrogels of different ratios ($S_{90}P_{10}$, $S_{80}P_{20}$, $S_{70}P_{30}$, $S_{60}P_{40}$). The temperature corresponding to the maximum rate of weight loss for the RSF hydrogel occurred at 292˚C, which is consistent with the reported behaviour of RSF films.[42] The results showed that the maximum rate of weight loss of PVCL occurred at 460˚C and a similar observation was made by Kozanoglu et al. (430˚C).[34]

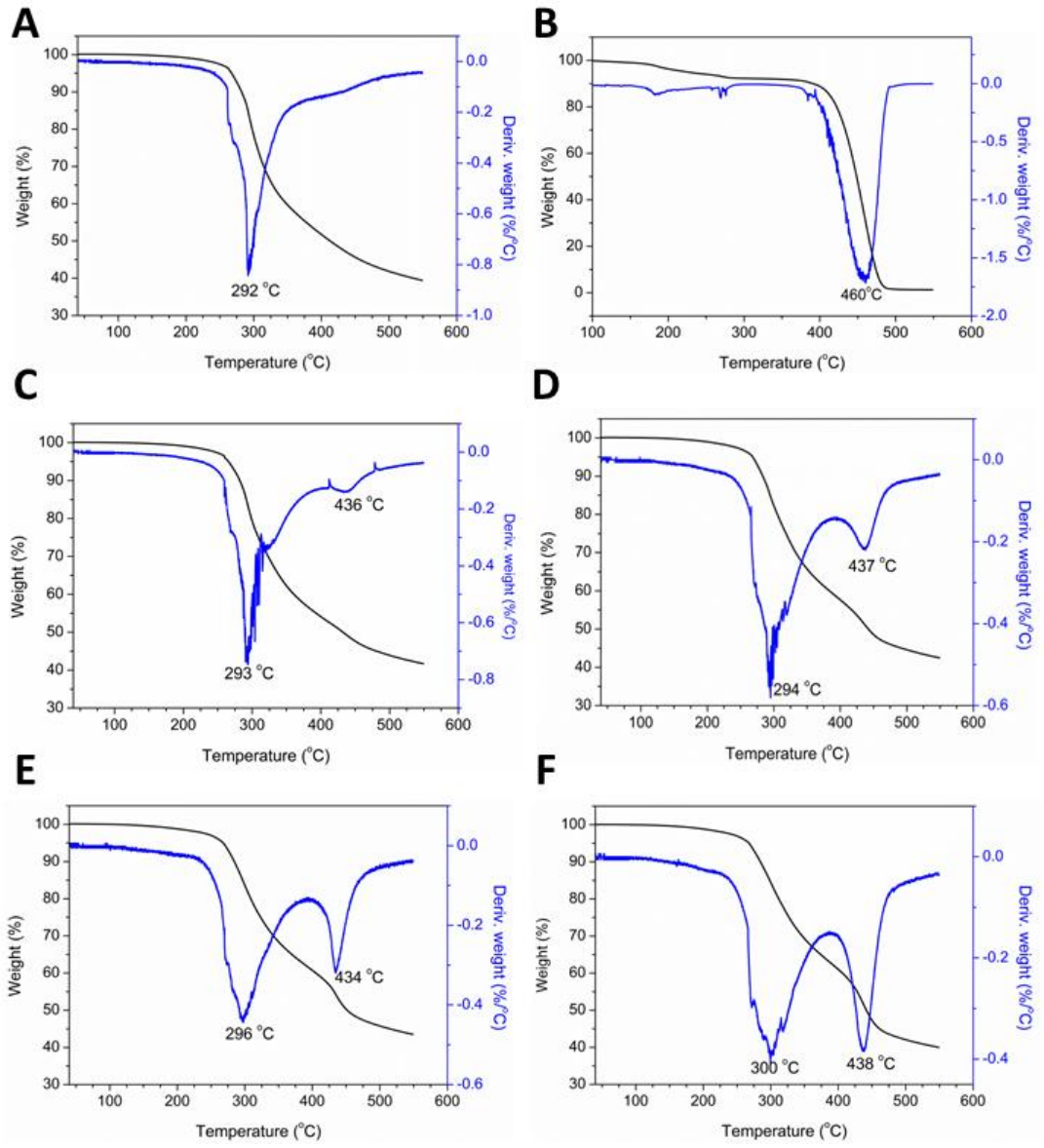


Figure 5.2 TGA thermograms of RSF/PVCL hydrogels prepared with different compositions. A) RSF; B) PVCL; C) $S_{90}P_{10}$; D) $S_{80}P_{20}$; E) $S_{70}P_{30}$; F) $S_{60}P_{40}$.

The mass composition of the crosslinked RSF/PVCL hydrogels was estimated from the corresponding TGA thermograms. On examination of the PVCL and RSF thermograms, it was observed that the residual mass at 550°C due to PVCL was negligible (~1%), whereas the RSF hydrogel was shown to have ~40% residue (Figures 5.2A and B). Therefore, this was taken into account when calculating the composition of the RSF/PVCL hydrogels. Table 5.1 summarises the theoretical and experimental mass compositions of the RSF/PVCL hydrogels prepared at different mass ratios. The experimental proportion of RSF in the hydrogels calculated from TGA analysis was less than the theoretical values, which agrees with previous observations that not all of the RSF protein participates in the photo-crosslinking

reaction.[29] However, it was clear that PVCL was retained within the hydrogel structure after crosslinking and that the amount of PVCL was controlled by the ratio of the initial solution.

Table 5.1 Mass ratio of RSF/PVCL solution before crosslinking, compared to calculated mass ratio from the TGA of the dried hydrogel.

Sample identification S=RSF, P=PVCL (S_xP_y)	**Theoretical mass ratio of RSF/PVCL solution**	**Experimental mass ratio of RSF/PVCL in DN hydrogels calculated by TGA**	**Residue (%)**
$S_{90}P_{10}$	96.4:3.6 (27:1)	88.3:11.7 (7.6:1)	41.7
$S_{80}P_{20}$	92.3:7.7 (12:1)	83.2:16.8 (4.9:1)	42.5
$S_{70}P_{30}$	87.5:12.5 (7:1)	81.5:18.5 (4.4:1)	43.5
$S_{60}P_{40}$	81.8:18.2 (4.5:1)	76.6:23.4 (3.3:1)	40.0

These results confirm that a new type of DN hybrid hydrogel was fabricated that exploits the features of RSF and PVCL in one material, which has not been achieved before. PVCL has been studied for drug delivery applications[43-45] due to its good biocompatibility properties; however there is a lack of use of this material for tissue engineering applications due to its low mechanical strength. In this study the aim is to modify this characteristic of PVCL by forming a DN hybrid system with RSF that improves the toughness properties. Figure 5.3 depicts the proposed structure of the hydrogels and demonstrates the combination of covalent crosslinking of RSF with the physical interactions between RSF and PVCL. There have been a number of studies that demonstrated the presence of strong hydrogen bonding interactions between RSF and PVCL that were stable over a range of pH values.[19, 36] As the crosslinking reaction was performed at room temperature, the DLS analysis indicated that the RSF/PVCL solutions will undergo phase separation and thus the PVCL phase is most likely to be present as globular structures within the hydrogel. The TGA results demonstrate that PVCL was retained in the RSF/PVCL hydrogel structure and did not wash out when the gels were immersed in water. This confirms the successful formation and stability of RSF/PVCL DN hydrogels of different compositions.

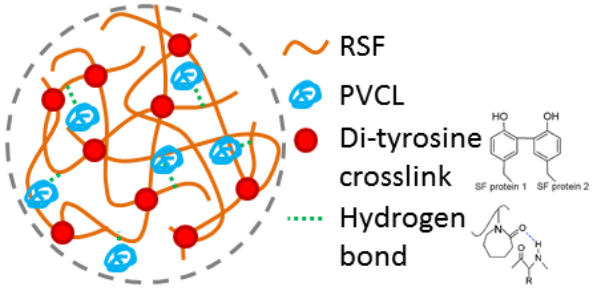


Figure 5.3 Schematic of proposed RSF/PVCL hybrid hydrogel structure

5.2.4.3 Effect of RSF/PVCL hydrogel composition on swelling capacity

The swelling capacity of hydrogels is an important property for tissue engineering applications as it is related to the diffusive properties of the material.[46] The diffusive properties allow for the transport of nutrients and other biological signalling molecules that are crucial to support cell growth. The swelling capacity of the RSF/PVCL hybrid hydrogels in aqueous media was evaluated to examine the effect of their unique composition on this property. The water uptake of the hydrogels with different ratios of RSF and PVCL was monitored over time until the system reached equilibrium (Figure 5.4). The results showed that the water uptake capacity (h) of the hydrogels increased with increasing PVCL content. A maximum equilibrium h value of 0.97 ± 0.06 g water/g dried gel was obtained for the $S_{60}P_{40}$ sample, compared to 0.62 ± 0.03 and 0.51 ± 0.02 g water/g dried gel for $S_{80}P_{20}$ and $S_{90}P_{10}$, respectively. There was no difference observed in the equilibrium h values of the $S_{70}P_{30}$ and $S_{60}P_{40}$ hydrogels. This suggests that the structure of the $S_{60}P_{40}$ hydrogel limits further absorption of water. The water uptake values for the RSF/PVCL hydrogels (0.51 to 0.97) were comparable to those obtained for a semi-interpenetrating network (semi-IPN) hydrogel composed of RSF and PEG that ranged from 0.75 to 0.93.[47] In addition, RSF/pectin hybrid hydrogels that were formed due to the induction of beta-sheet structures were shown to exhibit water contents ranging from 0.76 to 0.94.[48]

The increased water uptake with increasing PVCL content can be attributed to two contributing factors. Firstly, an increased equilibrium h is attributed to the fact that PVCL is more hydrophilic than RSF with cyclic amide side groups that have an affinity for water molecules. Also, the network structure and crosslink density plays an important role in dictating the swelling capability of hydrogels. It is known that lower crosslink densities result in looser networks that allow for the accommodation of more solvent molecules, which results in greater swelling ratios.[49] Therefore, this suggests that as the PVCL content is

increased, the crosslink density decreases resulting in a higher swelling ratio. To analyse this further, the crosslink density was calculated using the elastic modulus and is discussed in the following section. Overall, the results demonstrate that by forming a DN hydrogel composed of a chemically crosslinked RSF network containing hydrogen bonded PVCL; it is possible to tune the swelling behaviour of the resultant hydrogels and improve the swelling capacity compared to the pristine RSF hydrogel.

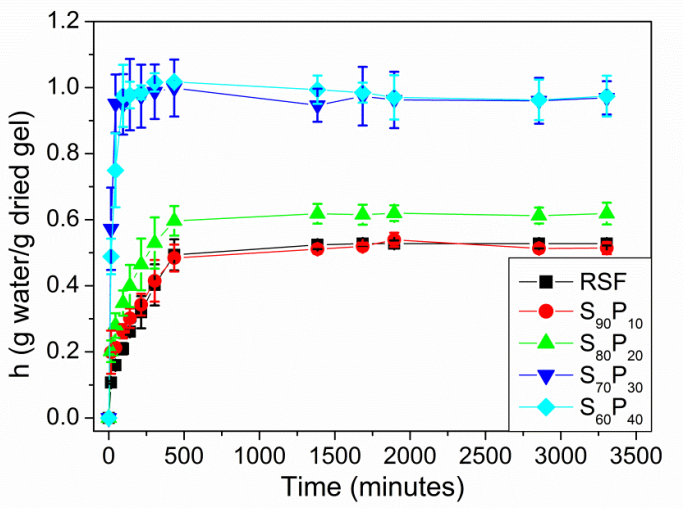


Figure 5.4 Water uptake curves of RSF and RSF/PVCL hydrogel over time. Data is presented as mean ± standard deviation.

5.2.4.4 Phase behaviour of dehydrated and swollen RSF/PVCL hydrogels

DSC was employed to analyse the phase behaviour of the dried and equilibrium swollen RSF/PVCL hydrogels. Figure 5.5A depicts the DSC thermograms of the RSF hydrogel, neat PVCL, and the RSF/PVCL DN hydrogels all in the dehydrated state. The T_g values are reported as the midpoint of the transition in the baseline of the thermogram. Individually, the RSF hydrogel and PVCL polymer exhibit T_gs of 104˚C and 116˚C, respectively. The difference between the reported T_g (147˚C) of dried PVCL may be due to differences in molecular weight.[50] The dehydrated RSF/PVCL hydrogels exhibit broad single T_gs that ranged from ~111 to 118˚C (Figure 5.5A). Notably, for hybrid polymer systems a single T_g indicates that the system is miscible due to favourable interactions between the components.[51, 52]

The phase behaviour of the equilibrium swollen RSF/PVCL hydrogels was also examined using DSC (Figure 5.5B). The DSC experiments for the swollen samples were started from -

75˚C to cover the largest temperature range possible as the T_g of swollen hydrogels is known to shift to low temperatures due to the plasticisation effect of water. The T_gs for the equilibrium swollen RSF and $S_{90}P_{10}$ hydrogels were measured as -24.1˚C and -23.8˚C, respectively. All hydrogels exhibit an exothermic peak at 0˚C due to the melting of frozen water. The exothermic peaks were broader with increasing PVCL content, which was attributed to the higher water uptake amount for these hydrogels. Also, the T_gs were not observed for the $S_{80}P_{20}$, $S_{70}P_{30}$ and $S_{60}P_{40}$ hydrogels, which suggests that for these samples the T_g was shifted to below the range of detection. The results demonstrate that all swollen hydrogels were rubbery at room temperature, which was also reflected in the elasticity results from DMA.

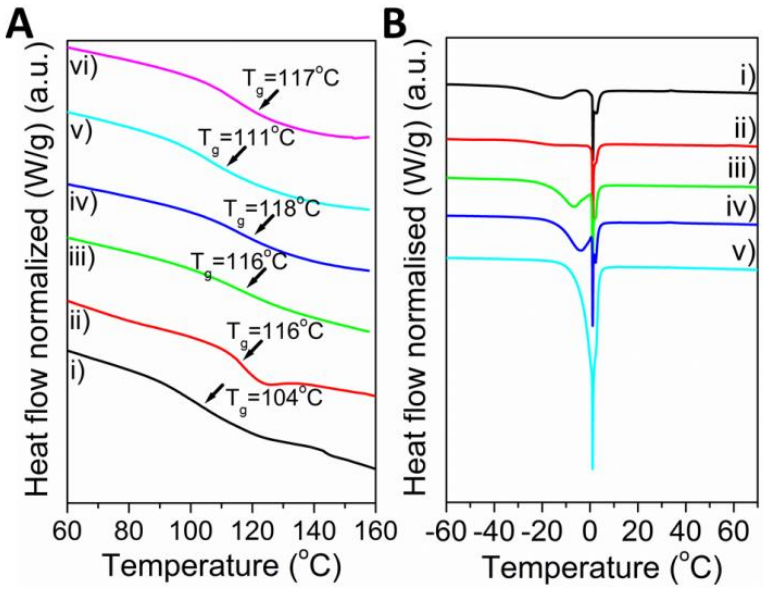


Figure 5.5 A) DSC thermograms of dehydrated RSF/PVCL DN hydrogels: i) RSF, ii) PVCL, iii) $S_{90}P_{10}$, iv) $S_{80}P_{20}$, v) $S_{70}P_{30}$, vi) $S_{60}P_{40}$. B) DSC thermograms of equilibrium swollen hydrogels: i) RSF, ii) S_{90}P10, iii) $S_{80}P_{20}$, iv) $S_{70}P_{30}$, v) $S_{60}P_{40}$.

5.2.4.5 Viscoelastic properties of the RSF/PVCL DN hydrogels by DMA

Articular cartilage is known to possess high viscoelastic and mechanical properties, which are required to perform their function and withstand millions of cycles of loading and unloading in the body.[2] The elastic modulus of articular cartilage has been found to range from ~180 to 2500 kPa.[15-17] Thus, in order to design suitable RSF/PVCL DN hydrogels for cartilage tissue engineering applications, it is crucial to tune their viscoelastic properties. The viscoelastic properties of the swollen RSF and RSF/PVCL hydrogel samples were measured using DMA.

Figure 5.6 depicts the storage modulus (E'), loss modulus (E") and tan delta results for the swollen RSF and RSF/PVCL hydrogels with increasing PVCL content. It is interesting that the E' was greater than E" for all swollen hydrogel samples indicating that the elastic response of the RSF/PVCL hydrogels was greater than the viscous response (Figure 5.6A). When comparing the elasticity of the swollen hydrogels, the RSF and $S_{90}P_{10}$ hydrogels exhibit similar E' values of 78.05 ± 15.91 MPa and 65.55 ± 11.67 MPa, respectively. However, the $S_{80}P_{20}$ and $S_{70}P_{30}$ DN hydrogels demonstrate lower modulus values of 22.82 ± 9.76 MPa and 21.11 ± 0.80 MPa, respectively. Furthermore, a decrease in E' of several orders of magnitude compared to the other RSF/PVCL hydrogels was observed. The $S_{60}P_{40}$ hydrogel exhibits an E' of 0.58 ± 0.28 MPa, which is several orders of magnitude less than the other RSF and RSF/PVCL DN hydrogels. Thus, the elasticity of the $S_{60}P_{40}$ DN hydrogel is closest to that of articular cartilage. A similar E' value of ~0.1 MPa was observed for DN hydrogels consisting of poly(2-acrylamido-2-methylpropanesulfonic acid) (PAMPS) as the first network and poly(acrylamide) (PAAm) as the second network.[53]

The decrease in E' (~65 to 0.58 MPa) that was observed with increasing PVCL content can be attributed to the differences in network structure of the hydrogels and also the increased water content that acts as a plasticiser. Similarly, Nakayama et al. observed a decrease in the elastic modulus of DN hydrogels composed of bacterial cellulose (BC) and gelatin from ~21 to 5 MPa with increasing water content.[54] In addition, Numata et al. reported an elastic modulus of ~4.7 MPa for RSF-pectin hydrogels and they observed the presence of water was crucial for the elastic properties of the hydrogel.[48] Gil et al. studied the elasticity of RSF/PNIPAM IPN and semi-IPN hydrogels and observed that the modulus was tuned by varying the ratio of components. They found that a greater amount of crystalline RSF that was crosslinked by beta-sheets resulted in an increase in the compressive modulus.[55, 56] For the RSF/PNIPAM hydrogels, crystallisation of the RSF through physical crosslinking was required to result in materials with improved strength. However, in this work it was observed that chemical crosslinking of RSF through formation of di-tyrosine can also result in hydrogels of high strength that may be tuned through the formation of a DN hybrid hydrogel with a synthetic polymer, PVCL.

The tan delta values are shown to decrease from 0.15 to 0.04 with increasing PVCL content, indicating more elastic behaviour as an ideal elastomer would have very low tan delta values (Figure 5.6B). In addition, the lower content of crosslinked RSF that occurs in the DN

hydrogels with increasing PVCL contributes to a lowering of the mechanical rigidity and thus lower E'. Zhai et al. investigated the viscoelastic behaviour of polyacrylamide/alginate DN hydrogels and observed tan delta values of around 0.1, which they compared to cartilage that has tan delta values ranging from 0.01 to 0.1.[57] This indicates that the RSF/PVCL hydrogels exhibit comparable damping characteristics to cartilage as the tan delta values were 0.11, 0.10 and 0.04 for the $S_{80}P_{20}$, $S_{70}P_{30}$ and $S_{60}P_{40}$ hydrogels, respectively.

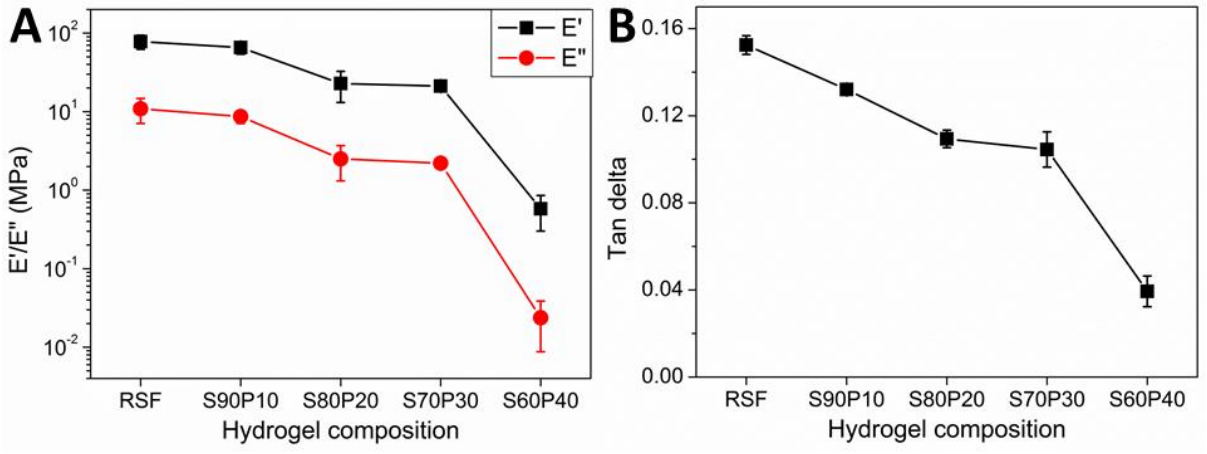


Figure 5.6 A) E' and E" and B) tan delta results for the RSF and RSF/PVCL swollen hydrogels. Data is presented as mean ± standard deviation.

In order to estimate the crosslink density (n) of the hydrogels, the expression from rubber elasticity theory: $n = E'/3RT = \rho/M_c$ was employed.[58-60] E' is the tensile storage modulus (MPa) as measured from DMA experiments, R is the universal gas constant (8.314 J/mol.K), T is the absolute temperature (298 K), and M_c represents the molecular weight between crosslinks (g/mol). The density (ρ) of the system was calculated by taking the weight average of RSF and PVCL in each hydrogel as determined from TGA measurements with the ρ of pure RSF and PVCL being 1.421 g/cm^3 and 1.0 g/cm^3.[61, 62] A summary of the n and M_c values for the RSF and RSF/PVCL hydrogels is shown in Table 5.2. It is clear from the table that n decreases from ~8800 mol/m^3 to ~78 mol/m^3 with an increase in PVCL content, which is attributed to a lower proportion of crosslinked RSF in the hydrogels. Consequently, the M_c increased from ~158 g/mol to ~19,000 g/mol with increasing PVCL content. Thus, by increasing the PVCL content a loosely crosslinked network was formed that contributed to differences in the water uptake capability and viscoelastic properties. Study into the swollen hydrogel network density and microstructural differences of the RSF/PVCL hydrogels using

neutron scattering experiments is currently underway to gain a deeper understanding into these systems and will be discussed in our future communication.

Table 5.2 Summary of crosslink density (n) and molecular weight between crosslinks (M_c) of RSF and RSF/PVCL DN hydrogels

Sample	**n (mol/m^3)**	**M_c (g/mol)**
RSF	9545.6 (±3097.6)	157.1 (±51.0)
$S_{90}P_{10}$	8819.1 (±1569.7)	158.1 (±28.1)
$S_{80}P_{20}$	3070.2 (±1312.9)	484.0 (±206.9)
$S_{70}P_{30}$	2839.5 (±107.5)	472.3 (±17.9)
$S_{60}P_{40}$	77.8 (±37.3)	19164.8 (±9181.2)

5.2.4.6 Toughness of the RSF and $S_{70}P_{30}$ hydrogels

Tensile testing of the RSF and $S_{70}P_{30}$ hydrogels was undertaken to compare the effect of network structure on the hydrogel mechanical properties. Figure 5.7 shows the stress-strain plots for the RSF and $S_{70}P_{30}$ hydrogels. It was observed that the RSF hydrogel exhibited a greater tensile stress in the dehydrated state (~800 kPa) compared to the equilibrium swollen state (~80 kPa) (Figure 5.7A). Also, the swollen RSF hydrogel exhibited a slightly larger elongation than for the dried gel. These results are consistent with the fact that water acts as a plasticiser and decreases the hydrogel stiffness. Furthermore, on comparison of the swollen RSF and $S_{70}P_{30}$ hydrogels, it is observed that the $S_{70}P_{30}$ DN hydrogel has over 2 times higher elongation than the RSF hydrogel before fracturing (Figure 5.7B). This is consistent with the more elastic behaviour of the $S_{70}P_{30}$ DN hydrogel compared to RSF as shown by the decreased elastic modulus and tan delta values measured by DMA (Figure 5.6). BC-gelatin DN hydrogels reported by Nakayama et al. demonstrated an elongation of ~17 to 28%, which is similar to our $S_{70}P_{30}$ DN hydrogel (~28%). The toughness values for the RSF and $S_{70}P_{30}$ swollen hydrogels were determined to be ~6 kJ/m^3 and 12 kJ/m^3, respectively. Suekama et al. reported on the formation of chondroitin sulphate-based DN hydrogels with varying crosslink density that exhibited toughness values ranging from approximately 30 to 2500 kPa/m^3.[63] Thus, comparatively the RSF/PVCL demonstrated a lower toughness than the chondroitin sulphate-based DN hydrogels. However, it should be noted that the tensile test was performed with RSF and $S_{70}P_{30}$ films. The results demonstrates that by forming a double network structure hydrogel, containing RSF and PVCL with chemical and physical interactions, the toughness and elongation before fracture of the hydrogels were greatly improved.

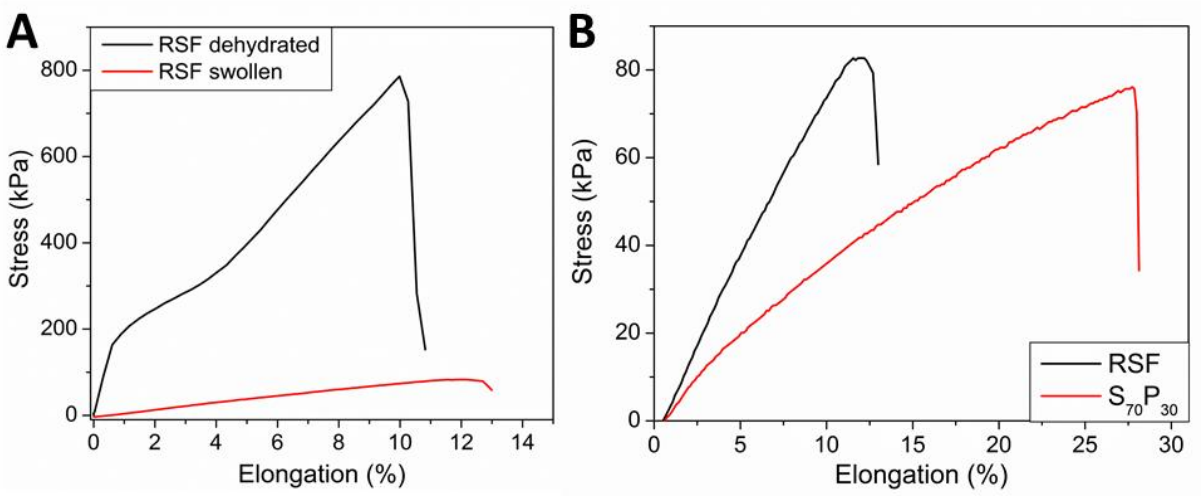


Figure 5.7 Stress vs elongation plots of A) RSF hydrogel in the dehydrated and equilibrium swollen states; and B) RSF and $S_{70}P_{30}$ in the equilibrium swollen states.

5.2.4.7 RSF/PVCL hydrogel secondary structure by FTIR

The secondary structure of the RSF/PVCL DN hydrogels was measured using Photoacoustic Fourier Transform Infrared Spectroscopy (PA-FTIR) (Nicolet Magna-IR Spectrometer 750). The amide I region (1600-1700 cm^{-1}) was deconvoluted to analyse the secondary structure content of the hydrogels as this region corresponds to the C=O stretching bonds in the peptide backbone (Figure 5.8).[51, 64, 65] To semi-quantitatively determine the proportion of different secondary structures in the DN hydrogels, the Magic Plot software was used to apply Gaussian curve fitting to the Amide I region.[66] Table 5.3 summarises the results from the curve fitting for the RSF and RSF/PVCL hydrogels. The beta-sheet content of the RSF and RSF/PVCL hydrogels was comparable (~17%), which confirms that the presence of PVCL does not induce the random coil to beta-sheet transition of RSF. Studies on the structure of RSF have shown that β-sheet contents of ~55% were observed for physically gelled RSF compared to ~20% for RSF solutions, which is much higher than the values reported here.[20, 67] In addition, with the exception of $S_{80}P_{20}$, the RSF/PVCL hydrogels exhibited a somewhat higher β-turn content (~40%) compared to the RSF hydrogel (~35%). However, due to the semi-quantitative nature of the analysis, this was not considered significant.

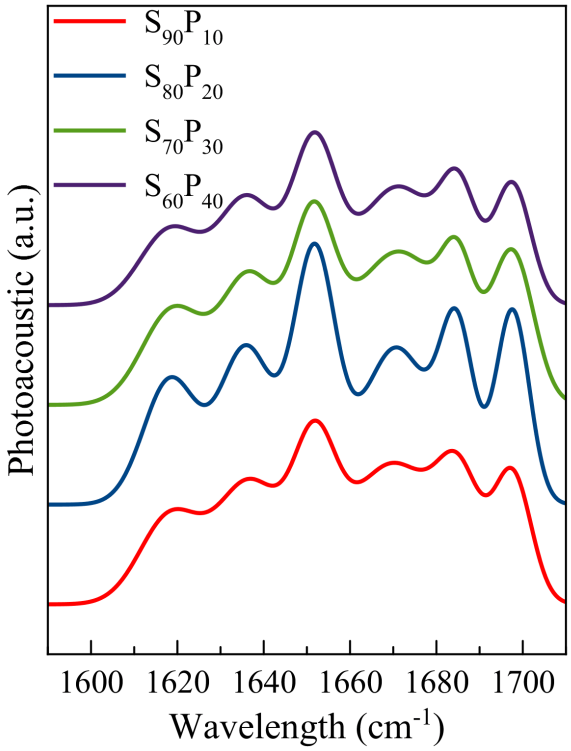


Figure 5.8 PA-FTIR spectra of the RSF/PVCL DN hydrogels showing the Amide I region.

Table 5.3 Secondary structure content of RSF and RSF/PVCL DN hydrogels measured from the Amide I region of the PA-FTIR spectrum.

Wavenumber range (cm^{-1})	**Secondary structure**	**RSF (%)**	**$S_{90}P_{10}$ (%)**	**$S_{80}P_{20}$ (%)**	**$S_{70}P_{30}$ (%)**	**$S_{60}P_{40}$ (%)**
1616-1621	Aggregate β-strand/ β-sheets (weak, intermolecular)	15.9 (±0.2)	13.27 (±0.23)	14.26 (±0.46)	14.09 (±0.88)	14.66 (±1.92)
1628-1637	β-sheets (strong, intramolecular)	16.7 (±1.8)	18.45 (±1.08)	17.20 (±0.16)	16.51 (±0.56)	16.24 (±1.58)
1638-1655	Random coils	17.7 (±0.6)	16.22 (±2.97)	20.91 (±0.94)	16.73 (±1.92)	19.74 (±0.58)
1663-1685	β-turns	35.2 (±0.1)	40.30 (±2.24)	34.45 (±1.27)	41.11 (±0.21)	38.19 (±1.40)
1697-1703	β-sheets (weak, intermolecular)	14.5 (±1.5)	11.76 (±0.12)	13.18 (±0.63)	11.55 (±3.16)	11.17 (±2.33)

5.2.4.8 Degradation in PBS

The *in vitro* degradation profile of the RSF and RSF/PVCL hydrogels was examined in PBS over a period of 21 weeks and the results of the mass change over time is shown in Figure 5.9. There is negligible mass change for all samples over this period. Horan et al. observed that there was no significant weight loss of RSF samples incubated in PBS over a period of 42 days.[68] However, She et al. observed that there was a 19.28% weight loss for a RSF/chitosan scaffold incubated in PBS at 37˚C for 8 weeks.[69] They attributed the weight loss to the degradation of chitosan as the degradation rate of chitosan is much faster than RSF and the chitosan content was observed to decrease during the degradation process.[69] Thus, as the RSF hydrogels and RSF/PVCL DN hydrogels exhibited negligible weight loss over the 21 week period it can be concluded that the covalent di-tyrosine crosslinks and strong hydrogen bonding formed a robust structure that is stable over an extended period of time.

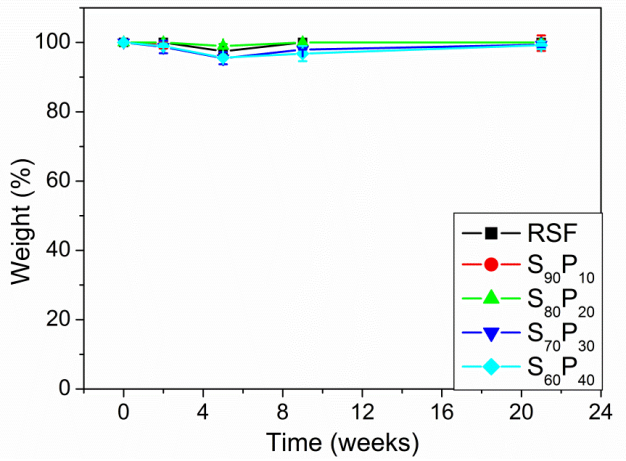


Figure 5.9 Mass of RSF and RSF/PVCL hydrogels in PBS as a function of time. Data is presented as mean ± standard deviation.

5.2.5 Conclusions

In this study we have reported the fabrication and properties of a new type of DN hybrid hydrogel composed of RSF and PVCL. The RSF/PVCL hydrogels can be synthesised by a facile one-pot method and combine chemical and physical interactions in a single DN hydrogel. From the study of the dilute solution properties of RSF/PVCL at different ratios, the LCST of PVCL is found to decrease with increasing RSF content. With increasing PVCL content improved water absorption capacity of the RSF/PVCL hydrogels was noticed. In addition, it was possible to tune the elasticity and toughness of the RSF/PVCL hydrogels to

values that are more relevant for cartilage tissue engineering applications. Thus, the improved swelling, elasticity and toughness of the RSF/PVCL DN hydrogels make them promising materials for cartilage tissue engineering applications. Investigations into the microstructure of the RSF/PVCL DN hydrogels using neutron scattering and also investigation of chondrocyte cell-biomaterials interactions are underway.

Acknowledgements

This research has been financially supported by the Australian Research Council (ARC) through Discovery Grant funding (DP1092678 and DP120103537).

5.2.6 References

1. Gong, J. P.; Katsuyama, Y.; Kurokawa, T.; Osada, Y., *Adv. Mater.* **2003,** *15* (14), 1155-1158.
2. Chen, Q.; Chen, H.; Zhu, L.; Zheng, J., *J. Mater. Chem. B* **2015,** *3* (18), 3654-3676.
3. Webber, R. E.; Creton, C.; Brown, H. R.; Gong, J. P., *Macromolecules* **2007,** *40* (8), 2919-2927.
4. Brown, H. R., *Macromolecules* **2007,** *40* (10), 3815-3818.
5. Tanaka, Y., *Europhysics Letters* **2007,** *78* (5), 56005.
6. Chen, P.; Wu, R.; Wang, J.; Liu, Y.; Ding, C.; Xu, S., *J. Polym. Res.* **2012,** *19* (3), 1-4.
7. Chen, Q.; Zhu, L.; Zhao, C.; Wang, Q.; Zheng, J., *Adv. Mater.* **2013,** *25* (30), 4171-4176.
8. Tang, T.; Takasu, A., *RSC Advances* **2015,** *5* (2), 819-829.
9. Haraguchi, K.; Takehisa, T., *Adv. Mater.* **2002,** *14* (16), 1120-1124.
10. Lin, W.-C.; Fan, W.; Marcellan, A.; Hourdet, D.; Creton, C., *Macromolecules* **2010,** *43* (5), 2554-2563.
11. Haque, M. A.; Kurokawa, T.; Kamita, G.; Gong, J. P., *Macromolecules* **2011,** *44* (22), 8916-8924.
12. Tuncaboylu, D. C.; Sari, M.; Oppermann, W.; Okay, O., *Macromolecules* **2011,** *44* (12), 4997-5005.
13. Henderson, K. J.; Zhou, T. C.; Otim, K. J.; Shull, K. R., *Macromolecules* **2010,** *43* (14), 6193-6201.
14. Hu, J.; Hiwatashi, K.; Kurokawa, T.; Liang, S. M.; Wu, Z. L.; Gong, J. P., *Macromolecules* **2011,** *44* (19), 7775-7781.

15. Armstrong, C. G.; Mow, V. C., *J. Bone Jt. Surg.* **1982,** *64* (1), 88-94.
16. Setton, L. A.; Mow, V. C.; Howell, D. S., *J. Orthop. Res.* **1995,** *13* (4), 473-482.
17. Zhu, W.; Mow, V. C.; Koob, T. J.; Eyre, D. R., *J. Orthop. Res.* **1993,** *11* (6), 771-781.
18. Xiao, W.; He, J.; Nichol, J. W.; Wang, L.; Hutson, C. B.; Wang, B.; Du, Y.; Fan, H.; Khademhosseini, A., *Acta Biomater.* **2011,** *7* (6), 2384-2393.
19. Kozlovskaya, V.; Baggett, J.; Godin, B.; Liu, X.; Kharlampieva, E., *ACS Macro Lett.* **2012,** *1* (3), 384-387.
20. Matsumoto, A.; Chen, J.; Collette, A. L.; Kim, U.-J.; Altman, G. H.; Cebe, P.; Kaplan, D. L., *J. Phys. Chem. B* **2006,** *110* (43), 21630.
21. Nagarkar, S.; Nicolai, T.; Chassenieux, C.; Lele, A., *Phys. Chem. Chem. Phys.* **2010,** *12* (15), 3834.
22. Vepari, C.; Kaplan, D. L., *Prog. Polym. Sci.* **2007,** *32* (8), 991-1007.
23. Lu, Q.; Huang, Y.; Li, M.; Zuo, B.; Lu, S.; Wang, J.; Zhu, H.; Kaplan, D. L., *Acta Biomater.* **2011,** *7* (6), 2394-2400.
24. Kojic, N.; Panzer, M. J.; Leisk, G. G.; Raja, W. K.; Kojic, M.; Kaplan, D. L., *Soft Matter* **2012,** *8* (26), 2897-2905.
25. Vasconcelos, A.; Freddi, G.; Cavaco-Paulo, A., *Biomacromolecules* **2008,** *9* (4), 1299-1305.
26. Liu, W.; Fan, H.; Dan, X.; Sun, J.; Xiao, W.; Wei, D., *J. Bioact. Compat. Polym.* **2012,** *27* (4), 327-341.
27. Silva, S. S.; Maniglio, D.; Motta, A.; Mano, J. F.; Reis, R. L.; Migliaresi, C., *Macromol. Biosci.* **2008,** *8* (8), 766-774.
28. Kang, G.; Lee, K.; Ki, C.; Park, Y., *Fiber Polym.* **2004,** *5* (3), 234-238.
29. Whittaker, J. L.; Choudhury, N. R.; Dutta, N. K.; Zannettino, A., *J. Mater. Chem. B* **2014,** *2* (37), 6259-6270.
30. Liang, X.; Kozlovskaya, V.; Chen, Y.; Zavgorodnya, O.; Kharlampieva, E., *Chem. Mater.* **2012,** *24* (19), 3707-3719.
31. Feldstein, M. M.; Bovaldinova, K. A.; Bermesheva, E. V.; Moscalets, A. P.; Dormidontova, E. E.; Grinberg, V. Y.; Khokhlov, A. R., *Macromolecules* **2014,** *47* (16), 5759-5767.
32. Webster, M.; Miao, J.; Lynch, B.; Green, D. S.; Jones-Sawyer, R.; Linhardt, R. J.; Mendenhall, J., *Macromol. Mater. Eng.* **2013**, *298*, 447-453.
33. Laukkanen, A.; Wiedmer, S. K.; Varjo, S.; Riekkola, M. L.; Tenhu, H., *Colloid Polym. Sci.* **2002,** *280* (1), 65-70.

34. Kozanoglu, S.; Ozdemir, T.; Usanmaz, A., *J. Macromol. Sci., Part A: Pure Appl. Chem.* **2011,** *48* (6), 467-477.
35. Hinkley, J. A.; Morgret, L. D.; Gehrke, S. H., *Polymer* **2004,** *45* (26), 8837-8843.
36. Espinosa-Dzib, A.; Chen, J.; Zavgorodnya, O.; Kozlovskaya, V.; Liang, X.; Kharlampieva, E., *Soft Matter* **2015,** *11* (25), 5133-5145.
37. Whittaker, J. L.; Dutta, N. K.; Knott, R.; McPhee, G.; Voelcker, N. H.; Elvin, C.; Hill, A.; Choudhury, N. R., *Langmuir* **2015,** *31* (32), 8882-8891.
38. Cordeiro, A. L., Stimuli-Responsive Polymer Nanocoatings. In *Nanotechnologies for the Life Sciences*, Wiley-VCH Verlag GmbH & Co. KGaA: 2007.
39. Ieong, N. S.; Hasan, M.; Phillips, D. J.; Saaka, Y.; O'Reilly, R. K.; Gibson, M. I., *Polym. Chem.* **2012,** *3* (3), 794-799.
40. Fernandez-Trillo, F.; van Hest, J. C. M.; Thies, J. C.; Michon, T.; Weberskirch, R.; Cameron, N. R., *Chem. Commun.* **2008,** (19), 2230-2232.
41. Liu, R.; Fraylich, M.; Saunders, B., *Colloid Polym. Sci.* **2009,** *287* (6), 627-643.
42. Motta, A.; Fambri, L.; Migliaresi, C., *Macromol. Chem. Phys.* **2002,** *203* (10-11), 1658-1665.
43. Wang, Y.; Nie, J.; Chang, B.; Sun, Y.; Yang, W., *Biomacromolecules* **2013,** *14* (9), 3034-3046.
44. Rejinold, N. S.; Chennazhi, K. P.; Nair, S. V.; Tamura, H.; Jayakumar, R., *Carbohydr. Polym.* **2011,** *83* (2), 776-786.
45. Prabaharan, M.; Grailer, J. J.; Steeber, D. A.; Gong, S., *Macromol. Biosci.* **2008,** *8* (9), 843-851.
46. Nicodemus, G. D.; Bryant, S. J., *Tissue Eng., Part B* **2008,** *14* (2), 149-165.
47. Kweon, H. Y.; Park, S. H.; Yeo, J. H.; Lee, Y. W.; Cho, C. S., *J. Appl. Polym. Sci.* **2001,** *80* (10), 1848-1853.
48. Numata, K.; Yamazaki, S.; Katashima, T.; Chuah, J.-A.; Naga, N.; Sakai, T., *Macromol. Biosci.* **2014,** *14* (6), 799-806.
49. Mandal, B. B.; Kapoor, S.; Kundu, S. C., *Biomaterials* **2009,** *30* (14), 2826-2836.
50. Kirsh, Y. E.; Yanul, N. A.; Kalninsh, K. K., *Eur. Polym. J.* **1999,** *35* (2), 305-316.
51. Hu, X.; Wang, X.; Rnjak, J.; Weiss, A. S.; Kaplan, D. L., *Biomaterials* **2010,** *31* (32), 8121-8131.
52. Liu, Y.; Cui, Y., *J. Appl. Polym. Sci.* **2011,** *120* (6), 3613-3620.
53. Tanaka, Y.; Kuwabara, R.; Na, Y.-H.; Kurokawa, T.; Gong, J. P.; Osada, Y., *J. Phys. Chem. B* **2005,** *109* (23), 11559-11562.

54. Nakayama, A.; Kakugo, A.; Gong, J. P.; Osada, Y.; Takai, M.; Erata, T.; Kawano, S., *Adv. Funct. Mater.* **2004,** *14* (11), 1124-1128.
55. Gil, E. S.; Park, S.-H.; Tien, L. W.; Trimmer, B.; Hudson, S. M.; Kaplan, D. L., *Langmuir* **2010,** *26* (19), 15614-15624.
56. Gil, E. S.; Hudson, S. M., *Biomacromolecules* **2007,** *8* (1), 258-264.
57. Zhai, Y.; Duan, H.; Meng, X.; Cai, K.; Liu, Y.; Lucia, L., *Macromol. Mater. Eng.* **2015**, DOI: 10.1002/mame.201500215
58. Wang, Y.; Ameer, G. A.; Sheppard, B. J.; Langer, R., *Nat. Biotech.* **2002,** *20* (6), 602-606.
59. Krongauz, V., *J. Therm. Anal. Calorim.* **2010,** *102* (2), 435-445.
60. Djordjevic, I.; Choudhury, N. R.; Dutta, N. K.; Kumar, S., *Polymer* **2009,** *50* (7), 1682-1691.
61. Schneider, F.; Balaceanu, A.; Feoktystov, A.; Pipich, V.; Wu, Y.; Allgaier, J.; Pyckhout-Hintzen, W.; Pich, A.; Schneider, G. J., *Langmuir* **2014,** *30* (50), 15317-15326.
62. Fossey, S. K., David, Silk Protein. In *Polymer Data Handbook*, Oxford University Press, Inc.: 1999.
63. Suekama, T. C.; Hu, J.; Kurokawa, T.; Gong, J. P.; Gehrke, S. H., *Macromol. Symp.* **2013,** *329* (1), 9-18.
64. Zhang, C.; Song, D.; Lu, Q.; Hu, X.; Kaplan, D. L.; Zhu, H., *Biomacromolecules* **2012,** *13* (7), 2148-2153.
65. Lin, S.; Lu, G.; Liu, S.; Bai, S.; Liu, X.; Lu, Q.; Zuo, B.; Kaplan, D. L.; Zhu, H., *J. Mater. Chem. B* **2014,** *2* (17), 2622-2633.
66. Hu, X.; Kaplan, D.; Cebe, P., *Macromolecules* **2006,** *39* (18), 6161-6170.
67. Silva, S. S.; Motta, A.; Rodrigues, M. T.; Pinheiro, A. F. M.; Gomes, M. E.; Mano, J. F.; Reis, R. L.; Migliaresi, C., *Biomacromolecules* **2008,** *9* (10), 2764-2774.
68. Horan, R. L.; Antle, K.; Collette, A. L.; Wang, Y.; Huang, J.; Moreau, J. E.; Volloch, V.; Kaplan, D. L.; Altman, G. H., *Biomaterials* **2005,** *26* (17), 3385-3393.
69. She, Z.; Zhang, B.; Jin, C.; Feng, Q.; Xu, Y., *Polym. Degrad. Stab.* **2008,** *93* (7), 1316-1322.

5.2.7 Supplementary information

S5.2.7.1 NMR analysis of PVCL

^{1}H NMR spectra of VCL and PVCL were obtained from 300 MHz Bruker Avance spectrometer operating at 300.138 MHz (S5.1). The solvent used was deuterated chloroform ($CDCl_3$). The peak assignments for the ^{1}H-NMR spectra of VCL and PVCL are shown in Table S5.1. All protons are accounted for and the disappearance of the signal for the vinyl proton indicated that there was no residual monomer in the polymer sample. The results agree with reported literature values for this material.[1, 2]

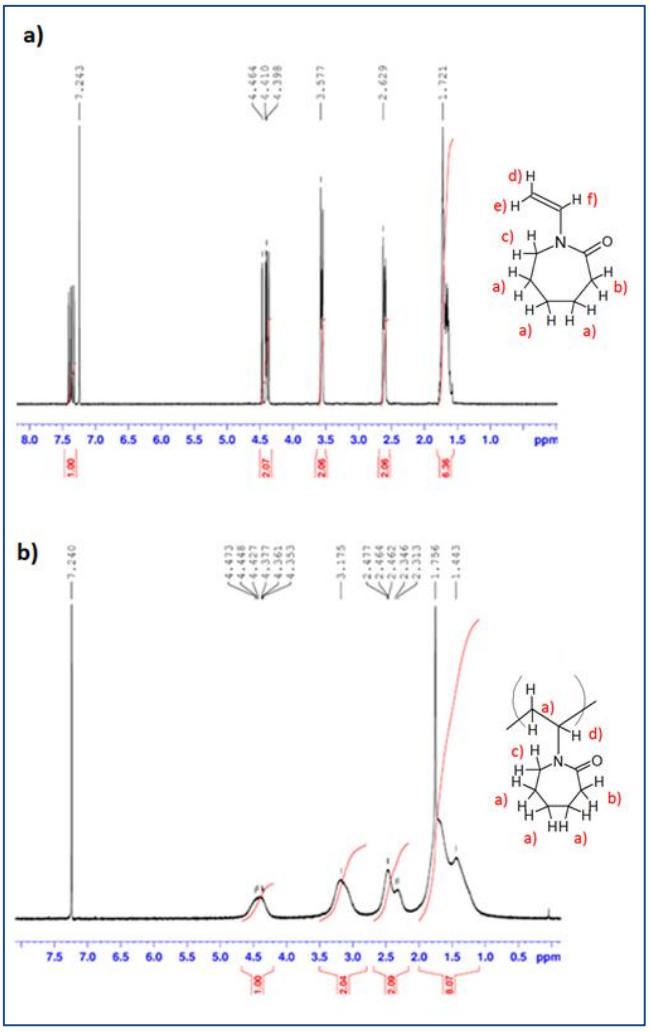


Figure S5.1 ^{1}H-NMR spectra of a) VCL and b) PVCL

Table S5.1 Peak assignment for ^{1}H-NMR spectra of VCL and PVCL

Proton type	Group	Shift (ppm)	
		VCL	PVCL
H_a	methylene	1.721	1.443, 1.756
H_b	methylene	2.629	2.313 – 2.477
H_c	methylene	3.577	3.175
H_d	ethylene	4.398	4.353 – 4.473
H_e	ethylene	4.464	-
H_f	ethylene	7.243	-

S5.2.7.2 Viscosity average molecular weight determination

The viscosity average molecular weight (M_v) of the synthesised PVCL was determined from the intrinsic viscosity ([η]) by employing the Mark-Houwink relation $[\eta] = K*M_v^a$, with K = 0.0105 ml/g and a = 0.69.[3] An Ubbelohde-type viscometer was used at 25˚C with water as the solvent. The reduced viscosity (η_{red}) and inherent viscosity (η_{inh}) were determined and the average of the Y-intercepts was used to calculate the [η] (Figure S5.2). Using the Mark-Houwink relation, the M_v was thus determined to be 35.4 kDa.

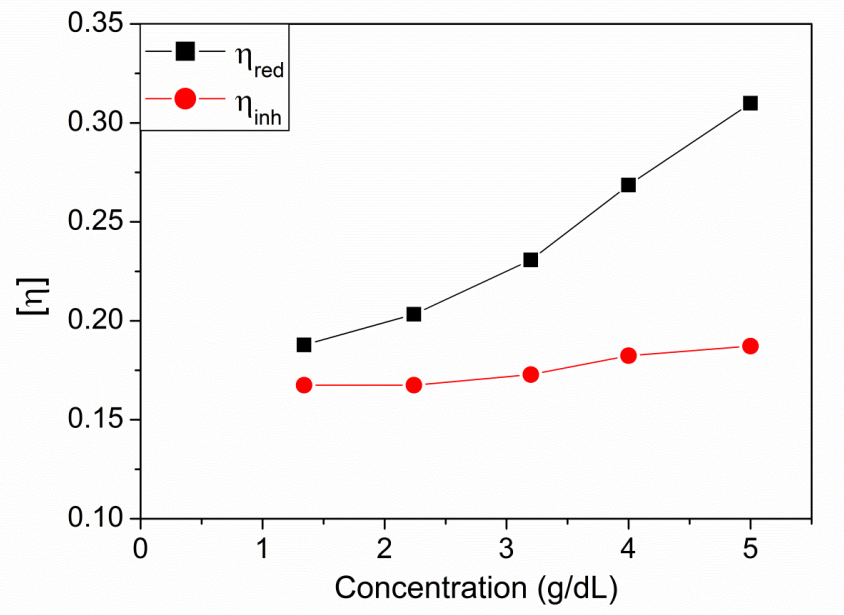


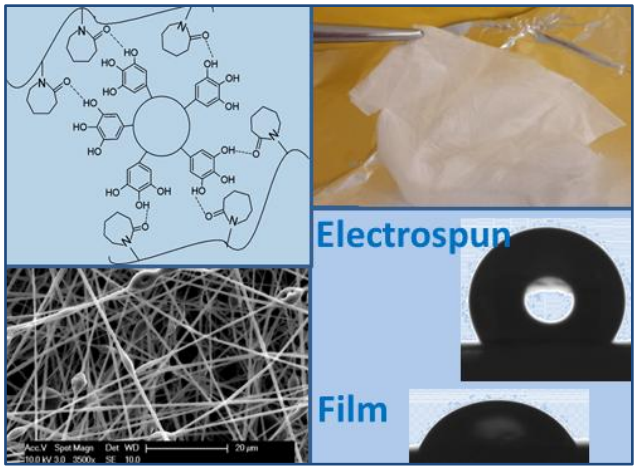
Figure S5.2 Plot of reduced and inherent viscosities determined for PVCL.

References

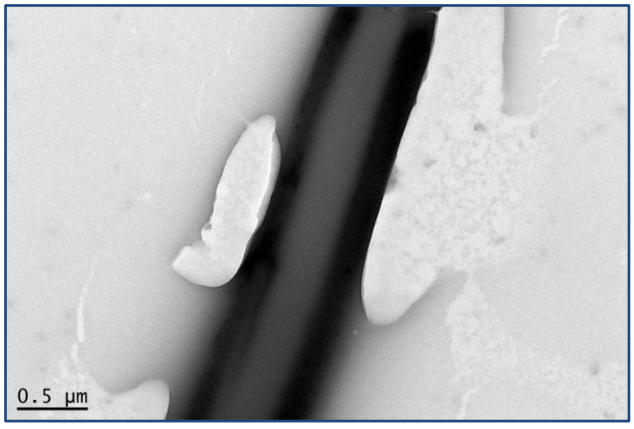
1. Webster, M.; Miao, J.; Lynch, B.; Green, D. S.; Jones-Sawyer, R.; Linhardt, R. J.; Mendenhall, *J. Macromol. Mater. Eng.* **2013**, 298, 447-453.
2. Kozanoglu, S.; Ozdemir, T.; Usanmaz, A., J. *Macromol. Sci., Part A: Pure Appl. Chem.* **2011,** 48 (6), 467-477.
3. Loos, W.; Verbrugghe, S.; Goethals, E. J.; Du Prez, F. E.; Bakeeva, I. V.; Zubov, V. P., *Macromol. Chem. Phys.* **2003,** 204 (1), 98-103.

Chapter 6: Electrospinning to form biomimetic nanofibrous mats

This chapter of the thesis is presented in two parts. Part 6.1 is presented as a research manuscript "Jasmin L. Whittaker, Surya Subianto, Naba K. Dutta and Namita R. Choudhury. Induced insolubility of electrospun Poly(N-vinylcaprolactam) fibres through hydrogen bonding with Tannic acid" submitted to *Polymer*.



Part 6.2 is presented as a research manuscript "Jasmin L. Whittaker, Surya Subianto, Naba K. Dutta, Namita Roy Choudhury. Facile fabrication of shell crosslinked core/shell Poly(N-vinylcaprolactam)/Silk fibroin fibres by co-axial electrospinning", to be submitted for peer review publication.



6.1 Induced insolubility of electrospun Poly(N-vinylcaprolactam) fibres through hydrogen bonding with Tannic acid

6.1.1 Abstract

Water-insoluble poly(N-vinylcaprolactam) (PVCL) electrospun nanofibres have been prepared for the first time by direct electrospinning with Tannic acid (TA) in apolar protic solvents. The PVCL/TA nanofibers were fabricated through a facile one-step procedure which will increase the potential applications in the biomedical field where material stability in an aqueous environment is crucial. Hydrogen bonding between TA and PVCL resulted in nanofibers that are non-water soluble after drying, and the TA/PVCL interactions were confirmed through rheological and infrared spectroscopy measurements. In addition, the optimum ratio of TA and PVCL essential for the production of uniform, insoluble fibres in the range of hundreds of nanometres was established. The contact angle (CA) measurements confirmed that the roughness induced by the fibrous morphology of the TA/PVCL mats resulted in hydrophobic surfaces (CA>120˚) from materials that otherwise exhibited hydrophilic behaviour (CA<90˚) on flat surfaces. This method of using TA as a crosslinker for direct electrospinning of PVCL fibres requires no chemical modification or complex post-synthesis steps, thus facilitating the potential use of these novel PVCL nanofibers for applications as biomedical scaffolds in aqueous environments.

6.1.2 Introduction

Nano and microstructured 1-D and 3-D materials such as nanofibres and mats have gained increasing interest for their use as tissue engineering scaffolds and drug delivery vehicles due to the fact that thin fibres facilitate large surface areas, high porosity, and increased mechanical properties.[1, 2] One of the emerging methods for the fabrication of such fibres is electrospinning.[3, 4] It is an attractive method as it is economical, easily scalable, versatile, and suitable for fabricating materials for a wide range of applications.[3, 5-7] In particular; recent trends in materials science have driven the research into stimuli-responsive polymers for use in applications such as drug delivery and tissue engineering. In these applications, temperature-responsive polymers, particularly those that possess a lower critical solution temperature (LCST) above which the polymer exhibits a phase separation and becomes insoluble, are of interest.[8] This property is very useful for biomedical applications including drug delivery and tissue engineering, where the LCST can be employed to allow for the

release of therapeutic agents or trigger a sol-gel transition. Poly(N-vinylcaprolactam) (PVCL) is a biocompatible, temperature-responsive synthetic polymer that has a LCST in the physiological temperature range (~32-35°C).[9-11] Unlike the more widely studied poly(N-isopropylacrylamide) (PNIPAm) that has an LCST in the same temperature range, PVCL does not generate low molecular weight degradation products, which makes it more suitable for biomedical applications.[8, 11] Another advantage of PVCL is that it can be readily electrospun at high concentrations (~40 wt%) from aqueous solutions to form fibrous mats that are relevant for a range of applications, including tissue engineering and drug delivery.[11] However, a major drawback of PVCL in many applications is that it is water-soluble. Thus, when electrospun on its own the resultant nanofiber mat cannot be used in aqueous environment for most physiological applications. In order to exploit the electrospinnability and temperature-responsive features of this polymer in many applications, it is critical to render the fibres insoluble in water after electrospinning.

Crosslinking has been widely used in polymers to improve mechanical properties, and crosslinked polymers are generally insoluble due to extensive, multi-point interactions between the polymer chains that can be either covalent or physical in nature. Covalent crosslinking of PVCL is complicated as it requires modification of PVCL to form copolymers with substituents that can partake in covalent bonding. Recently, Liang et al. reported synthesis of PVCL copolymers with amino crosslinking centres.[9] This required the synthesis step, followed by the formation of layer-by-layer assemblies that were then crosslinked with glutaraldehyde to form covalently crosslinked multilayer hydrogels.[9] Modification of PVCL with carboxylic acid end groups was also undertaken in order to form covalent crosslinks with cellulose acetate that resulted in crosslinked fibres.[11] However, such systems may not have the ease of electrospinnability of PVCL. So with an aim to retain the electrospinnability of PVCL, we have investigated a method of crosslinking PVCL in a one-step procedure without further chemical modifications. Hydrogen bonding, a convenient and powerful approach to crosslinking, can be readily applied to as synthesised PVCL due to the presence of the carbonyl group in the structure. Recent work by Feldstein et al. has shown that PVCL can be physically crosslinked by simply blending with low molecular weight poly(ethylene glycol) to form hydrogen bonding interactions.[10] In addition, researchers have reported hydrogen bonded layer-by-layer assemblies with PVCL and other polymer materials such as poly(methacrylic acid) (PMMA), poly(L-aspartic acid) and silk fibroin.[12, 13] Previous work by Eral-Unal et al. showed that hydrogen-bonded multilayers containing PVCL can be formed

with tannic acid (TA) that were stable up to pH 9.5.[14] Vihola et al. reported the formation of physically crosslinked PVCL hydrogel particles with the use of a number of different crosslinking stabilisers, including TA.[15] The use of TA allowed for the formation of a hydrogen bonded network that were stable in aqueous solutions and retained their temperature-responsive behaviour.[15] In addition, TA has been shown to have biofunctional properties such as antibacterial and antioxidant activities, which makes it suitable for biomedical applications for which such an electrospun PVCL mat would be applicable.[14]

In this work we have employed TA as a hydrogen bonding agent for PVCL to induce insolubility. TA/PVCL nanofibres were electrospun using a conventional, single-needle setup. The process is a one-step procedure that is facile and easily scalable. The presence of TA in the fibers resulted in crosslinking of PVCL through hydrogen bonding, rendering them insoluble in water after electrospinning and removal of solvent. The interactions between TA and PVCL were studied using rheology and the electrospun fibre mat was characterised by Scanning Electron Microscopy (SEM), Fourier Transform Infrared Spectroscopy (FTIR), contact angle measurements, and Thermogravimetric Analysis (TGA). This facile, single step procedure has the potential to exploit the advantageous properties of PVCL for a range of biomedical applications.

6.1.3 Materials and methods

6.1.3.1 Materials

Tannic acid (TA), N-vinylcaprolactam (VCL), Toluene, 2,2'-azoisobutyronitrile (AIBN) and N,N-dimethylformamide (DMF) were purchased from Sigma Aldrich and used as received. Poly(N-vinylcaprolactam) (PVCL) was prepared via free radical polymerisation of the VCL monomer with 2,2'-azoisobutyronitrile (AIBN) as the initiator and toluene as the solvent. The reaction proceeded for 24 hours under nitrogen atmosphere at 70°C. The polymer was recovered through precipitation in diethyl ether and purified by dissolving PVCL in a mixture of acetone and water (3:7), followed by precipitation by heating the solution to 80°C. This process was repeated twice, and the polymer was then dried at room temperature and finally vacuum dried at 50°C for 3 hours to remove any residual moisture. Nuclear magnetic resonance (NMR) spectrum was used to confirm the structure and purity of the polymer (S6.1.7.1). The average molecular weight (M_v) of PVCL was determined to be 35.4 kDa using capillary viscometer (S6.1.7.2).

6.1.3.2 Solution preparation

PVCL was dissolved in DMF to a concentration of 40 wt%. The solutions containing TA and PVCL with varying ratios (0.15:1, 0.29:1, 0.48:1, and 0.72:1) were prepared by adding the required amount of TA in DMF to the PVCL solution. The TA concentrations used were 5 wt%, 8.5 wt%, 12 wt%, and 15.5 wt%, respectively. However, increasing the TA resulted in gelation of the solution thus the PVCL concentration was subsequently diluted and the final concentrations were 33.3 wt%, 28.9 wt%, 25.5 wt%, and 21.5 %, respectively. The solutions were stirred overnight to ensure homogenous distribution.

6.1.3.3 Measurement of solution viscosity

The viscosities of the TA and PVCL solutions with varying ratios were measured using controlled stress rheometer Rheolyst 1000 N (TA Instruments, Delaware, U.S.A.). The measurements were undertaken at 25˚C using a 40 mm cone and plate geometry. The sample was placed between the fixed Peltier plate and a rotating cone attached to the driving motor spindle. The change in the shear stress with change in the shear rate was measured and the viscosity of solution was calculated. The viscosities of the solution are reported in Pa·s. Control measurements with PVCL alone (40 wt%) and Tannic acid alone (15 wt%) were measured in addition to the blend solutions.

6.1.3.4 Electrospinning

A horizontal electrospinning setup was employed where the polymer solution was placed in a 5 mL syringe that was mounted on a syringe pump (KD Scientific). An 18 gauge needle was connected to the syringe. A high voltage DC power source was used to generate a potential difference of 15 kV, and a distance of 10 cm was maintained between the tip of the needle and collector plate. The voltage was applied to the blunted metal needle, which acted as an electrode. Fibres were collected on an aluminium foil covered copper plate. The flow rate was maintained at 0.8 mL/h throughout the experiments. Following electrospinning, the mats were placed in an oven (130˚C) overnight.

6.1.3.5 Electrospun fibre characterisation by scanning electron microscopy (SEM)

The electrospun fibre morphology was examined through SEM measurements using the Philips XL30 FEG SEM. The samples were coated with platinum and examined at an

accelerating voltage of 10 kV. The fibre size distribution was quantified using the ImageJ software.

6.1.3.6 Porosity measurement

The porosity of the electrospun mats with TA/PVCL ratios of 0.15:1 and 0.29:1 were calculated by comparing the density of the electrospun mat to the density of a film that was non-porous. The density of the films was calculated using the liquid displacement method where a known mass of the film was added to a known amount of solvent (hexane). The amount of liquid displaced was measured and used to calculate the density. The density of the electrospun mats was calculated using Equation 1, where the mat thickness was measured using digital callipers.[16] The percent porosity was quantified using Equation 2.

$$\rho\left(\frac{g}{cm^3}\right) = \frac{mat\ mass\ (g)}{mat\ thickness\ (cm) \times mat\ area\ (cm^2)} \quad (1)$$

$$Porosity\ \% = \left(\frac{\rho_{film} - \rho_{mat}}{\rho_{film}}\right) \times 100\% \quad (2)$$

6.1.3.7 Interactions of water with the electrospun fibres

The stability of the TA/PVCL 0.15:1 and 0.29:1 electrospun samples was studied by immersing the samples in distilled water (DW) and 10 mM phosphate buffered saline (PBS) for 1 week. Following this the samples were dried under ambient conditions and examined with SEM.

6.1.3.8 Contact angle measurements

To determine the hydrophilicity of the electrospun TA/PVCL 0.15:1 and 0.29:1 samples, the contact angle was measured using the sessile drop method. A 5 μL drop of MilliQ water was placed on the surface of the electrospun mats and the average contact angle was calculated using the SCA20 software. The measurements were taken for up to 1 minute and average values were obtained from measurements from 5 to 7 positions.

6.1.3.9 Fourier transform infrared spectroscopy of TA/PVCL electrospun fibres

In order to investigate the chemical structure, infrared spectra of TA, PVCL and the TA/PVCL electrospun fibres were acquired using Nicolet Magna-IR Spectrometer 750 in

photo-acoustic mode using a carbon black reference. The spectra were obtained in the range 400 to 4000 cm^{-1} and the data was processed via the Omnic computer program.

6.1.3.10 Thermogravimetric analysis of TA/PVCL electrospun fibres

The mass content of TA and PVCL in the hydrogels was investigated using the TA Instruments Discovery TGA. Samples were heated from room temperature to 550˚C at a heating rate of 10˚C/min under N_2 atmosphere.

6.1.4 Results and Discussion

6.1.4.1 Interaction of TA and PVCL in solution using rheology

PVCL, as a water soluble polymer, can be electrospun directly from aqueous solutions at high concentrations.[11] However, such electrospun fibres would again be water soluble and thus of limited use for applications such as tissue engineering. As such, in order to make these fibres insoluble in water, we introduced Tannic Acid (TA) to crosslink the fibres through hydrogen bonding interactions. Although both TA and PVCL are water soluble, the mixture of PVCL/TA has been shown to be insoluble. The main issue arises when electrospinning was attempted with aqueous solutions of TA and PVCL: it was observed that the addition of even a small amount of TA to a PVCL aqueous solution resulted in instant gelation, thus making electrospinning infeasible. Thus, a number of other water miscible solvents for TA and PVCL were investigated and N,N-dimethylformamide (DMF) was found to be a suitable solvent where both TA and PVCL could be dissolved in solution without gelation. This was thought to be due to the polar but aprotic nature of DMF, which was able to dissolve both TA and PVCL (and thus solvates them) but unlike protic solvents, did not promote hydrogen bonding that led to gelation.

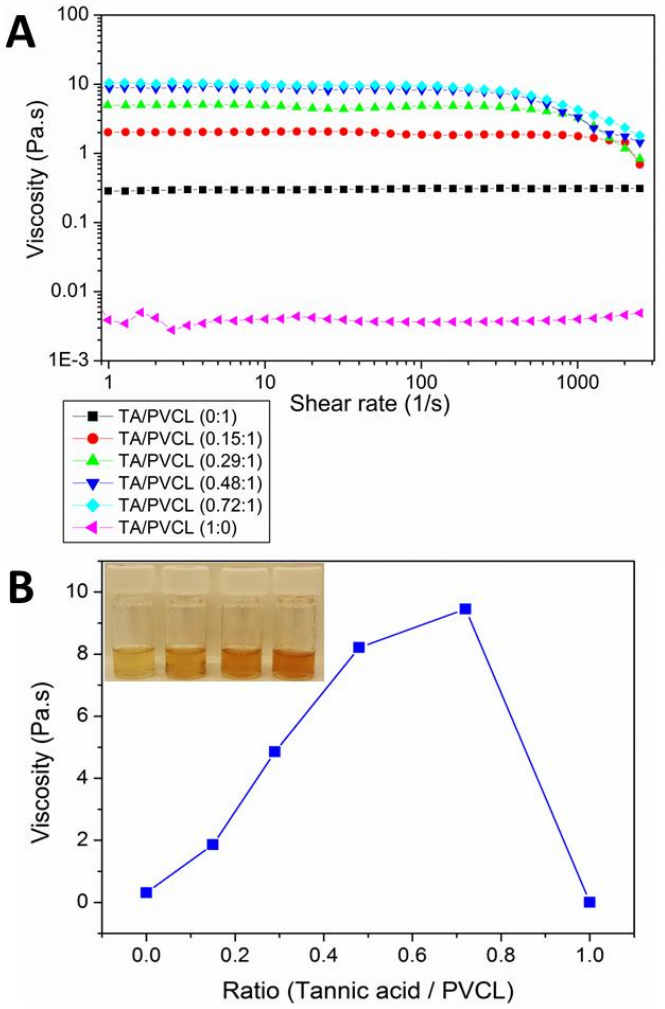


Figure 6.1 A) Plot of viscosity with increasing shear rate for the TA, PVCL and TA/PVCL samples. B) Value of the viscosity at a shear rate of 100 (1/s) with increasing TA content. Inset: Photograph of TA/PVCL solutions with increasing TA content (left to right).

In order to understand the interaction between TA and PVCL in solution, the rheology of the TA/PVCL solutions in DMF was first performed at 25°C. The solutions were made by slow addition of a solution of TA in DMF to a solution of PVCL in DMF. The addition of TA caused some gelation which redissolved in the solution with mechanical agitation. As the amount of TA was increased, the solution was diluted with DMF to the point where no gel is observed, and a series of samples were prepared by this method with varying TA:PVCL ratio.

The viscosity of various experimental solutions relative to the shear rates were determined from rheological analyses and are depicted in Figure 6.1A. The PVCL solutions (without TA) displayed Newtonian behaviour up to high shear rates with a value of approximately 0.31 Pa.s, while a 15 wt% TA solution showed a much lower value of 0.004 Pa.s. When they are mixed together, it was observed that the steady viscosity values increased from 1.9 to 9.5 Pa.s

with increasing TA content, despite the absolute PVCL concentration actually decreasing (Figure 6.1B). Indeed, the combined TA/PVCL solutions displayed increasingly higher viscosity than either solution alone despite the lower concentrations of the polymeric component (PVCL). TA is a weak polyacid with phenolic groups that can act as H donors to form hydrogen bonds with carbonyl groups of other compounds, including PVCL (Figure 6.2).[14] Therefore, the addition of TA to the PVCL solution can be expected to result in an increase in viscosity due to the hydrogen bonding interaction between the TA and PVCL molecules. This is confirmed by the experimental result which shows increasing viscosity with higher TA content. Higher TA content meant that more hydrogen bonding sites were available to create an extended crosslinked network with the PVCL through hydrogen bonding interactions. Without this interaction, one would expect that with increasing TA content the viscosity would decrease as TA itself, being a small molecule, has very low solution viscosity. However, similar viscosity of the solutions above 0.48:1 TA/PVCL ratio indicates that at this concentration saturation of hydrogen bonding between TA and PVCL has occurred. Thus, additional TA does not increase solution viscosity any further with the 0.48:1 and 0.72:1 ratio samples showing very similar properties.

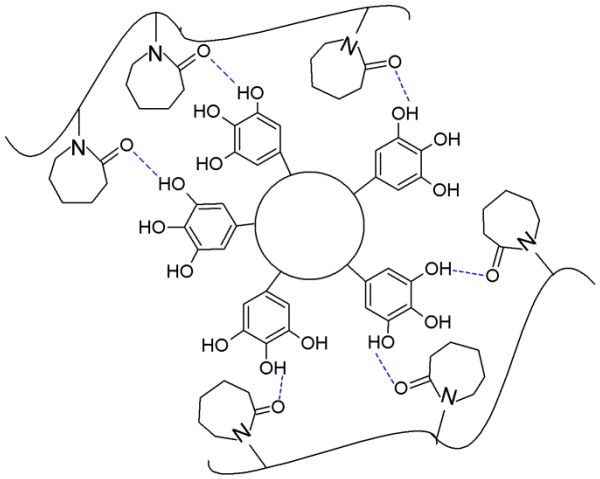


Figure 6.2 Schematic of the proposed hydrogen bonding interactions between PVCL groups and the TA molecule.

The TA/PVCL solutions also exhibit shear thinning behaviour not observed in the pure PVCL system. This behaviour has previously been reported for other systems, where hydrogen bonding interactions are present and is attributed to the shear stress disrupting the hydrogen bonds and thus making the solution less viscous.[17, 18] At low shear rates the solution showed a Newtonian plateau, where the viscosity remained constant, indicating good mixing and a dominant hydrogen bonding interaction between the PVCL and TA. However, at higher

shear rates the hydrogen bonds are disrupted which leads to the decrease in viscosity. The value of the shear rate at the onset of the shear thinning behaviour is observed to be progressively lower with increasing TA content up to a value of 0.48, above which the behaviour is similar. This earlier onset of shear thinning is expected due to the greater amount of hydrogen bonds in solutions with higher TA content, resulting in a greater effect due to the aforementioned disruption of hydrogen bonding through mechanical shear.

6.1.4.2 Characterisation of TA/PVCL electrospun fibre diameter and morphology

Electrospinning of PVCL from aqueous solutions has been known to yield nanofibrous mats in aqueous solutions at high concentrations.[11] As mentioned, the addition of TA increased solution viscosity (Figure 6.1), which meant that the solution concentration of PVCL required for electrospinning decreased. Variables such as, flow rate, collector distance and voltage were investigated by changing one at a time while keeping the others constant. The ranges for the flow rate, collector distance and voltage that were investigated were 0.5 to 1.5 mL/h, 5 to 15 cm, and 10 to 15 kV, respectively. As a result, the optimum conditions for producing a stable jet that produced a uniform fibre deposition were determined to be 0.8 mL/h, 10 cm, and 15 kV. However, it was observed that these parameters, although they affect the apparent stability of the jet, did not have a large effect on the fibre morphology.

In the electrospinning of PVCL/TA, the dominant parameter in determining fibre morphology was the PVCL/TA ratio as this determines the viscoelastic properties of the electrospinning solution. Figure 6.3 depicts the fibres with increasing tannic acid content and consequently decreasing PVCL content. It can be observed that the spinnability of the solution was dependent on the ratio of TA to PVCL. At low TA content the resultant mat was predominantly composed of fibres with some beaded fibres present, which indicates that there may be some gel formation due to TA, but the overall morphology was fibrous. With an increase in the TA proportion to 0.48:1 it was observed that the spinnability was greatly decreased with an increase in the amount of electrospraying that occurred. Some fibres were still present and the beaded fibre morphology was again observed, indicating inhomogeneity in the solution viscosity due to possible presence of gelled material in solution, which resisted stretching into fibres. When the TA/PVCL ratio was increased further to 0.72:1 the morphology was dominated by beads with very few fibres present. This is attributed to excess TA resulting in gelling of the solution and decreasing chain entanglement between polymer molecules in solutions, resulting in droplet formation due to Plateau-Rayleigh instability. As

was observed from rheological data, at this ratio (0.72:1) we are likely to be above the saturation point and thus the excess TA would promote droplet formation. We have previously observed a similar case in an ionomer/carrier polymer system, where an increase in ionic interaction is beneficial for electrospinning as it increases solution viscosity, however above a certain limit it inhibits electrospinning due to gel formation.[19] Thus, it was deemed that the ratios of 0.15:1 to 0.29:1 were optimum for producing electrospun fibres and these two ratios were selected for further analysis.

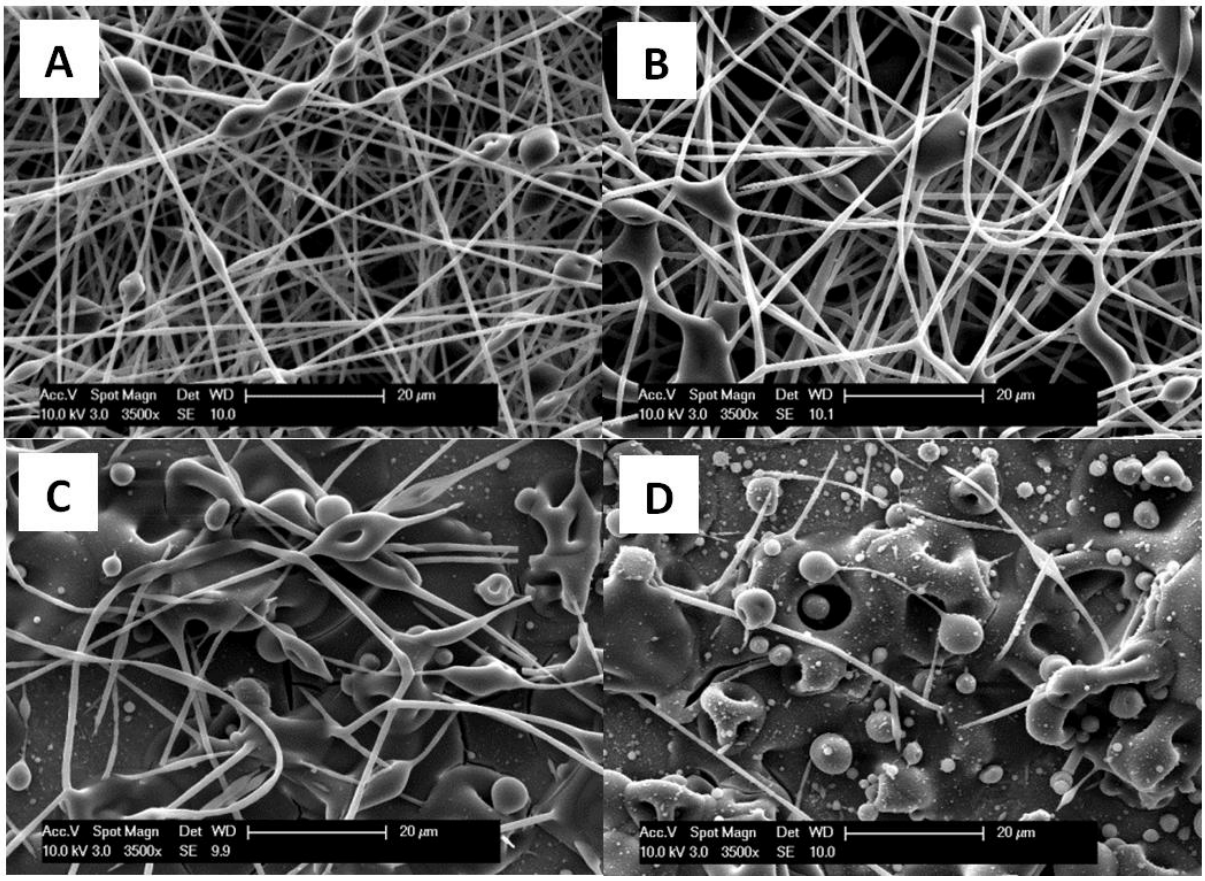


Figure 6.3 SEM micrographs of electrospun samples from solutions with TA/PVCL ratios of A) 0.15:1; B) 0.29:1; C) 0.48:1; D) 0.72:1.

The fibre size distribution was determined using the SEM images and is shown in Figure 6.4. The average fibre diameters for the TA/PVCL ratios of 0.15:1 and 0.29:1 are 700.4 ± 128.4 nm and 899.2 ± 166.7 nm, respectively. Thus, the average fibre diameter increased with TA content, which is attributed to the increase in solution viscosity as seen through rheological measurements (Figure 6.1). In addition, the average fibre size for our TA/PVCL samples was larger than those reported for PVCL alone at similar concentrations, and is attributed to the higher viscosity of the PVCL/TA system.[11] In addition, the fibre size distribution was very

broad for both ratios, ranging from several hundred nanometres to a few micron sized fibres, but this was expected as it has been observed for another PVCL-based electrospun system.[11] The porosity of the TA/PVCL 0.15:1 and 0.29:1 electrospun mats was calculated to be 89% and 85%, respectively, and the lower porosity of the mat with 0.29:1 TA/PVCL is likely due to the larger fibres reducing the pore space in that mat. The porosity of electrospun mats has been shown to affect their wettability and is also important for tissue engineering applications, where it is allows for nutrient transport, cell communication and migration.[20] In this case, both electrospun mats show a very high porosity, which would be suitable for these applications.

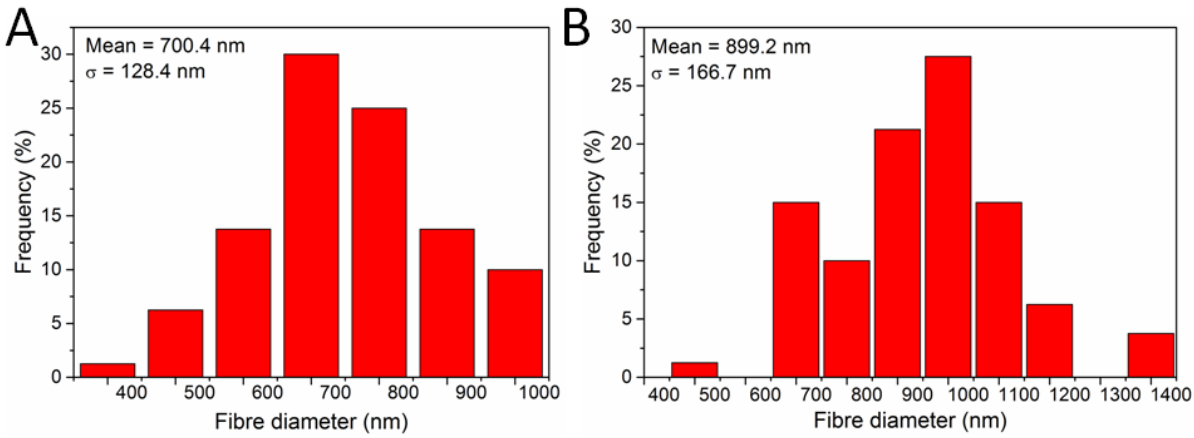


Figure 6.4 Distribution of fibre diameters for electrospun fibres from TA/PVCL blend solutions with ratios of A) 0.15:1 and B) 0.29:1.

6.1.4.3 Effect of water on the morphology of electrospun TA/PVCL fibres

Since the aim of the study is to produce fibres that are insoluble in water after electrospinning, the TA/PVCL 0.15:1 and 0.29:1 electrospun samples were exposed to water to investigate the effect of the crosslinking formed via hydrogen bonds. After drying in an oven to anneal the fibres and remove the electrospinning solvent (DMF), the samples were initially exposed to a droplet of deionised water (DW) on the surface of the mat and allowed to dry under ambient conditions, after which the area was examined using SEM (Figure 6.5). In addition, the mats were immersed in DW and phosphate buffered saline (PBS) over a period of 7 days to study the stability of the fibres over time and in the presence of salt. It was observed that in both ratios of TA and PVCL, the sample fibres were insoluble after exposure to water in the short as well as long term, which indicates successful crosslinking of the PVCL strands by strong hydrogen bonding with TA. In the case of TA/PVCL 0.15:1, there

was some fusing of the fibres observed in addition to some breakages, however overall the integrity of the mat was maintained. Initially, the TA/PVCL 0.29:1 fibres exposed to a droplet of water were relatively unchanged. However, immersion for 7 days in DW and PBS solutions appears to have resulted in some collapse of the mat structure due to swelling and fusing of the fibres. In addition, it can be seen that many of the fibres were fractured, which indicates that swelling and shrinkage has occurred during immersion and the subsequent drying process. Indeed, the average fibre diameters of the TA/PVCL 0.15:1 and 0.29:1 samples exposed to water on the surface were determined to be 766.3 ± 183.9 nm and 1022 ± 201.4 nm respectively (Figure 6.6). This correlates to an increase in diameter of approximately 9% and 14% for the 0.15:1 and 0.29:1 ratios after water immersion and subsequent drying. This can be explained by the combined effect of greater TA and reduced PVCL content in this system. Firstly, increased hydrophilicity of the fibres with higher TA content may lead to greater volumetric changes upon hydration. Also, there will be a decrease in the elasticity of the fibres due to the reduced PVCL content, as PVCL is the component that provides the mechanical strength to the fibres. Thus the fibres with greater TA content were more brittle and fractured more easily than the fibres with lower TA content (and higher PVCL content). However, despite the fractures observed in SEM the overall physical appearance of the mats remained dimensionally stable with only a few strand breakages due to drying induced rupture after immersion, with sufficient physical entanglement remaining between the fibres to maintain its form.

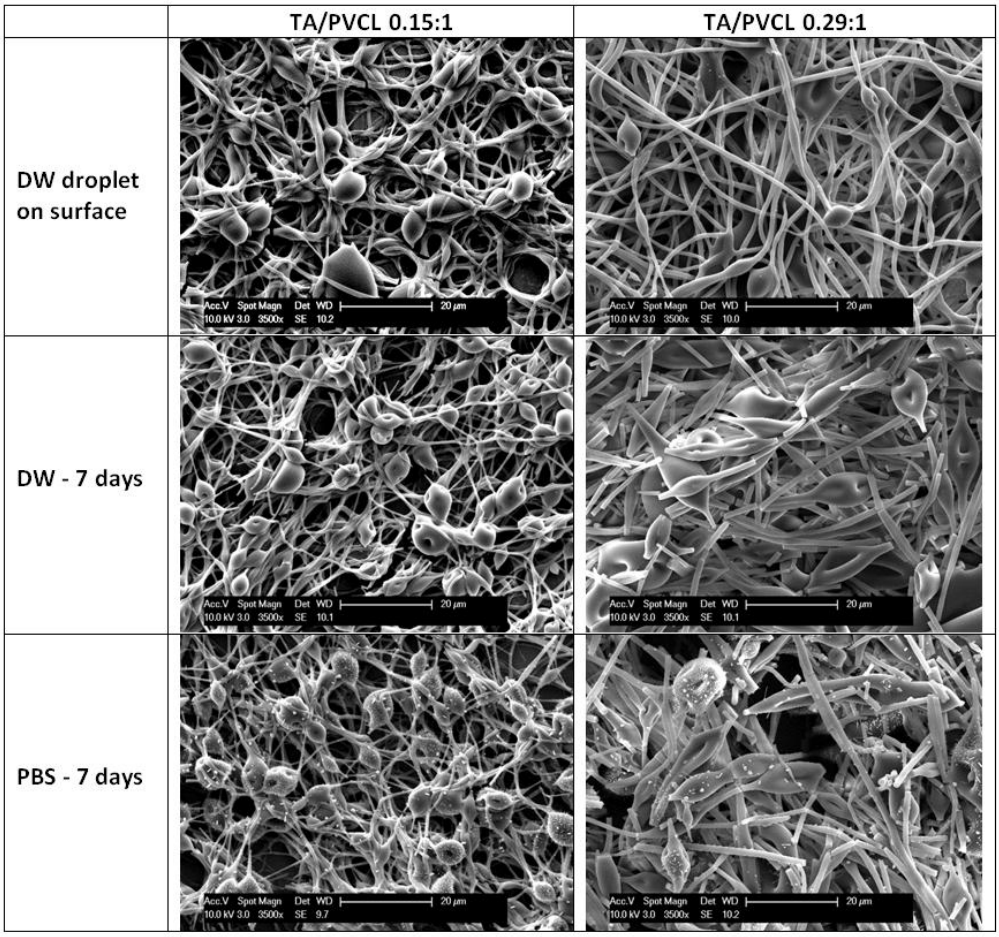


Figure 6.5 SEM micrographs of TA/PVCL electrospun samples immersed in DW and PBS for up to 7 days.

6.1.4.4 Wettability of TA/PVCL electrospun mats

PVCL, TA/PVCL 0.15:1, and TA/PVCL 0.29:1 samples were prepared in the form of cast films and electrospun mats to compare the influence of electrospinning induced morphology on wettability. The sessile drop method was employed to measure the contact angles and was conducted at room temperature (24˚C). The PVCL cast film was found to wet very quickly and had a low contact angle of 28.4˚ (±0.4) as expected due to the hydrophilic nature of PVCL. It was not possible to measure the contact angle of the PVCL electrospun mat as the droplet spread immediately on the surface, dissolving the fibres. Contact angles of TA/PVCL 0.15:1 and 0.29:1 cast films were measured as 70.0˚ (±1.6) and 54.0˚ (±0.1), respectively (Figure 6). However, the contact angle of the TA/PVCL films was observed to decrease over several minutes as the droplet spread over the surface. This observation indicates that through incorporation of TA, the contact angle of PVCL is initially increased somewhat. This can be explained as TA is occupying the hydrogen bonding sites of PVCL; however over several

minutes the contact angle was observed to decrease indicating that the water is able to penetrate into the hydrophilic structure. When comparing the contact angles of the TA/PVCL films, it may be observed that by increasing the TA content the contact angle of the cast films decreased, which is attributed to the hydrophilicity of TA. Zhang et al. reported that the use of TA as a crosslinker for Gelatin resulted in lower contact angles with increasing TA content from approximately 90˚ to 50˚, which is in line with our observations.[21] Similarly, Rivero et al. have shown that TA results in decreasing contact angles from approximately 88˚ to 78˚ when used as a crosslinker for Chitosan.[22] In both cases this has been attributed to the hydrophilic sites of the TA molecules that are exposed on the surface.[21, 22]

The contact angle measurements of the electrospun TA/PVCL 0.15:1 and 0.29:1 mats gave values of 126.4˚ (±1.9) and 131.2˚ (±4.6), respectively (Figure 6.6). The contact angle measurements were taken for up to 1 minute and did not change during this period of time. However, the droplets were observed to spread and fully wet the surface over an extended period of time (>10 minutes). Comparatively, the contact angle values for our TA/PVCL fibrous mats are initially much higher than the cast films and as the values are >90˚ this indicates the surface property has changed from hydrophilic to hydrophobic. Other reports have shown that the formation of nanofibres by electrospinning of hydrophilic or hydrophobic polymers results in surfaces that exhibited high contact angles due to the surface roughness.[23-25] In addition, However, if the mat is in contact with water for a prolonged period (>1 minute), it was observed that the water droplet is able to eventually wet the fibres and becomes absorbed in the pores, due to the hydrophilicity of PVCL and TA. This is likely due to water penetrating inside the fibres, which results in some disruption of the PVCL-TA structure and swelling of the fibres as observed from the increase in fibre diameter (Figure 6.6).

The temperature-responsiveness of the optimal TA/PVCL 0.15:1 electrospun mat was examined by measuring the contact angle at elevated temperature (50˚C). The TA/PVCL 0.15:1 mat shows hydrophobic nature, exhibiting a contact angle of 128.9˚ (±1.4) at 50˚C. Thus, the electrospun mat behaved hydrophobically above and below the LCST due to surface roughness effect. In order to understand the effect of the LCST, the time for the water droplet to spread on the surface was measured at room temperature (25˚C) and 50˚C. It was found that at room temperature the water droplet spread quite quickly over several minutes. However, at 50˚C, the time for the droplet to spread increased by about ten times. This is attributed to the inability for the water to penetrate due to the aggregation of the PVCL

particles above the LCST. In a similar system, it has been shown that the LCST behaviour of PVCL nanoparticles stabilised by hydrogen bonding interactions with a crosslinking agent was retained.[15] This observation indicates that the physically crosslinked PVCL electrospun fibres could potentially be used as controlled release systems.

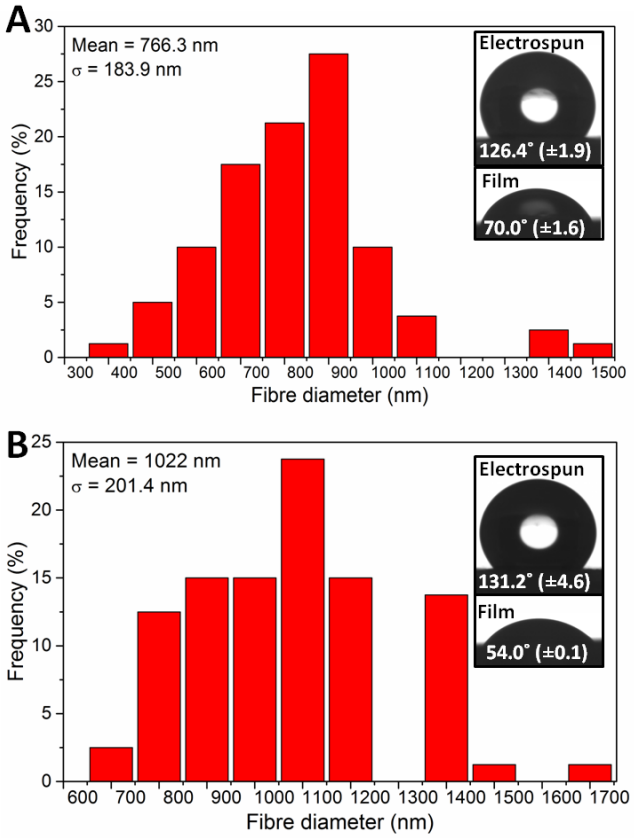


Figure 6.6 Distribution of fibre diameters of TA/PVCL electrospun mats with ratio A) 0.15:1 and B) 0.29:1 after exposed to a droplet of DW on the surface. Inset: Contact angle measurements on electrospun and cast films of TA/PVCL samples A) 0.15:1 and B) 0.29:1.

6.1.4.5 Structural analysis of TA/PVCL electrospun mats

To further study the structural features of the fibres, photo-acoustic FTIR was used as it allows us to obtain insight into the extent of hydrogen bonding of the solid electrospun mats (Figure 6.7). The PVCL, TA, and TA/PVCL 0.15:1 and 0.29:1 spectra show prominent peaks due to the carbonyl groups of PVCL and TA, and also a broad band at high wavenumbers in the case of TA typical of hydrogen-bonded OH groups (Figure 6.7). The peak at 2924 cm^{-1} in the spectra of PVCL and the electrospun TA/PVCL samples is due to the aliphatic C-H stretching.[11] The major peak at 1720 cm^{-1} is assigned to the stretching vibrations of the C=O groups of TA.[14] It can be observed that this peak is present in the spectra of the TA/PVCL

electrospun mats, indicating the presence of TA. In addition, the peaks at 1616 cm^{-1} for TA and 1640 cm^{-1} for PVCL are assigned to the carbonyl stretch vibrations of the caprolactam ring of PVCL and aromatic ring of TA.[14, 26] The broadening and presence of a shoulder at the peak centred at 1635 cm^{-1} is indicative of the increasing TA content in the electrospun mats, and is likely the result of specific interactions between these carbonyl groups (which is due to PVCL) and the phenolic OH of TA. Also, on comparison of the relative peak heights occurring at 1635 cm^{-1} and 1720 cm^{-1}, it can be seen that the height is approximately equal for TA/PVCL 0.15:1 electrospun mat. However, the peak due to TA at 1720 cm^{-1} for the 0.29:1 sample is observed to increase relative to the 1635 cm^{-1} peak, which further confirms the increased presence of TA in the 0.29:1 sample as expected. In addition, the broad band occurring at 3200 cm^{-1} is indicative of the hydrogen-bonded OH groups of TA. This absorption is shown to broaden with increasing TA content in the TA/PVCL 0.15:1 and 0.29:1 electrospun samples, confirming the presence of hydrogen bonding in this system.

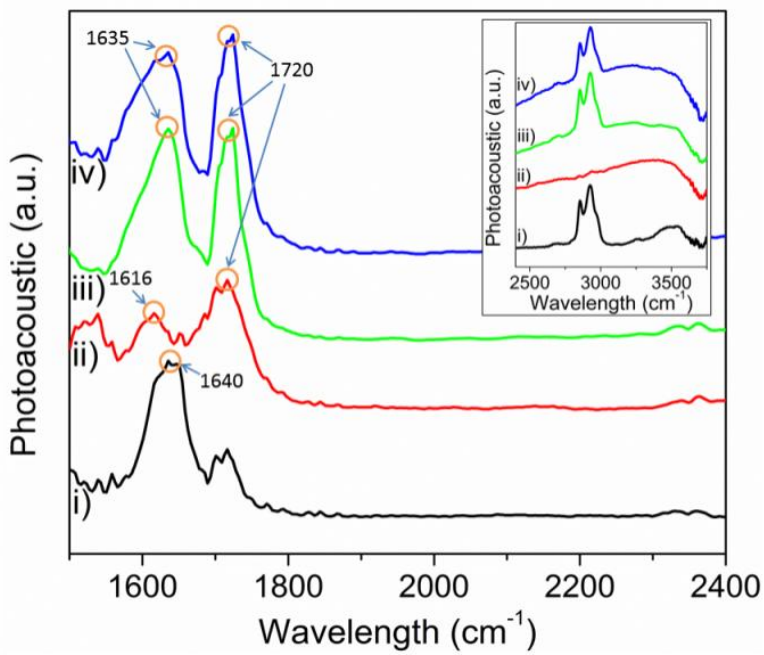


Figure 6.7 Photoacoustic FTIR spectra of i) PVCL, ii) TA, and electrospun TA/PVCL iii) 0.15:1 and iv) 0.29:1.

6.1.4.6 Thermogravimetric analysis of TA/PVCL electrospun mats

Thermogravimetric analysis (TGA) was employed to further confirm the content and ratio of TA and PVCL in the electrospun fibrous mats (Figure 6.8). PVCL shows a sharp degradation beginning at approximately 350˚C with the temperature corresponding to the maximum rate of weight loss at 450˚C, which is in agreement with literature values.[27] The thermogram for

TA shows multiple degradation processes with a residue of 21.5% at 550˚C, which is consistent with the known behaviour.[28] The electrospun TA/PVCL 0.15:1 and 0.29:1 samples show some degradation between approximately 250˚C to 370˚C as for TA, with a sharp decline from 370˚C being attributed to predominantly the PVCL component. The increasing proportion of mass loss between the 250˚C and 370˚C period, coupled with the increased amount of residue for the TA/PVCL 0.29:1 sample indicates the larger proportion of TA as also shown from the FTIR data. An estimate of the percentage of TA in the electrospun TA/PVCL 0.15:1 and 0.29:1 fibres was calculated by using the assumption that the residue consists solely of TA as the PVCL residue is extremely low and considered negligible. In addition, the initial weight loss from 250˚C to 370˚C was assigned to the presence of TA, with the remaining PVCL. Thus, from these calculations the mass percentage of TA was 18.1% and 32.4% for the TA/PVCL 0.15:1 and 0.29:1 electrospun samples, respectively. These correlate quite closely with the mass concentrations of the electrospinning solutions; however this should be considered an estimate due to the overlap of degradation temperature between PVCL and TA.

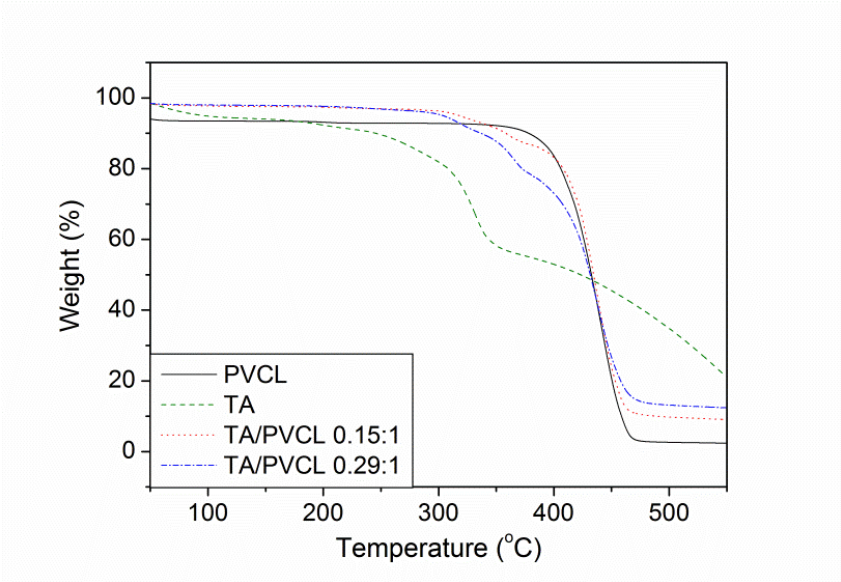


Figure 6.8 TGA thermograms of PVCL, TA and electrospun TA/PVCL 0.15:1 and 0.29:1.

6.1.5 Conclusions

In this work we report for the first time the fabrication of water-insoluble PVCL electrospun mats prepared by direct electrospinning and taking advantage of the hydrogen bonding interaction of PVCL with TA crosslinker. The rheology of the TA/PVCL solutions in DMF demonstrated shear-thinning behaviour, which indicated the presence of hydrogen bonding interactions between PVCL and TA that are disrupted at high shear rates. Several ratios of

TA/PVCL were studied and it was found that the optimum ratios for producing electrospun fibres were 0.15:1 and 0.29:1, where increased tannic acid content above this level resulted in the presence of droplets among the fibres. The lower TA content was found to be sufficient to induce water insolubility to the sample, which has the best overall morphology, with narrower fibre size distribution and less swelling when exposed to water. Fibres with the higher TA content appeared to be more brittle and fractured more easily. The contact angle measurements of both ratios resulted in values of 126.4˚ (±1.9) and 131.2˚ (±4.6), respectively, indicating that the fibrous morphology resulted in hydrophobic behaviour. However, over a longer time period the mats are wettable. The optimal TA/PVCL electrospun mat exhibited LCST behaviour indicated by the greatly increased time required for the penetration of the water droplet. By investigating a method for the simple crosslinking of electrospun PVCL nanofibres through the hydrogen bonding interactions with TA, we have increased the potential of this material for use in biomedical applications where the integrity of the fibres in the presence of water is highly important.

6.1.6 References

1. Agarwal, S.; Wendorff, J. H.; Greiner A., *Polymer* **2008**, *49*, 5603-21.
2. Min, B-M.; Lee, G.; Kim, S. H.; Nam, Y. S.; Lee, T.S.; Park, W. H., *Biomaterials* **2004**, *25*, 1289-97.
3. Zhang, Y. Z.; Huang, Z. M.; Xu, X. J.; Lim C, T.; Ramakrishna, S., *Chem. Mater.* **2004**, *16*, 3406-9.
4. Ma, P. X., *Adv. Drug Delivery Rev.* **2008**, *60*, 184-98.
5. Teo, W. E.; Ramakrishna, S., *Nanotechnology* **2006**, *17*, R89-R106.
6. Ashammakhi, N.; Ndreu, A.; Yang, Y.; Ylikauppila, H.; Nikkola, L., *Eur. J. Plast. Surg.* **2012,** *35*, 135-49.
7. Teo, W-E.; Inai, R.; Ramakrishna, S., *Sci. Technol. Adv. Mater.* **2011**, *12*, 013002.
8. Jeong, B.; Gutowska, A., *Trends Biotechnol.* **2002**, *20*, 305-11.
9. Liang, X.; Kozlovskaya, V.; Chen, Y.; Zavgorodnya, O.; Kharlampieva, E.; *Chem. Mater.* **2012**, *24*, 3707-19.
10. Feldstein, M. M.; Bovaldinova, K. A.; Bermesheva, E. V.; Moscalets, A. P.; Dormidontova, E. E.; Grinberg, V. Y.; Khokhlov, A. R., *Macromolecules* **2014**, *47*, 5759-67.
11. Webster, M.; Miao, J.; Lynch, B.; Green, D. S.; Jones-Sawyer, R.; Linhardt, R.J.; Mendenhall, J., *Macromol. Mater. Eng.* **2013**, *298*, 447-53.

12. Erel-Unal, I.; Sukhishvili, S. A., *Macromolecules* **2008**, *41*, 8737-44.
13. Kozlovskaya, V.; Baggett, J.; Godin, B.; Liu, X.; Kharlampieva, E.. *ACS Macro Lett.* **2012**, *1*, 384-7.
14. Erel-Unal, I.; Sukhishvili, S. A., *Macromolecules*, **2008**, *41*, 3962-70.
15. Vihola, H.; Laukkanen, A.; Tenhu, H.; Hirvonen, J. J., *Pharm. Sci.* **2008**, *97*, 4783-93.
16. Lee, J. B.; Jeong, S. I.; Bae, M. S.; Yang, D. H.; Heo, D. N.; Kim, C. H.; Alsberg, E.; Kwon, I. K., *Tissue Eng., Part A* **2011**, *17*, 2695.
17. Petravic, J.; Delhommelle, J. J., *Chem. Phys.* **2005**, *122*, 234509.
18. Burrell, G. L.; Dunlop, N. F.; Separovic, F., *Soft Matter*, **2010**, *6*, 2080-6.
19. Subianto, S.; Cavaliere, S.; Jones, D. J.; Rozière, J., *J. Polym. Sci. Part A: Polym. Chem.* **2013**, *51*, 118-28.
20. Wang, X.; Ding, B.; Li, B., *Mater. Today* **2013**, *16*, 229-41.
21. Zhang, X.; Do, M. D.; Casey, P.; Sulistio, A.; Qiao, G. G.; Lundin, L.; Lillford, P.; Kosaraju, S. J., *Agric. Food Chem.* **2010**, *58*, 6809-15.
22. Rivero, S.; Garcia, M. A.; Pinotti, A. *J. Mater. Phys. Chem.* **2013**, *1*, 51-7.
23. Papadopoulou, S. K.; Tsioptsias, C.; Pavlou, A.; Kaderides, K.; Sotiriou, S.; Panayiotou, C., *Colloids Surf., A* **2011**, *387*, 71-8.
24. Zhu, M.; Zuo, W.; Yu, H.; Yang, W.; Chen, Y., *J. Mater. Sci.* **2006**, *41*, 3793-7.
25. Ahmed, F.; Choudhury, N. R.; Dutta, N. K.; Zannettino, A.; Knott, R., *Biomacromolecules* **2013**, *14*, 3850-60.
26. Kozlovskaya, V.; Kharlampieva, E.; Drachuk, I.; Cheng, D.; Tsukruk, V. V., *Soft Matter* **2010**, *6*, 3596-3608.
27. Kozanoglu, S.; Ozdemir, T.; Usanmaz, A., *J. Macromol. Sci., Part A: Pure Appl. Chem.* **2011**, *48*, 467-77.
28. Pantoja-Castro, M. A.; González-Rodríguez, H. *Rev. Latinoam. Quím.* **2011**, *39*, 107-12.

6.1.7 Supplementary information

S6.1.7.1 NMR analysis of PVCL

^{1}H NMR spectra of VCL and PVCL were obtained from 300 MHz Bruker Avance spectrometer operating at 300.138 MHz (S6.1). The solvent used was deuterated chloroform ($CDCl_3$). The peak assignments for the ^{1}H-NMR spectra of VCL and PVCL are shown in Table S6.1. All protons are accounted for and the disappearance of the signal for the vinyl proton indicated that there was no residual monomer in the polymer sample. The results agree with reported literature values for this material.[1, 2]

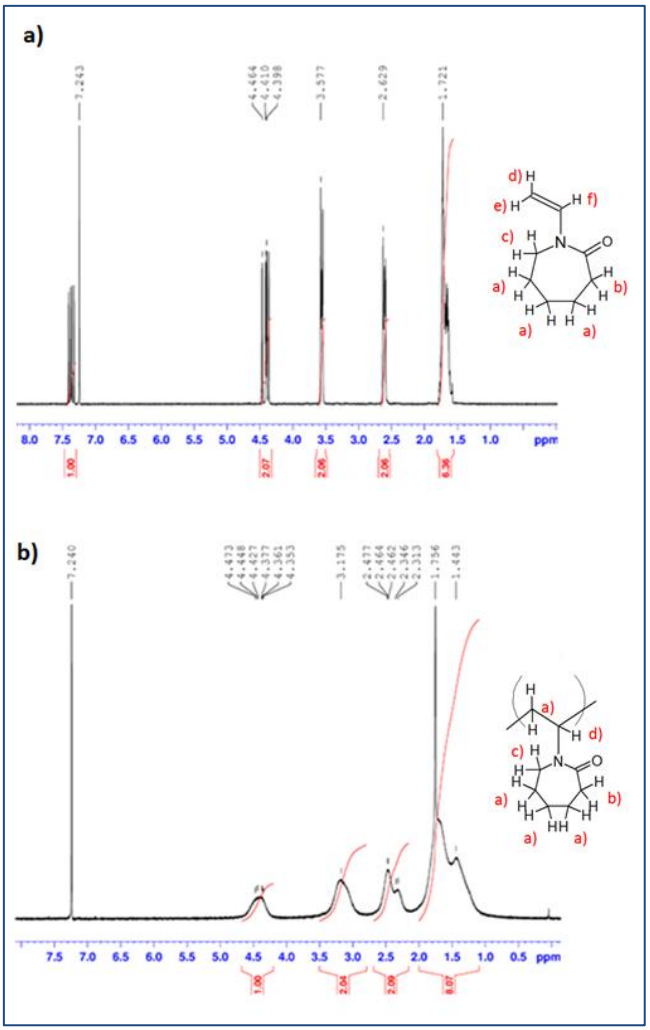


Figure S6.1 ^{1}H-NMR spectra of a) VCL and b) PVCL

Table S6.1 Peak assignment for ^{1}H-NMR spectra of VCL and PVCL

Proton type	Group	Shift (ppm)	
		VCL	PVCL
H_a	methylene	1.721	1.443, 1.756
H_b	methylene	2.629	2.313 – 2.477
H_c	methylene	3.577	3.175
H_d	ethylene	4.398	4.353 – 4.473
H_e	ethylene	4.464	-
H_f	ethylene	7.243	-

S6.1.7.2 Viscosity average molecular weight determination

The viscosity average molecular weight (M_v) of the synthesised PVCL was determined from the intrinsic viscosity ([η]) by employing the Mark-Houwink relation $[\eta] = K*M_v^a$, with K = 0.0105 ml/g and a = 0.69.[3] An Ubbelohde-type viscometer was used at 25˚C with water as the solvent. The reduced viscosity (η_{red}) and inherent viscosity (η_{inh}) were determined and the average of the Y-intercepts was used to calculate the [η] (Figure S6.2). Using the Mark-Houwink relation, the M_v was thus determined to be 35.4 kDa.

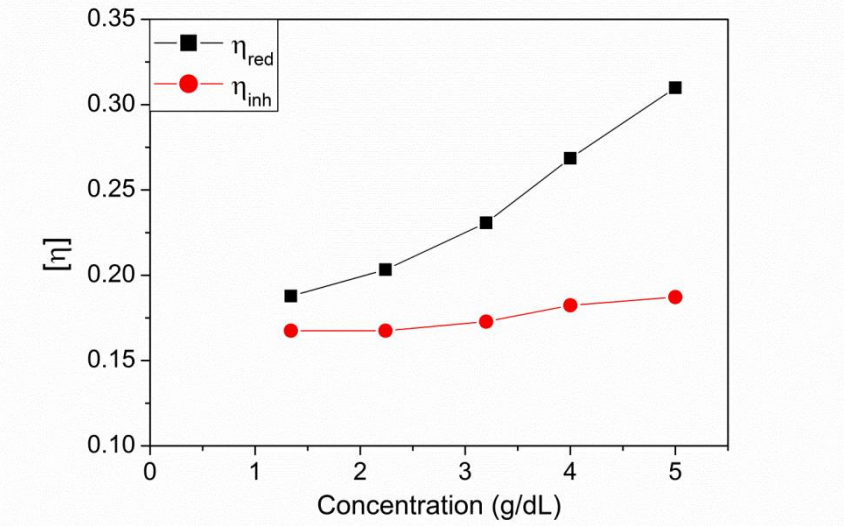


Figure S6.2 Plot of reduced and inherent viscosities determined for PVCL.

References

1. Webster, M.; Miao, J.; Lynch, B.; Green, D. S.; Jones-Sawyer, R.; Linhardt, R. J.; Mendenhall, *J. Macromol. Mater. Eng.* **2013**, 298, 447-453.
2. Kozanoglu, S.; Ozdemir, T.; Usanmaz, A., J. *Macromol. Sci., Part A: Pure Appl. Chem.* **2011,** 48 (6), 467-477.
3. Loos, W.; Verbrugghe, S.; Goethals, E. J.; Du Prez, F. E.; Bakeeva, I. V.; Zubov, V. P., *Macromol. Chem. Phys.* **2003,** 204 (1), 98-103.

6.2 Facile fabrication of shell crosslinked core/shell Poly(N-vinylcaprolactam)/Silk fibroin fibres by co-axial electrospinning

6.2.1 Abstract

The formation of PVCL/RSF core/shell electrospun fibres has been achieved for the first time using a facile co-axial electrospinning method. The solution and processing parameters for the co-axial electrospinning of poly(N-vinylcaprolactam) (PVCL) and regenerated silk fibroin (RSF) solutions were optimised for the production of fibres with core/shell morphology. The morphology of the fibres was confirmed using thermogravimetric analysis (TGA), scanning electron microscopy (SEM) and transmission electron microscopy (TEM). This work provides a platform for the formation of composite fibres that overcomes the aqueous solubility issue of PVCL without the need for further chemical modification and incorporates the biocompatibility of RSF. There is great potential to apply the PVCL/RSF core/shell electrospun fibres to biomedical applications where structural support and sustained release of therapeutic compounds is required.

6.2.2 Introduction

In recent years, co-axial electrospinning has gained significant importance for the formation of core/shell fibres with distinctly different properties. Such core/shell electrospun fibrous mats can be used as tissue engineering implants or wound dressings that combine mechanical support for cell growth and biocompatibility with the ability to deliver therapeutic compounds. For example, core/shell electrospinning can provide an effective way to fabricate thermo-responsive fibres whose temperature-responsiveness could be preserved and harnessed on demand by covering with a shell that can provide temporal protection. Compared to the widely studied poly(N-isopropylacrylamide) (PNIPAM), poly(N-vinylcaprolactam) (PVCL) is a promising thermo-responsive polymer, which is non-ionic, non-toxic and does not produce toxic small molecules on hydrolysis. However, electrospun PVCL nanofibres cannot maintain their shape or dimensional stability in aqueous solutions at temperatures below the LCST without any appropriate shell structure. So far, there are very few studies on fabricating PVCL based composite nanofibre systems for biomedical applications.

Silk fibroin is a highly biocompatible material that has been used as a shell material for a number of synthetic polymeric fibres. One advantage of regenerated silk fibroin (RSF)

electrospun nanofibres is that they have been shown to support cellular attachment and proliferation.[1-3] However, to date there are few studies that present the formation of core/shell fibres with silk fibroin and other water soluble polymers.[4-6] PVCL can be readily electrospun from aqueous solutions and is temperature-responsive at physiologically relevant temperatures. Chen et al. reported the fabrication of temperature-responsive electrospun nanofibres from PNIPAM and polycaprolactone (PCL).[7] However, PVCL has superior biocompatibility to PNIPAM due to its stability against hydrolysis.[8, 9] Despite this, to our knowledge there is no literature on core/shell electrospinning with neat PVCL, although there are some reports of electrospinning of PVCL copolymer with other synthetic polymers. Table 6.1 summarises the properties exhibited by RSF and PVCL, which highlights their complimentary properties that may be employed to develop functional materials. Thus, this work reports the facile fabrication of a new core/shell fibrous structure composed of silk fibroin and PVCL by co-axial electrospinning that incorporates the biocompatibility of silk with the responsiveness of PVCL in a symbiotic manner, which does not require any modification of PVCL.

Table 6.1 Summary of the properties of RSF and PVCL

RSF	**PVCL**
Tensile strength: 0.6 GPa	Thermo-responsive (LCST~35˚C)
Hydrophobic	Hydrophilic
Rigid	Electrospins easily
Crosslinkable	Water soluble, Difficult to crosslink

Co-axial electrospinning follows the same principles as conventional electrospinning, however the use of a smaller inner capillary that fits concentrically inside the larger outer capillary allows for the formation of core/shell fibres. A specially designed and prepared co-axial electrospinning setup was employed in this work to form core/shell fibres (Figure 6.9). Using this set up, core/shell electrospun fibres with defined boundaries between the core and shell materials can be formed due to the fact that the characteristic bending instability that occurs during electrospinning is shorter than the time taken for mixing and diffusion of two liquids.[4] There are a number of material parameters that must be optimised for the successful formation of core/shell fibres using co-axial electrospinning, including solvents, flow rates, and solution concentrations.[10] One important point to consider is the interaction between the

core and sheath solutions. Essentially, the interaction between the core and shell solutions at the tip of the capillary should not result in precipitation of either polymer. Silk fibroin has been shown to precipitate/gel rapidly when exposed to low pH, solvent exposure, and heat, among others, thus it was important to carefully select the solvents for the core and shell solutions. Thus, the first part of this work focuses on individual core or shell polymer's electrospinnability in a particular solvent, followed by co-axial electrospinning. Once a common solvent was identified for both silk and PVCL, then core/shell electrospinning was performed, which has the potential to attribute solvent welding with the formation of a diffused interface. Finally, the shell polymer has been crosslinked by exposure to ethanol vapour. The prepared fibres were characterised using thermal and microscopic methods.

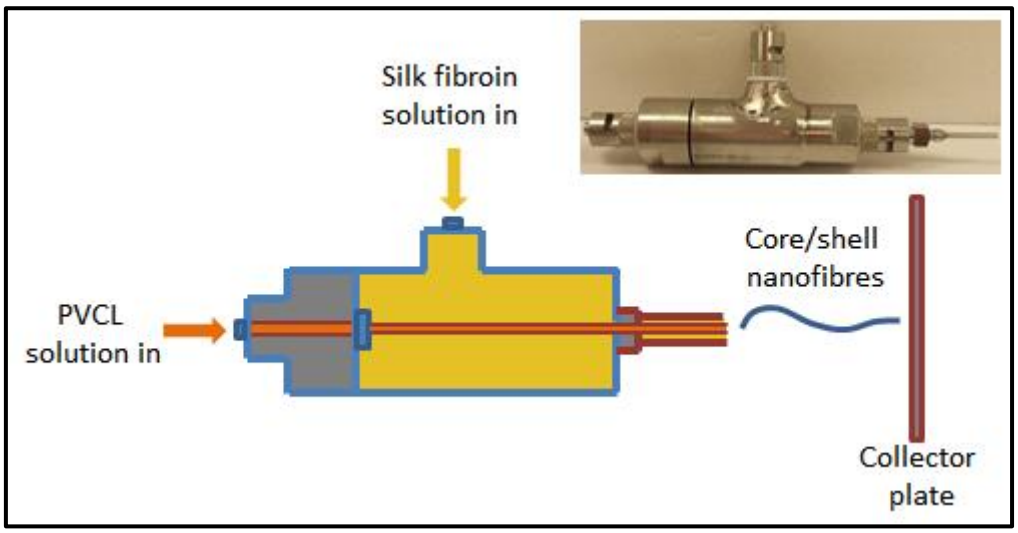


Figure 6.9 Schematic and photograph (inset) of co-axial electrospinning setup.

6.2.3 Materials and methods

6.2.3.1 Materials

Poly(N-vinylcaprolactam) (PVCL) was prepared via free radical polymerisation of the VCL monomer with 2,2'-azoisobutyronitrile (AIBN) and characterised as described in section 6.1. *Bombyx mori* silk was purchased as raw silk from Beautiful Silks, Australia. The regenerated silk fibroin (RSF) solution was prepared and characterised as described previously.[11] Hexafluoroisopropanol (HFIP) was purchased from CovaChem (United States).

6.2.3.2 RSF and PVCL solution preparation

PVCL was dissolved in water at concentrations of 30, 35 and 40 wt%.

RSF concentrated solution was obtained by evaporation at room temperature and diluted accordingly for rheology experiments.
RSF aqueous solution was dried in the fumehood at room temperature to obtain a solid film. The required mass of RSF, to prepare concentrations ranging from 8 to 12 wt%, was added to HFIP and allowed to dissolve at room temperature for several days. Similarly, solid PVCL was dissolved in HFIP to obtain concentrations ranging from 5 to 13 wt%.
The solutions were stirred overnight to ensure homogenous distribution.

6.2.3.3 Measurement of solution viscosity

The viscosities of the RSF and PVCL aqueous solutions with varying concentrations were measured using controlled stress rheometer Rheolyst 1000 N (TA Instruments, Delaware, U.S.A.). The measurements were undertaken at 25˚C using a 40 mm cone and plate geometry. The sample was placed between the fixed Peltier plate and a rotating cone attached to the driving motor spindle. The change in the shear stress with change in the shear rate was measured and the viscosity of solution was calculated. The viscosities of the solution are reported in Pa·s.

6.2.3.4 Conventional electrospinning of RSF and PVCL

A horizontal electrospinning setup was employed where the polymer solution was placed in a 5 mL syringe that was mounted on a syringe pump (KD Scientific). An 18 gauge needle was connected to the syringe. A high voltage DC power source was used to generate a potential difference ranging from 4 to 20 kV. The distance between the tip of the needle and collector plate was varied from 4 to 15 cm. Fibres were collected on an aluminium foil covered copper plate. The flow rate ranged for RSF was maintained at 0.5 mL/h and flow rates ranging from 0.25 to 0.5 mL/h were employed for electrospinning of PVCL.

6.2.3.5 Co-axial electrospinning of PVCL/RSF to form core/shell fibres

A horizontal co-axial electrospinning setup (Figure 6.9) was employed where the polymer solutions were placed in two 5 mL syringes that were mounted in two separate syringe pumps (KD Scientific). A 21 gauge needle was employed for the PVCL core solution and a 16 gauge needle was employed for the RSF shell solution. A high voltage DC power source was used to generate a potential difference of 15 kV, and a distance of 10 cm was maintained between the tip of the needle and collector plate. Fibres were collected on an aluminium foil covered copper plate. Flow rates ranging from 0.5 to 1.0 mL/h were investigated for the core and shell

solutions throughout the experiments. Following electrospinning, the mats were immersed in ethanol for 30 minutes to crosslink the RSF shell.[4]

6.2.3.6 SEM analysis of electrospun fibres

The appearance and morphology of the PVCL electrospun mats obtained from aqueous solutions was examined using the FEI Quanta 450 FEG ESEM. The fibre morphology of the RSF, PVCL and RSF/PVCL core/shell fibres from HFIP was examined using the on-axis in-lens secondary electron detector on a Zeiss MERLIN with GEMINI II column. The fibre size distributions for all samples were quantified using the ImageJ software.

6.2.3.7 Thermogravimetric analysis (TGA)

The mass content of PVCL and RSF in the electrospun mats obtained from co-axial electrospinning was investigated using the TA Instruments Discovery TGA. Samples were heated from room temperature to 550˚C at a heating rate of 10˚C/min under N_2 atmosphere.

6.2.3.8 Transmission electron microscopy (TEM)

TEM was employed to examine the core/shell morphology of the PVCL/RSF fibres. The JEM-2100F TEM (JEOL, MA, USA) was operated at 200 kV. For TEM analysis grid preparation, electrospun samples were crushed to a powder in liquid N_2 and dispersed in ethanol before deposition onto carbon coated 200 mesh TEM grid (ProSciTech, Australia). ImageJ software was used to determine fibre diameters.

6.2.4 Results and Discussion

In order to utilise the excellent electrospinnability of PVCL, studies into the aqueous PVCL system were undertaken as the core material with an aqueous RSF shell. As mentioned earlier, there has been little work to date on the electrospinning of PVCL, thus firstly the electrospinnability of PVCL from aqueous solvents was investigated. Initially, the viscosity of the PVCL aqueous solutions was measured to determine the concentrations that were most promising for electrospinning. Concentration and viscosity are two of the important parameters that govern the electrospinnability of a particular polymer.[12] Thus, it is important to optimise these for each polymer and solvent combination. It was observed that the viscosity of PVCL increased with concentration due to entanglement between polymer chains (Figure 6.10A). A dramatic increase in viscosity was observed at 30 wt% and above. Thus,

concentrations of 30, 35 and 40 wt% were deemed the most promising for electrospinning studies. All three concentrations (30, 35 and 40 wt%) were electrospun and the voltage and distances were varied from 10 to 20 kV and 5 to 15 cm, respectively. The conditions that allowed for a stable jet and adequate deposition of fibres were different for each PVCL concentration. The SEM images of the fibres prepared for each solution concentration at the optimum processing conditions are shown in Figures 6.10B-D. It was observed that the electrospun mats for 30 and 35 wt% exhibit a fibrous morphology with a number of beads. It has been observed for other polymer systems, such as PEO, that by increasing the concentration and consequently the viscosity, the number of beads decreased or disappeared.[12] This was also observed for the PVCL aqueous system where an increase in the concentration to 40 wt% resulted in a uniform electrospun mat void of beads (Figure 6.10D). The average fibre diameters for the 30, 35 and 40 wt% PVCL concentrations were measured as 555 ± 171 nm, 699 ± 144 nm, and 804 ± 92 nm, respectively. Thus, the fibre diameter is proportional to the solution viscosity and concentration, which is a general rule for the electrospinning of polymers.[12] In addition, the percent standard deviation decreased with increasing concentration as the fibre diameter became more uniform. Webster et al. reported nanofibres produced for 45 wt% PVCL aqueous solutions with diameters that ranged from 300 to 700 nm.[13] Thus, the optimum electrospinning conditions for PVCL aqueous solutions were established. However, on immersion in water the PVCL electrospun mats dissolved instantly. Thus, a method of rendering the PVCL electrospun fibres insoluble in aqueous solvent was required to make use of this material for biomedical applications.

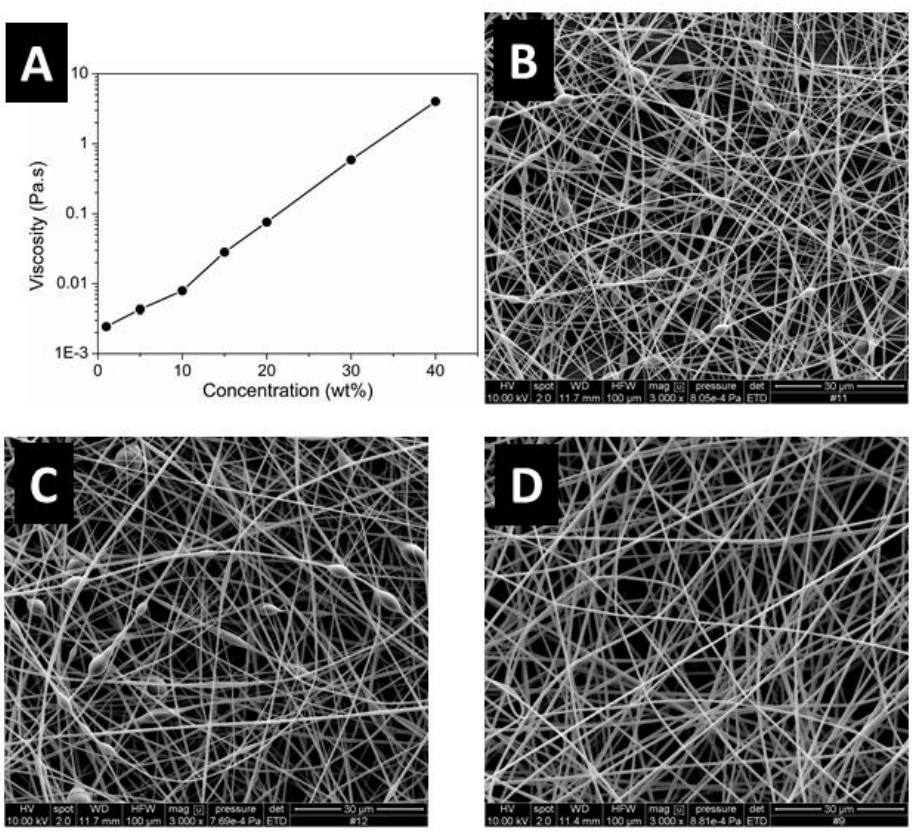


Figure 6.10 A) Plot of PVCL aqueous solution viscosity with concentration. B) PVCL nanofibres electrospun from a 30 wt% solution at 0.3 mL/h, 10 kV and 15 cm. C) PVCL nanofibres electrospun from a 35 wt% solution at 0.5 mL/h, 13 kV and 15 cm. D) PVCL nanofibres electrospun from a 40 wt% solution at 0.3 mL/h, 20 kV and 15 cm.

While RSF aqueous solutions have been electrospun to form nanofibrous scaffolds; however, the major drawback is that either very high concentrations of RSF are required or an additive polymer, such as polyethylene oxide (PEO), is required to facilitate electrospinning.[1, 14] The viscosity of RSF aqueous solutions at various concentrations was measured and the results are summarised in Figure 6.11. It was observed that the viscosity of RSF increased proportionally with concentration; however at high concentrations the viscosity remained less than 0.1 Pa.s. This agrees with the investigation by Zhu et al. where they found that it was not possible to electrospin RSF below 30 wt% due to the low viscosity observed.[15] Despite this, aqueous solutions of both PVCL and RSF were tested as core and shell solutions, respectively, and a stable cone and fibrous mat could not be produced despite testing a range of parameters. This was due to the fact that the solution gelled at the needle tip when electrostatic force was applied. This can be attributed to the interactions between RSF and PVCL that lowered the LCST of PVCL, which was discussed in Chapter 5.

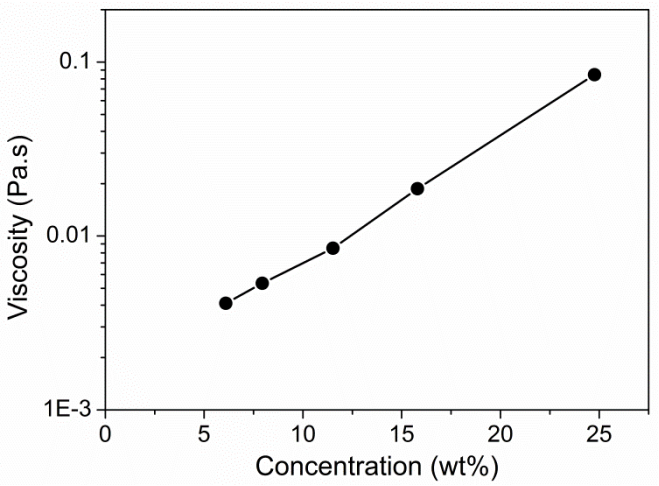


Figure 6.11 Plot of RSF aqueous solution viscosity with concentration.

Therefore, in order to utilise the excellent electrospinnability of PVCL, studies into the TA/PVCL system were undertaken as the core material with an aqueous RSF shell. As the TA/PVCL system was dissolved in DMF it was expected that the LCST effect would not contribute to gelling at the tip of the needle. However, a degree of reactivity of RSF with TA was observed and as a result the TA/PVCL system was not suitable for producing core/shell fibres with RSF. The Taylor cone gelled immediately at the tip of the electrospinning needle preventing drawing of the solution.

However, RSF has been shown to be readily electrospinnable at relatively low concentrations using hexafluoroisopropanol (HFIP).[4, 14, 16-18] In addition, it has also been shown that the use of HFIP for the electrospinning of silk fibroin did not compromise the biocompatibility of the final electrospun mat.[4, 5, 19] Li et al. examined the biocompatibility and release characteristics of core/shell fibres composed of poly(ε-caprolactone) (PCL) and silk fibroin spun from a combined solvent of dichloromethane (DCM) and HFIP.[5] They have shown that the adhesion and proliferation of normal human skin primary fibroblast cells was supported through the incorporation of silk fibroin as the shell component.[5] Liu et al. reported the fabrication of core/shell poly(lactide-co-ε-caprolactone) (PLCL)/silk fibroin nanofibres using HFIP-DCM as the solvent and that supported the adhesion, proliferation and spreading of a human endothelial cell hybridoma line.[4] Therefore, in this study HFIP was chosen as a suitable solvent for the co-axial electrospinning of PVCL and RSF. Initially, electrospinning of RSF and PVCL in HFIP were individually studied to establish the electrospinnability and parameters (concentration, flow rate, voltage and distance) required to produce fibres. Following this, the more complex co-axial electrospinning system of PVCL and RSF was studied with the aim of forming core/shell fibres that entrapped the PVCL in the core.

6.2.4.1 Electrospinning of RSF from HFIP

Firstly, electrospinning of RSF fibres from HFIP solutions was established by investigating a number of concentrations ranging from 8 to 12 wt%. The flow rate was maintained at 0.5 mL/h for all studies as this was found to result in a stable jet. In addition, the voltage and distance were varied to examine their effect on the fibre diameter. Representative SEM micrographs and size distribution plots for the electrospun RSF nanofibres from HFIP solutions at 12% and 8% are depicted in Figure 6.12. It was observed that nanofibres of approximately 300 nm were obtained from a solution concentration of 12%, whereas an 8% concentration produced somewhat smaller fibres of approximately 190 nm, which is consistent with the theory that lower polymer concentration results in smaller fibres. However, the change in fibre diameter when altering the voltage and distance was observed to be minimal. Park et al. reported RSF nanofibres with a much larger average diameter, 1260 nm, from a 7% solution in HFIP.[16] However, Zarkoob et al. obtained nanofibres from 6.5 to 100 nm in diameter from a 0.74% solution in HFIP.[18] The differences between the reported fibre diameters by Park et al. and Zarkoob et al., and the fibres produced in this study are attributed to differences in the RSF molecular weight, which is dependent on the process used to extract the silk. Also, other electrospinning conditions, such as voltage and distance contribute to developing fibres of differing sizes. Therefore, the successful formation of RSF nanofibres using relatively low concentrations in HFIP was demonstrated and this formed the basis for further study of core/shell electrospinning.

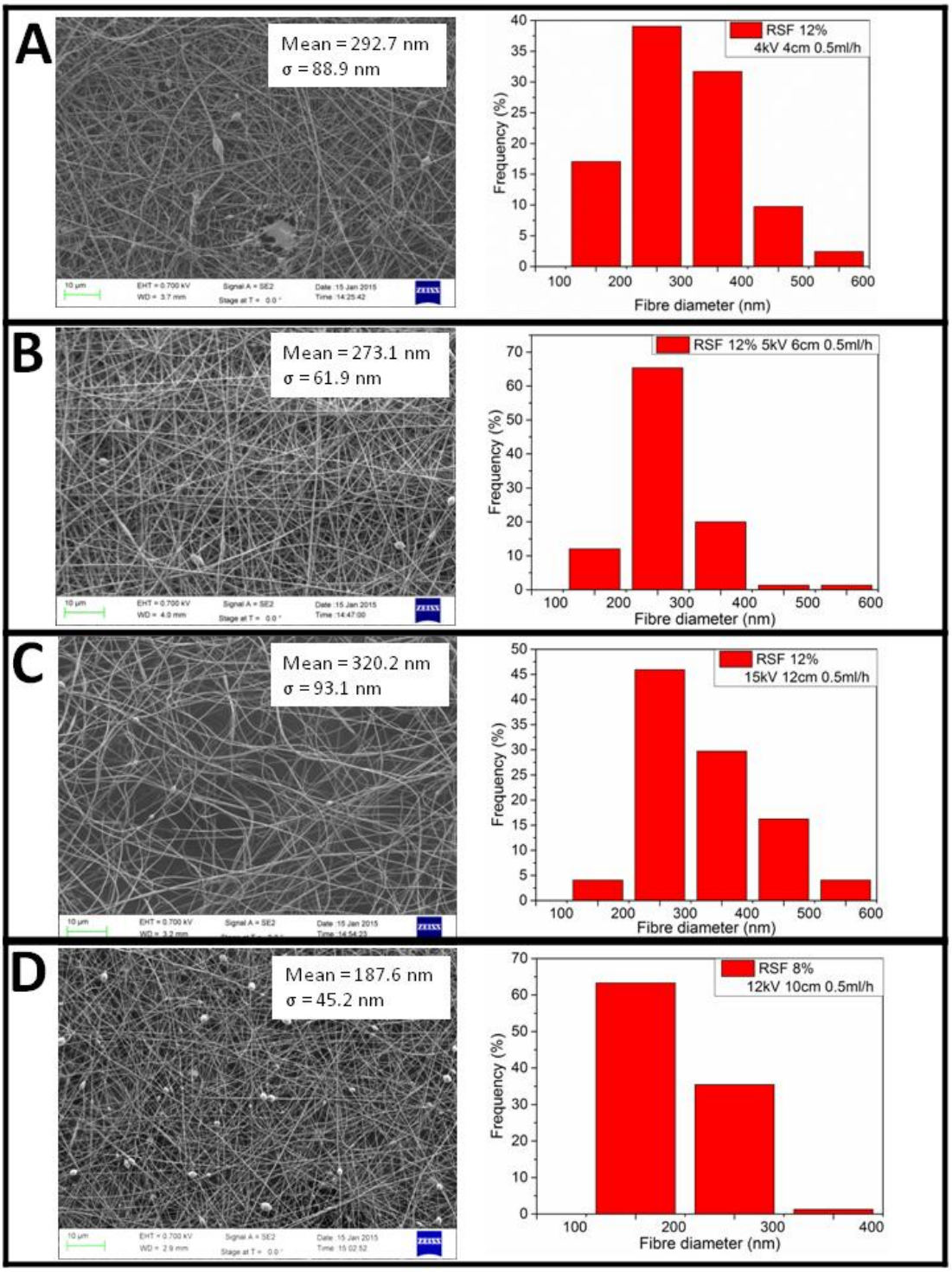


Figure 6.12 SEM micrographs and distribution of fibre diameter of RSF electrospun from HFIP with conditions, A) RSF 12%, 4 kV, 4 cm, and 0.5 mL/h; B) RSF 12%, 5 kV, 6 cm, and 0.5 mL/h; C) RSF 12%, 15 kV, 12 cm, and 0.5 mL/h; D) RSF 8%, 12 kV, 10 cm, and 0.5 mL/h.

6.2.4.2 Electrospinning of PVCL from HFIP

The purpose of the study was to employ a common solvent for the core and shell solutions to prevent gelation of RSF at the tip of the needle. This was due to the fact that immediate gelation and blocking of the electrospinning needle occurred when the TA/PVCL system was used in the core due to the hydrogen bonds formed between RSF and TA upon contact. Therefore, in this study electrospinning PVCL from HFIP was investigated for the first time. The PVCL concentration was varied from 8 to 13 wt% and the flow rates investigated ranged from 0.25 to 0.5 mL/h. In addition, the voltage and distance parameters were varied from 4 to 8 kV and 4 to 10 cm to determine the optimal conditions for the formation of a stable jet and deposition of fibres. Figure 6.13 depicts representative SEM micrographs of PVCL fibres obtained from 8 and 13 wt% at several different electrospinning parameters. It was clearly observed that ribbon-like fibres were obtained at all concentrations. In addition, for all concentrations there was a broad distribution of fibre diameters ranging from hundreds of nanometres to several microns (Figure 6.13). At a concentration of 13% and a distance of 10 cm, the largest fibres (~2500 nm) were observed. However, on decreasing the concentration to 8%, smaller ribbon-like fibres with average diameter of ~1340 nm were obtained. The diameter decreased further to ~980 nm by increasing the voltage to 6 kV. This is consistent with the fact that increased concentration results in fibres with larger diameters, while increasing the voltage results in decreased fibre diameters.[20] Webster et al. also observed the formation of flat PVCL fibres when electrospinning using ethanol as the solvent.[13]

The formation of ribbon-like fibres has been attributed to the formation of a polymer skin on the surface of the jet due to rapid evaporation of the solvent.[1, 21] Following the formation of the thin skin, the inner solvent diffuses out and atmospheric pressure causes the jet to collapse and form flat fibres.[1, 21] On decreasing the solution concentration further to 5%, a large number of collapsed bead-like structures and a small proportion of fibres were observed. This indicated that by decreasing the concentration there was decreased chain entanglement between the polymer molecules in solutions, which resulted in droplet formation. Therefore, PVCL can be successfully electrospun from HFIP; however the formation of ribbon-like fibres were observed for a range of experimental conditions.

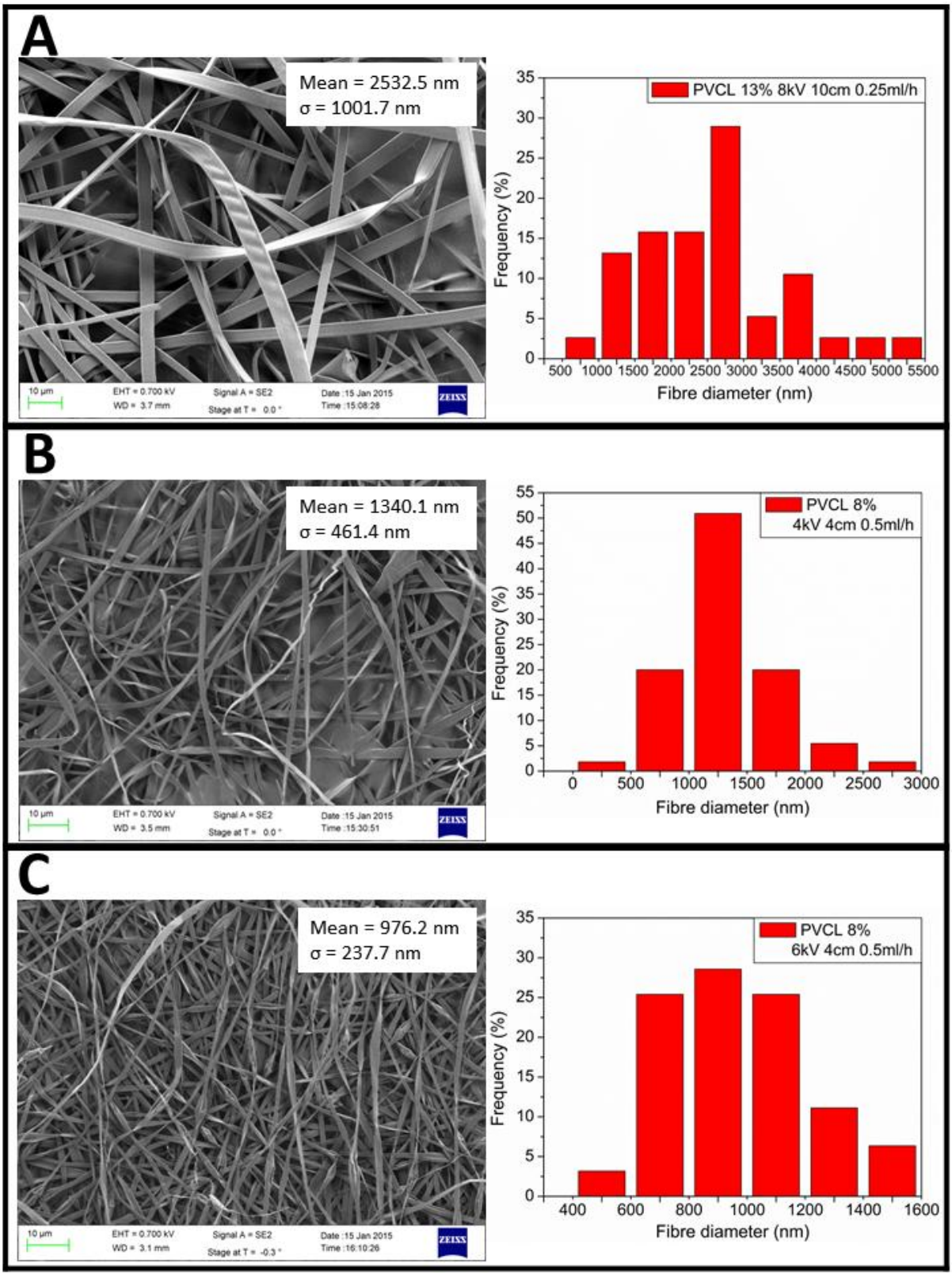


Figure 6.13 SEM micrographs and distribution of fibre diameter of PVCL electrospun from HFIP with conditions, A) PVCL 13%, 8 kV, 10 cm, and 0.25 mL/h; B) PVCL 8%, 4 kV, 4 cm, and 0.5 mL/h; C) PVCL 8%, 6 kV, 4 cm, and 0.5 mL/h.

6.2.4.3 Optimisation of co-axial electrospinning of PVCL and RSF for the production of core/shell fibres

The optimisation of electrospinning of individual RSF and PVCL solutions dissolved in HFIP provided a basis for studying the more complex co-axial system. Despite optimising the electrospinning conditions for the individual polymer, these were not necessarily the optimal conditions for the co-axial electrospinning process. Differences in the capillary diameters used for conventional and co-axial electrospinning, coupled with the concentric conformation used for the co-axial setup meant that the material and process parameters for co-axial electrospinning of RSF and PVCL required further optimisation. Regardless, it provided a benchmark for the co-axial electrospinning optimisation. It was observed that the Taylor cone of the co-axial jet dried quickly due to solvent evaporation, and by decreasing the PVCL concentration this was minimised. Therefore, the concentration of PVCL was reduced to 5% and the RSF concentration was maintained at 10% as this allowed for the production of a stable jet with minimal drying at the tip.

During the initial optimisation, a range of voltages (5 to 15 kV) and capillary to collector distances (4 to 15 cm) were employed to establish the conditions that produced a stable jet. It was determined that a voltage of 15 kV and distance of 10 cm were suitable for maintaining a stable jet that resulted in the deposition of fibres. Following this, the solution concentration, voltage and distance were fixed and the flow rate was varied to understand how it affected the dimensions of the electrospun fibres. It is noteworthy that the inner and outer flow rates have a direct effect on the size of the core and shell layers of the resultant fibres.[10] The core flow rate has shown to be proportional to the fibre diameter. However, the shell flow rate is inversely proportional to the fibre diameter. This is due to the solvent sheath effect where the presence of an outer solvent in the coaxial setup results in decreasing the fluid evaporation time and thus results in thinner fibres. This behaviour has been observed for a number of systems where electrospinning of high concentration polymers was made possible by the presence of an outer sheath solvent during electrospinning and a reduction in the fibre diameter was observed compared to conventional electrospinning.[22-24]

Figure 6.14 depicts the SEM images and corresponding fibre size distribution of electrospun mats obtained by varying the flow rates of the core (PVCL) and sheath (RSF). Taking into account the flow rates and concentrations of PVCL and RSF, the PVCL to RSF mass ratios of the three different samples were 1:4, 1:2 and 1:1. The SEM images were used to determine

the distribution of fibre diameters for the three different core/shell mass ratios. The PVCL/RSF mass ratio of 1:4 with core and shell flow rates of 0.5 and 1.0 mL/h, respectively, exhibited fibres ranging from 200 to 700 nm. This fibre size correlates well with the size of RSF fibres as shown in Figure 6.12 and thus suggests that the flow rate of 1.0 mL/h for the RSF shell solution was possibly too high and resulted in RSF jets breaking off and spinning alone to form RSF fibres. This was further examined by comparing with the TGA and TEM results and discussed later.

Altering the PVCL and RSF flow rates to 0.8 mL/h for both core and shell solutions (mass ratio of 1:2) resulted in diameters of 200 to 700 nm for the majority of the fibres. However, a smaller proportion of distinctly larger fibres of approximately 1100 nm were also observed. Thus, as expected by increasing the core flow rate larger fibres were observed. In addition, by further increasing the PVCL core flow rate to 1.0 mL/h and decreasing the RSF flow rate to 0.5 mL/h (equal mass ratio) it was observed that a larger proportion of fibres ranging from 800 to 1200 nm were exhibited in addition to those from 100 to 700 nm. This is consistent with the theory that by increasing the core flow rate, larger fibres will be generated. After ethanol crosslinking the co-axial electrospun mats were not soluble in water, which indicates that the RSF shell was successfully crosslinked. Crosslinking of the RSF shell in core/shell fibres using ethanol has also been reported in other studies where the core material was retained on exposure to water.[4, 5] Thus, these three conditions were chosen for further examination using TGA and TEM in order to determine the optimum ratio of flow rates and therefore concentrations for the production of core/shell fibres.

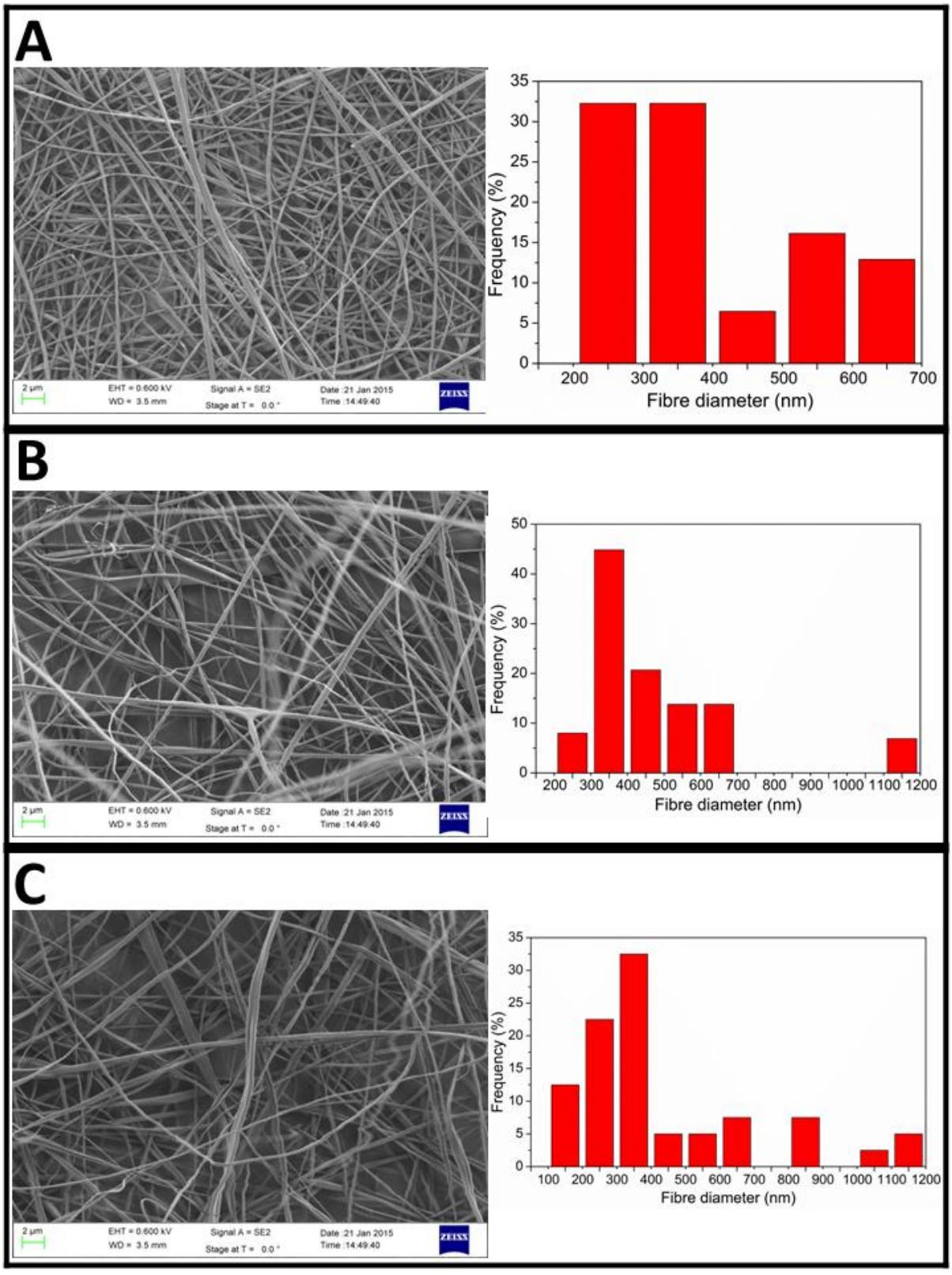


Figure 6.14 SEM micrographs and corresponding size distribution curves of core-shell PVCL/RSF electrospun from HFIP with conditions: A) Core: PVCL 5% 0.5 mL/h, Shell: RSF 10% 1.0 mL/h, 15 kV, 10 cm; B) Core: PVCL 5% 0.8 mL/h, Shell: RSF 10% 0.8 mL/h, 15 kV, 10 cm; C) Core: PVCL 5% 1.0 mL/h, Shell: RSF 10% 0.5 mL/h, 15 kV, 10 cm.

6.2.4.4 Composition of PVCL/RSF fibres from co-axial electrospinning

TGA was employed to examine the composition of the mats produced from the co-axial electrospinning of PVCL and RSF. Despite employing PVCL and RSF in the core/shell configuration in the co-axial setup, the fibre composition and morphology was also dependent on the parameters employed during electrospinning, such as flow rates of the core and shell solutions.

TGA thermograms for the electrospun mats prepared from the individual RSF and PVCL solutions and also from the co-axial electrospinning were measured (Figure 6.15). The peak below 100˚C in all of the thermograms was attributed to residual solvent HFIP, which has a boiling point of 58˚C. Interestingly, the TGA thermogram of electrospun RSF showed two peaks at 180˚C and 296˚C (Figure 6.15A). Upon crosslinking with ethanol for 30 minutes, a single degradation at 294˚C was observed (Figure 6.15B). This suggests that the wide range of molecular weight silk fibroin chains, as shown through SDS-PAGE analysis, result in the observation of two degradation peaks. Crosslinking with ethanol is known to induce the random coil to beta-sheet transition that results in a more rigid and uniform RSF structure and it was observed that this produced a single degradation peak (Figure 6.15B). On its own, PVCL exhibited a single degradation peak at 441˚C (Figure 6.15C).

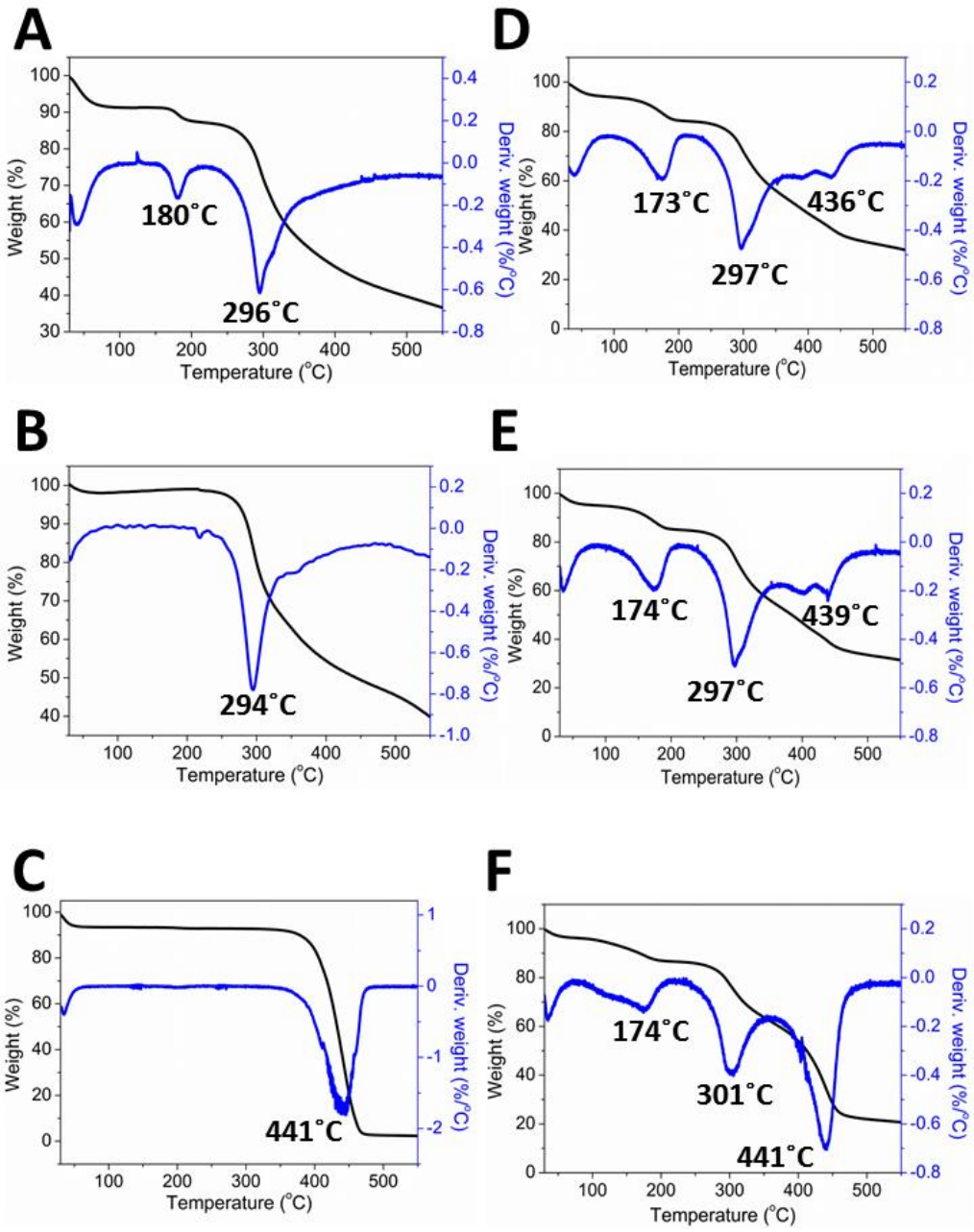


Figure 6.15 TGA thermograms of electrospun mats from HFIP with conditions: A) RSF 10% 0.5 mL/h, 15 kV, 10 cm; B) RSF 10% 0.5 mL/h, 15 kV, 10 cm, crosslinked in ethanol solution for 30 minutes; C) PVCL 8%, 6 kV, 4 cm, and 0.5 mL/h; D) Core: PVCL 5% 0.5 mL/h, Shell: RSF 10% 1.0 mL/h, 15 kV, 10 cm; E) Core: PVCL 5% 0.8 mL/h, Shell: RSF 10% 0.8 mL/h, 15 kV, 10 cm; F) Core: PVCL 5% 1.0 mL/h, Shell: RSF 10% 0.5 mL/h, 15 kV, 10 cm.

The derivative curves for all of the co-axial samples prior to ethanol crosslinking showed three distinct peaks corresponding to approximately 173˚C, 300˚C and 440˚C (Figure 6.15D-F). The peaks at ~173˚C and 300˚C were assigned to RSF and the peak at 440˚C to PVCL, as

they correspond to the individual degradation temperatures of the components. The ratio of PVCL and RSF in the co-axial electrospun mats was determined from the TGA thermograms. The residual mass due to PVCL was negligible (~1%), therefore the residue in the composite mats was attributed to RSF, which has ~37% residue on its own. The approximate mass ratios of PVCL and RSF in the co-axial electrospun mats were calculated by taking the mass % at the plateau of each derivative (Table 6.2). It was observed that RSF was the predominant component in the samples with core/shell mass ratios of 1:4 and 1:2. This suggests that the flow of PVCL in the inner needle was interrupted due to blockage on contact with RSF. In this scenario the jet produced would contain mainly the sheath RSF fibres. However, the measured mass ratio of PVCL and RSF in the electrospun mat was 1:1.3, which closely matched the input solution mass ratio (1:1). This suggests that the flow rates of 1.0 and 0.5 mL/h (1:1 mass ratio) for PVCL and RSF, respectively, were optimal for producing successful electrospinning of the core and shell solutions. By decreasing the flow rate of RSF, the PVCL flow became more dominant and as such was more likely to produce fibres with core/shell morphology. Furthermore, the residue for each of the mats at 550˚C was the lowest for the electrospun mat prepared with a 1:1 mass ratio in the core and shell solutions, which further confirms the low proportion of RSF in this sample as the residue was attributed to the presence of RSF. As the sample with PVCL and RSF flow rates of 1.0 and 0.5 mL/h was considered the most promising, this sample was studied further using TEM.

Table 6.2 Comparison of the theoretical mass ratios of PVCL and RSF in the core and shell solutions employed for electrospinning compared to the experimental mass ratio calculated from TGA analysis of the electrospun mats. The associated residue at 550˚C for the PVCL/RSF electrospun mats obtained from TGA analysis.

Theoretical PVCL/RSF mass ratio of core and shell solutions	**Experimental PVCL/RSF mass ratio of electrospun mat calculated from TGA**	**Residue (%)**
1:4	1:3.5	32.0
1:2	1:3.3	31.5
1:1	1:1.3	20.7

6.2.4.5 TEM analysis of PVCL/RSF core/shell fibres

The morphology of the core/shell fibres was investigated using TEM. TEM was performed on the equal mass ratio core/shell PVCL/RSF electrospun fibres as this sample was most promising for the production of core/shell fibres due to the SEM images and appropriate composition of PVCL in the TGA thermogram. Representative TEM images of a number of the core/shell PVCL/RSF fibres electrospun at identical conditions (1.0/0.5 mL/h; 1:1 mass ratio), are shown in Figure 6.16 and demonstrate the contrast between two different phases. The contrast observed between the two components in TEM was attributed to the sulphur present in the RSF as it has a cysteine content of 0.1 mol%.[25] Due to this contrast, it was observed that a number of the fibres indeed exhibited core/shell morphology where the boundaries between core and shell components are obvious. In addition, the fact that the shell was darker also emphasises that the fibres were core/shell as the thicker centre of the fibres was lighter in the TEM images. The darker component that forms the outer shell of the core/shell fibres and the smaller fibres was attributed to RSF. Also, the smaller sized fibre shows similar contrast and the fibre diameter corresponds to the size of the RSF fibres that were produced with single needle electrospinning. This further confirms that the smaller fibres present in larger proportions in SEM images of the electrospun mats from RSF shell flow rates of 1.0 and 0.8 mL/h were in fact RSF alone. Therefore, the lighter component that was present in the core of the fibres was attributed to PVCL. Furthermore, the interface between the RSF and PVCL components is likely to be a blend of the two polymers as there is no delamination observed between the two phases, and this is due to the use of the same solvent for the core and shell solutions. Notably, the solvent employed to disperse the core/shell fibres for TEM was ethanol, as PVCL is soluble in ethanol, the presence of PVCL in the core of the TEM fibres confirms that PVCL was successfully entrapped in the RSF crosslinked shell.

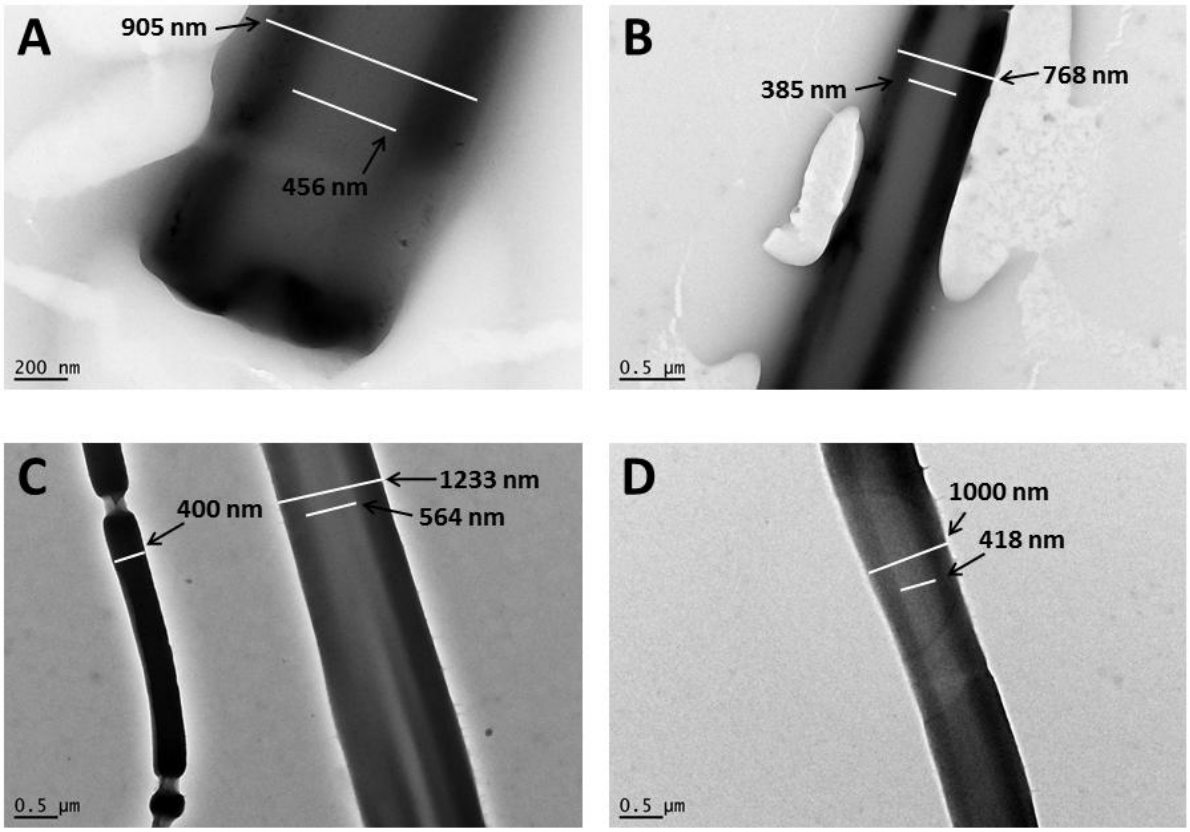


Figure 6.16 A-D) TEM micrographs of core-shell PVCL/RSF fibres from one sample at several magnifications that demonstrates the distribution of fibre morphology and diameters. Fibres were electrospun with conditions: Core: PVCL 5% 1.0 mL/h, Shell: RSF 10% 0.5 mL/h, 15 kV, 10 cm.

The size of the fibres measured from TEM matched closely with those measured from SEM images, which demonstrated a distribution of larger fibres, ranging from ~800 to 1200 nm, among other much smaller ones of ~100 to 700 nm. The outer fibre diameters of the core/shell fibres ranged from 768 to 1233 nm, while the inner diameters ranged from 385 to 564 nm. Liu et al. produced core/shell SF/PLCL electrospun fibres spun from HFIP with inner and outer diameters of 471 nm and 1016 nm, respectively, that were shown to support cell adhesion and proliferation.[4] They also observed the formation of some smaller diameter fibres in addition to the larger core/shell ones.[4] Therefore, it has been shown for the first time that by employing the co-axial electrospinning setup and using the same solvent for both the core and shell solutions, PVCL/RSF core/shell fibres can be fabricated. This presents a unique way of combining the excellent electrospinnability and stimuli-responsive properties of neat PVCL, without further modification, by encapsulating it in a crosslinked RSF outer shell.

6.2.5 Conclusions

The formation of PVCL/RSF core/shell electrospun fibres has been achieved for the first time in this study. It was concluded that at solution concentrations of 5% and 10% for PVCL and RSF, respectively, the inner and outer flow rates of 1.0 and 0.5 mL/h (1:1 mass ratio) were optimal for producing core/shell electrospun fibres. This work provides a solid platform for the formation of composite fibres that overcomes the aqueous solubility issue of PVCL without further chemical modifications and incorporates the biocompatibility of RSF. There is great potential for these biomaterials to be applied to biomedical applications where structural support and sustained release of therapeutic compounds is required. Study into the properties of the electrospun mats is outside the scope of this work. The biocompatibility of RSF combined with the temperature-responsiveness of PVCL allows for the development of sophisticated materials with optimised properties and has been examined for the RSF/PVCL hydrogel system in Chapter 8.

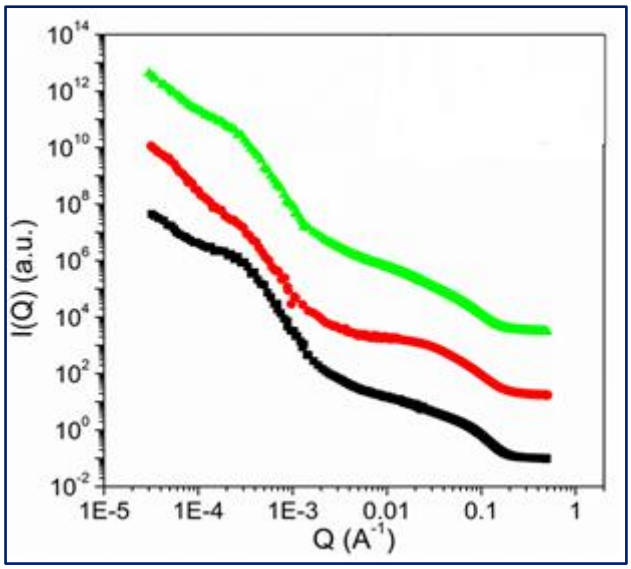
6.2.6 References

1. Zhang, K.; Mo, X.; Huang, C.; He, C.; Wang, H., *J. Biomed. Mater. Res., Part A* **2010,** *93A* (3), 976-983.
2. Cai, Z.-x.; Mo, X.-m.; Zhang, K.-h.; Fan, L.-p.; Yin, A.-l.; He, C.-l.; Wang, H.-s., *Int. J. Mol. Sci.* **2010,** *11* (9), 3529.
3. Min, B.-M.; Lee, G.; Kim, S. H.; Nam, Y. S.; Lee, T. S.; Park, W. H., *Biomaterials* **2004,** *25* (7-8), 1289-1297.
4. Liu, G.; Tang, Q.; Yu, Y.; Li, J.; Luo, J.; Li, M., *Polym. Adv. Technol.* **2014,** *25* (12), 1596-1603.
5. Li, L.; Li, H.; Qian, Y.; Li, X.; Singh, G. K.; Zhong, L.; Liu, W.; Lv, Y.; Cai, K.; Yang, L., *Int. J. Biol. Macromol.* **2011,** *49* (2), 223-232.
6. Tian, L.; Prabhakaran, M. P.; Hu, J.; Chen, M.; Besenbacher, F.; Ramakrishna, S., *RSC Adv.* **2015,** *5* (62), 49838-49848.
7. Chen, M.; Dong, M.; Havelund, R.; Regina, V. R.; Meyer, R. L.; Besenbacher, F.; Kingshott, P., *Chem. Mater.* **2010,** *22* (14), 4214-4221.
8. Laukkanen, A.; Wiedmer, S. K.; Varjo, S.; Riekkola, M. L.; Tenhu, H., *Colloid Polym. Sci.* **2002,** *280* (1), 65-70.
9. Kozanoglu, S.; Ozdemir, T.; Usanmaz, A., *J. Macromol. Sci., Part A: Pure Appl. Chem.* **2011,** *48* (6), 467-477.
10. Elahi, M. F.; Lu, W.; Guoping, G.; Khan, F., *J. Bioeng. Biomed. Sci.* **2013,** *3* (121).

11. Whittaker, J. L.; Dutta, N. K.; Knott, R.; McPhee, G.; Voelcker, N. H.; Elvin, C.; Hill, A.; Choudhury, N. R., *Langmuir* **2015,** *31* (32), 8882-8891.
12. Li, D.; Xia, Y., *Adv. Mater.* **2004,** *16* (14), 1151-1170.
13. Webster, M.; Miao, J.; Lynch, B.; Green, D. S.; Jones-Sawyer, R.; Linhardt, R. J.; Mendenhall, J., *Macromol. Mater. Eng.* **2013**, *298*, 447-453.
14. Jin, H.-J.; Fridrikh, S. V.; Rutledge, G. C.; Kaplan, D. L., *Biomacromolecules* **2002,** *3* (6), 1233-1239.
15. Zhu, J.; Shao, H.; Hu, X., *Int. J. Biol. Macromol.* **2007,** *41* (4), 469-474.
16. Park, K. E.; Jung, S. Y.; Lee, S. J.; Min, B.-M.; Park, W. H., *Int. J. Biol. Macromol.* **2006,** *38* (3–5), 165-173.
17. Sato, M.; Nakazawa, Y.; Takahashi, R.; Tanaka, K.; Sata, M.; Aytemiz, D.; Asakura, T., *Mater. Lett.* **2010,** *64* (16), 1786-1788.
18. Zarkoob, S.; Eby, R. K.; Reneker, D. H.; Hudson, S. D.; Ertley, D.; Adams, W. W., *Polymer* **2004,** *45* (11), 3973-3977.
19. Zhang, F.; Zuo, B.; Bai, L., *J. Mater. Sci.* **2009,** *44* (20), 5682-5687.
20. Chakraborty, S.; Liao, I. C.; Adler, A.; Leong, K. W., *Adv. Drug Delivery Rev.* **2009,** *61* (12), 1043-1054.
21. Koombhongse, S.; Liu, W.; Reneker, D. H., *J. Polym. Sci., Part B: Polym. Phys.* **2001,** *39* (21), 2598-2606.
22. Yu, D.-G.; Branford-White, C. J.; Chatterton, N. P.; White, K.; Zhu, L.-M.; Shen, X.-X.; Nie, W., *Macromolecules* **2010,** *43* (24), 10743-10746.
23. Yu, D. G.; Brandford-White, C.; White, K.; Chatterton, N. P.; Zhu, L. M.; Huang, L. Y., *Express Polym. Lett.* **2011,** *5* (8), 732-741.
24. Jorgensen, L.; Qvortrup, K.; Chronakis, I. S., *RSC Adv.* **2015,** *5* (66), 53644-53652.
25. Murphy, A. R.; Kaplan, D. L., *J. Mater. Chem.* **2009,** *19* (36), 6443-6450.

Chapter 7: Investigation into the microstructure of silk-based hydrogels using small and ultra small angle neutron scattering

This chapter of the thesis is presented as a research article "Whittaker, J. L.; Knott, R.; Mata, J.; de Campo, L.; Rehm, C.; Dutta, N. K.; Choudhury, N. R., Investigation into the microstructure of silk-based hydrogels using small and ultra small angle neutron scattering" to be submitted for peer review publication.



7.1 Abstract

This study demonstrates for the first time the analysis of regenerated silk fibroin (RSF) based hydrogels in the swollen state using neutron scattering techniques. A range of silk-based hydrogels that demonstrated tuneable elasticity and swelling properties, were investigated using small angle neutron scattering (SANS) and ultra-small angle neutron scattering (USANS) to gain an in-depth understanding of the network structure of these gels and how that relates to the observed bulk properties. This is the first work, to our knowledge, that delves into the structure of chemically crosslinked silk hydrogels using neutron scattering covering a wide Q range (~10 Å to 10 μm). Despite the hydrogels exhibiting features that correlated with a gel-like structure, it was not possible to fit the data with classical gel models. However, by employing the *PowerLaw* and *GuinierPorod* models it was observed that frozen-in structures in the range of tens of angstroms were present, in addition to much larger structures that were attributed to the presence of pores in the hydrogel structure.

7.2 Introduction

The development of novel biomaterials from natural and synthetic polymers has been of great research interest in recent years. In particular, silk based biomaterials have been identified as very promising for regenerative medicine applications, mainly due to their abundance, biocompatibility and mechanical strength. As discussed earlier (Chapter 4), a new, rapid method of photo-crosslinking of regenerated silk fibroin (RSF) to form three-dimensional hydrogels has been discovered that is not cytotoxic to cells and possesses an elastic modulus on the mega Pascal (MPa) scale.[1] Despite the ease of fabrication and advantageous properties of the RSF photo-crosslinked hydrogels, there remained a need to tune the swelling capability and mechanical properties of the gels for targeted tissue engineering applications. The mechanical requirements for such applications vary greatly, depending on the location, function and characteristics of the human tissue. For instance, biomaterials for articular cartilage tissue engineering require a modulus of ~500 to 1000 kPa[2].

To achieve the aforesaid goal of tuning the physical and mechanical characteristics of RSF-based hydrogels, two types of unique hybrid hydrogels were designed and successfully synthesised, which were composed of the highly crosslinked rigid phase of RSF in combination with softer, thermo-responsive materials including: (i) an biomimetic elastomeric protein (Rec1-resilin) and (ii) a synthetic polymer (poly(N-vinylcaprolactam) (PVCL)). An initial investigation into the co-assembly behaviour of Rec1-resilin/RSF and

RSF/PVCL has been presented previously (Chapters 3 and 5), where the ability to tune the phase transition behaviour of the thermo-responsive gels through co-assembly was successfully established.[3] Following the study of the co-assembly behaviour, the ability to co-crosslink RSF and Rec1-resilin via the ruthenium-mediated photo-crosslinking method was utilised due to the presence of the amino acid residue tyrosine in both proteins and a new co-crosslinked system containing RSF and Rec1-resilin was formed.[4] It was observed that the modulus and water uptake properties of the co-crosslinked hydrogels could be tuned relative to the individual RSF and Rec1-resilin di-tyrosine crosslinked hydrogels.[4] In addition, the formation of a hybrid hydrogel with the highly photo-crosslinked rigid RSF phase and a physically entrapped soft synthetic polymer (PVCL) was established. The detailed characterisation of the RSF/PVCL semi-IPN hydrogels revealed the possibility of tuning the bulk hydrogel properties by controlling the hydrogel composition.

In order to develop functional materials with readily tuneable properties, it is important to develop an in-depth understanding of the role of the microstructure on the bulk hydrogel properties. The method of crosslinking RSF, Rec1-resilin/RSF and RSF/PVCL solutions to form three-dimensional hydrogels involves the formation of covalent di-tyrosine crosslinks between amino acid side chains. In the case of Rec1-resilin/RSF, the di-tyrosine crosslinks may occur between RSF-RSF and Rec1-resilin-Rec1-resilin chains, between Rec1-resilin-RSF chains, or a random combination of both. However, in the case of the RSF/PVCL hydrogel the RSF chains are chemically crosslinked via di-tyrosine bonds and the PVCL phase is physically entrapped in the network. Whilst covalent crosslinking is the main mode of crosslinking in the RSF; in Rec1-resilin/RSF and RSF/PVCL hydrogels, a number of other physical interactions and conformational changes are also expected to contribute to the self-assembly and microstructure formation. The factors that govern the silk self-assembly during gelation include a number of physical interactions, including hydrogen bonding, hydrophobic interaction, van der Waals, electrostatic, solvation and steric forces.[5] Therefore, it can be reasonably assumed that in the RSF-based hybrid hydrogel systems multiple interactions involve and contribute to the changes in microstructure of the hydrogels that in turn results in a tuning of the final material properties. However, currently there is no literature, to our knowledge, that investigates the microstructure of such crosslinked silk fibroin hydrogels using neutron scattering; and thus it is important to develop a fundamental understanding of the mechanism that drives the changes in the properties of the RSF hydrogels on forming the hybrid systems.

Small and ultra small angle neutron scattering (SANS and USANS) (Chapter 2: Experimental Section) experiments were undertaken to investigate, in depth, the structural ensemble of the RSF-based hybrid hydrogels. Through a combination of SANS and USANS, structural information covering four orders of magnitude in size (~10 Å to 10 μm) can be obtained for the equilibrium swollen hydrogels.[6] SANS and USANS have been used successfully to study the microstructure of numerous types of chemical and physical hydrogels.[7-10] However, the majority of these studies have focused on synthetic polymer hydrogels and have not delved into the investigation of crosslinked RSF-based materials. Of direct relevance, Greving et al. performed a SANS study to compare the shape and structure of native and regenerated silk fibroin in solution.[5] In previous work, the structure of Rec1-resilin/RSF co-assemblies in dilute solution was investigated using small angle x-ray scattering (SAXS) (Chapter 3).[3] However, despite studies of RSF in the solution state, there has been no neutron scattering study of the RSF-based crosslinked hydrogels to elucidate the microstructure and how this influences the bulk properties of the hydrogels. Thus, SANS and USANS were employed for the first time to develop a fundamental understanding of the structure-property relationship of the crosslinked RSF-based hybrid hydrogels.

7.3 Experimental

7.3.1 Materials

Bombyx mori silk was purchased as raw silk from Beautiful Silks, Australia. Aqueous regenerated silk fibroin (RSF) solutions were prepared and characterized as described in Chapter 3.

Rec1-resilin was synthesised by cloning, expression, and purification of exon 1 of the *Drosophila Melanogaster* gene CG15920, as a water soluble protein as described elsewhere[11, 12]. Rec1-resilin has a molecular weight of 28.4 kDa with 310 amino acid residues.

Poly(N-vinylcaprolactam) (PVCL) was prepared via free radical polymerisation of the VCL monomer with 2,2'-azoisobutyronitrile (AIBN) and characterised as described in Chapter 5.

7.3.2 Solution Preparation

RSF solution of high concentration (~15 wt%) was obtained via the above protocol and was diluted to 1, 2, 5, and 10 wt% with distilled water (DW) for SAXS experiments and with D_2O for SANS experiments. The RSF 15 wt% solution was in H_2O for SAXS, SANS, and

USANS experiments. Solid Rec1-resilin and PVCL were dissolved in D_2O to obtain 2 wt% solutions for SANS experiments.

7.3.3 Hydrogel Preparation and Properties

The RSF, Rec1-resilin/RSF and RSF/PVCL hydrogels were prepared as described in Chapters 4 and 5 with the composition of each hydrogel outlined in Table 7.1. After leaching in DW and vacuum drying, all hydrogels were swollen in D_2O for 24 hours prior to neutron scattering experiments.

Table 7.1 Hydrogel composition

Sample Identification S=RSF, P=PVCL	**Volume fraction RSF 15 wt%**	**Volume fraction Rec1 20 wt%**	**Volume fraction PVCL 5 wt%**
RSF	1	-	-
Rec1-resilin/RSF	0.5	0.5	-
$S_{90}P_{10}$	0.9	-	0.1
$S_{80}P_{20}$	0.8	-	0.2
$S_{70}P_{30}$	0.7	-	0.3
$S_{60}P_{40}$	0.6	-	0.4

7.3.4 Small angle X-ray scattering

SAXS experiments were performed to analyse the structure and morphology of the RSF solution at different concentrations. Data were collected on a NanoSTAR II SAXS instrument (Bruker AXS, Karlsruhe Germany).[13] For each sample, the 2D SAXS data were collected for 3600 seconds as a function of the scattering vector (Q) over the range $0.011<Q<0.39$ Å^{-1}. The samples were loaded into 2 mm ID quartz capillaries (using a gel-tip pipette) and the temperature was maintained at 25˚C. The 2D data were corrected for detector spatial effect and variation in sensitivity, and reduced to 1D data using routines in the Bruker software. The 1D data were analysed using Igor Pro software (Wavemetrics Inc, Portland, USA) and macros developed at NIST.[14]

7.3.5 Small angle neutron scattering

SANS experiments were performed with Quokka, SANS instrument at OPAL - Australian Nuclear Science and Technology Organization (ANSTO, Lucas Heights, Sydney) with a neutron beam from a large liquid-D_2 cold source (5 Å) using the sample to 2D detector distances of 2, 8 and 20 m, respectively. All hydrogel samples were swollen in D_2O to enhance the contrast between the hydrogel and the solvent and mounted in the demountable sample cells with quartz windows. The solution samples were run using Helma quartz cells (1 mm path length for samples in H_2O, 2 mm path length for samples in D_2O). The measurements and analyses were conducted at 25˚C using a scattering vector, Q, ranging from 6.9×10^{-4} to 0.5 $Å^{-1}$. For all the samples the D_2O background was subtracted from the sample, except for the RSF 15 wt% solution where a H_2O background was subtracted.

7.3.6 Ultra small angle neutron scattering

USANS experiments were carried out with Kookaburra Ultra small angle neutron scattering USANS instrument at OPAL (ANSTO, Lucas Heights, Sydney)[6], using the long wavelength 4.74 Å. All the hydrogel samples were swollen in D_2O to enhance the contrast between the hydrogel and solvent, and mounted in sample cells with quartz windows. The measurements were conducted at room temperature. The beam, and therefore sample area, was defined with a Cd aperture of 25 mm diameter. The USANS data were reduced using an empty sample container as background, and converted to absolute scale using python scripts based on the standard procedure.[14] The Q-range covered using USANS was 2.9×10^{-5} to 1.8×10^{-2} $Å^{-1}$.

The experimental data were desmeared using the Lake algorithm, incorporated in the NIST USANS macros[14], before they were merged with the SANS data. A considerable overlap in the Q range between the SANS and USANS datasets – Q_{min} 6.9×10^{-4} $Å^{-1}$ for SANS and Q_{max} 1.8×10^{-2} $Å^{-1}$ for USANS are evident in the merged dataset.

7.3.7 Background to Hydrogel Structure and Data Analysis

In general, crosslinked polymer hydrogels have a hierarchical structure introduced by the formation of crosslinks and hence have a range of spatial heterogeneities ranging in size from angstroms to microns. The types of heterogeneities include: spatial heterogeneities as a result of spatial variations in the crosslink density, topological heterogeneities due to defects in the network, connectivity heterogeneities, and heterogeneities in the local degree of mobility.[15] The complex microstructure of gels, due to these heterogeneities, can be elucidated using

neutron scattering techniques that provide structural information on a range of length scales. The scattering function of a gel consists of a dynamic component, $I_{soln}(Q)$, that represents the mobile network polymer chains; and a static component, $I_{ex}(Q)$, that arises due to the heterogeneities present as a result of the crosslinks or other interactions in the system, which lead to regions of higher and lower polymer density on the molecular scale.[16, 17] The use of USANS and SANS for structural characterisation of polymer gels is particularly useful based on the fact that scattering contrast can be introduced by simply immersing the gel in deuterated water (D_2O), which allows for the study of the gel in the swollen state. Theoretically, the scattering function of equilibrium swollen polymer gels is the same as polymer solutions at identical concentrations.[15] However, due to the heterogeneities present in the gel that are not present in the solution; it has been found that there is usually a strong upturn, at low Q, in the scattering of hydrogels.[15]

All of the gels produced for this study clearly display a hierarchical structure with distinct features over a number of length scales. The aim was to fit theoretical functions to the experimental data in order to obtain parameters that can be interpreted in terms of the bulk properties. In general, the low Q data characterise the large length scale clusters, and the high Q data characterise the small length scale in particular the polymer chains.

There are a number of function forms that have been employed to fit SANS data. The total scattered intensity for the gel, $I_{gel}(Q)$ may be considered as the sum of a high Q, thermodynamic component, $I_{soln}(Q)$, and a low Q static, frozen-in component, $I_{ex}(Q)$:

$$I_{gel}(Q) = I_{soln}(Q) + I_{ex}(Q) \quad (1)$$

(Here $I_{soln}(Q)$ means 'solution' scattering, and $I_{ex}(Q)$ means 'excess' scattering at low Q). For a typical hydrogel the polymer chains are in the semi-dilute regime and the high Q $I_{soln}(Q)$ is well described by a Lorentz function:

$$I_{soln}(Q) = \frac{A_1}{1+\xi^2 Q^2} \quad (2)$$

where ξ is a correlation length.

Several functional forms of the excess scattering at low Q have been used, including:

Gaussian or Guinier approximation [18]:

$$I_{ex}(Q) = A_2 \exp\left[-\frac{Q^2\Xi^2}{2}\right], \quad (3)$$

stretched exponential[18-20]:

$$I_{ex}(Q) = A_3 \exp[-(Q\Xi)^{\alpha}], \quad (4)$$

where Ξ is a characteristic length and α is a fitted exponent;

Debye-Bueche relationship for a two phase system with sharp boundary[8, 21]:

$$I_{ex}(Q) = \frac{A_4}{(1+\Xi^2Q^2)^2}; \quad (5)$$

and power law to account for the large static structures usually beyond the Q range of the SANS experiment[22]:

$$I_{ex}(Q) = \frac{A_4}{Q^{\alpha}}. \quad (6)$$

In these equations A_n and α are fitted parameters.

In the present study, the USANS data extended the Q range into the micron length scale, which provides an exceptional view of the hydrogel structure over a wide length scale. It was anticipated that this additional Q range would provide insight into the nature of the large scale structures alluded to in many previous studies of gel structure.

The SasView package (http://www.sasview.org/) was used to analyse the data. For practical reasons, the SANS data was analysed first in an attempt to understand the structure on the shortest length scale (i.e. the building blocks for the larger structural features) before progressing to understanding the larger structure features (particularly those in the USANS region). As will be explained in more detail later the following functional forms were used to fit the SANS data:

GaussLorentzGel: This model combines a low Q exponential decay with a Lorentzian function at higher Q values and is generally applied for gel structures that exhibit classic dynamic and static contributions.[23]

GelFitModel: The gel fit model takes into account the two characteristic length scales exhibited by polymer gels, with a shorter correlation length due to the thermodynamics of the polymer chains and a longer distance due to the static crosslinked junction points.[18]

Lorentz: This model is a simple expression of the Lorentz (Ornstein-Zernicke) equation plus a Q-independent background.

UnifiedPowerRg: This model allows for the characterisation of structures consisting of one or more fractally related structural levels.[24] Each structural level is characterised by an exponential (Guinier) regime accounting for the size, and an associated power law regime.

GuinierPorod: This is a very useful empirical model that can be used to explore the size and dimensionality of scattering objects, which can provide valuable clues to the underlying structure and hence direct more detail studies.[25] The scattering intensity is the combination of two contributions:

$$I(Q) = \frac{G}{Q^s} \exp\left(\frac{-Q^2 R_g^2}{3-s}\right) \text{ for } Q \leq Q_1, \quad (7)$$

$$I(Q) = \frac{D}{Q^d} \text{ for } Q \geq Q_1 \quad (8)$$

where Q is the scattering vector, I(Q) is the scattered intensity, R_g is the radius of gyration, 'd' is the Porod exponent, 's' is the dimensional variable, and G and D are the Guinier and Porod scaling factors, respectively.[25]

PowerLaw: This is a simple yet powerful inverse Q dependence to a given exponent. Scattering theory establishes that an exponent between 1 and 3 indicates mass fractal scattering, and from 3 to 4 indicates surface scattering.

Note: The R_g is a very useful model-independent parameter to compare scattering models however it must be used with caution. A direct comparison is only relevant when the scattering objects have the same geometric shape, and there are a number of well-established formulae that relate the R_g to geometric parameters.[26, 27] For example, for a sphere of radius R:

$$R_g = R\sqrt{\frac{3}{5}} \quad (9)$$

For hydrogels prepared from bulk solution, the shapes are probably more-or-less spherical, or perhaps rod-like (or filamentous) for the connecting regions.

7.4 Results

7.4.1 Physical properties of RSF-based hydrogels

The crosslink density (n), molecular weight between crosslinks (M_c), equilibrium water uptake, and storage modulus (E') at equilibrium swelling conditions for the RSF-based hybrid hydrogels (Chapters 4 and 5) are summarised in Table 7.2. The crosslink density was calculated using rubber elasticity theory[28-30] and it was observed that the RSF hydrogel had the highest value. The Rec1-resilin/RSF hydrogel had a much lower crosslink density than the RSF hydrogel, which was reflected in the increased water uptake capacity and decreased elastic modulus, E'. Also, it was observed that the RSF/PVCL hydrogels exhibited progressively decreasing crosslink densities with an increase in PVCL content, which can be related to the lower proportion of crosslinked RSF in the hydrogel. It is known that the hydrogel properties, such as equilibrium swelling degree and elastic modulus, E' depend on the crosslink density and crosslinked polymer concentration of the hydrogel.[31]

Table 7.2 Summary of the properties of RSF-based hybrid hydrogels

Sample	**n (mol/m^3)**	**M_c (g/mol)**	**Equilibrium water uptake (g water/g dried gel)**	**E' (equilibrium swollen) (MPa)**
RSF	9545.6 (±3097.6)	157.1 (±51.0)	0.59 (±0.05)	78.05 (±15.91)
Rec1/RSF	840.8 (±240.8)	1676.7 (±480.2)	0.85 (±0.02)	6.56 (±1.35)
$S_{90}P_{10}$	8819.1 (±1569.7)	158.1 (±28.1)	0.51 (±0.02)	65.55 (±11.67)
$S_{80}P_{20}$	3070.2 (±1312.9)	484.0 (±206.9)	0.62 (±0.03)	22.82 (±9.76)
$S_{70}P_{30}$	2839.5 (±107.5)	472.3 (±17.9)	0.97 (±0.05)	21.11 (±0.80)
$S_{60}P_{40}$	77.8 (±37.3)	19164.8 (±9181.2)	0.97 (±0.06)	0.58 (±0.28)

7.4.2 Structure, conformational ensemble and morphology of RSF, Rec1-resilin and PVCL in dilute solution by SANS

Initially, the size, structure, conformational ensemble and morphology of RSF, Rec1-resilin and PVCL in dilute solution were investigated using SANS experiments at room temperature. Figure 7.1 depicts the SANS scattering cross-section of 2 wt% solutions of RSF, Rec1-resilin and PVCL. The experimental data fitted with a *GuinierPorod* model are also shown in the

plot.[25] The parameters obtained from the *GuinierPorod* fit include the R_g and Porod exponent (Table 7.3). The R_g values for RSF, Rec1-resilin and PVCL in solution were determined to be 31.5, 42.1 and 28.5 Å, respectively (Table 7.3).

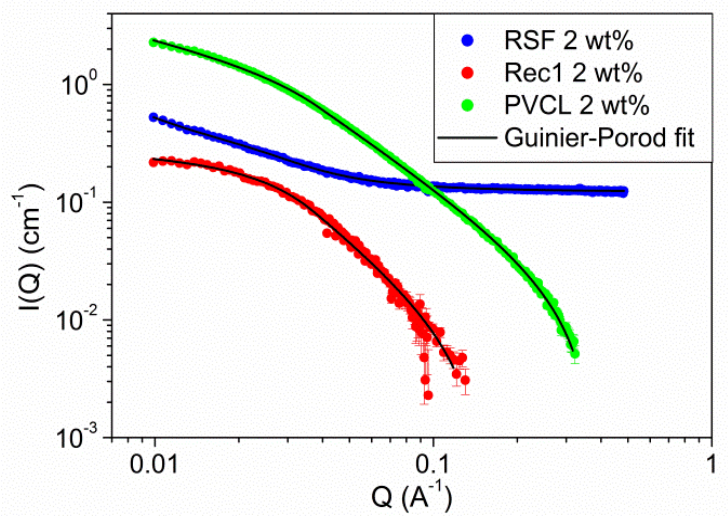


Figure 7.1 SANS curves of 2 wt% RSF, Rec1-resilin and PVCL solutions all fitted with the *GuinierPorod* model.

The R_g value of RSF agrees with our previous measurements using SAXS and also to the reported literature values.[3, 5] The Porod exponent of RSF in solution was ~2, which is indicative of Gaussian chain in dilute environment.[25] This observation conforms to investigations in the literature that reported that RSF chains were unfolded at low concentrations.[5] However, if RSF is considered as a polydispersed distribution of protein molecules consisting of unfolded structures of approximately 500 to 5000 amino acid residues, the R_g is expected to be in the range ~50 to ~200 Å based on the following power-law relationship between polymer length and ensemble average R_g[32]:

$$R_g = R_0 N^{\nu}, \qquad (10)$$

where N is the number of monomers in the polymer chain, R_0 is a constant (1.33 Å) that is a function of, among other things, the persistence length of the amino-acid polymer, and ν is a scaling factor (0.588). Under a particular set of experimental conditions, Greving et al. found the ensemble averaged R_g for RSF to be in the range 35-55 Å, and for native SF in the range 80-215 Å.[5] Therefore, the R_g (31.5 Å) observed in this study is an ensemble average and the differences in theoretical R_g and experimental can be attributed to differences in M_w as a result of the dissolution process. As observed from the SDS-PAGE characterisation, the M_w

of RSF ranges from ~37 to 200 kDa, which is similar to that observed in other studies of RSF.[33, 34] In addition, whilst exhibiting scattering indicative of a Gaussian chain, RSF is known to form micellar structures in solution,[35, 36] which may also result in lower R_g values. Clearly RSF (and SF) has extraordinary molecular and bulk properties and in many ways is not a typical protein in terms of its function. Many of the important details of the structure in solution have yet to be understood in detail.

The R_g value for Rec1-resilin was observed to be 42.1 Å and had a Porod exponent ~2. These values closely match with previous reported values by our group using SAXS.[37] Rec1-resilin's secondary structure has been interpreted as primarily an extended chain with regions of partially collapsed structure, which is consistent with its behaviour as an intrinsically disordered protein (IDP) – at least as far as is presently known about IDP's.[37]

From *GuinierPorod* fitting, the Porod exponent of PVCL was ~1.6, which suggests scattering from fully swollen chains in a good solvent and is in agreement with the behaviour of PVCL in aqueous systems below the LCST.[25] PVCL would therefore be expected to be an 'ideal' component for a physical hydrogel.

Table 7.3 Summary of R_g and Porod exponents of RSF, Rec1-resilin and PVCL in dilute solution obtained from *GuinerPorod* fitting of SANS data

Sample	**R_g (Å)**	**m (Porod exponent)**
RSF 2 wt% solution	31.5 (± 1.7)	1.86 (± 0.02)
Rec1-resilin 2 wt% solution	42.1 (± 0.9)	1.95 (± 0.04)
PVCL 2 wt% solution	28.5 (± 0.2)	1.61 (± 0.003)

7.4.3 Effect of concentration on the size and morphology of RSF in solution by SAXS and SANS

Because of the fundamental importance to this study, a more comprehensive SAXS study was employed to gain an understanding of the effect of concentration on the size and morphology of RSF in solution. Figure 7.2A shows the SAXS curves of RSF aqueous solutions of concentrations 1, 5, 10 and 15 wt% respectively; all fitted with a *GuinierPorod* function.[25] The *GuinierPorod* model was fitted to the data using the SasView program and the R_g and Porod exponent values at different concentrations are summarised in Table 7.4. The R_g was shown to progressively decrease from 26.8 to 18.2 Å as the of RSF concentration increased

from 1 to 15 wt%. The Porod exponent for all of the concentrations ranged from 1.9 to 2, which indicated that the RSF was essentially a Gaussian chain in solution. The SAXS scattering curves were normalised for RSF concentration (Figure 7.2B) and it was observed that the curves do not overlay, indicating that there are structural differences in RSF molecules due to the change in concentration. These observations are similar to those by Greving et al. that studied RSF solutions of different concentrations using SANS.[5] They reported a decrease in the R_g and the evolution of a shoulder in the scattering curve with increasing RSF concentration.[5]

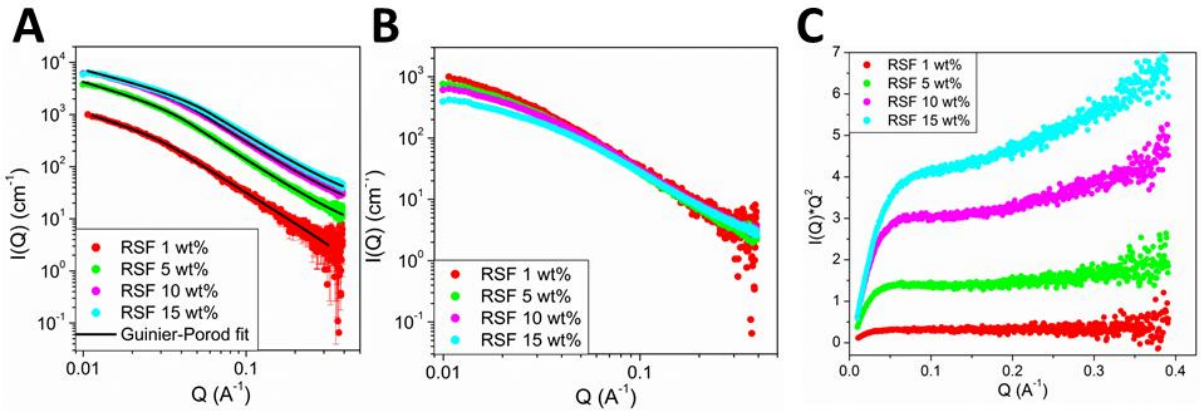


Figure 7.2 SAXS analysis of RSF solutions with concentrations of 1, 5, 10 and 15 wt%. A) SAXS data fitted with *GuinierPorod* model. B) SAXS data corrected for concentration. C) Kratky plot of the SAXS data.

A Kratky plot[38] is a useful display to indicate the 'folded-ness' of a polymer chain (Figure 7.3), and was employed to qualitatively examine the structure of RSF at different solution concentrations. At 1 wt%, the Kratky plot (Figure 7.2C) exhibited an initial increase at low Q followed by a plateau at mid Q and high Q, indicative of Gaussian chains. At concentrations of 10 wt% and 15 wt% there was a slight increase in the intensity at mid Q and high Q, compared to lower concentrations. This general shape *suggests* that the RSF at higher concentrations the RSF conformational ensemble remains Guassian; however there is some level of compaction reflected from the reduced R_g with concentration. A quite large polydispersity in Mw may be having a dominant effect on the observed structure in solution (eg $I(Q) \propto Mw^2$).

Table 7.4 Summary of R_g and Porod exponents of RSF solutions (1, 5, 10 and 15 wt%) obtained from *GuinerPorod* fitting of SAXS data.

Concentration (wt%)	**R_g (Å)**	**m (Porod exponent)**
1	26.8 (±1.2)	1.92 (±0.01)
5	24.0 (±0.3)	2.01 (±0.01)
10	19.9 (±0.2)	1.99 (±0.004)
15	18.2 (±0.1)	1.91 (±0.004)

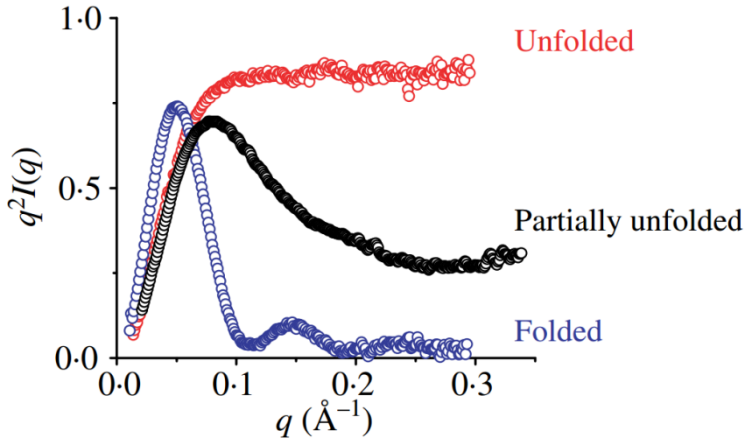


Figure 7.3 Cartoon illustrating the general shapes of Kratky plots for experimental SAXS data.[39]

Since the SAXS and SANS techniques are complementary, SANS was used to evaluate the size and morphology of the RSF solution at 2 and 15 wt% at room temperature. Figure 7.4 depicts the SANS curves of 2 and 15 wt% solutions of RSF fitted with a *GuinierPorod* model.[25] The parameters obtained from the *GuinierPorod* fit include the R_g and Porod exponent (Table 7.5). The R_g values for RSF at 2 and 15 wt% were 31.5 and 19.6 Å, respectively. These values closely match those measured from the *GuinierPorod* fitted SAXS data and confirm the observation that the RSF molecules were more compact as the concentration was increased. The Porod exponents of RSF in solution at 2 and 15 wt% were 1.86 and 1.84, respectively, which are indicative of Gaussian chain in solution.[25] The presence of a broad Q-region of increased intensity in the scattering curve of the concentrated (15 wt%) RSF solution is consistent with observations by Greving et al.[5] USANS was also employed to examine whether any large scale structures were present in the un-crosslinked dense RSF solution (15 wt%) and to provide a basis for comparison with the crosslinked RSF

hydrogel. There was no scattering above background observed for the RSF solution in the USANS range. This observation indicated that the RSF solution did not contain any large scale ordered structure and/or aggregates.

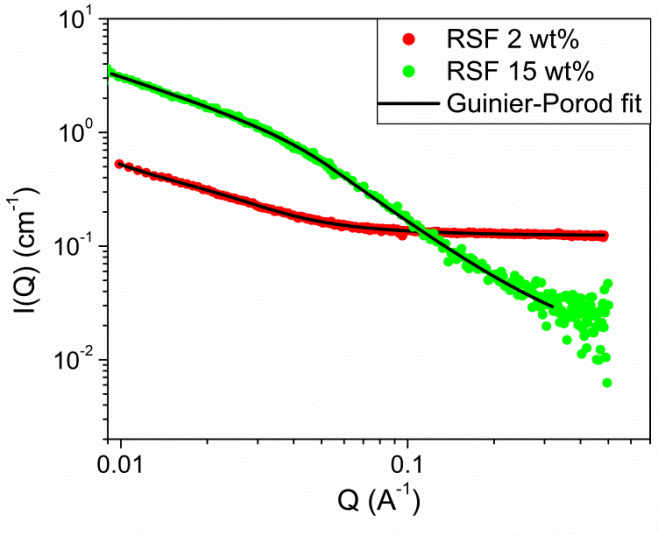


Figure 7.4 SANS curves of 2 and 15 wt% RSF fitted with the *GuinierPorod* model.

Table 7.5 Summary of R_g and Porod exponents of RSF at 2 and 15 wt% obtained from *GuinerPorod* fitting of SANS data.

Sample	**R_g (Å)**	**m (Porod exponent)**
RSF 2 wt%	31.5	1.86
RSF 15 wt%	19.6	1.84

In summary, the results from these experiments established the following:

- *sample preparation procedures were well-developed and the key hydrogel components were well-characterised;*
- *SAXS/SANS/USANS data collection was well-understood;*
- *SAXS/SANS/USANS data analysis procedures were developed and plausible structural models were obtained for Rec1-resilin and PVCL in dilute solution, and RSF from dilute to concentrated solutions.*

This formed a sound framework for the study of the more complex hydrogel systems.

7.4.4 USANS/SANS data for RSF-based hydrogels

A detailed SANS and USANS study was undertaken to characterise the microstructure of the crosslinked RSF, Rec1-resilin/RSF and RSF/PVCL hydrogels in order to understand the bulk structure-property relationships. Figure 7.5 shows the merged SANS/USANS data for the experimental gels, which provides an extraordinary opportunity to describe the structure of hydrogels over an extended Q range. Traditionally, most published studies on gel systems only have access to the typical SANS Q range. The pure RSF hydrogel and its crosslinked hybrid hydrogels with Rec1-resilin and PVCL (Figure 7.5A) clearly have comparable structural features on the short length scale (~10's to 100's Å) and on the longer length scale (1000's Å). All hydrogels exhibit a strong scattering at low Q values indicative of the presence of large heterogeneities in the systems, as expected. Figure 7.5B represents the SANS profiles of a series of RSF/PVCL hydrogels (Table 7.1) that has progressively increased level of PVCL. The crosslink density, water uptake capacity and modulus values of the series shows a systematic trend with composition (Table 7.2) and the expectation was that the structure on the molecular scale would reflect the trend. Overall the structural features are very similar with evidence of hierarchical structure covering the entire Q range. However, on closer inspection there are significant differences that had a major impact on the interpretation of the data and assignment of plausible structural models. The detailed analyses of the assembly and organization at different length scales are presented in the following sections.

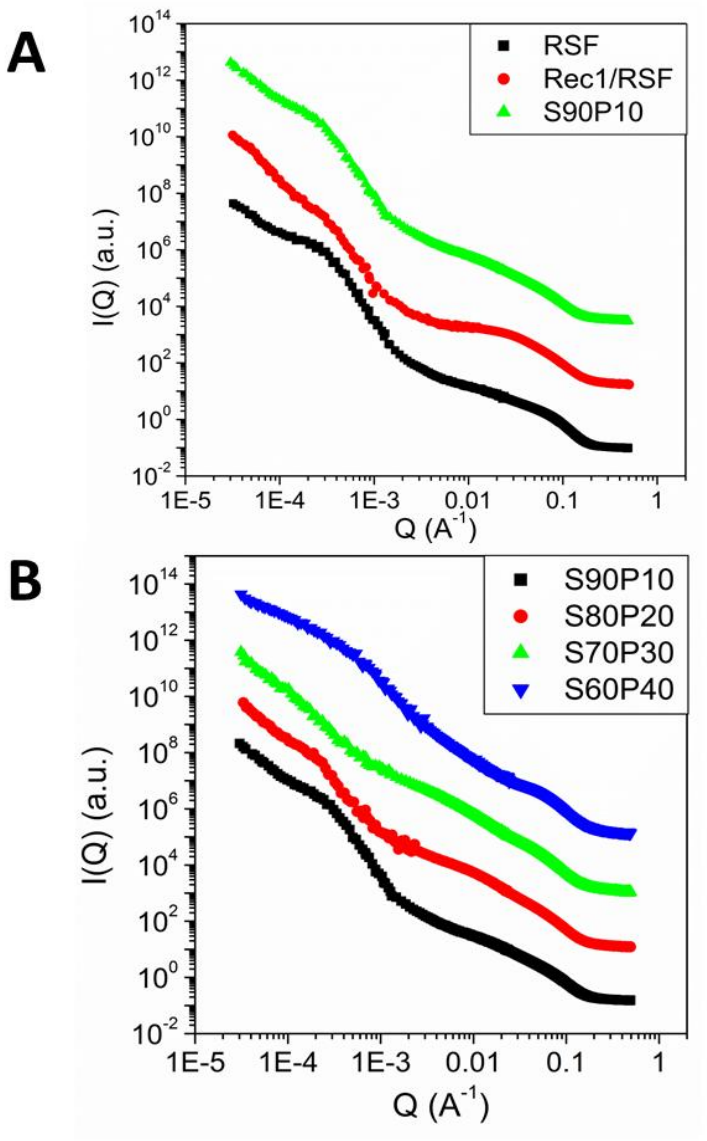


Figure 7.5 Combined USANS and SANS curves for A) RSF, Rec1-resilin/RSF, $S_{90}P_{10}$ and B) $S_{90}P_{10}$, $S_{80}P_{20}$, $S_{70}P_{30}$ and $S_{60}P_{40}$ hydrogels swollen in D_2O.

7.4.4.1 SANS analysis of RSF-based hydrogels

The SANS data for the experimental hydrogels was analysed first to gain an understanding of the structure at the smaller length scales before progressing to the USANS data on the large length scale. Initially, the standard gel models (*GaussLorentzGel*; *GelFitModel*; *Lorentz*) were employed to attempt to fit the SANS data for all samples. These models have been very successful in depicting the structure of hydrogels that are mainly composed of 'regular' polymers i.e. homopolymers with properties uniformly distributed along the polymer chain.[40, 41] Within this context, PVCL is a model polymer for hydrogel formation; however the RSF and Rec1-resilin biopolymers may behave quite differently. Inspection of the hydrophobicity

plots for the Rec1-resilin and RSF[3] (Chapter 3) suggests a reasonably regular distribution of hydrophobic index i.e. one segment of the chain appears to be similar to other parts. However both RSF and Rec1-resilin polymers are known to have regions that lead to specific structural elements (partially collapsed, beta sheet, etc.) and indeed these structural elements are required to fulfil the very special functions. What roles the RSF and Rec1-resilin played in the formation of a hydrogel remained to be uncovered.

Based on the previous results from the large range of hydrogels studied and well-established models for 'standard' hydrogels, the expectation was a correlation length ξ (describing the polymer chain in solution) would have a value around 10's Å; and the correlation length Ξ (describing the frozen-in structure caused by the swelling) would have values around 100's Å. Based on this, Figure 7.6 illustrates the proposed structure of the RSF-based hydrogels and indicates the different length scales present along with the obvious complexity of the systems due to the different components and interactions involved in the hydrogel formation.

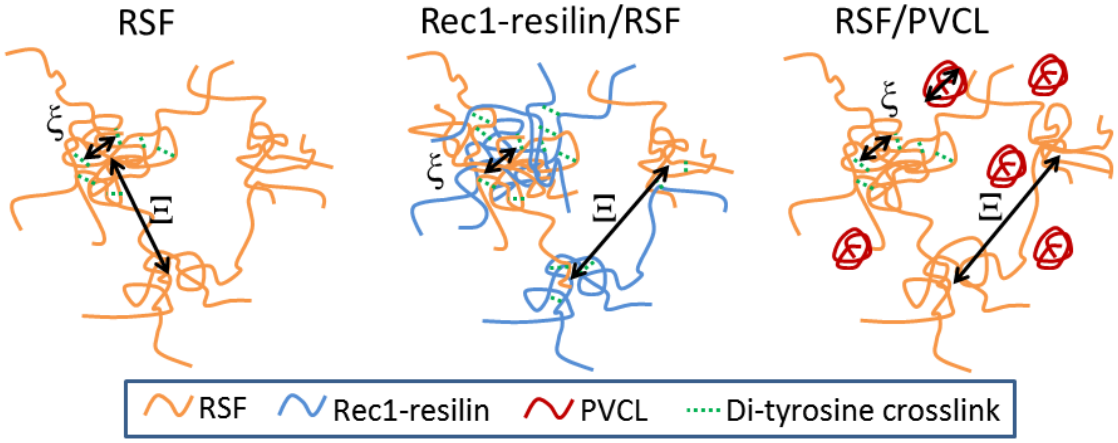


Figure 7.6 Schematic illustrating the proposed structure of the silk-based hydrogels.

Figure 7.7 shows the fitting of the scattering of the swollen RSF hydrogel using the *GaussLorentzGel*, *GelFitModel* and *Lorentz* models in SasView. The Q range was selected for the fit and then extrapolated for Figure 7.7 to demonstrate the additional excess scattering at low Q.

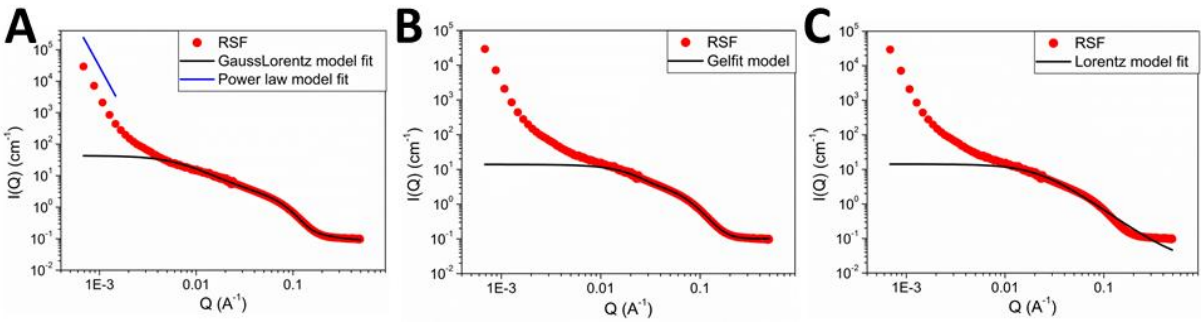


Figure 7.7 Fitting of the RSF SANS data with standard gel models: A) *GaussLorentzGel* model and *PowerLaw* model, B) *GelFitModel*, and C) *Lorentz* model.

Table 7.6 Values for important parameters obtained from unconstrained fitting of standard gel models to the SANS data for the RSF hydrogel.

Model	**ξ (Å)**	**Ξ (Å)**
GaussLorentzGel	139.2 ± 154.0	19.7 ± 2.3
GelFitModel	5.7 ± 5.8	89.2 ± 62.8

The *GaussLorentzGel* model was fitted over the Q range 0.0146 to 0.494 $Å^{-1}$ and produced values for ξ and Ξ that could not be interpreted in terms of a suitable structural model (Table 7.6). Fitting of the *GelFitModel* over the Q range 0.0185 to 0.494 $Å^{-1}$ produced values for ξ and Ξ with large errors and hence were assessed as unreliable (Table 7.6). The *Lorentz* model was clearly a poor fit to the data (poor chi square). Notably, in some cases the fit appears satisfactory, however the parameters obtained from the fit may have large errors; and hence were considered unreliable, or may have values that are not consistent with the mathematical model and/or a 'generic' hydrogel structure.

Constraining the fitting procedure in the initial steps by selecting values and/or limiting parameter ranges to 'expected' values, did not improve the ultimate results.

It became clear that the structure of the RSF hydrogel could not be well-described by these standard hydrogel models.

Given the complexity of the system, the broad 'correlation' peak (from ~0.007 to ~0.1 $Å^{-1}$) could be caused by a number of structural features including standard hydrogel features and/or simple phase separation, and/or a combination of both.

The excess scattering at low Q is due to larger structures and as an aid to the subsequent fitting/interpreting of the USANS data, a *PowerLaw* model was fitted where possible. It is noted that a rigorous application of the *PowerLaw* model requires an order of magnitude in Q, however a shorter Q range (as is the case here) can often be a useful guide to interpret the SANS and USANS data. Fitting of the *PowerLaw* model to the low Q data produced an exponent value of ~5.6, which exceeds the physically meaningful value of a little over 4.0. This observation implied that either there were insufficient data points to obtain an accurate estimate of the exponent, or the low Q data is due to some other form of scattering (e.g. structure factor).

Similarly, the standard gel models (*GaussLorentzGel*; *GelFitModel*; *Lorentz*) were employed to fit the Rec1-resilin/RSF SANS data (Figure 7.8). The Q range was selected for the fit and then extrapolated to demonstrate the excess scattering at low Q. All three models were clearly a poor fit for the data.

Thus, it became clear that the structure of the Rec1-resilin/RSF was not that of a 'standard' hydrogel, which is perhaps not surprising given the complexity of the system.

Fitting of a *PowerLaw* model to the low Q data (0.0007 to 0.0017 $Å^{-1}$) produced an exponent of 3.9, which indicated a surface fractal structure with scattering from a smooth interface.

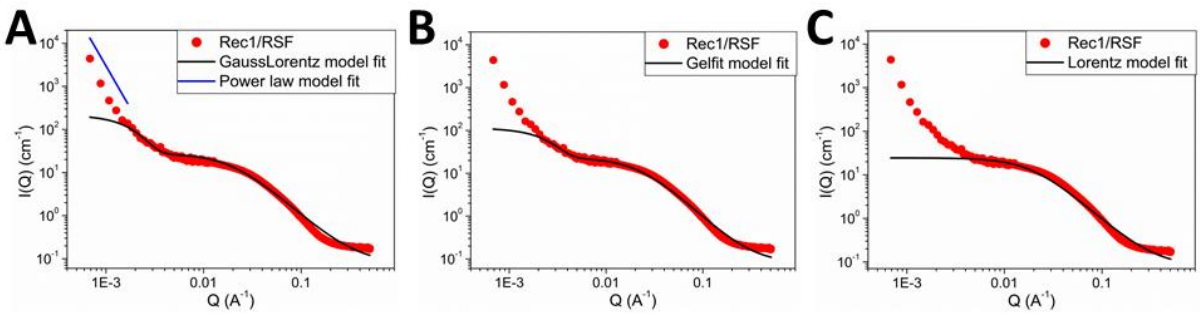


Figure 7.8 Fitting Rec1-resilin/RSF SANS data with standard gel models: A) *GaussLorentzGel* model and *PowerLaw* model, B) *GelFitModel*, and C) *Lorentz* model.

Next, the standard gel models (*GaussLorentzGel*; *GelFitModel*; *Lorentz*) were employed to fit the SANS data for the RSF/PVCL hydrogels. Recall that the expectation was that gross similarity in the SANS profiles for this series, observed in Figure 7.5B, would lead to a systematic trend in the fitted results that would reflect somehow the trends observed in the crosslink density, for example. Figure 7.9 shows the fitting of the $S_{90}P_{10}$, $S_{80}P_{20}$, $S_{70}P_{30}$ and $S_{60}P_{40}$ hydrogels with the *GaussLorentzGel* model. The *GaussLorentzGel* model produced

poor fits for all of the RSF/PVCL hydrogels and gave physically meaningless values for ξ and Ξ. Similarly, employing the *GelFitModel* did not result in a good fit of the SANS data, and for all of the RSF/PVCL hydrogel samples, the *Lorentz* model did not fit the data adequately and thus was not considered suitable for these systems. In all samples (with the possible exception of $S_{60}P_{40}$), the broad correlation peak appears to be the convolution of two distinct peaks and hence would require a more sophisticated model (and perhaps more experimental data) to provide useful information on the hydrogel structure.

Similar to the RSF and Rec1-resilin/RSF hydrogels, it became clear that the structure of the RSF/PVCL hydrogels did not conform to that of a 'standard' hydrogel model.

A *PowerLaw* model was fitted to low Q SANS data for the $S_{90}P_{10}$, $S_{80}P_{20}$, $S_{70}P_{30}$ and $S_{60}P_{40}$ systems (Figure 7.9) that produced exponents of 4.5, 3.8, 2.1, and 3.7, respectively. Thus, $S_{90}P_{10}$, $S_{80}P_{20}$ and $S_{60}P_{40}$ exhibited low Q scattering indicative of surface fractal structures with smooth interfaces. However, the $S_{70}P_{30}$ hydrogel low Q exponent of 2.1 implied mass fractal scattering.

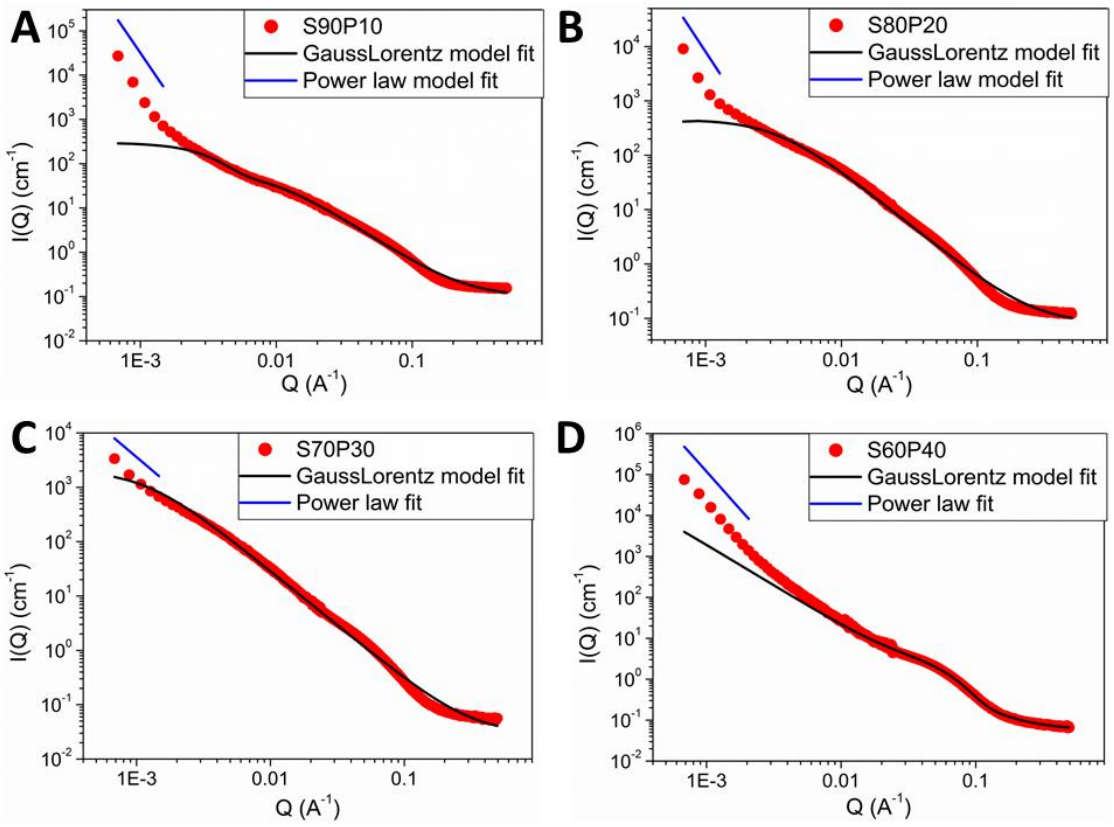


Figure 7.9 Fitting of RSF/PVCL hydrogel SANS data using *GaussLorentzGel* and *PowerLaw* model for samples: A) $S_{90}P_{10}$, B) $S_{80}P_{20}$, C) $S_{70}P_{30}$ and D) $S_{60}P_{40}$.

In addition, fitting of more generalised model-independent functions (two-level *UnifiedPowerRg*; *GuinierPorod*) was attempted to systematically search for clues to the underlying structures. The two-level *UnifiedPowerRg* model produced a poor fit to the data and results that could not be successfully interpreted in terms of a 'generic' hydrogel structure. However, the *GuinierPorod* model produced good fits with the data and gave valuable insights into the underlying structure. Figure 7.10 shows the *GuinierPorod* fitting for the RSF, Rec1-resilin/RSF and RSF/PVCL hydrogels and the R_g and Porod exponent values obtained from the fitting are summarised in Table 7.7. It was observed that the RSF di-tyrosine crosslinked hydrogel had an R_g of 14.6 Å, which is somewhat lower than RSF in solution at 15 wt% (19.6 Å – SANS, 18.2 Å – SAXS). As a first approximation to give some physical meaning to these fitted values, it was assumed that at the resolution of the SANS experiments, the hydrogel was composed of a polydispersed population of roughly spherical regions of increased scattering length density (SLD) (ie a 'blob'), randomly distributed in a background of reasonably uniform SLD (ie a mixture of solubilised polymer chains and water). The fitted R_g was that of the 'blob'.

The RSF hydrogel was crosslinked at a concentration of 15 wt%; however after crosslinking, the gel was leached to remove some unreacted RSF and dried before re-swelling the hydrogel. Therefore, as the equilibrium swelling value for RSF was measured as ~0.59, the concentration of protein in the gel was ~60 wt%. These results may suggest that the partially collapsing structure observed at increasing RSF concentration in solution may be frozen in the hydrogel structure, which may account in part for the complex hydrogel structure.

GuinierPorod fitting of the Rec1-resilin/RSF hydrogel gave an R_g of 35.9 Å. This represents an ensemble average of the Rec1-resilin and RSF protein chains in the system. The R_g of Rec1-resilin at the crosslinking concentration (20 wt%) was measured as ~35 Å by our group[42], which closely agrees with the R_g of the Rec1-resilin/RSF hydrogel. Furthermore, the RSF/PVCL hydrogels showed increasing R_g values from 11.6 to 21.9 Å with increasing PVCL content. This may be attributed to the decreasing network density as the crosslinked RSF content also decreased with increasing PVCL.

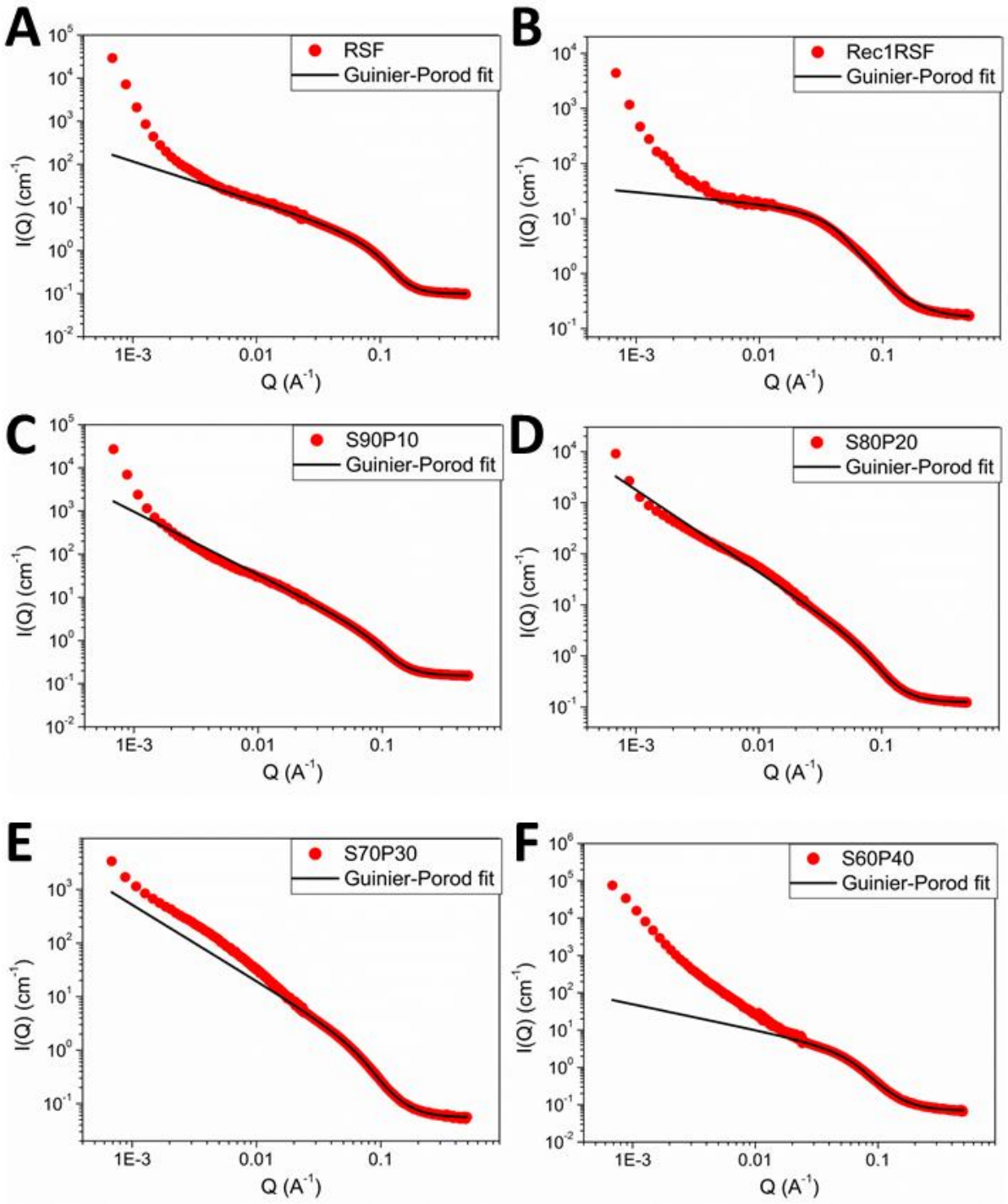


Figure 7.10 *GuinierPorod* fitting of SANS data for hydrogel samples: A) RSF, B) Rec1-resilin/RSF, C) $S_{90}P_{10}$, D) $S_{80}P_{20}$, E) $S_{70}P_{30}$ and D) $S_{60}P_{40}$.

Table 7.7 Summary of R_g and Porod exponent values determined from fitting the *GuinierPorod* model to the SANS hydrogel data.

Sample	R_g (Å)	m (Porod exponent)
RSF	14.6	4.5
Rec1/RSF	35.9	2.7
$S_{90}P_{10}$	11.6	3.8
$S_{80}P_{20}$	12.0	3.6
$S_{70}P_{30}$	14.4	3.4
$S_{60}P_{40}$	21.9	3.3

7.4.4.2 USANS analysis of RSF-based hydrogels

The USANS data can provide information on the micron length scale (~0.3 – 200 microns) for bulk systems in their fully hydrated state. This is an important length scale to understand the structure of hydrogels since the observed size distribution and interconnectivity of the porosity undoubtedly makes a major contribution to the gel strength, swelling behaviour (i.e. access of solvent to the polymer matrix) and responsiveness to external stimuli (i.e. diffusion of ions). These are the important properties that set hydrogels apart from the solution state, and the solid state. Direct imaging techniques such as TEM, SEM and AFM etc., have been employed to observe morphological characteristics in small regions of hydrogels and suggest a polydispersed distribution of pores acting as both reservoirs of water as well as interconnectivity for efficient water and ion transport.[43, 44]

From a scattering perspective, the hydrogel should appear more or less as a two phase system with the swollen polymer matrix as one phase, and water as the other. Figure 7.11 is the USANS data for all the experimental samples. It is noted that there is a reasonably well-defined region of increased intensity in the RSF, $S_{90}P_{10}$, $S_{80}P_{20}$ and $S_{60}P_{40}$ samples; and a less well-defined region for the Rec1-resilin/RSF and $S_{70}P_{30}$ samples. At this stage of the investigation, there was no *ab initio* reason for such an observation. Since in some USANS profiles the broad 'peak' covered a substantial portion of the available Q range, a *PowerLaw* model was fitted to each profile to obtain the best estimate of the overall Q dependence. The fitted data is shown in the plots (Figures 7.11A and B) and Table 7.8 summarises the results of the fitting parameters. As a generalisation, with perhaps one exception ($S_{60}P_{40}$), the value of the Porod exponent is around 3, which indicates a molecularly 'rough' surface on this

length scale. This may in fact be a 'smooth' surface on a shorter length scale (e.g. like a tightly packed bunch of grapes), which is more consistent with some of the TEM/SEM images of 'standard' hydrogels. For the exception sample ($S_{60}P_{40}$ Porod exponent 2.4) the broad 'peak' is very broad and the estimated Porod exponent may have considerable experimental error due to limited data points.

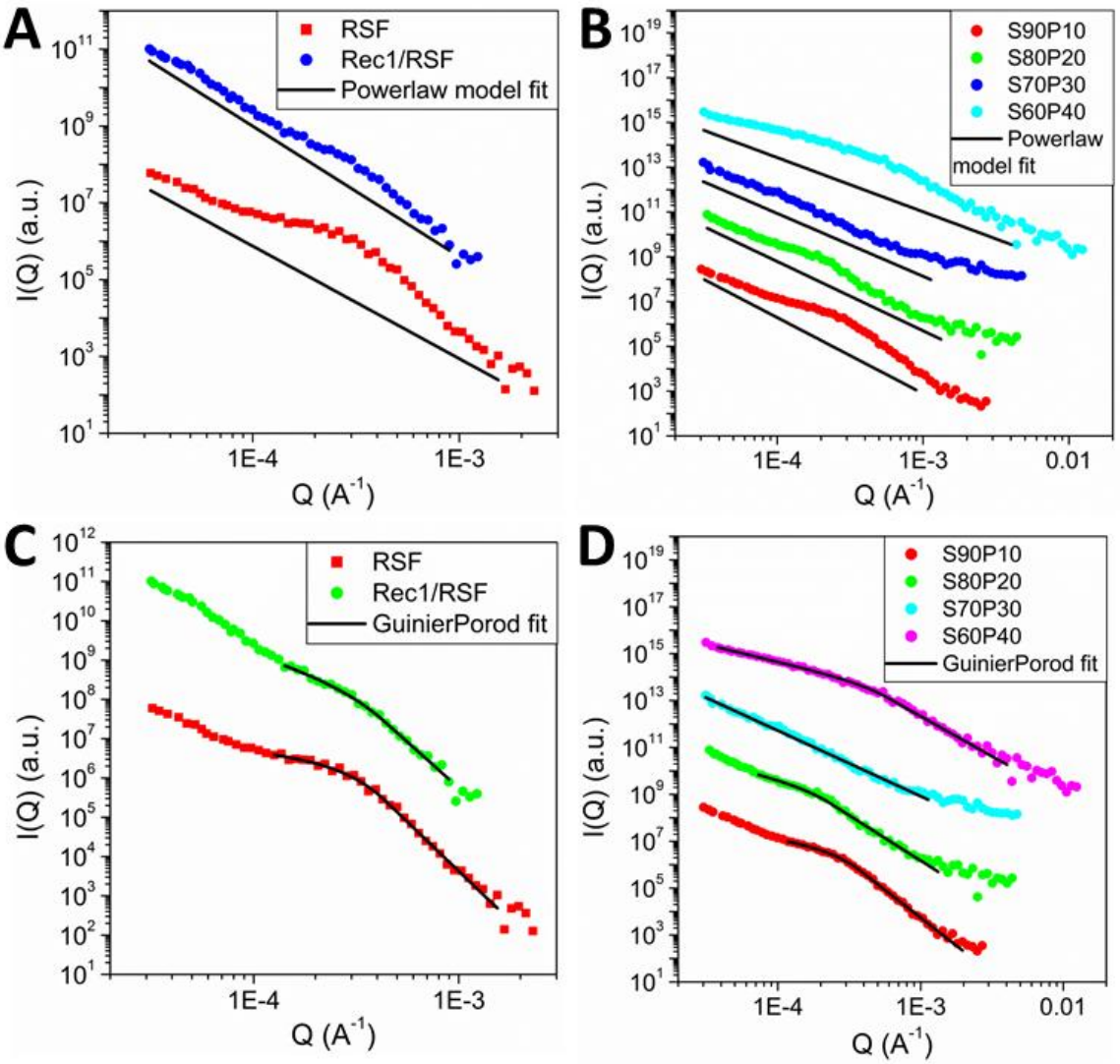


Figure 7.11 USANS data of silk-based hydrogels. A) RSF and Rec1-resilin/RSF fitted with *PowerLaw* model; B) $S_{90}P_{10}$, $S_{80}P_{20}$, $S_{70}P_{30}$ and $S_{60}P_{40}$ fitted with *PowerLaw* model; C) RSF and Rec1-resilin/RSF fitted with *GuinierPorod* model; D) $S_{90}P_{10}$, $S_{80}P_{20}$, $S_{70}P_{30}$ and $S_{60}P_{40}$ fitted with *GuinierPorod* model.

Table 7.8 Fitted parameters for the *PowerLaw* model and the USANS data

Sample	Porod exponent
RSF	2.9 ± 0.1
Rec1/RSF	3.4 ± 0.1
$S_{90}P_{10}$	3.3 ± 0.1
$S_{80}P_{20}$	3.1±0.1
$S_{70}P_{30}$	2.8 ± 0.1
$S_{60}P_{40}$	2.42 ± 0.08

As with the analysis of the SANS data, the generalised *GuinierPorod* model is very useful in providing the initial overview of the structure, which may then guide the application of more detailed models. Figures 7.11C and D show the experimental USANS data with the fitted *GuinierPorod* model, and the results are presented in Table 7.9. Consistent with the initial inspection of the experimental data, fits to the data for samples RSF, $S_{90}P_{10}$, $S_{80}P_{20}$ and $S_{60}P_{40}$ were reliable, and for the Rec1-resilin/RSF and $S_{70}P_{30}$ samples less so. In this model, the R_g is an ensemble average value describing an undoubtedly polydispersed distribution of pores. Hence the uncertain values for the Rec1-resilin/RSF and $S_{70}P_{30}$ samples suggest the structure may be essentially homogeneous on this length scale and hence the pores are very large, or very small (i.e. outside the USANS Q range).

The R_g values do not seem to correlate with the measured properties, such as crosslink density, swelling behaviour and modulus as we would expect larger pore sizes for the $S_{60}P_{40}$ and Rec1-resilin/RSF hydrogels that exhibit the highest swelling capacity and lowest modulus. The R_g value for RSF is larger than for Rec1-resilin/RSF and also $S_{90}P_{10}$ and $S_{60}P_{40}$. This may be due to the fact that despite being a relatively large molecule, RSF forms much more compact structures in solution than Rec1-resilin and PVCL as observed by SAXS and SANS measurements (Section 7.4.3). Of course, if the shape of the structural feature had changed between the different hydrogel compositions, then the R_g is not a good indicator for a systematic change.

Note that the Porod exponents from the *GuinierPorod* model fit for the RSF, Rec1-resilin/RSF and $S_{90}P_{10}$ are very high and do not agree with the values initially fitted to the entire Q range. This is due in part to the limited number of data points in the high Q range of the USANS data.

Table 7.9 Fitted parameters for the *GuinierPorod* model and the USANS data

Sample	R_g (Å)	Porod exponent	Dimensional variable
RSF	5548 ± 110	5.00 ± 0.02	0.45 ± 0.04
Rec1/RSF	3245 ± 228	4.7 ± 0.1	1.70 ± 0.09
$S_{90}P_{10}$	5079 ± 100	4.75 ± 0.02	1.02 ± 0.03
$S_{80}P_{20}$	5677 ± 203	3.85 ± 0.02	1.51 ± 0.04
$S_{70}P_{30}$	75438	2.79 ± 0.01	1.58
$S_{60}P_{40}$	2092 ± 24	3.40 ± 0.01	1.45 ± 0.01

7.5 Discussion

7.5.1 Solution study by SANS, USANS and SAXS

As a preliminary to the hydrogel experiments, the structure of RSF, Rec1-resilin and PVCL at various concentrations in solution was studied using SANS, USANS and SAXS. The results were internally consistent, that is, if the concentration was increased, the I(Q) increased in a systematic way. Analysis of the data provided structural parameters that agreed with the results from other studies. In particular, Greving et al. used SANS to study the size and morphology of RSF in solution at a range of concentrations (~2.5 to 97.4 mg/mL).[5] They have also observed molecular weight (M_w) polydispersity (~50 to 250 kDa) and thus the R_g (~35 to 55 Å) was an ensemble average.[5] Greving et al. observed the emergence of a shoulder in the scattering curve of RSF at higher concentration; along with an increase in the intensity at low Q increased, which was attributed to large-scale aggregates in the solution.[5] Larger aggregates are consistent with the reported behaviour of silk fibroin, which involves the formation of micelles that aggregate to form nanofilament structures.[35, 45] In this investigation SAXS and SANS analyses confirmed that the individual RSF protein chains became more compact with increasing concentration, as demonstrated by decreasing R_g values from ~30 Å to ~18 Å. RSF is known to form larger aggregates at higher concentrations,[35, 45] which has implications for the structure formation that occurs during gelation. This may result in phase separated regions of higher crosslink density that lead to heterogeneities in the system. The structural studies of the RSF/Rec1-resilin/PVCL solutions established a good understanding of the molecular components and helped formulate the studies of the considerably more complex hydrogels. Notably, the concentrated RSF solution did not exhibit any scattering

above background in the USANS region, which confirmed that there were no structural features at longer length scales.

7.5.2 USANS/SANS study of RSF-based hydrogels

The USANS/SANS data show that the RSF-based hydrogels have a gel-like structure, with characteristic monotonic decrease in scattered intensity plus regions of increased intensity due to the structural inhomogeneities. However, it was not possible to fit the data using the available models for classical gel theory. Perhaps this is not surprising given the enormous complexity of the possible interactions involved in these systems, including covalent, hydrogen bonding, hydrophobic, electrostatic, van der Waals, solvation, etc. Also, the M_w polydispersity of RSF (~37 to 200 kDa) and the different regions of the RSF sequence that can form random coil and beta-sheet conformations may contribute to the differences in structure from conventional hydrogels. For example, it is conceivable that the RSF chain could partially collapse before or during the crosslinking process and hence lead to regions of increased scattered intensity unrelated to the regions created by the crosslinks. Note that there is no supporting experimental evidence presently available for such a collapse, or any other confounding process for that matter. In addition, the complex structural behaviour of IDPs, such as Rec1-resilin, is just beginning to be understood. For example, what happens when the hydrogel components are mixed in a suitable solvent and the solvent environment is changed as crosslinking progresses? What are the detailed consequences of various molecular interactions, particularly crosslinking, in the present study? Are the crosslinks uniformly distributed along the IDP chain, or are there sequences of preferential crosslinks perhaps created by the solvent conditions?

Figure 7.12 depicts summary plots of the merged SANS/USANS data (repeat of Figure 7.5) with the best fits superimposed of the *PowerLaw* and *GuinierPorod* models. Note that there is considerable overlap in the Q range between the two datasets which helps desmear the USANS data and is useful in linking fitted data between the two Q ranges i.e. the low Q SANS data should provide an indication of the Q dependence of the high Q data in the USANS data. For example, in Figure 7.12A(ii) the low Q Porod exponent of the SANS data for Rec1-resilin/RSF predicts the overall Q dependence of USANS data.

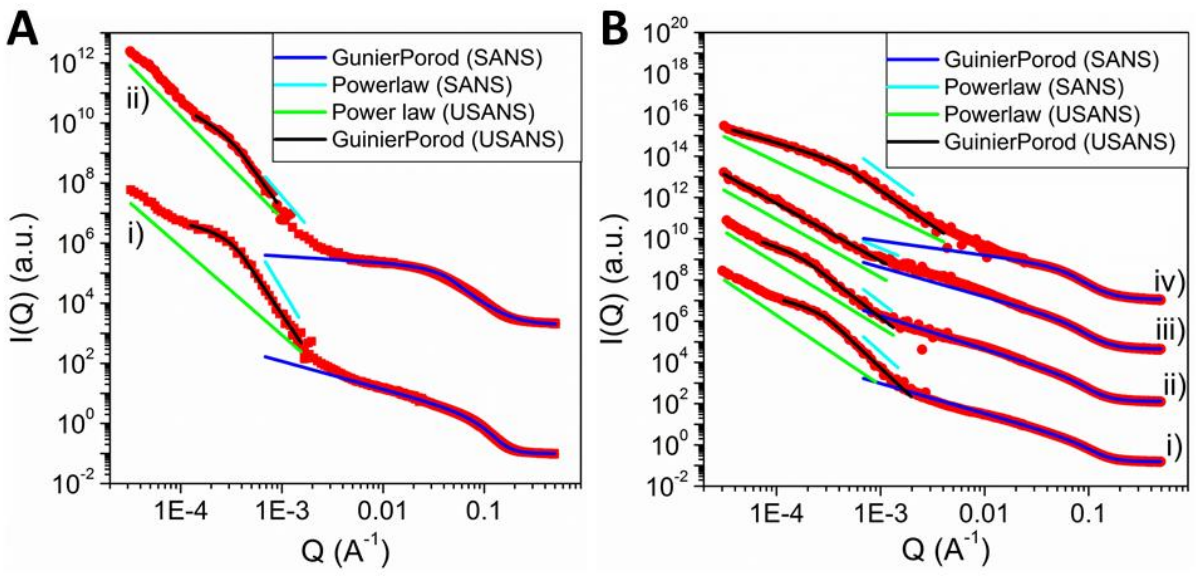


Figure 7.12 A) Merged SANS/USANS data for (i) RSF, and (ii) Rec1-resilin/RSF with superimposed fits for the *PowerLaw* and *GuinierPorod* models. B) Merged SANS/USANS data for i) $S_{90}P_{10}$, ii) $S_{80}P_{20}$, iii) $S_{70}P_{30}$ and iv) $S_{60}P_{40}$ with superimposed fits for the *PowerLaw* and *GuinierPorod* models. The *PowerLaw* fits have been offset from the experimental data for clarity.

7.5.3 *GuinierPorod* fitting of SANS data of RSF-based hydrogels

The plots of the merged SANS/USANS data show that the RSF, Rec1-resilin/RSF and RSF/PVCL hydrogels display similar structural features over the Q range measured, however certain structural differences are evident. The SANS region was expected to give information relating to the frozen-in crosslinks present in the hydrogel. Fitting of the SANS region of the RSF hydrogel with the *GuinierPorod* model gave a R_g of 14.6 Å, which correlated well with the observed behaviour of RSF at higher concentrations (18.2 Å – SAXS; 19.6 Å – SANS). In comparison to the RSF gel, the shoulder region present in the scattering curve of the Rec1-resilin/RSF hydrogel was much broader, suggesting a higher degree of polydispersity in the size of the frozen-in structures, which is not surprising given the presence of Rec1-resilin and RSF in the hybrid hydrogel. As previously mentioned, the crosslinks possible included Rec1-resilin-RSF, RSF-RSF and Rec1-resilin-Rec1-resilin, which would lead to a range of sizes for the frozen-in crosslinks.

The hybrid RSF/PVCL gels, $S_{90}P_{10}$, $S_{80}P_{20}$ and $S_{70}P_{30,}$ all exhibited broad correlation peaks that appeared to be the convolution of two peaks (Figures 7.9, 7.10 and 7.12). As the RSF/PVCL hydrogel was composed of two types of polymers (bio-polymer RSF and

synthetic polymer PVCL), the results suggest the presence of two types of heterogeneities on the nanometer scale in the hydrogel structure. From *GuinierPorod* fitting, the R_g of the features ranged from 11.6 to 14.4 Å for $S_{90}P_{10}$, $S_{80}P_{20}$ and $S_{70}P_{30}$, respectively, which is consistent with a progressively lower proportion of RSF. Also, the R_g was inversely proportional to the reported crosslink density values for the RSF/PVCL hydrogels (Table 7.2). Similarly, Hule et al. reported that the compactness of the network was inversely proportional to the crosslink density for a self-assembled peptide hydrogel.[46] The $S_{60}P_{40}$ hydrogel was an exception as it exhibited a single correlation peak and *GuinierPorod* fitting gave a R_g of 21.9 Å. Comparison of the scattering intensity in the low Q region of the SANS data of the RSF/PVCL hydrogels with increasing PVCL concentration shows a progressive increase in excess scattering. This observation suggests an increasing proportion of structural heterogeneities in the hydrogels with the addition of PVCL. In addition, all of the RSF/PVCL hydrogels exhibited surface fractal scattering in the SANS range as the Porod exponents for all samples were between 3 and 4. The Porod exponents were progressively lower with increasing PVCL content suggesting increased roughness of the surface.

7.5.4 *GuinierPorod* fitting of USANS data of RSF-based hydrogels

As the SANS region is indicative of the frozen-in crosslinked structure on the smaller length scale, the USANS region is expected to give information about the larger structures present in the hydrogel structure, such as the pores that act as reservoirs and channels for water. From the characterisation of the water uptake capacity and storage modulus, it was hypothesised that the RSF hydrogel would possess the smallest pore size as it exhibits the lowest water uptake capacity and highest storage modulus compared to the hybrid hydrogels. The R_g values obtained from the *GuinierPorod* fitting of the USANS data (Table 7.9) indicate the presence of structures with R_g values in the range of hundreds on nanometres. However, the R_g values from obtained from *GuinierPorod* fitting of the USANS data do no follow the expected trend as the R_g is higher for the RSF hydrogel than the Rec1-resilin/RSF, $S_{90}P_{10}$ and $S_{60}P_{40}$ hydrogels. However, the USANS peaks are broad for the RSF/PVCL samples indicating that the features in this range are particularly polydisperse. As noted previously direct comparison of the R_g values may be deceptive and the interpretation of it depends on the shape of the structure. The power law dependence of the USANS data indicated that the silk-based hydrogels possessed a rough interface to the surrounding solvent in this size range. Furthermore, all of the hydrogel samples exhibited an upturn in the low Q region of the

USANS data suggesting the presence of larger pores or cracks that formed during the gelation process. This behaviour has also been observed for other polymer hydrogels.[47, 48]

7.6 Conclusions

This investigation provides an understanding of the microstructure formation of a range of silk-based hydrogels based on photochemical crosslinking of RSF. Notably, this is the first report, to our knowledge, that delves into the structure of chemically crosslinked silk hydrogels using neutron scattering. Whilst it was observed that the features of the scattering curves suggested that the hydrogels exhibited an overall gel-like structure; it was not possible to fit the data using classical gel models. However, using *PowerLaw* and *GuinierPorod* models, an understanding of the heterogeneities and types of structures over four orders of magnitude (~10 Å to 10 μm) was established. It was clearly identified that there were structures present in the hydrogels in the SANS range that correlated with the size measured from studies of the solution state. Also, the frozen-in structures had R_g values that were inversely proportional to the crosslink density. However, much larger heterogeneities on the order of thousands of Å were identified in the USANS range, which are expected to be related to the porous nature of the hydrogels. In addition, all of the hydrogels exhibited increased scattering at low Q, which indicates that there were larger structures present that were beyond the measurable range. Ideally and certainly a goal for future studies, is to fit a more sophisticated model to the entire Q range and provide a complete description to the hierarchical hydrogel structure over the many length scales evident in these plots. Further USANS/SANS experiments are required to unravel the complex structure of the photo-crosslinked silk-based hydrogels including, contrast variation (systematically changing the H/D ratio of the solvent), response to applied shear, and dehydration (stepwise dehydration/hydration).

7.7 References

1. Whittaker, J. L.; Choudhury, N. R.; Dutta, N. K.; Zannettino, A., *J. Mater. Chem. B* **2014,** *2* (37), 6259-6270.
2. Armstrong, C. G.; Mow, V. C., *J. Bone Jt. Surg.* **1982,** *64* (1), 88-94.
3. Whittaker, J. L.; Dutta, N. K.; Knott, R.; McPhee, G.; Voelcker, N. H.; Elvin, C.; Hill, A.; Choudhury, N. R., *Langmuir* **2015,** *31* (32), 8882-8891.
4. Whittaker, J. L.; Dutta, N. K.; Elvin, C. M.; Choudhury, N. R., *J. Mater. Chem. B* **2015,** *3* (32), 6576-6579.

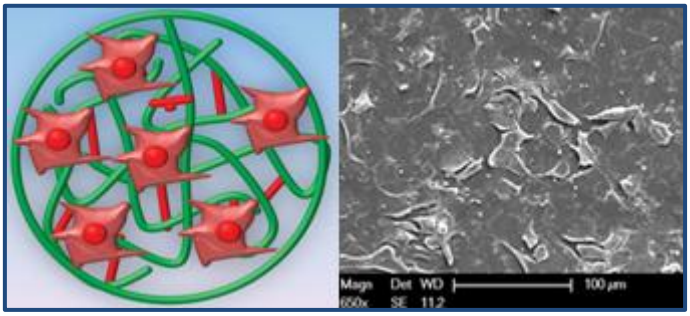
5. Greving, I.; Dicko, C.; Terry, A.; Callow, P.; Vollrath, F., *Soft Matter* **2010,** *6* (18), 4389-4395.
6. Rehm, C.; Brule, A.; Freund, A. K.; Kennedy, S. J., *J. Appl. Crystallogr.* **2013,** *46* (6), 1699-1704.
7. Crompton, K. E.; Forsythe, J. S.; Horne, M. K.; Finkelstein, D. I.; Knott, R. B., *Soft Matter* **2009,** *5* (23), 4704-4711.
8. Mangiapia, G.; Frielinghaus, H.; Derrico, G.; Ortona, O.; Sartorio, R.; Paduano, L., *Phys. Chem. Chem. Phys.* **2007,** *9* (46), 6150-6158.
9. Dandu, R.; Cresce, A. V.; Briber, R.; Dowell, P.; Cappello, J.; Ghandehari, H., *Polymer* **2009,** *50* (2), 366-374.
10. Hudson, S. D.; Hutter, J. L.; Nieh, M.-P.; Pencer, J.; Millon, L. E.; Wan, W., *The J. Chem. Phys.* **2009,** *130* (3), 034903.
11. Elvin, C. M.; Carr, A. G.; Huson, M. G.; Maxwell, J. M.; Pearson, R. D.; Vuocolo, T.; Liyou, N. E.; Wong, D. C. C.; Merritt, D. J.; Dixon, N. E., *Nature* **2005,** *437*, 999-1002.
12. Kim, M.; Elvin, C.; Brownlee, A.; Lyons, R., *Prot. Expression Purif.* **2007,** *52* (1), 230-236.
13. Pedersen, J., *J. Appl. Crystallogr.* **2004,** *37* (3), 369-380.
14. Kline, S., *J. Appl. Crystallogr.* **2006,** *39* (6), 895-900.
15. Shibayama, M.; Sakai, T., Chapter 2. Fabrication, Structure, Mechanical Properties, and Applications of Tetra-PEG Hydrogels. In *Polymeric and Self Assembled Hydrogels: From Fundamental Understanding to Applications*, The Royal Society of Chemistry: 2013; pp 7-38.
16. Norisuye, T.; Masui, N.; Kida, Y.; Ikuta, D.; Kokufuta, E.; Ito, S.; Panyukov, S.; Shibayama, M., *Polymer* **2002,** *43* (19), 5289-5297.
17. Geissler, E.; Hecht, A.-M.; Rochas, C.; Horkay, F.; Basser, P. J., *Macromol. Symp.* **2005,** *227* (1), 27-38.
18. Shibayama, M.; Tanaka, T.; Han, C. C., *J. Chem. Phys.* **1992,** *97* (9), 6829-6841.
19. Mallam, S.; Horkay, F.; Hecht, A. M.; Rennie, A. R.; Geissler, E., *Macromolecules* **1991,** *24* (2), 543-548.
20. Geissler, E.; Horkay, F.; Hecht, A.-M., *Phys. Rev. Lett.* **1993,** *71* (4), 645-648.
21. Tian, J.; Seery, T. A. P.; Ho, D. L.; Weiss, R. A., *Macromolecules* **2004,** *37* (26), 10001-10008.

22. Horkay, F.; Magda, J.; Alcoutlabi, M.; Atzet, S.; Zarembinski, T., *Polymer* **2010,** *51* (19), 4424-4430.
23. Evmenenko, G.; Theunissen, E.; Mortensen, K.; Reynaers, H., *Polymer* **2001,** *42* (7), 2907-2913.
24. Beaucage, G., *J. Appl. Crystallogr.* **1995,** *28* (6), 717-728.
25. Hammouda, B., *J. Appl. Crystallogr.* **2010,** *43* (4), 716-719.
26. Pedersen, J. S., *Adv. Colloid Interface Sci.* **1997,** *70* (1), 171-210.
27. Hammouda, B., Probing Nanoscale Structures - The SANS Toolbox. 2012. http://www.ncnr.nist.gov/staff/hammouda/the_SANS_toolbox.pdf (accessed 10 January 2015).
28. Wang, Y.; Ameer, G. A.; Sheppard, B. J.; Langer, R., *Nat. Biotech.* **2002,** *20* (6), 602-606.
29. Krongauz, V., *J. Therm. Anal. Calorim.* **2010,** *102* (2), 435-445.
30. Djordjevic, I.; Choudhury, N. R.; Dutta, N. K.; Kumar, S., *Polymer* **2009,** *50* (7), 1682-1691.
31. Okay, O., General Properties of Hydrogels. In *Hydrogel Sensors and Actuators*, Gerlach, G.; Arndt, K.-F., Eds. Springer Berlin Heidelberg: 2010; Vol. 6, pp 1-14.
32. Kohn, J. E.; Millett, I. S.; Jacob, J.; Zagrovic, B.; Dillon, T. M.; Cingel, N.; Dothager, R. S.; Seifert, S.; Thiyagarajan, P.; Sosnick, T. R.; Hasan, M. Z.; Pande, V. S.; Ruczinski, I.; Doniach, S.; Plaxco, K. W., *Proc. Natl. Acad. Sci. U. S. A.* **2004,** *101* (34), 12491-12496.
33. Wang, H.-Y.; Zhang, Y.-Q., *Soft Matter* **2013,** *9* (1), 138-145.
34. Vasconcelos, A.; Freddi, G.; Cavaco-Paulo, A., *Biomacromolecules* **2008,** *9* (4), 1299-1305.
35. Lu, Q.; Zhu, H.; Zhang, C.; Zhang, F.; Zhang, B.; Kaplan, D. L., *Biomacromolecules* **2012,** *13* (3), 826-832.
36. Jin, H.-J., *Nature* **2003,** *424* (6952), 1057-1061.
37. Balu, R.; Knott, R.; Cowieson, N. P.; Elvin, C. M.; Hill, A. J.; Choudhury, N. R.; Dutta, N. K., *Sci. Rep.* **2015,** *5*.
38. Receveur-Bréchot, V.; Durand, D., *Curr. Protein Pept. Sci.* **2012,** *13* (1), 55-75.
39. Putnam, C. D.; Hammel, M.; Hura, G. L.; Tainer, J. A., *Q. Rev. Biophys.* **2007,** *40* (03), 191-285.
40. Shibayama, M., *Soft Matter* **2012,** *8* (31), 8030-8038.
41. Shibayama, M., *Polym. J.* **2011,** *43* (1), 18-34.

42. Balu, R. Resilin-mimetic protein polymers: Fundamental structure-property relationship and controlled nano-bioconjugates. University of South Australia, 2015.
43. Xia, L.-W.; Xie, R.; Ju, X.-J.; Wang, W.; Chen, Q.; Chu, L.-Y., *Nat. Commun.* **2013,** *4*.
44. Nazarov, R.; Jin, H.-J.; Kaplan, D. L., *Biomacromolecules* **2004,** *5* (3), 718-726.
45. Shulha, H.; Po Foo, C. W.; Kaplan, D. L.; Tsukruk, V. V., *Polymer* **2006,** *47* (16), 5821-5830.
46. Hule, R. A.; Nagarkar, R. P.; Altunbas, A.; Ramay, H. R.; Branco, M. C.; Schneider, J. P.; Pochan, D. J., *Faraday Discuss.* **2008,** *139*, 251-264.
47. Iannuzzi, M. A.; Reber Iii, R.; Lentz, D. M.; Zhao, J.; Ma, L.; Hedden, R. C., *Polymer* **2010,** *51* (9), 2049-2056.
48. Schexnailder, P.; Loizou, E.; Porcar, L.; Butler, P.; Schmidt, G., *Phys. Chem. Chem. Phys.* **2009,** *11* (15), 2760-2766.

Chapter 8: Chondrocyte response to regenerated silk fibroin-based hybrid hydrogels

This chapter of the thesis is presented as a research article "Jasmin L. Whittaker, Andrew Zannettino, Naba K. Dutta and Namita R. Choudhury. Chondrocyte response to regenerated silk fibroin-based hybrid hydrogels" to be submitted for peer review publication.



8.1 Abstract

This study demonstrates the potential of engineered regenerated silk fibroin (RSF)-based hybrid hydrogels to provide a biomimetic environment for cell growth. An *in vitro* study to investigate the adhesion, proliferation and differentiation of a mouse pre-chondrocyte cell line (ATDC5) was conducted using microscopic analysis, a cell proliferation assay and real-time polymerase chain reaction (RT-PCR). The RSF-based hydrogels were shown in previous work to possess tuneable mechanical and swelling characteristics and these were observed to effect the proliferation and differentiation of the ATDC5 cell in this study. In particular, the cells cultured on the less stiff hydrogels demonstrated the most favourable chondrogenic response. Thus, this study demonstrates the potential of RSF-based hybrid hydrogels for cartilage tissue engineering applications.

8.2 Introduction

Adult cartilage has a limited self-repair capacity in response to age-related degeneration and trauma. As such, there is a need to develop biomaterials for cartilage tissue engineering, as current treatments do not adequately restore normal physiological function.[1-3] Scaffolds for cartilage regeneration must have the ability to stimulate chondrogenic cell growth, differentiation, and cartilage-specific extracellular matrix (ECM) synthesis and deposition.[2] In addition, articular cartilage tissue has a modulus of ~180 to 2500 kPa, a feature that must be considered when designing biomaterials for this application.[4-6] Previous reports suggest that a multitude of factors, including the rigidity and surface chemistry properties of biomaterials can significantly affect chondrocyte (cartilage cell) adhesion and differentiation.[7] On attachment to a substrate, cells are known to exert contractile forces that lead to tensile stresses in the cytoskeleton.[8] The correlation between these forces and the stiffness of the substrate is known to affect cell differentiation.[8] As a result, scaffold stiffness has been shown to control chondrogenic differentiation.[9-11] In addition, the hydrophobicity of biomaterials can affect chondrocyte cell attachment, cell shape and cartilage-related gene expression.[7] Figure 8.1 summarises some of the contributing factors that determine the cell-biomaterial interaction and must be considered when designing scaffolds for tissue engineering applications. Thus, development of biomaterials that meet and match the structural and functional criteria for cartilage regeneration whilst also inducing the desired cellular response, remains a significant challenge.

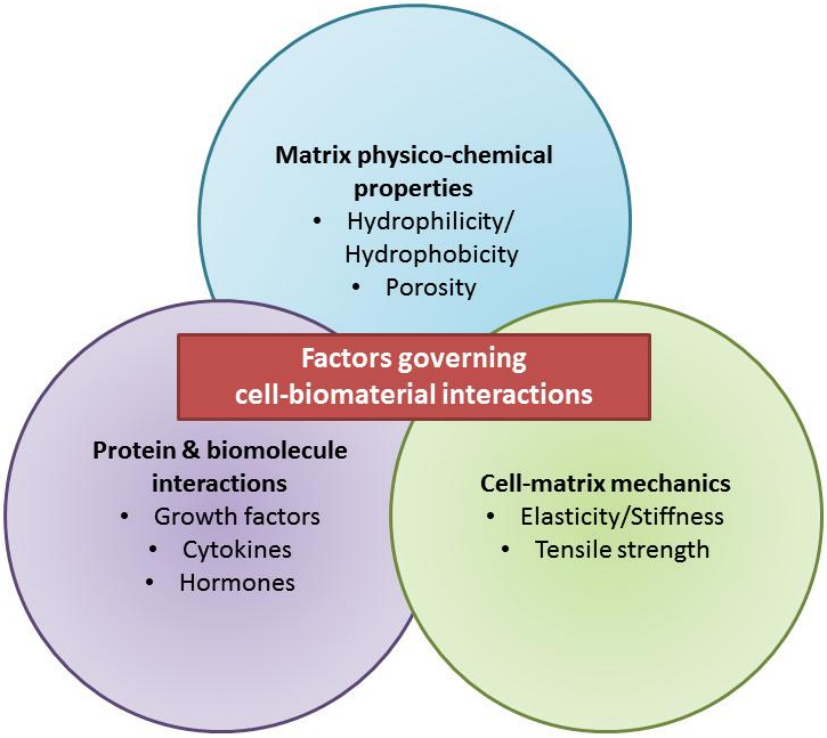


Figure 8.1 Summary of factors that govern cell-biomaterial interactions.

We have previously described the fabrication of a photo-crosslinked regenerated silk fibroin (RSF) hydrogel.[12] In these studies, this RSF material was found to possess a modulus of ~80 MPa. However, the stiffness and hydrophobicity of the RSF hydrogel limits its use as a biomaterial for cartilage tissue engineering applications, as articular cartilage has a modulus of ~180 to 2500 kPa.[4-6] To overcome these deficiencies, two unique types of hybrid hydrogels were fabricated by combining the rigid phase of RSF with softer, more hydrophilic materials. The recombinant protein, Rec1-resilin, was co-crosslinked in solution with RSF to form a hydrogel with tuneable modulus values and improved water absorption capacity.[13] A series of double network (DN) hydrogels were fabricated containing a highly rigid crosslinked RSF phase interpenetrated with a softer biocompatible stimuli-responsive polymer (poly(N-vinylcaprolactam) (PVCL)) network that was entrapped with weak phase interactions (Chapter 5). Notably, the RSF/PVCL hydrogels exhibited tuneable modulus values and an increased capacity to absorb water in response to increasing PVCL content.

In line with their modulus values, the suitability of the RSF-based hydrogels (RSF, Rec1-resilin/RSF and RSF/PVCL) for application in cartilage regeneration was evaluated. Earlier studies have shown that RSF-based scaffolds support the growth and differentiation of

chondrocytes.[1, 3] However, an understanding of how the modulus of RSF-based materials regulates the chondrogenic phenotype and chondrogenesis is lacking. Also, despite being identified as a biocompatible polymer, there are limited studies examining the growth of cells on PVCL-based scaffolds for tissue engineering. One study showed that PVCL cryogels supported fibroblast cell attachment.[14] However, there is poor understanding of how the physical and chemical properties of materials regulate the differentiation and biological response of cells. Therefore, in this work, we created a range of RSF–based hybrid hydrogels (Rec1-resilin/RSF and RSF/PVCL) with the aim of obtaining a deeper understanding of the cell responses to hydrogels of different stiffness and swelling capacity. It was hypothesized that by tuning the hydrogel modulus to values closer to that of articular cartilage, the chondrogenic differentiation of chondrocytes would be improved.

The effect of RSF-based hydrogels containing a recombinant protein (Rec1-resilin) and a synthetic polymer (PVCL) were compared for their ability to create a microenvironment for tissue regeneration. More specifically the chondrocyte response to matrix modulus was investigated. Until now, the 3D culture of chondrocytes alone, is insufficient to promote the differentiation of chondrocytes and it requires a defined culture medium with bioactive growth factors, such as transforming growth factor beta 1 (TGF-β1). Thus, in this work the ability of the RSF-based hydrogels (RSF, Rec1-resilin/RSF and RSF/PVCL) to support the initial attachment, proliferation and differentiation of a mouse pre-chondrocyte cell line (ATDC5) was examined using scanning electron microscopy (SEM), the WST-1 proliferation assay and real-time polymerase chain reaction (RT-PCR) for cartilage-specific gene markers, respectively. The differentiation studies were undertaken using a defined medium containing the growth factor TGF-β1.

8.3 Experimental

8.3.1 Assessment of ATDC5 cell adhesion and proliferation

The ability of the RSF, Rec1-resilin/RSF and RSF/PVCL hydrogels to support adhesion and proliferation of ATDC5 pre-chondrocyte cells (Riken laboratories, Japan) was examined using SEM.[15, 16] The dried hydrogel samples (6 x 6 mm) were sterilized in 70% ethanol for 2 hours followed by overnight drying. Following this, the gels were immersed in sterile phosphate buffered saline (PBS) and rehydrated until equilibrium swelling was reached. The sterilized, swollen gels were transferred to individual wells of a 48 well plate (Corning, USA) in preparation for cell culture. The ATDC5 cell line was culture expanded in Alpha Modified Minimum Eagle Medium (α-MEM) supplemented with 10% fetal calf serum (FCS) as

previously described.[17] Prior to seeding the cells onto the hydrogels and tissue culture polystyrene (TCP), the cells were detached with 0.05% trypsin, enumerated using a hemocytometer and the cell concentration adjusted to 14.4 x 10^4 cells/mL. A 20 μL droplet of the cell suspension was placed in the centre of each hydrogel/TCP control and allowed to adhere for 30 mins. Thus, the concentration of cells was 8 x 10^3 cells/cm^2. Following this, the wells were topped up with 300 μL of media. The cells were cultured for 2 and 4 days and then fixed with a biological fixation agent (glutaraldehyde/paraformaldehyde) for 30 minutes, washed with PBS for 5 minutes and post-fixed with 2% osmium tetroxide for 30 minutes. The hydrogel/ATDC5 cell constructs were serially dehydrated with 70%, 90% and 100% ethanol for 10 minutes each cycle and followed by rinsing with hexamethyldisilazane (HMZ) diluted with an equal volume of ethanol for 10 minutes, then undiluted HMZ for 10 mins and left to dry overnight. The hydrogel/ATDC5 cell constructs were sputter coated with platinum and samples analyzed using a SEM (Philips XL30 FEGSEM) at an accelerating voltage of 10 kV as previously described.[18]

ATDC5 cells proliferation on the RSF, RSF/PVCL hydrogels and TCP surfaces was quantified using the WST-1 assay. ATDC5 cells were seeded at a density of 8.3 x 10^3 cells/cm^2 by adding a 20 μL droplet of the cell suspension onto the sample surfaces and topping up with media, as described above. After 1 and 7 days of culture, the relative amount of viable, metabolically active ATDC5 cells on each surface was quantified with the WST-1 assay using an established protocol.[19] Triplicate experiments were performed for each sample type.

8.3.2 Total RNA extraction, cDNA synthesis, and real-time PCR (RT-PCR) analysis

ATDC5 cells were seeded at 15 x 10^4 cells/mL (8.3 x 10^3 cells/cm^2) by adding a 20 μL droplet of the cell suspension on the hydrogels and topping up with media as described above. Samples were incubated under chondrogenic culture conditions in α-MEM supplemented with 10% FCS and TGF-β1 (10 ng/mL). The media was changed twice weekly and after 1, 7 and 14 days, the media was removed from the wells, and the cell/hydrogel constructs were rinsed with PBS and then transferred to new wells prior to the addition of TRIzol reagent for 5 minutes. The TRIzol solubilized cellular extracts were transferred to a fresh tube prior to the addition of 200 μL chloroform. Samples were vortexed briefly for 15 seconds and subsequently incubated for 2-3 minutes at room temperature. The tubes were centrifuged at 12,000 x g for 15 minutes at 4˚C and the aqueous layer was extracted and

transferred to a new tube. 1 μL of RNase free glycogen (20 mg/mL) was added to the tube, followed by the addition of 150 μL of isopropanol. The tube was gently mixed and incubated at room temperature for 10 minutes. The RNA precipitate was pelleted by centrifugation at 12,000 x g for 10 minutes at 4˚C. The supernatant was removed and the pellet washed in 75% ethanol followed by centrifuging at 7,500 x g for 5 minutes at 4˚C. The supernatant was removed and the tube spun again, followed by removal of any residual ethanol. The air-dried RNA pellet was dissolved in 20 μL RNase free water at 55˚C for 10 minutes, and the RNA concentration was quantified using the Nanodrop spectrophotometer.

Complementary DNA (cDNA) was synthesized from 1500 ng of the RNA for each sample using a Superscript III kit. The RT-PCR reactions were conducted with the Bio-Rad CFX Connect Real-Time PCR machine and monitored using the SYBR Green PCR Mastermix. Transcript levels of cartilage-related genes, Collagen type I (Col I), Collagen type II (Col II), and Sox9 were analysed, with β-Actin as the reference gene. In addition, the expression of osteogenic markers, Runx2, osteonectin (Sparc), osteocalcin (Bglap), osterix (Sp7), integrin-binding saloprotein (Ibsp), osteopontin (Spp1), and alkaline phosphatase (Alpl) were analysed. The details of the PCR primers are listed in Table 8.1. Each PCR reaction was performed in a 15 μL reaction mixture containing 2 μL of cDNA, 7.5 μL of SYBR Green, 0.75 μL of primer pair, and 4.75 μL of nuclease free water. RT-PCR was performed according to the following conditions: 50˚C for 2 minutes and 95˚C for 15 minutes, followed by 39 cycles of 95˚C for 15 seconds, 55˚C for 25 seconds and 72˚C for 10 seconds. The samples were kept at 72˚C for 3 minutes and 65˚C for 15 seconds, followed by melt curve analysis (0.5˚C/second increase from 65 to 95˚C) at the end of the cycles to confirm that a single PCR product was obtained. The RT-PCR procedure was performed in the same manner for all genes of interest. For each gene, triplicate PCRs were conducted for each experimental sample. The C_t value for each gene marker was defined as the cycle number at which the fluorescence intensity reached a certain threshold where amplification of each target gene was within the linear region of the reaction amplification curves. The relative expression for each gene was normalized by the C_t value of the housekeeping gene (β-actin).

Table 8.1 Oligonucleotide sequences used for Real-time PCR

Gene	**Forward (5' – 3')**	**Reverse (5' – 3')**	**Mw (Da)**
β-actin	TTGCTGACACCATGCAGAAG	AAGGGTGTAAAACGCAGCTC	6126.1 /6175.1
Col I	AAAGGGTCCCTCTGGAGAAC	CACCTCTAGAGCCAGGGAGAC	6151.0 /6425.2
Col II	CGAGTGGAAGAGCGGAGACTAC	CCAGTTTTTCCGAGGGACAGT	6858.5 /6437.2
Sox9	ACGGCTCCAGCAAGAACAAG	TTGTGCAGATGCGGGTACTG	6129.0 /6204.1
Runx2	ATGATGACACTGCCACCTCTG	ATGAAATGCTTGGGAACTGC	6366.2 /6181.1
Sparc	ACTACATCGGACCATGCAAATAC	CGTACAAGGTGACCAGGACAT	6985.6 /6464.3
Bglap	AAGCAGGAGGGCAATAAGGT	TCAAGCCATACTGGTCTGATAGC	6264.2 /7023.7
Sp7	ATGGCGTCCTCTCTGCTTG	GTCCATTGGTGCTTGAGAAGG	5761.8 /6517.3
Ibsp	CAGTCCAGGGAGGCAGTG	GGAAAGTGTGGAGTTCTCTG	5589.7 /6228.1
Spp1	AGCAAGAAACTCTTCCAAGCAA	GATTCGTCAGATTCATCCGAGT	6705.4 /6725.4
Alpl	GCCTTACCAACTCTTTTGTGC	GGCTACATTGGTGTTGAGCTT	6323.2 /6483.3

8.3.3 Statistical analysis

All experiments were performed in triplicate and the results presented as mean ± standard deviation (SD). Data were analysed using a Two-way ANOVA with a Sidak's multiple comparisons test. A p-value less than 0.05 was considered statistically significant.

8.4 Results and Discussion

8.4.1 Physical properties of RSF-based hydrogels

Table 8.2 summarises the RSF-based hydrogel properties such as water uptake capacity, storage modulus (E') and crosslink density (n). The sample identification is presented in Table 8.2 and shows the composition of the different types of RSF-based hydrogels. Hydrogels with appropriate stiffness/elasticity and hydrophobicity/hydrophilicity can be used effectively to control cell-biomaterial interactions, to mimic the environment of the natural ECM and stimulate matrix production by cells due to their hydrated mechanically supportive 3D structure.[20, 21] Chondrocyte cells are known to be highly sensitive to changes in the matrix mechanical properties, which affect their survival, adhesion, growth and differentiation.[22, 23] In light of this, the viability of the cells cultured on the RSF-based hydrogels was investigated. Furthermore, the results were correlated with the material properties to obtain a fundamental understanding of the response of chondrocytes to RSF-based materials with different modulus.

Table 8.2 Summary of composition and properties of RSF-based hydrogels

Sample Identification S=RSF, P=PVCL	Volume fraction RSF 15wt%	Volume fraction Rec1-resilin 20wt%	Volume fraction PVCL 5wt%	Equilibrium water uptake (g water/g dried gel)	E' (equilibrium swollen) (MPa)	n (mol/m^3)
RSF	1	-	-	0.59 (±0.05)	78.05 (±15.91)	9545.6 (±3097.6)
Rec1-resilin/RSF	0.5	0.5	-	0.85 (±0.02)	6.56 (±1.35)	840.8 (±240.8)
$S_{80}P_{20}$	0.8	-	0.2	0.62 (±0.03)	22.82 (±9.76)	3070.2 (±1312.9)
$S_{70}P_{30}$	0.7	-	0.3	0.97 (±0.05)	21.11 (±0.80)	2839.5 (±107.5)
$S_{60}P_{40}$	0.6	-	0.4	0.97 (±0.06)	0.58 (±0.28)	77.8 (±37.3)

8.4.2 Comparison of growth of ATDC5 cells on RSF hydrogels and TCP

Owing to their high modulus, RSF hydrogels are likely to be the most suitable materials for cartilage tissue engineering applications. In view of this, RSF hydrogels were assessed for their ability to support the adhesion and growth of the pre-chondrocyte cell line, ATDC5 *in vitro.* In all cases, tissue culture plastic (TCP) was used as a control. To assess adhesion and

proliferation, 8 x 10^3 cells/cm^2 ATDC5 cells were seeded onto the RSF hydrogels and TCP control surfaces. Figures 8.2A and B show the SEM micrographs of the ATDC5 cells fixed at days 2 and 4 on the RSF hydrogels and TCP control, respectively. It is evident from the SEM images that the ATDC5 cells adopt an adherent and elongated stellate morphology on both RSF and TCP surfaces. Notably, on both the RSF hydrogel and TCP surfaces, an increase in cell number was evident on day 4 when compared with the number of cells at days 2, indicating that the cells had proliferated on both surfaces.

In order to quantitatively measure the proliferation of the ATDC5 cells on the RSF hydrogels compared to the TCP control, the tetrazolium salt, WST-1 [2-(4-iodophenyl)-3-(4-nitrophenyl)-5-(2,4-disulfophenyl)-2H-tetrazolium] assay was employed. ATDC5 cells were seeded at a density of 8.3 x 10^3 cells/cm^2 and the proliferation measured on days 1 and 7. Figures 8.2C and D summarise the results of the WST-1 assay for the proliferation of ATDC5 cells on the RSF hydrogels and TCP for 1 and 7 days. The data is presented as the absorbance signal obtained from ATDC5 cells on the RSF surfaces as a percentage of the TCP. As seen in Figures 8.2C and D, the ATDC5 cells remained viable throughout the culture period and expanded in cell number from days 1 to 7 on both the RSF and TCP, in accord with the SEM images (Figures 8.2A and B). The increased proliferation of RSF compared to TCP from ~27% (day 1) to ~68% (day 7) suggests that the initial attachment of the cells was lower on the RSF; however the RSF supported cell growth over a period of time. Similarly, Wang et al. reported that adult human chondrocytes attached more slowly to RSF films than TCP, however the cell number expanded on the RSF films over time.[1] Thus, it is evident that the RSF hydrogels are non-toxic *in vitro* and have the capacity to support cell adhesion and proliferation of a pre-chondrocyte cell line.

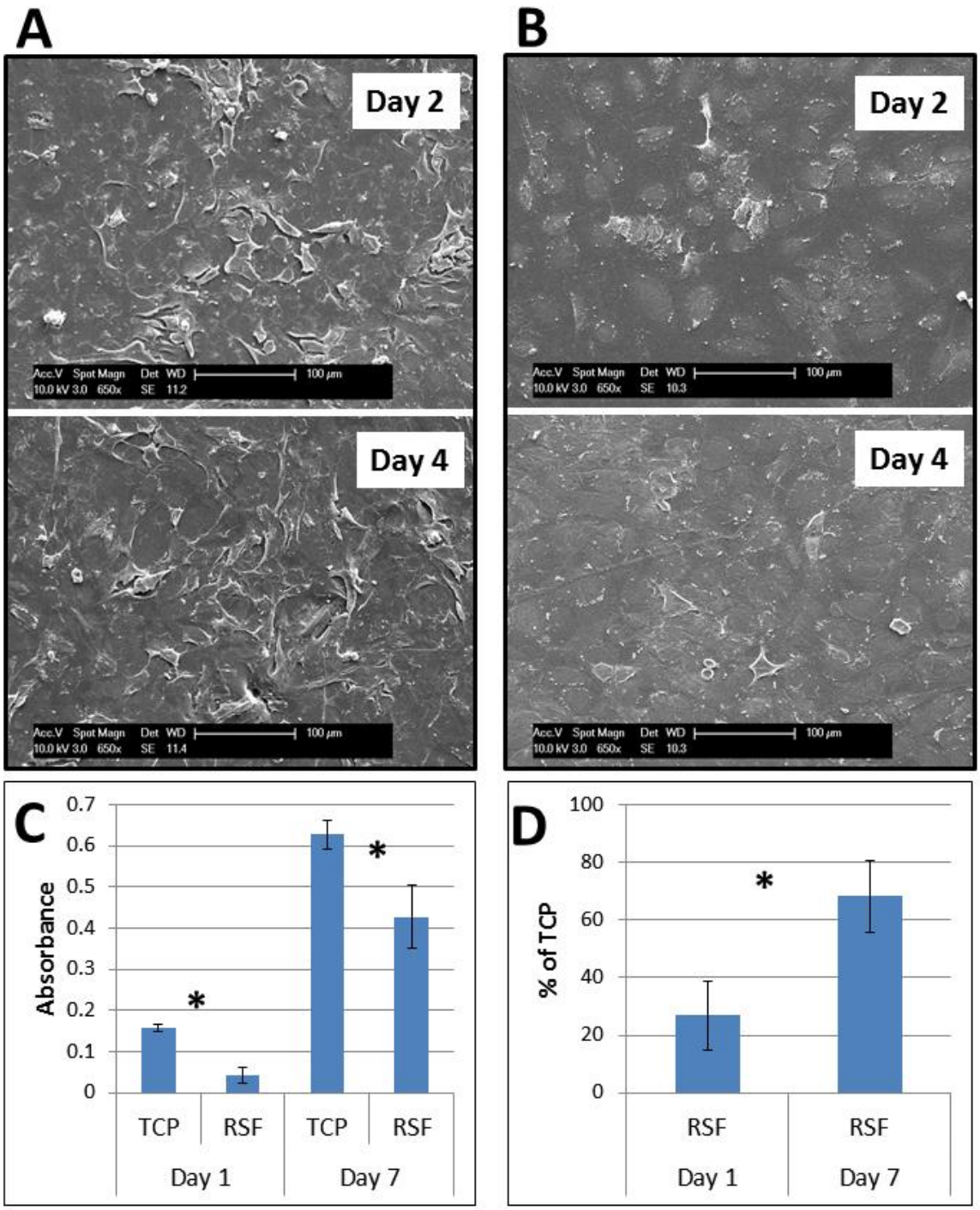


Figure 8.2 SEM micrographs of growth of ATDC5 cells after 2 and 4 days of culture on A) RSF hydrogel and B) TCP. WST-1 proliferation assay results for ATDC5 growth for 1 and 7 days on C) RSF and TCP reported as absorbance and D) on RSF relative to TCP. * Represents groups that are statistically different ($p<0.05$).

8.4.3 Gene analysis for chondrogenic and osteogenic markers on RSF hydrogels and TCP

Following the examination of the initial attachment and proliferation, the potential of the RSF hydrogel for use in cartilage tissue engineering was evaluated by examining the chondrogenic differentiation of the ATDC5 cells when cultured for 1, 7 and 14 days on the RSF samples and TCP surfaces. The ATDC5 cells were seeded at a density of 8.3 x 10^3 cells/cm^2 and supplemented with media containing the cartilage-inducing growth factor TGF-β1 (10 ng/mL).[1, 2, 24] TGF-β1 has been reported to accelerate chondrogenic differentiation at the early stages of culture.[25] The RNA was extracted from the cells at 1, 7 and 14 days, followed by cDNA synthesis. The expression of cartilage-related genes (Col I, Col II and Sox9) was quantified by performing real-time PCR. For all samples, β-actin was employed as the housekeeping gene. Figure 8.3 summarises the relative expression levels of the cartilage-related genes at 1, 7 and 14 days of culture on the RSF hydrogel and TCP surfaces. The expression levels of Col I, Col II and Sox9 in ATDC5 cells cultured on RSF were comparable to the TCP surfaces. Two-way ANOVA analysis with Sidak's multiple comparison test confirmed that there was no statistical difference between the expression of Col I, Col II and Sox9 on RSF and TCP at days 1, 7 and 14. These findings support the fact that the RSF hydrogels could potentially be used in cartilage tissue engineering applications. However, in order to improve the differentiation of chondrocytes in the presence of RSF hydrogels, it may be necessary to tune the stiffness and surface characteristics of the hydrogel as these have been shown to be integral for chondrogenic differentiation.[7] In addition, increasing the pore size and level of porosity of the hydrogels has also been shown to significantly improve the expression of Col II in RSF-based materials.[1, 3] However, the level of porosity has been shown to be related to the water uptake behaviour and mechanical strength of the hydrogel and thus the right balance of properties should be maintained.

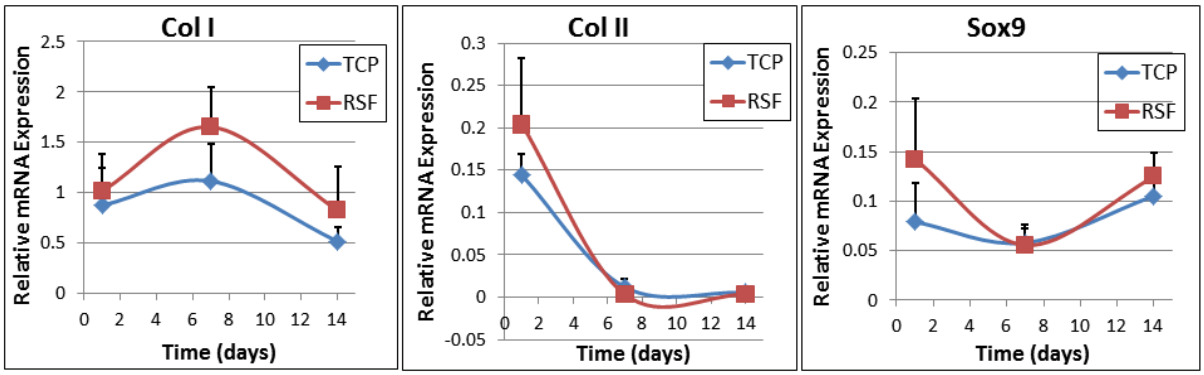


Figure 8.3 Real-time PCR analysis of cartilage-related gene expression by ATDC5 cells on RSF and control TCP after 1, 7 and 14 days of culture with induction media. Data is presented as mean + standard deviation.

In order to confirm that the RSF hydrogels could be used for cartilage tissue engineering applications, the osteogenic potential of the ATDC5 cells when cultured on the hydrogels was evaluated using RT-PCR to ensure there was no tendency for osteogenic differentiation. As with the chondrogenic study, the ATDC5 cells were cultured with inductive media and the RNA was extracted at days 1, 7 and 14, followed by cDNA synthesis and RT-PCR. The osteogenic markers investigated included Runx2, osteonectin (Sparc), osteocalcin (Bglap), osterix (Sp7), integrin-binding saloprotein (Ibsp), osteopontin (Spp1), and alkaline phosphatase (Alpl). Figure 8.4 depicts the relative expression of the osteogenic markers for the ATDC5 cells grown on the RSF hydrogels and TCP at 1, 7 and 14 days. It was observed that there were no statistical differences in the expression of Runx2, Sp7, Ibsp and Spp1 for the cells cultured on RSF and TCP as confirmed by two-way ANOVA analysis with Sidak's multiple comparisons test. The cells cultured on TCP exhibited significantly higher expression of Sparc at day 1 (~2.5) relative to β-actin, compared to RSF (~0.9). Also, the expression of Bglap after 14 days of culture was significantly higher on TCP (~0.005) relative to β-actin, compared to RSF (~0.002). In addition, expression of Alpl was statistically higher for the cells cultured for 1 and 7 days on RSF compared to TCP. These results further support the proposed use of the RSF hydrogels for cartilage tissue regeneration applications. As discussed above, there is further scope to tune the hydrogel properties in order to stimulate a more favourable cellular response for cartilage regeneration applications.

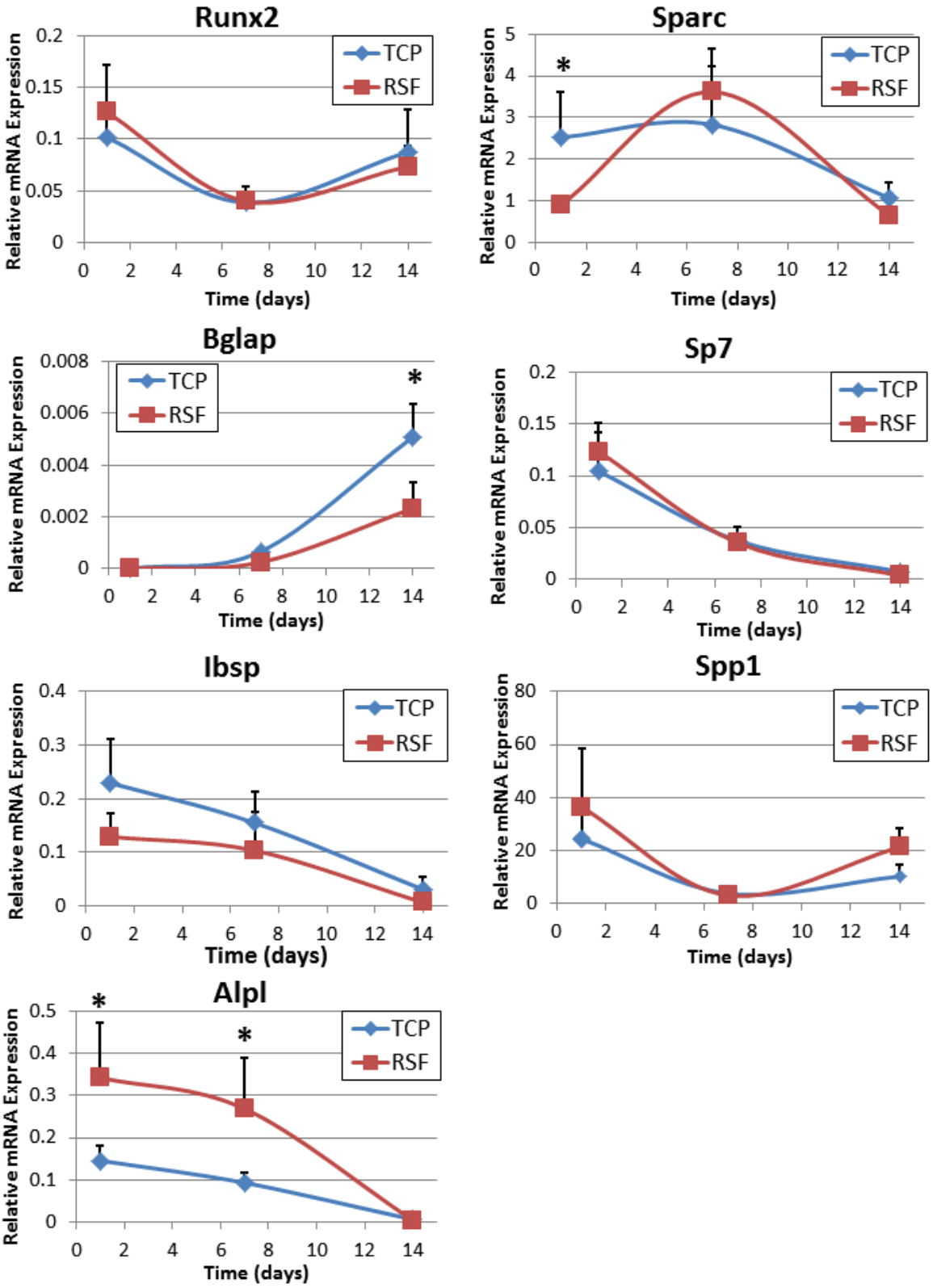


Figure 8.4 Real-time PCR analysis of osteogenic-related gene expression by ATDC5 cells on RSF and control TCP after 1, 7 and 14 days of culture with induction media. * Represents groups that are statistically different ($p<0.05$).

8.4.4 ATDC5 cell growth on Rec1-resilin/RSF hybrid hydrogels

In our previous work, it has been shown that the RSF hydrogel properties may be tuned by combining the rigid phase of RSF with the soft thermo-responsive protein (Rec1-resilin) and the soft thermo-responsive polymer (PVCL) (Chapter 5).[13] The modulus values of both the Rec1-resilin/RSF and RSF/PVCL hydrogels are closer to that of cartilage[4-6], suggesting that they may be more suitable for cartilage regeneration applications.

SEM was used to assess the ability of the Rec1-resilin/RSF hydrogel to support ATDC5 cell growth and proliferation. As with the RSF hydrogels, the cells were seeded at a density of 8 x 10^3 cells/cm^2, fixed after 2 and 4 days of culture and analysed with SEM. Figures 8.5A and B depict the morphological characteristics of the ATDC5 cells cultured on the Rec1-resilin/RSF hydrogels for 2 and 4 days, respectively. It was evident from the SEM images that the cells exhibited an adherent and elongated stellate morphology on the Rec1-resilin/RSF hydrogels at 2 and 4 days of culture. In comparison with the RSF hydrogel, it was clear that the number of cells on the Rec1-resilin/RSF hydrogels was somewhat less than RSF.

To quantify the differences in adhesion and growth on the RSF and Rec1-resilin/RSF hydrogels, the number of cells on each hydrogel was determined by direct cell counting of the SEM images using the ImageJ software. Average cell numbers were obtained from at least 3 images for each gel and time point. Figure 8.5C summarises the cell count per square cm for the RSF and Rec1-resilin/RSF gels at days 2 and 4. Statistical analysis showed that there was a significant difference between the cell numbers on the RSF and Rec1-resilin/RSF hydrogels at days 2 and 4. In particular, the number of cells on the RSF and Rec1-resilin/RSF hydrogels at day 2 was ~46,000 and ~26,000 cells/cm^2, respectively. In addition, both RSF and Rec1-resilin/RSF showed increased cell numbers at day 4 of ~51,000 and ~33,000 cells/cm^2, respectively.

On the contrary, the attachment of human chondrocytes to photo-crosslinked Rec1-resilin was investigated by Elvin et al. and it was observed that Rec1-resilin did not support cell attachment or proliferation.[26] However, it was concluded that all of the components involved in the crosslinking reaction (Rec1-resilin, tris(2,2-bipyridyl)dichlororuthenium(II) and ammonium peroxodisulfate) were not cytotoxic to cells.[26] In addition, Vashi et al. reported the attachment of Rec1-resilin to TCP surfaces by the ruthenium-mediated photo-crosslinking of the tyrosine residues present in Rec1-resilin to surface phenolic groups on the TCP.[27] They evaluated the capacity of the Rec1-resilin modified surfaces to support fibroblast cell

attachment and observed that cells did not attach; however the cross-linked Rec1-resilin surfaces were not cytotoxic to cells as the cell viability was maintained at approximately 98%.[27] In addition, it was observed that cell adhesion could be restored by co-crosslinking Rec1-resilin with a cell-binding peptide containing the RGD sequence.[27] Another study by Renner et al. reported that resilin-like peptides (RLPs), containing the RGD cell-binding sequence, formed hydrogels when cross-linked and had the ability to support mesenchymal stem cell (MSC) adhesion and growth and proposed that these materials could be employed for cartilage regeneration.[28] Despite the lower proportion of attachment compared to the RSF hydrogels, the Rec1-resilin/RSF hydrogels were found to be not cytotoxic to the ATDC5 cells *in vitro* and supported cell attachment and growth over time. Notably, unlike the Rec1-resilin-modified TCP reported by Vashi et al. and RLP hydrogels by Renner et al., the co-crosslinking of RSF with Rec1-resilin in the Rec1-resilin/RSF hydrogels allowed cells to attach and grow without the need for additional cell-binding domains.

In addition, these findings suggest that the differences in hydrophobicity, water absorption capacity and modulus between the RSF and Rec1-resilin/RSF hydrogels contributed to an altered cellular response. The Rec1-resilin/RSF hydrogel exhibited a higher water uptake capacity (~0.85 g water/g dried gel) compared to RSF (~0.59). Vashi et al. suggested that the low contact angle of the Rec1-resilin surfaces (27°) contributed to the lack of cell binding as cells have been shown to attach best to surfaces with contact angles ranging from 50° and 70°.[27] Thus, the increased hydrophilicity of the Rec1-resilin/RSF hydrogels contributed to a lower level of cell attachment. However, compared to cross-linked Rec1-resilin, which demonstrated no cell attachment, there was a significant improvement in the attachment of cells on the Rec1-resilin/RSF hydrogels. In addition, the Rec1-resilin/RSF hydrogel was less stiff than the RSF hydrogel, as the storage modulus was ~6.6 MPa compared to 78 MPa, for RSF. Notably, Schuh et al. observed an increase in proliferation of chondrocytes on stiffer (~100 kPa) polyacrylamide gel surfaces compared to less stiff surfaces (~4 kPa).[10] However, Chao et al. observed that the greatest amount of cell proliferation on RSF-based hydrogels did not correspond with glycosaminoglycan (GAG) synthesis, a biosynthetic marker of chondrocyte differentiation.[29] Further study of the differentiation response of the ATDC5 cells grown on the Rec1-resilin/RSF hydrogels is required to confirm their suitability for cartilage regeneration and is the subject of future studies. Despite this, these studies demonstrate that the Rec1-resilin/RSF hydrogels are promising materials for tissue engineering applications.

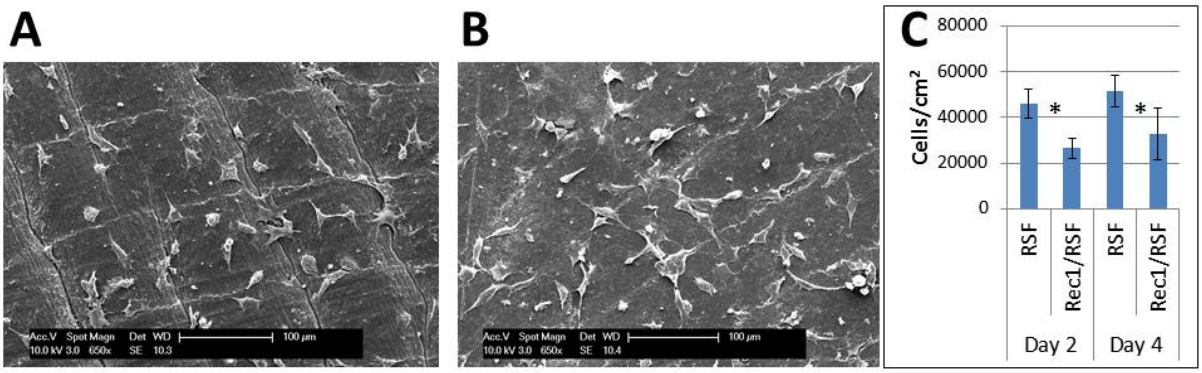


Figure 8.5 SEM micrographs of growth of ATDC5 cells on Rec1-resilin/RSF hydrogels at A) 2 days and B) 4 days of culture. C) ATDC5 proliferation on RSF and Rec1-resilin/RSF hydrogels determined from cell counting of SEM images. * Represents groups that are statistically different ($p<0.05$).

8.4.5 ATDC5 cell growth on RSF/PVCL DN hydrogels

The growth of ATDC5 cells seeded at 8 x 10^3 cells/cm^2 on the RSF/PVCL hydrogels ($S_{80}P_{20}$, $S_{70}P_{30}$ and $S_{60}P_{40}$) was assessed after 2 days of culture using SEM (Figures 8.6A-C). It was observed that all three types of RSF/PVCL hydrogels supported the growth of ATDC5 cells as the SEM images clearly demonstrated an adherent and elongated stellate morphology on samples. However, in comparison with the RSF hydrogel it was clear that the cell number on the RSF/PVCL hydrogels was somewhat less.

The WST-1 assay was employed to quantitatively assess the proliferation of the ATDC5 cells (8.3 x 10^3 cells/cm^2) on the RSF and RSF/PVCL hydrogels after 1 and 7 days of culture. Figures 8.6D and E summarise the results of the WST-1 assay for the proliferation of ATDC5 cells on the RSF and RSF/PVCL hydrogels for 1 and 7 days. The data is presented as the absorbance signal obtained from ATDC5 cells on the hydrogel surfaces as a percentage of TCP. As seen in Figures 5D and E, the ATDC5 cells remained viable throughout the culture period and expanded in cell number over time on all hydrogel samples. However, there were clear differences in the attachment and proliferation between the RSF and RSF/PVCL hydrogel samples of different composition at both time points. At day 1, there was a statistically significant increase in the level of adhesion on the RSF hydrogel (~27%) compared to the $S_{80}P_{20}$ (~7%) and $S_{60}P_{40}$ (~7%) hydrogels. However, the growth on RSF and $S_{70}P_{30}$ hydrogels was comparable. As seen in Figures 8.5D and E, the greatest level of proliferation after 7 days of culture was observed for the RSF (~68%) and $S_{70}P_{30}$ (~63%)

samples. Statistically significant differences between the levels of proliferation for the different gel types are shown in Figure 8.6E. There was no significant difference between the proliferation of the RSF (~68%) and $S_{70}P_{30}$ (~63%) at both time points; however both showed a significant increase compared to $S_{80}P_{20}$ (~16%) and $S_{60}P_{40}$ (28%). These results demonstrate that all of the RSF/PVCL hydrogels were non-toxic *in vitro* and displayed the capacity to support cellular growth and proliferation over time. However, for the RSF/PVCL gels, the $S_{70}P_{30}$ composition stimulated greater proliferation of the ATDC5 cells.

Wang et al. investigated a series of gelatin-hydroxyphenylpropionic acid (Gtn-HPA) hydrogels with tuneable stiffness. Using a rabbit chondrocyte cell line, they found that the greatest proliferation was achieved on hydrogels with an intermediate modulus value (~1000 Pa).[9] In addition, Schuh et al. observed an increase in proliferation of chondrocytes on stiffer (100 kPa) polyacrylamide gel surfaces.[10] Thus, it is evident that the stiffness and surface properties of the RSF and RSF/PVCL hydrogels affect the proliferation of the ATDC5 cell line. The results suggest that compared to the other RSF/PVCL hydrogels, the $S_{70}P_{30}$ hydrogel that demonstrates an intermediate modulus (~21 MPa) and a water uptake capacity of ~0.97 g water/g dried gel is the most suitable matrix for encouraging chondrocyte proliferation.

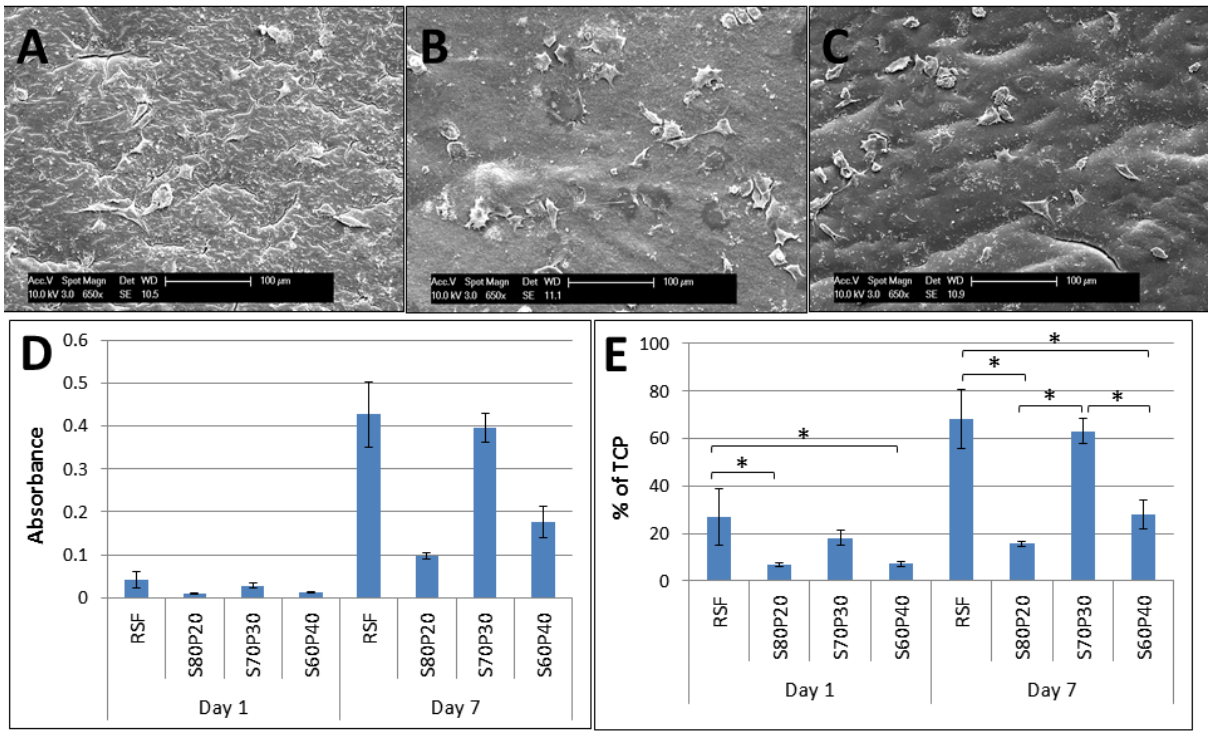


Figure 8.6 SEM micrographs of growth of ATDC5 cells after 2 days of culture on RSF/PVCL hydrogels: A) $S_{80}P_{20}$, B) $S_{70}P_{30}$ and C) $S_{60}P_{40}$. WST-1 proliferation assay results for ATDC5 growth for 1 and 7 days on C) RSF and TCP reported as absorbance and D) on RSF relative to TCP. * Represents groups that are statistically different ($p<0.05$).

8.4.6 Analysis of chondrogenic markers on RSF-based hybrid hydrogels

The ability of the RSF and RSF/PVCL hydrogels to support chondrogenesis was evaluated by analyzing the relative expression of cartilage-related genes (Col I, Col II and Sox9) using real-time PCR (Figure 8.7). One-way ANOVA analysis with Sidak's multiple comparisons test was employed to determine the statistical differences between expression levels for cells cultured on the different hydrogel samples. There were no statistically significant differences in Col I expression of ATDC5 cells on the RSF and RSF/PVCL hydrogels after one day culture. However, there was a statistically significant increase in the expression of Col I on all RSF/PVCL samples compared to RSF at day 7. In addition, there was a significant difference between the expression of Col I on RSF (0.83) and S60P40 (3.01) at 14 days of culture. Initially, there was a significant increase in Col II expression on RSF (0.2) compared to $S_{80}P_{20}$ (0.04) and $S_{70}P_{30}$ (0.03). However, after 7 days of culture, the expression of Col II was significantly higher for $S_{80}P_{20}$ (0.18) than for RSF (0.003). There were no significant differences observed in Col II expression for all samples after 14 days of culture. Sox9

expression in ATDC5 cells cultured on $S_{60}P_{40}$ samples (0.19) was significantly higher than on $S_{80}P_{20}$ (0.06) and $S_{70}P_{30}$ (0.06) after 1 day of culture. However, there were no significant differences between expression levels of Sox9 at day 7. In addition, there was a significant increase in Sox9 expression for cells cultured on $S_{70}P_{30}$ (0.27) and $S_{60}P_{40}$ (0.27) for 14 days compared to RSF (0.12).

Therefore, it may be concluded that the RSF/PVCL hydrogels elicited some differences in the expression levels of Col II and Sox9, with an increase in Col II expression at 7 days culture on $S_{80}P_{20}$ and an increase in Sox9 on $S_{70}P_{30}$ and $S_{60}P_{40}$ at day 14 compared to the RSF hydrogel. It was observed that the expression of Col II was quite low compared to Col I for all samples, which indicates that further surface modification may be required to improve the differentiation of chondrocytes in the presence of the RSF/PVCL hydrogels.

Similarly, Wang et al. observed differences in chondrogenic differentiation on Gtn-HPA hydrogels of different stiffness.[9] The hydrogels with an intermediate storage modulus of ~1000 Pa were shown to maintain their chondrogenic phenotype better than the gels of lower and higher stiffness.[9] In addition, it has been shown that encapsulating the cells inside the hydrogels to create a three-dimensional environment resulted in an induction of the chondrogenic phenotype compared to monolayer culture.[30] In monolayer culture an increase in Col I expression was observed compared to three-dimensional culture.[30] Schuh et al. observed an increase in proliferation of chondrocytes on stiffer polyacrylamide gel surface; however an increase in Col II expression in the less stiff surfaces was observed.[10] Furthermore, as previously indicated, Chao et al. observed that the greatest amount of proliferation on RSF-based hydrogels did not correspond to the amount of GAG synthesis.[29] This is similar to our observations where the RSF/PVCL gels exhibited a more limited capacity to support cell proliferation, but stimulated an increase in Col II content with time.

It has also been reported that the scaffold swelling ratio and water uptake capacity has an influence on cartilage gene expression.[7] In particular, several studies have shown that increased swelling capacity of hydrogels, which is related to the material hydrophilicity and also hydrogel crosslink density, has been linked to an increase in chondrogenic differentiation.[31, 32] Therefore, it can be concluded that by tuning the stiffness and swelling capacity of the RSF hydrogels through formation of a hybrid system with PVCL, the adoption of the cartilage phenotype of the ATDC5 pre-chondrocyte cell line was improved. In particular, the softer RSF/PVCL hydrogels with moduli ranging from ~0.5 to 22 MPa

resulted in an increase in Col II and Sox9 expression, which suggests that less stiff RSF-based materials are more promising as scaffolds for cartilage regeneration.

The effect of growth factors on chondrogenic differentiation has been studied extensively. In particular, the use of growth factors of the TGF-β family, such as TGF-β1, as additives to the growth media have been employed by many studies to analyse the ability of different biomaterials to support chondrogenic differentiation.[1, 2, 24] Han et al. reported that TGF-β1 accelerated the early adoption of the chondrogenic phenotype for ATDC5 cells; however they observed that under prolonged culture, TGF-β1 did not stimulate further differentiation.[25] Similarly, for the RSF hydrogels and TCP employed in this study, it was observed that there were initially higher levels of Col II and Sox9 on day 1, which decreased over 7 and 14 days of culture. Kim et al. encapsulated MSCs into photo-polymerizable chitosan hydrogels that were functionalized with Col II and TGF-β1 and observed that the combination of Col II and TGF-β1 resulted in an increase in cartilage-specific markers compared to either alone.[33] Similarly, Boznakovski et al. observed that MSC chondrogenic differentiation was enhanced in alginate, Col I and Col II hydrogels supplemented with TGF-β1 in the culture media.[34] However, this group observed a greater increase in the production of cartilage related genes when TGF-β1 was employed for hydrogels composed of Col II.[34] Thus, the chondrogenic differentiation of ATDC5 cells cultured on the RSF hydrogels could be further improved by incorporating other additives, such as Col II. Comparatively, the RSF/PVCL hydrogels demonstrated an increased expression of Col II and Sox9 over time, which indicates that in addition to the effect of TGF-β1, the hydrogel properties also play a role in dictating the chondrogenic differentiation of the ATDC5 cells. Specifically, the lower stiffness and increased water absorption capacity of these hydrogels stimulated increased Col II and Sox9 expression in ATDC5 cells. The present studies serve as a basis for further work to study the RSF-based hydrogels for cartilage regeneration applications. Formation of hydrogels embedded with cells may allow for improved chondrogenic properties as a three-dimensional environment has been shown to be more favourable for cartilage tissue engineering applications.[1, 3]

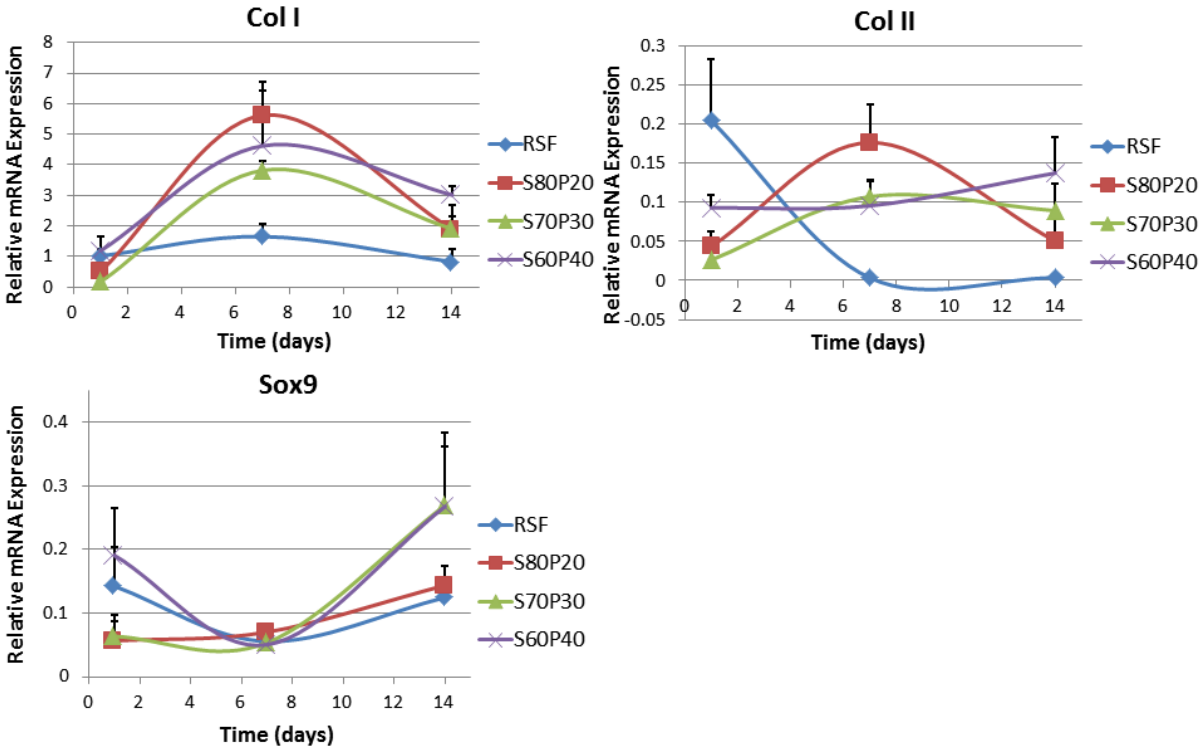


Figure 8.7 Real-time PCR analysis of cartilage-related gene expression by ATDC5 cells on RSF and RSF/PVCL after 1, 7 and 14 days of culture with induction media.

8.5 Conclusions

The current study demonstrates that the RSF and hybrid Rec1-resilin/RSF and RSF/PVCL hydrogels have the capacity to support the adhesion and proliferation of a pre-chondrocyte cell line (ATDC5). Furthermore, tuning the stiffness and water uptake capacity of the hydrogels altered the hydrogels capacity to support cellular proliferation. Notably, the less rigid RSF/PVCL hydrogels exhibited the most favourable chondrogenic differentiation properties. However, there is scope to further modify the surfaces to stimulate greater levels of Col II and Sox9 expression by the chondrocytes cultured on these hydrogels. This study shows, for the first time, the potential of RSF-based hybrid hydrogels, containing a recombinant protein (Rec1-resilin) and a synthetic polymer (PVCL), to be used in cartilage tissue regeneration.

8.6 References

1. Wang, Y.; Blasioli, D. J.; Kim, H.-J.; Kim, H. S.; Kaplan, D. L., *Biomaterials* **2006,** *27* (25), 4434-4442.
2. Seda Tığlı, R.; Ghosh, S.; Laha, M. M.; Shevde, N. K.; Daheron, L.; Gimble, J.; Gümüşderelioğlu, M.; Kaplan, D. L., *J. Tissue Eng. Regener. Med.* **2009,** *3* (5), 348-360.
3. Wang, Y.; Kim, U.-J.; Blasioli, D. J.; Kim, H.-J.; Kaplan, D. L., *Biomaterials* **2005,** *26* (34), 7082-7094.
4. Armstrong, C. G.; Mow, V. C., *J. Bone and Jt. Surg.* **1982,** *64* (1), 88-94.
5. Setton, L. A.; Mow, V. C.; Howell, D. S., *J. Orthop. Res.* **1995,** *13* (4), 473-482.
6. Zhu, W.; Mow, V. C.; Koob, T. J.; Eyre, D. R., *J. Orthop. Res.* **1993,** *11* (6), 771-781.
7. Kwon, H.; Sun, L.; Cairns, D. M.; Rainbow, R. S.; Preda, R. C.; Kaplan, D. L.; Zeng, L., *Acta Biomater.* **2013,** *9* (5), 6563-6575.
8. Guilak, F.; Cohen, D. M.; Estes, B. T.; Gimble, J. M.; Liedtke, W.; Chen, C. S., *Cell Stem Cell* **2009,** *5* (1), 17-26.
9. Wang, L.-S.; Du, C.; Toh, W. S.; Wan, A. C. A.; Gao, S. J.; Kurisawa, M., *Biomaterials* **2014,** *35* (7), 2207-2217.
10. Schuh, E.; Kramer, J.; Rohwedel, J.; Notbohm, H.; Mueller, R.; Gutsmann, T.; Rotter, N., *Tissue Eng., Part A* **2010,** *16* (4), 1281-1290.
11. Subramanian, A.; Lin, H.-Y., *J. Biomed. Mater. Res., Part A* **2005,** *75A* (3), 742-753.
12. Whittaker, J. L.; Choudhury, N. R.; Dutta, N. K.; Zannettino, A., *J. Mater. Chem. B* **2014,** *2* (37), 6259-6270.
13. Whittaker, J. L.; Dutta, N. K.; Elvin, C. M.; Choudhury, N. R., *J. Mater. Chem. B* **2015,** *3* (32), 6576-6579.
14. Srivastava, A.; Kumar, A., *J. Mater. Sci.: Mater. Med.* **2010,** *21* (11), 2937-2945.
15. Shukunami, C.; Ohta, Y.; Sakuda, M.; Hiraki, Y., *Exp. Cell Res.* **1998,** *241* (1), 1-11.
16. Shukunami, C.; Ishizeki, K.; Atsumi, T.; Ohta, Y.; Suzuki, F.; Hiraki, Y., *J. Bone Miner. Res.* **1997,** *12* (8), 1174-1188.
17. Vandyke, K.; Fitter, S.; Zannettino, A. C. W., *Blood Cancer J.* **2011,** *1*, e2.
18. Ahmed, F.; Choudhury, N. R.; Dutta, N. K.; Zannettino, A.; Knott, R., *Biomacromolecules* **2013,** *14* (11), 3850-3860.
19. Vandyke, K.; Dewar, A. L.; Diamond, P.; Fitter, S.; Schultz, C. G.; Sims, N. A.; Zannettino, A. C. W., *J. Bone Miner. Res.* **2010,** *25* (8), 1759-1770.

20. Aoki, H.; Tomita, N.; Morita, Y.; Hattori, K.; Harada, Y.; Sonobe, M.; Wakitani, S.; Tamada, Y., *Bio-med. Mater. Eng.* **2003,** *13* (4), 309.
21. Bryant, S. J.; Anseth, K. S., *J. Biomed. Mater. Res.* **2002,** *59* (1), 63-72.
22. Allen, J. L.; Cooke, M. E.; Alliston, T., *Mol. Biol. Cell* **2012,** *23* (18), 3731-3742.
23. Kim, J.-H.; Lee, G.; Won, Y.; Lee, M.; Kwak, J.-S.; Chun, C.-H.; Chun, J.-S., *Proc. Natl. Acad. Sci.* **2015,** *112* (30), 9424-9429.
24. Barry, F.; Boynton, R. E.; Liu, B.; Murphy, J. M., *Exp. Cell Res.* **2001,** *268* (2), 189-200.
25. Han, F.; Adams, C. S.; Tao, Z.; Williams, C. J.; Zaka, R.; Tuan, R. S.; Norton, P. A.; Hickok, N. J., *J. Cell. Biochem.* **2005,** *95* (4), 750-762.
26. Elvin, C. M.; Werkmeister, J. A.; Misook, K.; Lyons, R.; Tebb, T.; Ramshaw, J., Synthesis and properties of cross-linked recombinant pro-resilin: an insect rubber-like biomaterial. In *Fibrous Protein workshop*, Mount Eliza, Australia, 2008.
27. Vashi, A.; Ramshaw, J.; Glattauer, V.; Elvin, C. M.; Lyons, R. E.; Werkmeister, J. A., *Biofabrication* **2013,** *5* (3), 035005.
28. Renner, J. N.; Cherry, K. M.; Su, R. S. C.; Liu, J. C., *Biomacromolecules* **2012,** *13* (11), 3678-3685.
29. Chao, P.-H. G.; Yodmuang, S.; Wang, X.; Sun, L.; Kaplan, D. L.; Vunjak-Novakovic, G., *J. Biomed. Mater. Res., Part B* **2010,** *95B* (1), 84-90.
30. Sanz-Ramos, P.; Mora, G.; Vicente-Pascual, M.; Ochoa, I.; Alcaine, C.; Moreno, R.; Doblaré, M.; Izal-Azcárate, Í., *Connect. Tissue Res.* **2013,** *54* (3), 159-166.
31. Park, H.; Guo, X.; Temenoff, J. S.; Tabata, Y.; Caplan, A. I.; Kasper, F. K.; Mikos, A. G., *Biomacromolecules* **2009,** *10* (3), 541-546.
32. Park, J. S.; Woo, D. G.; Sun, B. K.; Chung, H.-M.; Im, S. J.; Choi, Y. M.; Park, K.; Huh, K. M.; Park, K.-H., *J. Controlled Release* **2007,** *124* (1–2), 51-59.
33. Kim, J.; Lin, B.; Kim, S.; Choi, B.; Evseenko, D.; Lee, M., *J. Biol. Eng.* **2015,** *9* (1), 1-11.
34. Bosnakovski, D.; Mizuno, M.; Kim, G.; Takagi, S.; Okumura, M.; Fujinaga, T., *Biotechnol. Bioeng.* **2006,** *93* (6), 1152-1163.

Chapter 9: Summary and Recommendations

9.1 Summary

This chapter summarises the outcomes of the research investigations carried out in this thesis. In this work three types of biomimetic hydrogels have been developed based on: i) physical interactions, ii) chemical crosslinking and iii) chemical crosslinking in the presence of non-covalent interactions.

The key research outcomes and highlights of the present investigation are as follows.

1) In Chapter 3 the structure and morphology of a biomimetic hybrid physical hydrogel was investigated by inducing the coassembly of the recombinant resilin protein, Rec1-resilin, with rigid protein-based materials. The addition of a rigid model polypeptide, poly-L-proline, or a hydrophobic rigid protein, regenerated silk fibroin (RSF) to Rec1-resilin, was shown to induce more ordered conformations and increased the hydrophobicity, which tuned the lower critical solution temperature (LCST) of the system to lower values close to room temperature. It was observed that time and temperature were critical parameters to control the coassembly behaviour of both systems. In addition, the Rec1-resilin/RSF coassembly resulted in the formation of an irreversible physical gel, and this facile method of gelation and tuning material properties can be useful for a range of applications, including drug delivery and tissue engineering applications.
2) The photo-chemical crosslinking of RSF was investigated to achieve a hydrogel with covalent network and is presented in Chapter 4. A ruthenium-mediated photo-crosslinking method was employed that covalently crosslinked the tyrosine residues present in the structure of RSF within minutes of irradiation with white light. The RSF hydrogels exhibited impressive modulus values that were tuned from 4000 MPa to 81 MPa with hydration levels of 0.08 and 0.454 g water/g RSF, respectively. These RSF hydrogels were also shown to support the attachment and growth of pre-chondrocyte cells, highlighting their potential for tissue engineering applications.
3) The high modulus values of the RSF photo-crosslinked hydrogels in Chapter 4 indicate their potential use for load-bearing tissue engineering applications; however,

in order to be used for these applications it is necessary to tune the elasticity of the hydrogels to lower values and improve the swelling characteristics as RSF is a predominantly hydrophobic protein. Thus, the formation of two types of RSF-based hybrid hydrogels, Rec1-resilin/RSF and RSF/PVCL, were presented in Chapter 5. Both fabrication methods employ the rapid ruthenium-mediated photo-crosslinking method that forms covalent di-tyrosine crosslinks. The ability to co-crosslink a resilin-based material and a silk-based material by taking advantage of the tyrosine residues present in both proteins was demonstrated for the first time. Also, the DN hydrogel technique was employed for a silk-based material for the first time in the formation of the RSF/PVCL DN hydrogels that contain the rigid chemically crosslinked phase and the softer PVCL phase entrapped by strong physical interactions. It was observed the by combining rigid and soft phases in one material, Rec1-resilin/RSF and RSF/PVCL, the bulk properties of the materials could be tuned to values that were more relevant for cartilage tissue engineering. In particular, the storage modulus of the Rec1-resilin/RSF hydrogel was tuned to ~6.56 MPa, which is close to that of articular cartilage or the intervertebral disc (IVD). Also, the RSF/PVCL hydrogels demonstrated tuneable modulus values ranging from ~22 to 0.58 MPa that were more relevant for cartilage tissue engineering. Both types of RSF-based hybrid hydrogels demonstrated tuneable swelling capacity. This work demonstrates the potential of RSF-based hybrid hydrogels for cartilage tissue engineering.

4) In chapter 6, the use of a different fabrication method to prepare hybrid biomimetic nanofibrous mats with physical interactions was examined. The excellent electrospinnability of PVCL from aqueous solutions was exploited; however, the resultant fibres were observed to dissolve rapidly in water. Thus, a one-step electrospinning method that utilises the hydrogen bonding interactions between PVCL and tannic acid (TA) was optimised to form insoluble TA/PVCL nanofibres, which improves the potential use of PVCL in biomedical applications without further chemical modification. Also, the development of core/shell nanofibres composed of the thermo-responsive PVCL polymer and RSF has been achieved for the first time. This work provides a solid platform for the formation of composite fibres that overcomes the aqueous solubility issue of PVCL without the need for further chemical modification. Also, these materials have potential to provide a biomimetic environment for cell growth due to the RSF shell combined with promising controlled drug delivery due to the thermo-responsiveness of PVCL.

5) The tuneable bulk properties, including elasticity and swelling capacity, of the RSF, Rec1-resilin/RSF and RSF/PVCL hybrid hydrogels were evaluated in Chapters 4 and 5. According to hydrogel theory, the crosslink density and mesh size of hydrogels dictate their overall mechanical and swelling properties. Thus, a detailed understanding of the microstructure of the RSF-based hydrogels using combined small angle neutron scattering (SANS) and ultra small angle neutron scattering (USANS) is presented in chapter 7, which covers microstructural information of the gels over four orders of magnitude in size (~10 Å to 10 μm). Based on the obtained results, it was concluded that the RSF-based hydrogels possessed characteristic features of a gel-like structure; however, the classical gel models did not provide a suitable fit for the data. The results showed that the R_g values of the frozen-in heterogeneities were inversely proportional to the crosslink density. Also, USANS analysis demonstrated the presence of much larger structures in the order of thousands of Å that are expected to be related to the porous nature of the hydrogels.
6) In this work, the ability of various engineering RSF-based hydrogels to provide a biomimetic environment for cell growth was studied in chapter 8. By forming hybrid RSF-based hydrogels, the swelling and elasticity properties were tuned to values more relevant for cartilage and thus, the capacity of the RSF, Rec1-resilin/RSF and RSF/PVCL hydrogels to support the adhesion and proliferation of a pre-chondrocyte cell line (ATDC5) was investigated. The stiffness and water content of the hydrogels were observed to alter the cellular proliferative and differentiation capacity. In particular, the less rigid RSF/PVCL hydrogels exhibited the most favourable chondrogenic differentiation properties. However, the surfaces could be modified further to stimulate greater levels of collagen type II and Sox9 expression. This study shows for the first time the potential of the Rec1-resilin/RSF and RSF/PVCL hydrogels for cartilage tissue engineering and provides a platform for further development in this area.

9.2 Recommendations

This research investigation clearly demonstrates the fabrication of biomimetic RSF-based hydrogels that employ physical and chemical interactions to tune the bulk properties of the hybrid hydrogels. Also, it provides a platform for the development of RSF-based hydrogels and electrospun mats that demonstrate potential use for cartilage tissue engineering. The

hydrogel must be able to withstand the shear, tensile and compressive forces in order to be suitable for cartilage tissue engineering applications. Due to time constraints, study into the tensile properties of the hydrogels was only undertaken and significant scope remains for future work to study the hydrogels compressive modulus in the future. The Rec1-resilin/RSF hydrogels were studied at one mass ratio (1:0.75); however, the study of additional ratios is expected to lead to further potential applications in two-dimensional coating or drug delivery. In the future, the study of different ratios of Rec1-resilin and RSF would be useful to develop and understanding of the level of tuneability possible. The PVCL/RSF core/shell nanofibres were fabricated using co-axial electrospinning and the optimum solution and processing conditions to achieve a core/shell morphology were established. However, further study of the properties of the core/shell fibres, including wettability, porosity, mechanical properties, thermo-responsiveness and ability to support cell attachment, proliferation and differentiation were not possible due to time constraints. It is recommended that future work to establish these properties of the PVCL/RSF core/shell fibres is required to reveal the full potential of this novel material. The SANS/USANS study provided an insight into the microstructure-property relationship of the RSF-based hydrogels; however, further study into the hydrogel structure with SANS/USANS experiments are required, including contrast variation (systematically changing the H_2O/D_2O ratio of the solvent), response to applied shear, and dehydration (stepwise dehydration/hydration). Also, supporting information from other techniques (SEM, TEM and EPR) would also be valuable and complimentary; however, were not possible within the scope of this research. The potential of the RSF, Rec1/RSF and RSF/PVCL hydrogels to induce chondrocyte cell growth and differentiation was only elucidated in this study; however, further modification and cell encapsulation studies are necessary to improve chondrocyte differentiation and further optimise these materials for cartilage tissue engineering applications, but were not possible within the timeframe. Finally, this research contributes to the overall goal of developing an important class of biomimetic hydrogels with facile synthesis approaches, understanding material interactions, structure-property relationship and developing biomaterials with enhanced properties that can be injected *in vivo* for cartilage tissue engineering applications.